ÉCOLE POLYTECHNIQUE DE BRUXELLES
UNIVERSITÉ LIBRE DE BRUXELLES

Optimization and Uncertainty Quantification of kinetic mechanisms for renewable fuels and sustainable combustion technologies

Thesis presented by Andrea Bertolino
in fulfilment of the requirements of the PhD Degree in Engineering Sciences and Technology (ULB - "Docteur en Sciences de l'ingénieur et technologie") & Industrial Chemistry and Chemical Engineering (POLIMI)

Academic year 2020-2021

Supervisor : Professor Alessandro PARENTE
Université Libre de Bruxelles
Co-supervisor : Professor Alessio FRASSOLDATI
Politecnico di Milano

Thesis jury :
Axel COUSSEMENT (Université libre de Bruxelles, Chair)
Alberto CUOCI (Politecnico di Milano)
Alison Tomlin (University of Leeds)
Liming Cai (Tongji University)

fnrs
LA LIBERTÉ DE CHERCHER

UNIVERSITÉ LIBRE DE BRUXELLES
POLITECNICO DI MILANO

OPTIMIZATION AND UNCERTAINTY QUANTIFICATION OF KINETIC MECHANISMS FOR RENEWABLE FUELS AND SUSTAINABLE COMBUSTION TECHNOLOGIES

Doctoral Dissertation of:
Andrea Bertolino

Supervisor:
Prof. Alessandro Parente

Co-supervisor:
Prof. Alessio Frassoldati

Doctoral Committee:
Prof. Alison Tomlin
Prof. Liming Cai
Prof. Alberto Cuoci

Secretary:
Prof. —

The Chair of the Doctoral Program:
Prof. Axel Coussement

Abstract

In the present thesis, a data-driven approach for the optimization of detailed kinetic mechanisms is proposed. This methodology is based on heuristic optimization algorithms. The curve matching (CM) index is proposed as alternative error function to classical norms. In CM calculation the similarities between model' responses and experimental data is measured quantitatively and qualitatively, considering also the first derivatives and shapes of corresponding splines. A novel protocol for the optimization of PLOG reactions is established. The interdependencies between Arrhenius expressions at different pressures were accounted for by handling three random variables for each PLOG, regardless of the number of discrete pressures specified in the mechanism. The Cumulative Sensitivity Function (CSF) and a Cumulative Impact Function (CIF) were introduced to make reaction selection automatic, fast, and efficient. The development above-mentioned methodology represents the underlying functioning of the OptiSMOKE++, a new C++ toolbox for the optimization of detailed kinetic mechanisms. OptiSMOKE++ is an flexible interface for the communications between other open source softwares like OpenSMOKE++, DAKOTA, Curve Matching and SciExpeM. This framework enables the simultaneous use of experimental targets from different facilities, i.e. Batch Reactors, Plug Flow Reactors (PFR), Perfectly Stirred Reactor (PSR), Shock Tubes (ST), Rapid Compression Machines (RCM) and 1D flames. Using this methodology, an optimized mechanism for ammonia combustion is obtained over a wide range

of operating conditions. The approach involved all 101 kinetic parameters simultaneously. The role of diluents like H_2O and CO_2 in operating conditions relevant to applications for MILD combustion of hydrogen and syngas was discussed and analysed by means of a virtual species analysis (VSA), Global Sensitivity Analysis (GSA), and Optimization. The VSA suggests that measurements of ignition delay time (IDT) and species concentrations in perfectly stirred reactors (PSR) in diluted conditions are ideal candidates for the estimation of collision efficiencies as their physics is significantly third body driven. Eventually, the errors introduced by the replacement of the TROE formulation for fall-off reactions with PLOG were quantified for hydrogen combustion, and a method to extract information from data about third body efficiency of strong colliders in PLOG formulation was proposed in case high-level ab-initio calculations are not available. Finally, an experimental campaign was performed to investigate options for optimal operating conditions for the Université Libre de Bruxelles (ULB) flameless furnace fired with ammonia/hydrogen blends. In particular, the campaign aimed at identifying trade-off between NOx emissions and ammonia slip. In Reynolds-averaged Navier-Stokes simulations, substantial differences between mechanisms predictions and experimental data were observed in terms of NOx emissions. A combination of Uncertainty Quantification (UQ) and Chemical Reactor Network (CRN) was adopted to propagate the uncertainty of NOx kinetics to the CFD simulations.

Résumé

Dans cette thèse, une approche basée sur les données pour l'optimisation des mécanismes cinétiques détaillés est proposée. Cette méthodologie est basée sur des algorithmes d'optimisation heuristiques. L'indice de correspondance des courbses (Curve Matching) est proposé comme fonction de perte alternative aux normes classiques. Dans le calcul du CM, les similarités entre les réponses du modèle et les données expérimentales est mesurée quantitativement et qualitativement, en considérant les dérivées premières et les formes des splines correspondants. Un nouveau protocole pour l'optimisation des réactions de PLOG est établi. Les interdépendances entre les expressions d'Arrhenius à différentes pressions ont été prises en compte en manipulant trois variables aléatoires pour les réactions PLOG, et ce quelque soit soit le nombre de pressions discrètes spécifiées dans le mécanisme. Les fonctions de sensibilité cumulée (CSF) et d'impact cumulé (CIF) sont introduites afin d'améliorer la qualité de l'analyse et pour rendre la sélection des réactions automatique, rapide et efficace. La méthodologie de développement mentionnée ci-dessus représente le fonctionnement sous-jacent d'OptiSMOKE++, une nouvelle boîte à outils C++ pour l'optimisation des de mécanismes cinétiques détaillés. OptiSMOKE++ est une interface flexible que Pouvant être couplée avec des logiciels open-source tels que OpenSMOKE++, DAKOTA, Curve Matching et SciExpeM. Ce cadre permet l'utilisation simultanée de cibles expérimentales provenant de différentes installations, comme des réacteurs dis-

continus, PFRs, PSRs, ST, RCMs et flammes 1D. En utilisant cette méthodologie, un mécanisme est optimisé pour la combustion de l'ammoniac sur une large gamme de conditions de fonctionnement. L'approche fait intervenir simultanément les 101 paramètres cinétiques. Le rôle des diluants tels que H2O et CO2 dans les conditions d'opérations pertinentes pour les applications de combustion MILD de l'hydrogène et du gaz de synthèse a été a effacer discuté et analysé à l'aide d'une analyse virtuelle des espèces (VSA), d'une analyse de sensibilité globale (GSA) et de l'optimisation. Dans des conditions de dilution, la VSA suggère que les mesures du délai d'allumage (IDT) et des concentrations d'espèces dans les réacteurs parfaitement mélangés (PSR) sont des candidats idéaux pour l'estimation de l'efficacité des collisions. L'estimation de l'efficacité des collisions, car leur physique est fortement influencée par les corps tiers. Les erreurs introduites par le remplacement de la formulation TROE pour les réactions de retombée avec PLOG ont été quantifiées pour la combustion de l'hydrogène, et une méthode pour extraire des informations à partir des données sur l'efficacité du troisième corps des collisionneurs forts dans la formulation PLOG a été proposée dans le cas où des calculs d'abitio de haut niveau ne sont pas disponibles. Enfin, une campagne expérimentale a été réalisée pour étudier les options de conditions de fonctionnement optimales pour le brûleur sans flamme de l'ULB alimenté par des mélanges ammoniac/hydrogène. En particulier, la campagne visait à identifier le compromis entre les émissions de NOx et de l'ammoniac. Dans les simulations RANS, des différences substantielles entre les prédictions des mécanismes et les données expérimentales ont été observées en termes d'émissions de NOx. Une combinaison de quantification d'incertitude (UQ) et de réseau de réacteurs chimiques (CRN) a été adoptée pour propager l'incertitude de la cinétique des NOx aux simulations CFD.

Sommario

Questa tesi propone un approccio per l'ottimizzazione di meccanismi cinetici dettagliati. Questa metodologia è basata su algoritmi di ottimizzazione euristici. L'indice di similarità tra curve (Curve Matching) è proposto come funzione obiettivo alternativa alle classiche norme (L2/L1). Nel calcolo del CM, la somiglianza tra le risposte dei modelli e i dati sperimentali viene misurata quantitativamente e qualitativamente, considerando anche le derivate prime e le forme delle corrispondenti spline. Un nuovo protocollo per l'ottimizzazione delle reazioni PLOG è stabilito, dove le interdipendenze tra le espressioni di Arrhenius a diverse pressioni vengono prese in considerazione gestendo tre variabili casuali per ogni PLOG, indipendentemente dal numero di pressioni discrete specificate nel meccanismo. La funzione di sensibilità cumulativa (CSF) e una funzione di impatto cumulativo (CIF) sono stati introdotti per rendere la selezione delle reazioni automatica, veloce ed efficiente. La metodologia di sviluppo di cui sopra rappresenta il funzionamento di base di OptiSMOKE++, un nuovo toolbox C++ per l'ottimizzazione di meccanismi cinetici dettagliati. OptiSMOKE++ è un'interfaccia flessibile per la comunicazione tra altri software open source come OpenSMOKE++, DAKOTA, Curve Matching e SciExpeM. Questa struttura permette l'uso simultaneo di target sperimentali da diverso tipo, come ad esempio reattori batch, PFRs, PSRs, ST, RCMs e fiamme 1D. Usando questa metodologia, un meccanismo ottimizzato per la combustione dell'ammoniaca è ottenuto su una vasta gamma di condizioni operative.

Quest'ultimo lavoro coinvolge 101 parametri cinetici simultaneamente. Il ruolo dei diluenti come H2O e CO2 nelle condizioni operative rilevanti per le applicazioni di combustione MILD di idrogeno e syngas è stato discusso e analizzato per mezzo di un'analisi alle specie virtuali (VSA), Global Sensitivity Analysis (GSA) e ottimizzazione. La VSA suggerisce che le misurazioni del tempo di ritardo dell'accensione (IDT) e delle concentrazioni di specie in reattori perfettamente agitati (PSR) in condizioni diluite sono candidati ideali per la stima delle efficienze di collisione in quanto la loro fisica è significativamente guidata dal terzo corpo. Alla fine, gli errori introdotti dalla sostituzione della formulazione TROE con il formato PLOG sono stati quantificati per la combustione dell'idrogeno, e un metodo per estrarre informazioni dai dati sull'efficienza di terzo corpo nella formulazione PLOG è stato proposto nel caso in cui calcoli abitio di alto livello non siano disponibili. Infine, una campagna sperimentale nel forno dell'ULB è stata eseguita per studiare la fattibilità della combustione senza fiamma con miscele di ammoniaca/idrogeno. In particolare, la campagna mira a identificare il trade-off tra emissioni di NOx e ammoniaca. Nelle simulazioni RANS, sono state osservate differenze sostanziali tra previsioni e i dati sperimentali in termini di emissioni di NOx. Una combinazione di Uncertainty Quantification (UQ) e Chemical Reactor Network (CRN) è stata adottata per propagare l'incertezza della cinetica di NOx attraverso le simulazioni CFD.

Contents

Nomenclature

Acronyms

Abbrevation	Description
GHG	greenhouse gas
RE	renewable energy or relative error
SEC	smart energy carriers
SEC	smart energy carriers
P2F	power to fuel
HC	hydrocarbons
SNCR	selective non-catalytic reduction
MILD	moderate or intense low-oxygen dilution
EGR	exhaust gases recirculation

HITAC	high temperature air combustion
CDC	colorless distributed combustion
DNS	direct numerical simulations
PSR	perfectly stirred reactor
WSR	well stirred reactor
JHC	jet in hot coflow
PFR	plug flow reactor
ER	equivalence ratio
PLOG	pressure logarithmic interpolation
IDT	ignition delay time
RBG	reference bath gas
CFD	computational fluid dynamics
AI-TST-ME	abinitio transition stat theory-based master equation
UQ	uncertainty quantification
B2B-DC	bound to bound data collaboration
PCE	polynomial chaos expansion
MUMPCE	method of uncertainty minimization using PCE
FFCM	foundational fuel chemistry model
GA	genetic algorithm
PSO	particle swarm optimization
EA	evolutionary algorithm
CM	curve matching
ULB	université libre de bruxelles
obj	objective function

NE	number of experimental dataset
NY	number of data point in a dataset
LHS	latin hypercube sampling
HDMR	high-dimensional model representation
SM	solution mapping
MC	monte carlo
TC	test case
CSF	cumulative sensitivity function
CIF	cumulative impact function
RCM	rapid compression machine
ST	shock tube
PES	potential energy surface
VRC-TST	variable reaction coordinate transition state theory
JSR	jet stirred reactor
HAB	height above the burner
LSA	local sensitivity analysis
GSA	global sensitivity analysis
VSA	virtual species analysis
LFS	laminar flame speed
FTIR	fourier transform infrared
ID	internal diameter
RANS	Reynolds-averaged Navier-Stokes
PaST	Partially stirred reactor
ROPA	rate of production analysis

Latin Symbols

Symbol	Description	Units
A	pre-exponential factor	$\mathrm{cm}-\mathrm{mol}-\mathrm{s}$
n	temperature exponent	$\mathrm{cm}-\mathrm{mol}-\mathrm{s}$
E_a	activation energy	calmol^{-1}
F	fuel or canonical distribution	$-$
OX	oxidiser	$-$
P	products or pressure	$-$
$[X_i]$	molar concentration	molm^3
k	kinetic constant	$\mathrm{cm}-\mathrm{mol}-\mathrm{s}$
$\tilde{C}_p$	molar specific heat	$\mathrm{calmol}^{-1}\mathrm{K}^{-1}$
$\tilde{H}$	molar specific enthalpy	calmol^{-1}
$\tilde{S}$	molar specific entropy	$\mathrm{calmol}^{-1}\mathrm{K}^{-1}$
K^e	equilibrium constant	$-$
R	ideal gas constant	$\mathrm{calmol}^{-1}\mathrm{K}^{-1}$
r	reaction rate	$\mathrm{molcm}^{-3}\mathrm{s}^{-1}$
f	uncertainty factor	$-$
P	probability	$-$
V	covariance matrix or variance	$-$
d	dissimilarity measure	$-$
L_1	L1 norm	$-$
L_2	L2 norm	$-$

C	concentration or correction	molm^{-3} or $-$
B	sensitivity matrix	$-$
p	parameter or pressure	$-$
J	Jacobian matrix	$-$
s	local sensitivity coefficient	$-$
$\tilde{s}$	normalized local sensitivity coefficient	$-$
I	impact coefficient	$-$
S	global sensitivity coefficient	$-$
E	estimated value	$-$
U	random variable	$-$
H	hessian	$-$
X	random variable for PLOG optimization	$-$
x	molar fraction	molmol^{-1}
$[M]$	mixture concentration	molm^{-3}

Greek Symbols

Symbol	Description	Units
υ	stoichiometric coefficients	$-$
α	third body efficiency or logarithm of pre-exponential factor or mode strengths in PCE	$-$

κ	natural logarithm of kinetic constant	–
ϵ	activation temperature or experimental error	–
σ	standard deviation	–
ζ	independent variable	s or m
$\boldsymbol{\theta}$	vector of model parameters	–
$\boldsymbol{\omega}$	vector of selected model parameters	–
$\boldsymbol{\xi}$	vector active model parameters or germ	–
Λ	PCE functional	–
λ	set of multi-indices	–
γ	single multi-index	–
ψ	polynomial belonging to family of orthogonal polynomials	–
ω	entire sample space	–
∇	mathematical operator	–
χ	canonical distribution	–
β	third body efficiency in PLOG extended format	–
τ	time scale or residence time	s

Superscripts-Subscripts

Symbol	Description
f	forward
b	backward
$-$	average or reference
0	nominal or initial
p	pearson
SP	species
*	re-parametrized
TH	thermal effect
TB	third body effect
CH	chemical effect
∞	high-pressure limit
low	low-pressure limit
r	reduced or relative to the r^{th} reaction
mix	mixing
a	air
f	fuel
rec	recirculated

CHAPTER 1

Introduction and State-of-the-art

Nowadays our society massively relies on energy. Our lifestyles contribute to increase consumption, which is estimated to grow of about 20% by 2040. The way we produce energy has a demonstrated impact over the environment: climate-change is affected by greenhouse gas production, particularly by CO_2 emissions, which represents 80% of the global anthropogenic emissions [174]. Global warming and air pollution is pushing to identify new solutions that can reduce CO_2 and Greenhouse Gas (GHG) emissions ([187]), through the replacement of fossil fuels with renewable energy (RE) (e.g. solar, wind). In this context, a significant adoption of renewable sources is expected in the future years, to meet the long-term objective of CO_2 neutrality and mitigate the effects of global warming. The European objectives for 2030 consist in cutting at least 50% of greenhouse gas (GHG) emissions (from 1990 levels), with a minimum sharing of renewable of 32%, and improving energy efficiency of about 32.5% [1]. However, The intermittent nature of renewable sources requires the development of storage solutions that can guarantee the availability of the

required energy supply, when renewable sources are not available. Indeed, chemical molecules are characterised by very large energy densities (tens of MJ/kg), and they are ideal candidates for energy-intensive processes, where the use of renewable sources (e.g. wind and solar) and other storage solutions (e.g. batteries) is not realistic. Thus, energy storage in the form of chemical compounds, sometimes indicated as Smart Energy Carriers (SEC), can lead to a true integration between renewable sources and existing infrastructure for energy conversion, such as combustion systems. Notwithstanding the intermittent nature of RE sources (wind, solar), continuous, and on demand, power production can be achieved by exploiting RE surplus in Power to Fuel (P2F) techniques ([50]). Nevertheless, combustion science will need to undergo profound innovation, to promote novel technologies able to deal simultaneously with resources availability, and environmental impact, by avoiding pollutants formation at the source, rather than treat them downstream. The fuels, industry relies upon, are and will continue changing asking for the new technology to be fuel flexible. Syngas, biogas, natural gas, hydrogen and ammonia enriched fuels are emerging. Yet, attention must be paid also to pollutants such as NOx and soot. Since even “clean gases” (i.e. hydrogen) form NO and NO_2 (i.e. nitric oxides: NOx) at high temperatures via the Zeldovich mechanism [67], also known as "Thermal NOx" mechanism. Other kinetics paths lead to NO formation (prompt, fuel, N_2O-intermediate, NNH-intermediate); NO is subsequently converted to NO_2 in the atmosphere, contributing to photochemical smog and acid rains. Soot is a known human carcinogen, also responsible for other respiratory diseases, since it contributes to particulate matter. It derives from incomplete combustion of hydrocarbons in fuel-rich mixtures, and once widespread into the atmosphere, soot can directly absorb incoming solar radiation, causing warming and playing a role in ice melting, due to its high emissivity.

1.1 Hydrogen and Ammonia as Smart Energy Carriers

Hydrogen is one of the most promising among the SEC, in spite of the challenges related to its storage and transportation. In order to bypass these complications, "green" H_2 may be converted to other molecules with different properties. For instance, H_2 can be produced via water electrolysis exploiting the energy surplus of solar panels [12], converted into ammonia to facilitate its

storage and transportation [91], eventually re-converted in-situ for power generation [12]. Originally, ammonia was given prominence for its role in both fuel NO_x formation and abatement through selective non-catalytic reduction (SNCR) (see [34]). The importance of ammonia is also related to other renewable energy sources: for example, it is a by-product of anaerobic digestion of municipal wastewater sludges [5], and it is found in trace amounts in biogas [171]. However, Ammonia shows a very high potential ([91]), as it has very high H_2 density and it can be liquefied at pressures higher than 9.9 bar at ambient temperature. From an economical perspective, "green ammonia" was also found to be competitive with natural gas-based ammonia plants ("gray ammonia"), as a result of the recent cost reductions in solar and wind technologies ([132]). However, compared to other liquid fuels (e.g. gasoline), ammonia presents some safety issues, being considered a high health hazard, since it is corrosive to the skin, eyes and lungs. Once it turns to gas, ammonia is colorless with a sharp, penetrating, intensely irritating odor, and it contributes to atmospheric aerosol loading, particularly to particulate matter (PM) 2.5 (i.e. small particles). Takizawa [175] and Hayakawa [73] performed laminar flame speed measurements for ammonia in different conditions, showing its limited reactivity, which may lead to combustion instabilities ([189]). To overcome these practical issues, NH_3 combustion doped with hydrogen was tested in internal combustion engines ([62]), rapid compression machines ([134]), and swirl burners ([188,189]) for utilisation within a gas turbine environment, where it was found to have significant NOx emissions. Recently, Dai et al. [38] performed experiments using $NH_{3/}$DME mixture, and studied their interaction in a rapid compression machine.

The pioneering work of Miller and Bowman [113] in modelling of ammonia kinetics, was validated via several species measurements and laminar flame speeds ([71, 106]). Lately, Glarborg [67] reviewed the nitrogen chemistry in combustion, including the NH_3 sub-mechanism. Nowadays, other widely validated kinetic models for ammonia oxidation are available in literature, for instance those from Shrestha [157], Otomo [127] and Stagni [170]. The combustion kinetics of ammonia (NH_3) is one of the most active research fields, due to the high potential of ammonia as a fuel, from both an economic and a technical perspective [91]. The combined use of NH_3 with conventional fuels like H_2 or CH_4 has also been studied in order to improve shortcomings related to its low

reactivity [99, 189]. Also, optimal operating conditions were found to minimize NOx emissions [91]. Therefore, several mechanisms describing the oxidation of NH_3 and NH_3/H_2 fuel blends were developed [8, 100, 107, 157]. Glarborg et al. [67] recently proposed a comprehensive nitrogen chemistry model, including ammonia itself. This mechanism was recently updated to account for the interactions between DME and NH_3 during ignition at high pressure and low-temperatures [38]. Anyway, uncertainties still persist in the characterization of ammonia chemistry for an accurate prediction of ignition, speciation, and laminar flame speed [67]. The optimization of relatively compact kinetic mechanisms, such as methane, hydrogen, and ammonia is particularly attractive, because of i) the large availability of high-fidelity data [36], ii) the current interest in e-fuels produced from renewable energy [50], and iii) their compact size allowing to benchmark the suitability of different optimization algorithms before their application to more complex networks.

1.2 MILD combustion

Oxyfuel combustion [201] overcomes NOx formation by eliminating or strongly limiting nitrogen content in the oxidizer. Over the last years, particular attention was paid to flameless combustion, introduced by [206], which is characterized by preheated and diluted reactants, non-visible flame, and uniform distributed temperatures, induced by internal exhaust gas recirculation (EGR). Later on, high temperature air combustion (HiTAC) ([85]), Moderate or Intense Low oxygen Dilution (MILD) ([28]) and Colorless Distributed Combustion (CDC) ([6, 7]) were also investigated. Moderate or Intense Low-oxygen Dilution (MILD) [28], or flameless, combustion is well-known for the inhibition of pollutant formation, such as NOx and soot. This regime is obtained through preheating of the oxidizer flow, and a specific internal fluidynamics of the burner in conjunction with high velocity inlets, responsible for internal flue gases recirculation [206]. This results in a localized reduction of O_2, and a strong dilution of the fuel/oxidizer mixture in combustion products (i.e CO_2 and H_2O), leading to delayed ignition and to a homogeneous as well as distributed reaction zone [174] operating at intermediate temperatures. This guarantees very large combustion and energy efficiencies, while suppressing both soot and thermal NOx formation, and causes the disappearance of the flame front and the asso-

ciated temperature gradients [128], with beneficial effects on metallic materials longevity and reliability [28]. In recent years, researchers focused on the nature of the reaction structure, and recent evidences suggest that it is made of many thin reaction zones, interacting with each other [128]. From a modelling perspective, the macroscopically distributed nature of MILD combustion questions the use of flamelet-like models, as shown in Direct Numerical Simulations (DNS) [114]. Minamoto and Swaminathan [114] confirmed the need for non-flamelet approaches to deal with the frequent interactions between reaction zones in MILD combustion, advocating canonical reactors, such as perfectly stirred reactors (PSR). Cavaliere and De Joannon [28] suggested that, in terms of fluid-dynamics, the reactive zone in MILD combustion might evolve as in a well stirred reactor (WSR). The feasibility of such an approximation was recently demonstrated through systematic comparison with experimental data from attached flames (see Chen et al. [31]). Lately, Medwell et al. [110] successfully extended such hypothesis to the Jet in Hot Coflow (JHC) flames, focusing on the chemistry dominated effects, to distinguish among two different resembling regimes in non-premixed flames, i.e. MILD combustion and autoignitive lifted flames. Conclusively, Zieba et al. [212] proposed to adopt a series of plug flow reactors (PFRs) with recirculation, while Rocha et al. [141] adopted a freely-propagating-flame model with exaust gas recirculation (EGR). From the chemical kinetics perspective, MILD combustion is a very challenging process to model. The well mixed conditions of the process imply that fuel conversion is chemically controlled, thus requiring detailed kinetic mechanisms to capture relevant phenomena. Experimental data are crucial to understand the kinetic role of diluents such as CO_2 and H_2O, especially in third body reactions [66, 146], and to assess the uncertainty related to currently employed kinetic parameters, in particular collision efficiencies, whose knowledge is crucial in low-temperature combustion [36,86]. Other open issues in MILD regime concern the formation of pollutants. Indeed, unconventional routes, such as N_2O and NNH intermediate drive NOx formation [65], since thermal NOx is inhibited by the reduced temperatures. In spite of the reasonable number of investigations involving natural gas or methane (See [39,79,128,133,174,194,195]), the amount of detailed studies available for furnaces operating under flameless or MILD conditions using non-conventional fuels is scarce and limited to few operating conditions (see [10, 53, 116, 147]). For the first time in literature, [169]

investigated the feasibility of pure ammonia combustion MILD using a lab-scale cyclonic burner, varying the mixture equivalence ratio, nominal thermal power and inlet preheating level. They pointed out the need of operating above 1300 K to ensure both combustion stability and low NOx emissions. A minimum in NO_x emissions (less than 100 ppm) was observed for equivalence ratios (ER) between 1 and 1.1, with tolerable ammonia slip.

1.3 Open challenges in combustion kinetics for diluted conditions

Due to the role of diluents in MILD regime, kinetic mechanisms validated using conventional combustion data usually result in non-accurate estimation for these conditions [11, 63, 105, 146] . In several recent studies of methane combustion [11, 145], the kinetic and thermal contributions of diluents like CO_2 and H_2O was isolated by introducing fictitious inert species, with the same thermodynamic properties of the diluent, inside the mechanism. Sabia et al. [146] demonstrated that the high collisional efficiencies of CO_2 and H_2O affect the ignition delay time of low-alkanes, mainly through reactions which are related to the H_2/O_2 mechanism. Recently, Sabia and De Joannon [145] experimentally studied hydrogen oxidation in lean and highly diluted conditions using a perfectly stirred reactor, and showed inconsistencies with recent model predictions. Curran [36] briefly described the impact of third body efficiencies for the laminar flame speed of methane/air mixtures at different pressures, and suggested that they could have major impact in oxy-fuel conditions. The rate of fall-off reactions is usually modelled using the Troe format [182], which is characterized by non-negligible fitting errors. PLOG [140] expressions are gradually substituting the previous formulation of pressure-dependent rate constants, as they offer a higher accuracy [86]. However, the current CHEMKIN implementation for PLOG reactions does not include the parametrization of third body efficiencies. Klippenstein [86] and Curran [36] pointed this out as a major issue for kinetic modelling of EGR, MILD and oxy-fuel combustion. Recently, a modified PLOG format was proposed [87], where one PLOG might be specified for each bath gas and the conversion to the overall rate constant can be calculated through a linear mixture rule. To use this format, high-level theoretical calculations or experiments for each bath gas should be performed for each reaction. Additionally, it was demonstrated that non-linear mixture rules

should be implemented in future formulations as they significantly impact on the model performance [97]. However, the outstanding main problem consist in ab-initio calculations being more likely to be carried out for weak colliders (i.e. $He, Ar, Kr, H_2, N_2, O_2$) [74, 86], as more complex protocols need to be employed for strong ones, such as CO_2 [86] and H_2O [97]. For this reason, Jasper [82] predicted trajectory-based collision parameters for 307 pressure-dependent unimolecular decompositions of alcohols, hydroperoxides, and hydrocarbons in several bath gases, excluding CO_2 and H_2O. The latter was also shown to have a temperature-dependent collision efficiency relative to others colliders [83]. It is worth noting that the modified PLOG formalism allows describing temperature-dependent collision efficiencies. On the contrary, defining separate Arrhenius parameters for different bath gases using the TROE formalism produces incorrect results at high pressures, since the calculated rate coefficients are effectively multiplied by the number of collider specific reactions [86, 193]. Nevertheless, this practice is adopted in some kinetic mechanisms available in the literature. The estimation of plausible values for the Chaperon efficiencies by comparison between experimental data and models predictions started with the pioneering work of Slack [162], who estimated the efficiency of argon and nitrogen in $H + O_2 + M = HO_2 + M$ from shock tube measurements of ignition delay time (IDT). Brabbs and Robertson [21] estimated that of CO_2 following a similar procedure. Since then, much effort was put in this direction [9, 52, 112, 152]. In practice, the IDT is measured in a pure reference bath gas (RBG) (e.g. Ar or N_2) in conditions relevant to the smallest possible set of reactions, including the one of interest. Then, the rate constant for the RBG is inferred, considering the other sensitive reactions as certain. Secondly, experiments of the same macroscopic quantity are carried out in mixtures of inert compounds (e.g. H_2O/Ar or H_2O/N_2) and the rate constant for the second diluent can be inferred using experimental data assuming a linear mixture rule. The ratio between the two rate constants, at the pressure of the experiment, is a measure of the third-body efficiency of the stronger collider. However, four flaws can be identified for this procedure: (i) fall-off reaction rate constants not necessarily follow a linear mixture rule [97]; (ii) there often is a mismatch between the operating pressure of the experiment and the true low-pressure limit for the investigated reaction [23]; (iii) The inferred rate parameters values strongly depend on the adopted kinetic model, and (iiii) the

results strongly depend on the particular set of experimental data used as target. Recently, Lei and Burke [97] discussed, and quantified the uncertainties introduced by the assumptions of the linear mixture rule and low-pressure limit, and suggested best practices to design experiments where their influence is reduced to a minimum. Nowadays, advanced tools and protocols are available for parameters estimation allow to account for parameter uncertainties using large amount of experimental data as targets.

1.4 Quantification and Optimization in detailed kinetic mechanisms

The steady increase in computational power enables us to describe the behavior of complex combustion processes with more detail in Computational Fluid Dynamics (CFD) simulations, thus allowing us to more accurately predict how changes to the system would affect critical parameters, such as emissions, maximum temperature, efficiency, etc. This is crucial in the development of novel technologies, as a more traditional trial-and-error approach for many cases quickly becomes unfeasible, due to both time consumption and costs. Yet, we are far from a day-to-day use of CFD simulations for proper design purposes. However, as regulations are growing stricter and industries need to quantitatively prove compliance with limits on main pollutants, such tools have seen their popularity increase as powerful alternative or complement to experimental measurements. The complexity of a combustion simulation can be expressed in many ways, i.e. geometric, flow modeling, chemical mechanism complexity, etc. Only in recent years it became feasible to account for more detailed chemical mechanisms in large scale simulations [104]. The development of detailed kinetic mechanisms for fuels combustion supports and facilitates the implementation of cleaner fuels and more efficient combustion technologies, in the perspective of a reduced environmental impact, a differentiation of energy sources and their wiser utilization [104]. From a chemical kinetics perspective, a combustion process involves a considerable amount of species connected by a complex network of reactions. The increase in computing capabilities and in the accuracy and availability of experimental data [2, 3] pushes the development of kinetic models of increasing complexity in terms of number of species (10^3) and reactions (10^4) [104]. The rate constants of these reactions constitute the parameters of such models, together with thermody-

namic and transport properties can be determined experimentally, theoretically or based on analogy with similar compounds for which kinetic subsets already exist [36]. Each chemical reaction consists of rate constants (k), which in turn can be expressed as a function of temperature and pressure with some empirical parameters (the pre-exponential factor A, the temperature exponent n, and the activation energy Ea). Their definitions come from fitting model equations to experimental data or theoretical calculations [184]. The last decade was characterized by a more frequent adoption of theoretical methods (e.g. ab initio transition state theory-based master equation, AI-TST-ME) [86], for the determination of kinetic parameters and thermodynamic properties. Beyond the intrinsic advantages derived from the massive use of AI-TST-ME methods in terms of model predictive capabilities, the increasing popularity of such methods is justified by improved theoretical methods and algorithms currently available, and by the capability of measuring rate constants for elementary steps in a more accurate way, thus providing an immediate validation target for the theoretical results. In addition, automated computational protocols implementing the state-of-the-art AI-TST-ME methods [29, 42, 191] are reaching out to a much wider audience, thus paving the way to a more standardized approach to theoretical calculations within the combustion chemistry community. Nonetheless, adopting the best rate parameters does not necessarily lead to improved model performances when looking at a wide range of experimental targets [36, 56]. This is due to multiple reasons: i) reference kinetic mechanisms within the combustion science and engineering community have a long and consolidated history, or, in machine learning terms, are “well-trained” models, iteratively validated over a wide range of experimental targets over decades of research activities [56, 139]. ii) Models that have been historically developed largely relying on analogy rules and on semi-empirical, or at least less complex, thermochemical kinetics principles [16] are typically self-consistent, even in terms of the very likely possibility of hiding error compensation phenomena. iii) Every rate constant, including those from theoretical methods, is affected by an uncertainty [14, 15, 56, 180]. Regarding theoretical determinations the uncertainty can be intuitively considered as decreasing with an increasing detail in the level of theory [89]. In the past, uncertainty propagation methods were used to quantify the level of uncertainty of phenomenological rate coefficients, in n-propyl radical oxidation, obtained from theory [69]. In recent

times, quantum chemistry calculations are said to have reached a level of accuracy comparable to that of experimental measurements [86], promoting their applicability in combustion mechanism development. The recent mechanism for oxidation and pyrolysis of Ammonia by Stagni [170] is an excellent example of such integration. A multi-scale modelling approach was proposed by Burke et al. [22], who optimized a set of uncertain theoretical kinetics parameters directly relating their uncertainties to the combustion behaviour in terms of macroscopic targets (ignition delay time, laminar flame speed, etc.). Shannon et al. [151] proposed the use of experimental data and uncertainty quantification to constrain and optimize input parameters in the master equation using MESMER [68]. Essentially, each parameter of a kinetic model, expressed in any form, can be considered as a randomly distributed variable within its uncertainty range [180]. Thus, as the size of the mechanism grows, also the number of uncertain parameters increases. In order to cope with the large amount of uncertain parameters, Uncertainty Quantification (UQ) and Optimization have been increasingly adopted in the process of chemical mechanism development [203]. In the context of chemical mechanisms, Solution Mapping [61] was the first optimization method applied to a large, complex system. This method faces the multi-modality of the problem through polynomial response surfaces, and it was applied for the development of the GRI-MECH [60]. This mechanism was trained on a heterogeneous (i.e. containing different type of targets) set of 77 well-documented experiments describing the combustion of natural gas. In the development of the GRI mechanisms [60], especially the pre-exponential factors for the most impactful reactions were optimized. More recently, Frenklach et al. [58] introduced the concept of collaboration of data, and demonstrated that a joint analysis on the entire data sample can increase the amount of extracted information and improve the results. Feeley et al. [51] showed that the technique of data collaboration can be used to rigorously assess the mutual consistency of experimental results and identify potential outliers, using a chemical kinetic model. The methodology, called Bound-to-Bound Data Collaboration (B2B-DC) has been successfully applied and refined in several other works [57, 80, 143, 144, 163, 209]. Najm et al. [122] applied forward Uncertainty Quantification (UQ) and Polynomial Chaos Expansion (PCE) to chemical kinetics. Wang and co-workers later developed the Method of Uncertainty Minimization using Polynomial Chaos Expansion (MUMPCE) [156], which again utilizes

surrogate modeling for representing the model responses. Then by finding the least-squares point within the parameter space, they determined the optimal mechanism. They used this approach for several different fuels [130, 154, 207], and also to develop the Foundational Fuel Chemistry Model (FFCM) [164] for small hydrocarbon fuels. However, in these works [130, 154, 156, 164, 177, 207] they only considered the pre-exponential factors and some third body efficiencies as active parameters. A species is considered as a third body if it stays inert though the reaction process, and only transfers/removes energy from the process. Only in a recent study [178], they applied the MUMPCE approach considering the joint probability distribution of the pre-exponential factors and the activation energies of some reactions. Cai and Pitsch [25, 26] also used the MUM-PCE [156] methodology, but for the optimization of rate rules instead of specific reactions. In the optimization method proposed by Cai and Pitsch [25, 26], each rate rule is supposed to be a potential active parameter of the model calibration. Later, they also applied a Bayesian approach for the optimization of rate rules for alkanes [27]. Rate rules are used to derive kinetic parameters for reactions that behave in a similar way. As the determination of one rate rule directly inflicts changes to many reactions, it is a very efficient approach for developing kinetic mechanisms for fuels with larger molecules. Recently, this approach was combined with the optimization of thermochemical properties in the works of vom Lehn et al. [197–199], showing a large impact of the thermochemical parameters, especially at intermediate temperatures. However, in all these works [25–27, 197–199], only the pre-exponential factors for the rate rules were considered for the optimization. Vom Lehn et al. [200] also proposed an iterative model-based experimental design for efficient uncertainty minimization.

The approach based on the use of response surfaces can be highly efficient for mechanism optimization, but the resulting procedure would be mechanism dependent. In fact, as metamodels are built for each model response based on chemical combustion model. Intuitively, if the nominal model changes, then also the surrogate modelling phase has to be repeated. Additionally, as mentioned by Sikalo et al. [161], the nature of the objective function in mechanism optimization can be highly complex, since it consists of many local minima and maxima. Therefore, Sikalo et al. [161] suggest to use the Genetic Algorithm (GA) global optimization approach, which has been proven to perform

very well in these conditions [49, 135, 161]. Turányi [185] proposed a sum-of-squared-error-based methodology, but, differently from others, they included all three Arrhenius parameters in the optimization, i.e. A, n and Ea, as well as third body collision efficiencies. This approach accounts for both direct and indirect measurements, where direct experimental values refer to experimental data of the rate constant k, while the indirect targets consist of concentration profiles, ignition delay times, and laminar burning velocities. The methodology from the ELTE group was successfully applied to H_2/O_2 [192], H_2/O_2/NOx [93], H_2/CO mixtures [193], CH_2O and CH_3OH [125], and ethanol [126]. Sheen and Wang introduced the method of uncertainty minimization by polynomial chaos expansion (MUM-PCE) [156, 203]. Cai and Pitsch [25] minimized the uncertainty in a n-pentane combustion mechanism by applying the MUM-PCE method to the optimization of rate rules. They also proposed a strategy to optimize pressure-dependent reactions, formulated via logarithmic interpolation, i.e. PLOG standard [140]. PLOG expressions are indeed gradually substituting the previous formulation of pressure-dependent rate constants, as they yield a better fitting to experiments or calculations [86]. As this formalism uses accurate rates for discrete pressures, the parameters of each pressure value were considered independent from each other in [25]. The use of heuristic optimization methods, such as the genetic algorithm (GA), and particle swarm optimization (PSO) for parameter estimation is very promising [148]. Heuristic optimization methods are global optimization methods based on empirical rules inspired by evolution-based strategies in nature. They are usually very flexible and can be applied to many types of objective functions and constraints. The word “heuristic” is used to refer to these methods because convergence is not guaranteed, although a useful and good approximation of the searched optimum can frequently be obtained. These methods can be used in problems for problems characterized by high-dimensionality, as they are poorly sensitive to the initial parameter guesses, gradient-free, and are able to perform global optimization. The applicability of Evolutionary/Genetic Algorithms (EA/GA) to optimization problems involving detailed kinetics was broadly investigated by Elliott and co-workers [47–49]. EA/GA were found particularly suitable for searching objective-function spaces characterized by high dimensionality. **So far, optimization studies in chemical kinetics have been relying on objective functions based on the L_1 and L_2 norms of the difference between**

models predictions and corresponding experimental targets [47,177,193]. Recently, You et al. [209] minimized the 1-norm of the difference between the active variables values and the nominal ones, constrained on the feasible set of combinations identified with B2B-DC [56]. The formulations in [209] not only improve the model performance, but also minimize the number of parameters and the deviations of the new values from the literature recommendations. Recently, Bernardi et al. [17] presented an innovative framework based on Curve Matching (CM), consisting in a multi-faceted functional analysis of the profiles obtained from both models and experiments. In this approach, they introduced a proper metric to quantify the similarity between the curves representing experiments and simulations, rather than a point-wise measure of the distance between them.

1.5 Objective of the present work

The objective of the present thesis is multiple:

- Propose a methodology for the optimization of kinetic mechanisms based on heuristic optimization algorithms. Most of existing methods do not discuss the challenges in PLOG reactions optimization and are based on the minimization of a point-wise error measure, i.e. classical norms. This methodology includes, for the first time in literature, the possibility to optimize PLOG reactions by accounting for interdependencies between rates at different pressures and uses the CM index [17] as the error function, which accounts for similarity of curves shapes. The effectiveness of such approach was verified using an extensive dataset for a recent kinetic model of ammonia combustion [170]. This model largely relies on theoretical calculations of key reaction rate constants. As an added value, this work also presents guidelines for attributing reasonable uncertainty factors for theoretical determinations performed with different theory levels. More details are available in chapter 3.
- Describe the authors contribution to the development and refinement of an open source toolbox, named OptiSMOKE++. This toolbox, enables the user to perform optimizations of detailed kinetic mechanisms performances handling numerous kinetic parameters, under uncertainty. More features of OptiSMOKE++ are demonstrated in chapter 4.

- Study how diluents affect hydrogen/syngas combustion thermally and by participating to reactions, both directly and indirectly. Additionally, a procedure for the estimation of third-body efficiencies of H_2O and CO_2 in impactful fall-off reactions is described, which considers experimental data from different sources and facilities, as well as the uncertainties of all impactful reactions, simultaneously. Finally, quantify the impact of missing collision efficiencies in PLOG reactions on mechanism performance for hydrogen combustion data and propose a novel optimization-based protocol to compensate for induced errors. All this is described in chapter 5.
- Identify influential reactive steps for NOx formation in the ULB industrial flameless burner fired with H_2/NH_3 blends over a wide range of operating conditions.Also, verify whether the origin of the deviation between experimental measurements and predictions of NOx emissions from numerical simulations is attributable to uncertainty in ammonia kinetics. These problems are tackled in chapter 6.

CHAPTER 2

Methodology

THE present chapter is meant to discuss theoretical elements of existing methods for UQ, sensitivity analysis and optimization, which are used throughout this thesis.

The aim of a combustion kinetic modeller is to characterise the conversion of one mole of fuel (F) and *a* moles oxidiser (OX) to *b* moles of product *b* (P). In *Global* terms, this process can be summarized as follows:

$$F + aOX \Longrightarrow bP \tag{2.1}$$

The rate of fuel consumption can be then expressed as:

$$\frac{d[X_F]}{dt} = -k(T,P)[X_F]^n[X_{OX}]^m \tag{2.2}$$

where $[X_i]$ is used to denote the molar concentration in $kmol/m^3$, *n/m* are related to the reaction order, and *k* is a temperature (and pressure) dependent costant of proportionality, known as **global rate coefficient**. In general, the expression 2.2 holds for a very limited set of operating conditions (i.e. T and P). On this set, *n*, *m* and *k* can be obtained by means of curve fitting is measurements of X_F in time are available. However, "*global*" approaches to combustion chemistry are far from a fair representation of the underlying physics. Indeed, during conversion from reactants to products, a number of **intermediate** species and/or radicals are formed and destroyed in as many **elementary** kinetic steps. Furthermore, depending on the operating conditions and fuel/oxidiser/diluent composition the system can follow a different kinetic pathway. The collection of all elementary reactions, and species, describing the kinetics of F is known as its **detailed kinetic mechanism**. Reaction mechanisms may involve only a few steps or as many as several hundreds. Examples of the size of existing mechanisms for hydrogen, ammonia, and small hydrocarbons are displayed in Figure 2.1.

Figure 2.1 also reports a rough estimation of the number of kinetic parameters, which are present in a model. This estimation is obtained by multiplying the number of reactions by 3. In fact, the logarithmic functional form (i.e. modified Arrhenius' law) of the rate constant yields:

$$ln(k) = ln(A) + nln\,(T) - \frac{E_a}{RT} = \alpha + nln(T) - \frac{\epsilon}{T} \tag{2.3}$$

where A, n and E_a are empirical parameters known as pre-exponential factor, temperature exponent, and activation energy, respectively. In general, the rate

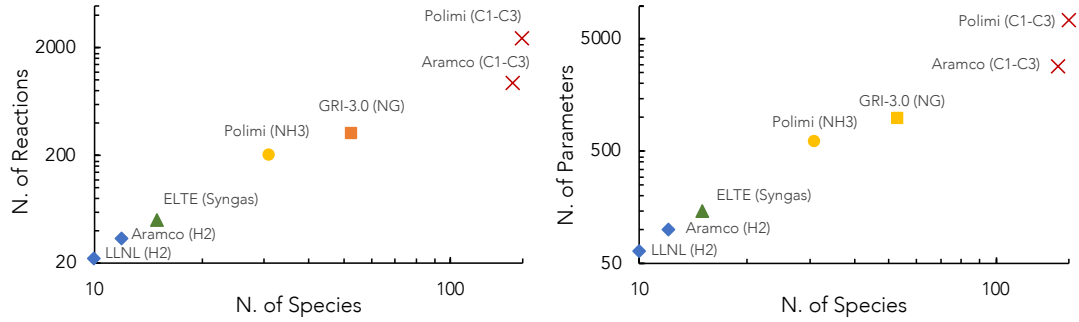

Figure 2.1: *Size of selected detailed mechanisms for hydrogen, ammonia, natural gas and low-hydrocarbons. Adapted from Lu and Law [104]*

parameters for a certain reaction can be:

- estimated from curvefitting experiments using a kinetic model. The revisions from Cohen and Westberg [32, 33] and Baulch [14, 15] are perfect examples;
- estimated through curvefitting of $\kappa(T, P)$ values determined from first principle calculations;

However, a kinetic model is also composed by thermodynamic [70] and transport [76] properties for each species i taking part to elementary reactions. In CHEMKIN, the thermodynamic properties are tabulated as temperature dependent polynomials, known as NASA polynomials:

$$\begin{aligned}
\frac{\widetilde{C_{p,i}}}{R} &= a_{i,1} + a_{i,2}T + a_{i,3}T^2 + a_{i,4}T^3 + a_{i,5}T^4 \\
\frac{\widetilde{H_i}}{RT} &= a_{i,1} + \frac{a_{i,2}}{2}T + \frac{a_{i,3}}{3}T^2 + \frac{a_{i,4}}{4}T^3 + \frac{a_{i,5}}{5}T^4 + \frac{a_{i,6}}{T} \\
\frac{\widetilde{S_i^0}}{R} &= a_{i,1}ln(T) + a_{i,2}T + \frac{a_{i,3}}{2}T^2 + \frac{a_{i,4}}{3}T^3 + \frac{a_{i,5}}{4}T^4 + a_{i,7}
\end{aligned} \tag{2.4}$$

where, $\widetilde{C_{p,i}}$, $\widetilde{H_i}$, and $\widetilde{S_i^0}$ are the molar specific heat constant pressure, the molar specific enthalpy and the molar specific entropy at 1 atm for the i^{th} species, respectively. Finally, $\boldsymbol{a_i}$ is a vector of 7 fitting parameters. The first five are used to compute $\widetilde{C_{p,i}}$. An additional (two) parameter is required for $\widetilde{H_i}$ ($\widetilde{S_i^0}$).

In CHEMKIN, two different sets are usually reported, for each species i, to represent two different temperature ranges, namely, mid-low (e.g. [300, 1200]) an mid-high ([1200, 3500]). Once the forward kinetic constant k_j^f for the j^{th} reaction is computed using equation 2.3 that of its backward reaction k_j^b can be computed through the equilibrium constant K_j^e:

$$\begin{aligned} k_j^b &= \frac{k_j^f}{K_j^e} \\ K_j^e &= exp\left(\frac{\widetilde{\Delta S_i^0}}{R} - \frac{\widetilde{\Delta H_i}}{RT}\right)\left(\frac{p_{atm}}{RT}\right)^{\sum_{i=1}^{N_s}(\upsilon_{i,j}^b - \upsilon_{i,j}^f)} \end{aligned} \tag{2.5}$$

where, $a_{i,j}$ are fitting parameters available in CHEMKIN while $\upsilon_{i,j}^b$ and $\upsilon_{i,j}^f$ are the stoichiometric coefficients of the species i in reaction j. The reaction entropy $\widetilde{\Delta S_i^0}$ and enthalpy $\widetilde{\Delta H_i}$ are defined as:

$$\begin{aligned} \widetilde{\Delta S_i^0} &= \sum_{i=1}^{N_s}(\upsilon_{i,j}^b - \upsilon_{i,j}^f)\widetilde{S_i^0} \\ \widetilde{\Delta H_i} &= \sum_{i=1}^{N_s}(\upsilon_{i,j}^b - \upsilon_{i,j}^f)\widetilde{H_i} \end{aligned} \tag{2.6}$$

Finally, the net reaction rate can be obtained through the difference between forward and backward (if reversible) reactions rates:

$$r_j = k_j^f \prod_{i=1}^{N_s} c^{\upsilon_{i,j}^f} - k_j^b \prod_{i=1}^{N_s} c^{\upsilon_{i,j}^b} \tag{2.7}$$

Here, c_i represents the concentration of the i^{th} species. **Unimolecular** dissociation reactions (e.g. $C_2H_6(+M) \rightleftharpoons CH_3 + CH_3(+M)$) are of utmost importance in combustion. Reactions of this type exhibit a first order behavior at high pressure, while a second order behavior is observed at low pressure. This is due to the concentration of any other molecule, M, with which the reacting species may collide. Each molecule have its own collisional or third body efficiency, α_i. So, the average third body efficiency of the reacting mixture can be computed as follows:

$$\overline{\alpha} = \sum_{i=1}^{N_s} \alpha_i x_i \tag{2.8}$$

Here, x_i represents the molar fraction of the i^{th} species. **Termolecular** reactions correspond to the revers of unimolecular reactions at low pressure. In CHEMKIN [140], the format for kinetic mechanisms, pressure dependent reactions can be expressed in Lindemann [101], Troe [182] or PLOG [140] formats. Nowadays, these formats are widely used in combustion kinetic models. In TROE and Lindemann formulations, two different triplets of Arrhenius' parameters are used to describe the temperature-dependent k at two discrete pressure values, i.e. low P_0 and high P_∞ limits, which vary according to the specific reaction j. Their ratio is termed reduced pressure:

$$P_r(M) = \frac{k_{low}[M]}{k_\infty} \tag{2.9}$$

here, $[M]$ represents the mixture concentration enhanced by the average collision efficiency of the mixture.

$$[M] = \sum_{i}^{N_s} x_i \alpha_i = \frac{P\overline{\alpha}}{RT} \tag{2.10}$$

So equation 5.4 , tells us that molecules with strong collision efficiency have an impact on the kinetic constant k, as its equation yields:

$$k = k_\infty \frac{P_r(M)}{1 + P_r(M)} F \tag{2.11}$$

The parameter F has values of 1 in the Lindemann formulation, while it is an elaborated empirical function of temperature in TROE's. The latter formulation forces the user to fit 3 or 4 additional parameters, which make the fitting procedure more challenging and sometimes reduce its accuracy. For this reason, the PLOG formulation for fall-off reactions was recently introduced in the CHEMKIN format, as alternative to TROE's, for its lower fitting error. A PLOG reaction consists of multiple Arrhenius rate constants at discrete pressures p_i (with i = 1, ..., N_p), individually accounting for temperature dependence. Indeed, k_{p_1} and k_{p_n} correspond to the low ($k_{low}[M]$) and high-pressure limit k_∞,

respectively. A logarithmic interpolation is then adopted at intermediate pressures $\overline{p}$:

$$ln(k_{\overline{p}}) = ln(k_{p_i}) + \left[ln(k_{p_{i+1}}) - n(k_{p_i})\right] \left[\frac{ln(\overline{p}) - ln(p_i)}{ln(p_{i+1}) - ln(p_i)}\right] \tag{2.12}$$

The transport properties of the i^{th} species are its dynamic viscosity η_i, thermal conductivity λ_i and its binary mass diffusion coefficient $\Gamma^0_{i,j}$ at atmospheric pressure, relative to the j^{th} species. These three quantities can be computed using the following polynomial fit of the logarithm of the quantity:

$$ln(\nu_i) = \sum_{k=1}^{N} b^{\nu}_{i,k} (lnT)^{k-1} \tag{2.13}$$

$$ln(\lambda_i) = \sum_{k=1}^{N} b^{\lambda}_{i,k} (lnT)^{k-1} \tag{2.14}$$

$$ln(\Gamma^0_i) = \sum_{k=1}^{N} b^{\Gamma}_{i,j,k} (lnT)^{k-1} \tag{2.15}$$

where $b^{\nu}_{i,k}$, $b^{\lambda}_{i,k}$, and $b^{\Gamma}_{i,j,k}$ are fitting parameters available in CHEMKIN format. OpenSMOKE++ [35], and therefore OptiSMOKE++ [64], uses third-order polynomials fit to ensure and average error with respect to data below 1 %. When the operating pressure is different from atmospheric, the binary diffusion coefficients need to be corrected as follows:

$$\Gamma_{i,j} = \frac{\Gamma^0_{i,j}}{p} \tag{2.16}$$

Finally, the mixture average properties are computed from those of single compounds, by using proper mixing rules.

2.1 The uncertainty of reaction rate constants

Over time, kinetic rate constants for elementary reactions have been indirectly estimated from experiments. Figure 2.2 reports examples of "experimental datasets" representing the dependence of rate constant of the well-known O + OH=H + O_2 reaction on temperature. As shown in figure 2.2, not all "exper-

imental datasets" covers the entire temperature range typical of combustion, and even those overlapping covering similar ranges do not always show comparable trends and absolute values. This is a clear sign of the uncertainty which is embedded even in the better known kinetic constants.

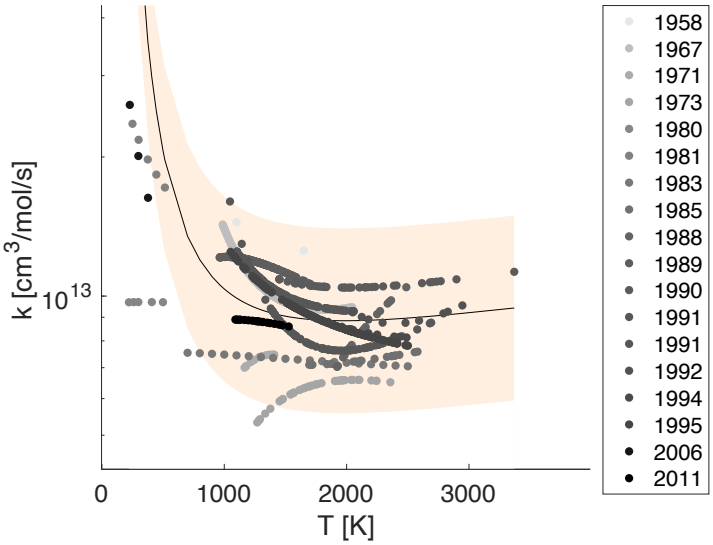

Figure 2.2: *Collection of experimental data for the reaction O + OH=H + O_2 from 1958 to 2011. On the chart, the best estimate k(T) is reported using a straight line, experimental data are represented by markers, while the deducible reaction uncertainty by the orange shaded area. The data collection is a courtesy of Matteo Pelucchi.*

In principle, a single perfect fourmulation for each reaction rate constant in a kinetic mechanisms should exist, but in practice it does not. Shannon [151] demonstrated that relatively small uncertainties in the input parameters may lead to large uncertainties in calculated rate coefficients even in theoretical calculation. Additionally, the reaction uncertainty is both pressure and temperature dependent. Moreover, a kinetic mechanism is a complex system of reactions interconnected with each other, thus, in terms of macroscopic performance, different combinations of rates in a mechanism may lead to similar macroscopic behavior. Extensive work was done to characterize the uncertainty in crucial reaction rate constants for low hydrocarbons [14, 15]. In these works, recommendations for temperature-independent uncertainty coefficients are given under the form of *f* factor:

$$f(T,P) = \frac{\kappa_{max} - \kappa_0}{ln(10)} = \frac{\kappa_0 - \kappa min}{ln(10)} \tag{2.17}$$

This formulation can be interpreted with the help of figure 2.2, where the black straight line represent the best estimate or nominal kinetic rate constant (i.e. κ_0), while the extreme curves of the orange shaded area are its maximum κ_{max}, and minimum κ_{max} value, respectively. Here, an uncertainty of 60% was assumed, which corresponds to a temperature-independent f value of 0.2. Nagy [119] considered the dependence of f_r on temperature. In a later study, Nagy et al. [120] recommended the adoption of temperature-independent uncertainty and uniform distributions for Arrhenius parameters when little prior information is available. Since the thermodynamic properties of small molecules is very well-known parameters of equations 2.4 can be assumed to be certain. However, the excellent work of Vom Lehn [197–199] shows that this assumption does not hold for bigger molecules and it is crucial to also optimize thermodynamic parameters, which are involved in the computation of the equilibrium constant in equation 2.5. In this work, we will always consider temperature independent uncertainty factors f_j, and the uncertainty of thermodynamic parameters to be negligible. This is an acceptable approximation, since the uncertainty of thermodynamic properties for small molecules as ammonia and hydrogen is considerably low. However, for models describing the kinetics of larger fuels this hypothesis might decay for a large number of molecules, and radicals due to scarsity of experimental data, which induces a greater lack of knownledge in the fitting parameters of equations 2.4. For such cases, it is beneficial to consider these parameters as active variables in optimization or UQ together with Arrhenius' ones in order to avoid bias.

2.1.1 Transferring uncertainty from the kinetic constant to Arrhenius empirical parameters

Even though the uncertainty of rate constants is available through equation 2.17, what in general is optimized are the empirical parameters α, n and ϵ of the Arrhenius extended formulation. In fact, their optimized values need to be reported in a kinetic model in CHEMIKIN format. For this reason, the reaction uncertainty needs to be translated into parameters bounds to be used in optimization. If only the logarithm of the pre-exponential factor α is optimized, this be-

comes a trivial task. Indeed, It is easy to show that $\alpha \in [-fln(10)\alpha_0, +fln(10)\alpha_0]$. However, when all three parameters are meant to be optimized their dependence has to be accounted for.

Let's consider the case where only α and ϵ are uncertain. In this case, the procedure to derive bounds is depicted in figure 2.3.

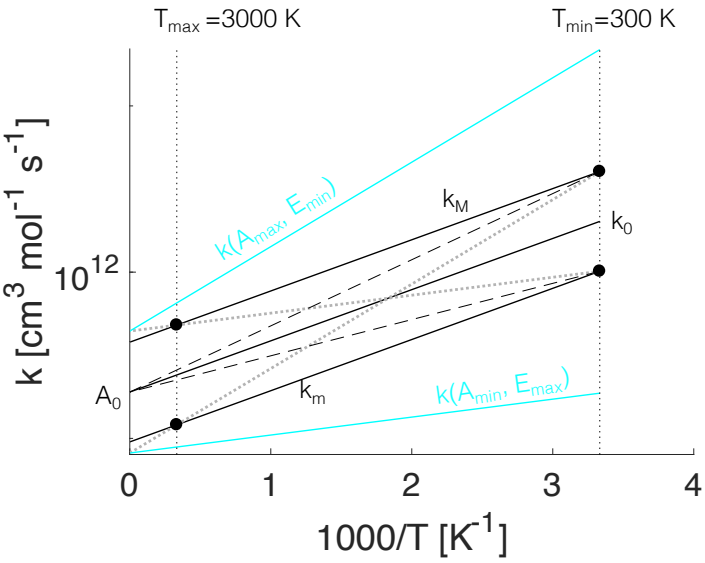

Figure 2.3: *Graphical representation of bounding methods accounting for statistical dependence of Arrhenius parameters. Adapted from [120]*

Here, the nominal kinetic constant κ_0 is multiplied and divided by 10^f to obtain the two linear contraints κ_M and κ_m. Since considering E_a^* introduces the dependence on temperature, a suitable temperature range needs to be chosen. For combustion applications, it is realistic to assume $T \in [300, 3000]K$. Now, we know the values of $\kappa_M(T_{max/min})$ and $\kappa_m(T_{max/min})$. So we only need to find the values of A and E for the to lines crossing these points, by solving:

$$\begin{cases} ln(\kappa_M(T_{max})) = ln(A^*) + n_0 ln(T_{max}) - \frac{E_a^*}{RT_{max}} \\ ln(\kappa_m(T_{min})) = ln(A^*) + n_0 ln(T_{min}) - \frac{E_a^*}{RT_{min}} \end{cases} \tag{2.18}$$

for A_{max} and $E_{a,max}$, and:

$$\begin{cases} ln(\kappa_M(T_{min})) = ln(A^*) + n_0 ln(T_{min}) - \frac{E^*}{RT_{min}} \\ ln(\kappa_m(T_{max})) = ln(A^*) + n_0 ln(T_{max}) - \frac{E^*}{RT_{max}} \end{cases} \tag{2.19}$$

for A_{min} and $E_{a,min}$. In figure 2.3, it is interesting to notice that $A_{max/min}$ represent the projection of the rate constant at infinitely high temperature. However, the uncertainty of κ forces statistical dependence between parameters. This becomes clear when plotting the extremes points of the parameters uncertainty region, i.e. $\kappa(A_{max}, E_{a,min})$ and $\kappa(A_{min}, E_{max})$, which are outside the uncertainty of κ (see fig. 2.3). This means that not all parameters combination are eligible as optimal point during search performed by the optimisation algorithm of choice. In particular, all viable parameters combinations are contained inside a convex region, which is displayed in figure 2.4 a for A and E_a. Here, all the combinations within the green area will respect constraints on κ

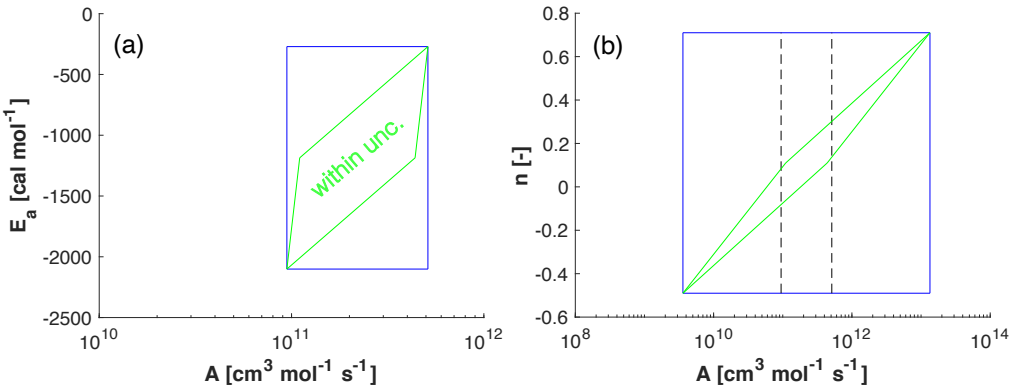

Figure 2.4: *Graphical example of statistical dependence of constrained Arrhenius parameters. Adapted from [63, 120]*

To avoid sampling non-viable combinations during the optimization proceduce, Nagy [119] proposed the use of the multivariate normal distribution of the transformed Arrhenius parameters from prior information on the rate constant, and a procedure to estimate its covariance matrix. In his work, Nagy assumed initial bounds for $n \in [n_0 - 2, n_0 + 2]$, which can be used as input to the procedure to estimate the covariance matrix of the parameters joint distribution. However, in some cases, one may be interested in optimizing the parameters independently. Fürst et al. [64] proposed the use of a penalty function, capable of excluding non-viable combinations. Finally, Fürst [63] proposed a protocol to determine bounds for n, applying a similar procedure to the one described above and displayed in figure 2.3, where E_a was considered certain. The resulting convex region for A and n, is reported in figure 2.4 b.

2.2 Penalty function

As mentioned, although the limits of each uncertain kinetic parameter are individually specified with the procedure described above, the non-linear nature of the modified Arrhenius curve does not necessarily ensure that during optimization the rate constant stay within its initially prescribed bounds for the complete temperature span (considered as 300–3000 K to correctly account for realistic temperature conditions in combustion applications). It is therefore important to do a check of the proposed parameter combinations, to see that the rate constants are within the uncertainty limits. This can be handled by utilizing a so-called penalty function. Penalty functions can be used for many purposes. For example, Sikalo et al. [161] used a penalty function for keeping the optimized parameters close to the original values. Alternatively, the penalty function can be implemented to forcefully increase the objective function value for parameter combinations which do not respect the uncertainty limits of the rate constants, for all of the reactions considered. This ensures that the optimizer does not choose a parameter combination which violates this restriction, and finds the optimal combination of parameters which satisfies the constraints. Consequently, the use of this penalty function results in quite significant computational savings, as the penalized parameter combinations are not simulated. However, it should be said that for gradient based optimization approaches, penalty functions are not a good choice, as these algorithms depend on the prior evaluations for the estimation of the slope of the objective function. The use of penalty functions disrupts the natural slope of the objective function and gradient based algorithms would then face issues in finding the optimal solution. Finally, the combination of a penalty function and non-gradient based global optimizers is very efficient for constrained optimization problems such as kinetic mechanism optimization.

2.3 Evolutionary Algorithm

In this work, objective function minimization is mainly performed by means of a global, mono-objective Evolutionary Algorithm (EA) in DAKOTA [4], whose solution is less dependent on the initial guess compared to other algorithms [47]. When this algorithm is applied to the optimization of n reactions in a detailed kinetic model, an individual "DNA" string (see figure 2.5) is composed

of random values of kinetic parameters A, n and E for each reaction rate R_n. By drawing S random samples from individual distribution of kinetic parameters, a *population* is built, which is nothing but a set of randomly initialized DNA strings.

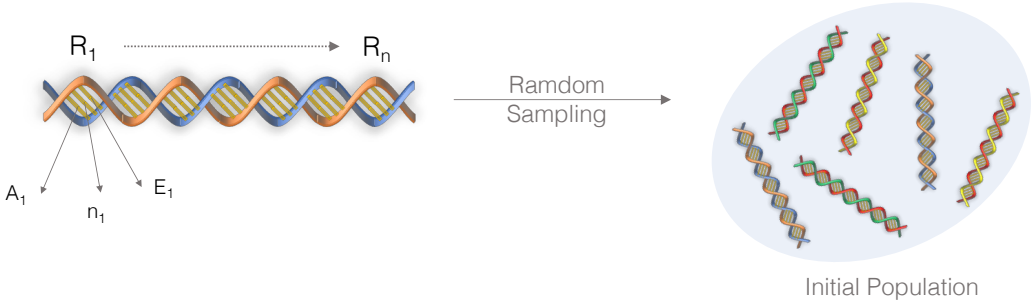

Figure 2.5: *Graphical representation of a DNA string in evolutionary algorithm applied to chemical kinetics.*

Initially, a population of S different combinations of parameters is sampled, evaluated and labelled with objective function values. Then, the algorithm starts the first iteration (a 'generation') (see figure 2.6), where the elements of the current population (the 'parents') are ranked applying a linear scaling of probability based on the corresponding objective function values. In general, the best fittest parents undergo uniform crossover, where a couple of parents or a 'chromosome' is selected, and each parameter value can be swapped between the two with a probability equal to the crossover rate pc. This operation produces a new pair of elements (the 'off-springs'), resulting from the cross-over of as many parents. Subsequently, mutation is introduced. In particular, for each new off-spring, every variable has the same probability to mutate, according to the mutation rate p_m. A non-uniform mutation operator was adopted to assign a new parameter value by sampling from its distribution. When mutation and cross-over are complete, a resulting population of $2S$ elements is obtained, i.e. twice the size of the initial one. In this work, a replacement strategy, which selects the $S/2$ best individuals in $2S$ elements, and randomly selects other $S/2$ from the remaining $3S/2$, was adopted. This ensures the balance between global and local search. The adopted probability of cross-over ($p_c = 0.65$) and mutation ($p_m = 0.5$) were suggested by Elliott [47]. The new parent population undergoes the same procedure iteratively until satisfactory accuracy is achieved.

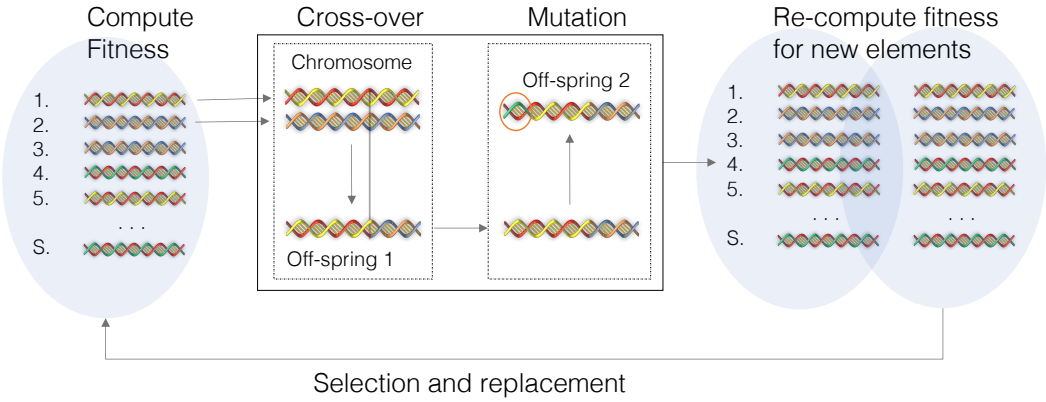

Figure 2.6: *Graphical representation of an example generation in Evolutionary Algorithms.*

2.4 Objective/Error/Loss functions

Given a set of experiments $\boldsymbol{y}^e$ and a corresponding mathematical model $f(\boldsymbol{\theta})$, where $\boldsymbol{\theta}$ is the vector of model parameters. The goal of parameters estimation is to maximize the probability of obtaining experimental data from model responses. As they are inherently uncertain, experimental data can be regarded as random variables with joint probability distribution:

$$P(\boldsymbol{y}^e, \boldsymbol{y}, \boldsymbol{\varepsilon}) \tag{2.20}$$

which decribes the probability to get the experimental values $\boldsymbol{y}^e$, given the real unknown values $\boldsymbol{y}$ and the experimental errors $\boldsymbol{\varepsilon}$. Given the model functions:

$$\boldsymbol{f}(\boldsymbol{x}, \boldsymbol{\theta}) \tag{2.21}$$

where $\boldsymbol{x}$ is the vector of independent variables. The vector of model parameters $\boldsymbol{\theta}$ can be estimated by maximizing 2.20. When the experimental errors follow the normal distribution, maximization of 2.20 is equivalent to the minimization of:

$$Obj(\boldsymbol{\theta}) = (\boldsymbol{f}(\boldsymbol{x}, \boldsymbol{\theta}) - \boldsymbol{y}^e)^T \boldsymbol{V}_y^{-1} (\boldsymbol{f}(\boldsymbol{x}, \boldsymbol{\theta}) - \boldsymbol{y}^e) \tag{2.22}$$

In equation 2.22, it is implicitly assumed that the uncertainty of the independent variables is negligible. If the dependent variables measurement are uncorre-

lated, the covariance matrix $\boldsymbol{V}_y^{-1}$ is diagonal and equation 2.22 takes the form of weighted least squares:

$$Obj(\boldsymbol{\theta}) = \sum_{i=1}^{NE}\sum_{j=1}^{NY}\frac{(f_{i,j} - y_{i,j}^e)^2}{\sigma_{i,j}(y_{i,j}^e)^2} \tag{2.23}$$

NE and NY are the number of experiments and dependent variables, respectively, and $\sigma_{i,j}$ is the experimental variance of the j^{th} dependent variable in the i^{th} experiment. In this manuscript, it will always be assumed that measured dependent variables are gaussian random variables with mean $y_{i,j}^e$ and standard deviation $\sigma_{i,j}$. Given the relative error (RE) of the experimental measurement, the standard deviation can be calculated as follows:

$$\sigma_{i,j} = \frac{RE \times y_{i,j}^e}{m} \tag{2.24}$$

In equation 2.24, m can assume values of 1,2 or 3, depending on the uncertainty analysis of the experimentalist. However, when this information is not available from literature, the value of m can be assigned based on the degree of belief associated to that particular experiment. It is important to point out that when the functional relation between dependent and independent variables is exponential, $y_{i,j}$ needs to be replace by it's natural logarithm. This is done to avoid giving higher relative weight to points with higher absolute values. In kinetics, this is the case for ignition delay times of a given mixture. Another popular objective function in optimization problems is the sum of weighted absolute deviations:

$$Obj(\boldsymbol{\theta}) = \sum_{i=1}^{NE}\sum_{j=1}^{NY}\frac{|f_{i,j} - y_{i,j}^e|}{\sigma_{i,j}(y_{i,j}^e)} \tag{2.25}$$

In the following chapters, the terms L_2-norm and L_1-norm will refer to equation 2.23 and 2.25, respectively.

2.4.1 Curve Matching

Recently, Bernardi et al. [17] presented an innovative framework based on Curve Matching (CM), consisting in a multi-faceted functional analysis of the profiles obtained from both models and experiments. In this approach, they

introduced a proper metric to quantify the similarity between the curves representing experiments and simulations, rather than a point-wise measure of the distance between them. Pelucchi et al. [131] revised and proposed such framework as a further step towards an automatic model validation protocol. In general, functional representations of both experiments, $g(\boldsymbol{x})$, and model responses, $f(\boldsymbol{x})$ (and their derivatives $g'(\boldsymbol{x})$ and $f(\boldsymbol{x})$) are obtained by interpolating smoothed splines, which result in satisfactory approximations of both data points and first derivatives. Based of these estimations, four dissimilarity indices can be computed:

$$d^0_{i,L_2} = \frac{1}{1 + \frac{\|\boldsymbol{f}-\boldsymbol{g}\|}{|D|}} \in [0,1] \tag{2.26}$$

$$d^1_{i,L_2} = \frac{1}{1 + \frac{\|\boldsymbol{f'}-\boldsymbol{g'}\|}{|D|}} \in [0,1] \tag{2.27}$$

$$d^0_{i,p} = 1 - \frac{1}{2}\left\| \frac{\boldsymbol{f}}{\|\boldsymbol{f}\|} - \frac{\boldsymbol{g}}{\|\boldsymbol{g}\|} \right\| \in [0,1] \tag{2.28}$$

$$d^1_{i,p} = 1 - \frac{1}{2}\left\| \frac{\boldsymbol{f'}}{\|\boldsymbol{f'}\|} - \frac{\boldsymbol{g'}}{\|\boldsymbol{g'}\|} \right\| \in [0,1] \tag{2.29}$$

where |D| is the intersection of the domain between $g(\boldsymbol{x})$ and $f(\boldsymbol{x})$. For instance, if the abscissa values of $g(\boldsymbol{x})$ belong to [500,1500], and those of $f(\boldsymbol{x})$ belong to [400, 1800], the value of |D| would be 1000 (i.e. |D| =1500-500). The $\|g(\boldsymbol{x})\|$ is the L_2-norm of the function $g(\boldsymbol{x})$. All the dissimilarity indices are intrinsically constrained between 0 and 1, where 1 indicates maximum similarity, and 0 maximum dissimilarity. Individually, d^0_{i,L_2} depends on the area enclosed by g and m, while d^1_{i,L_2} evaluates the same quantity between their respective derivatives. Hence, the first generalizes a classical L2-norm, while the second extends it. On the other side, the Pearson dissimilarity measures $d^0_{i,p}$ and $d^1_{i,p}$ indicate perfect matching if g and m, and their derivatives, only differ by vertical translation. Figure 2.7 offers a graphical representation of how the curve matching framework enables the comparison between model responses and data, together with their derivatives. Finally the curve matching index for the i^{th} pair or experiments/model responses can be computed as:

$$CM_i = \frac{d^0_{i,L_2} + d^1_{i,L_2} + d^0_{i,p} + d^1_{i,p}}{4} \in [0,1] \tag{2.30}$$

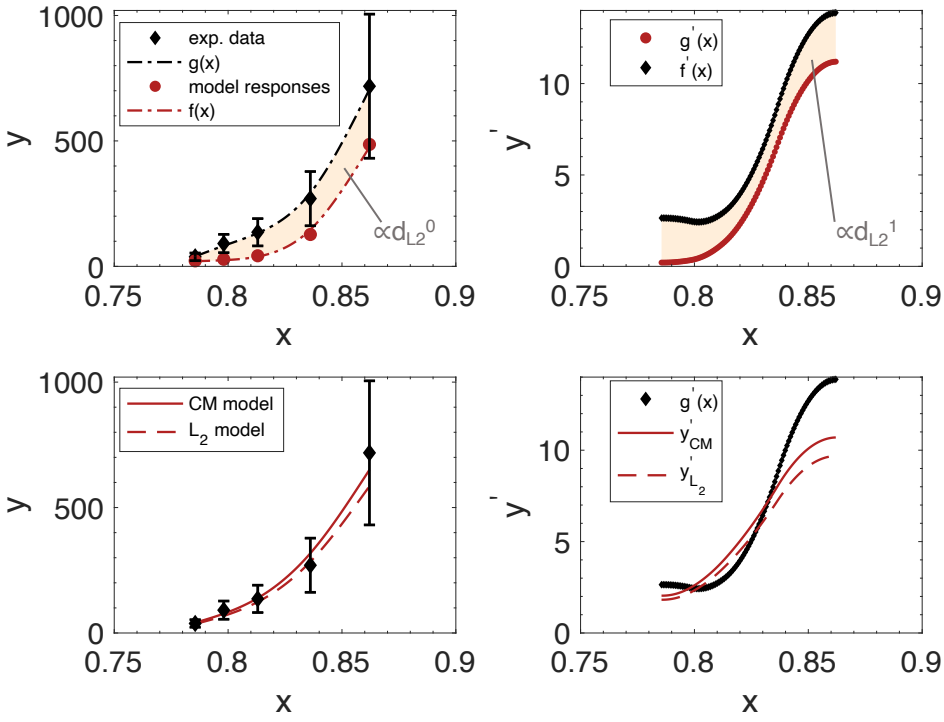

Figure 2.7: *Graphical example of how the splines and their derivatives are compared in the Curve Matching index. The top layer panels describe the model responses as well as reference data (left), and their derivatives (right). The bottom panel reports a comparison between optimized model responses obtained with CM and L_2 norm (left) as well as experiments, and their derivatives (right).*

Further mathematical details and examples are given in [17, 131]. In order to account for the uncertainty in the evaluation of (10), a bootstrapping procedure on the experimental data is carried out. This procedure relies on the assumption that each data point is normally distributed within its experimental uncertainty. A sufficiently large set of possible experimental trends is generated taking random samples from the above-mentioned distributions. Figure 2.8 displays an example of the application of the bootstrap procedure for laminar flame speed data, where 7 gaussian distributions (i.e. one for each data

point) were sampled 10 times to generate as many bootstrap variations.

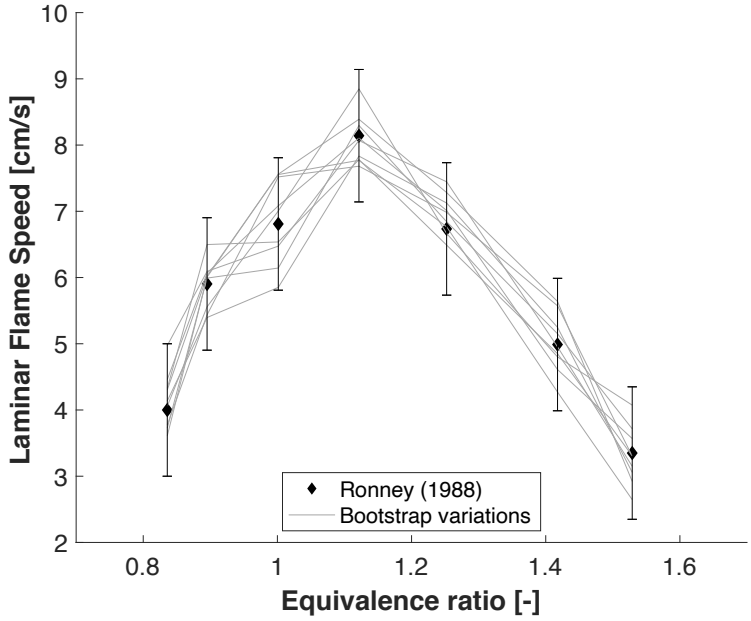

Figure 2.8: *Example of bootstrap procedure with 10 variations. Experimental data from [45]*

A set of 50 bootstrap variations (N_b=50) for each data point was adopted after verifying the substantial independence of the final output on a further broadening of the set. Thus, the objective function in case of DS number of experimental target datasets is defined as:

$$CM_{obj} = \frac{1}{DS}\sum_{j=1}^{DS}\left[1 - \frac{1}{N_b}\sum_{i=1}^{N_b}(CM_i)\right]_j \in [0,1] \tag{2.31}$$

2.4.2 Correlation between Arrhenius parameters and reparametrization

One additional challenge in optimization of detailed kinetics is the enhanced non-linearities of the models to be optimized. Such non-linearity introduces strong correlations between the variation of model responses due to perturbation model parameters. Parameters correlations effects on model tuning were discussed by Valko et al. [190], who also discussed their impact on global sensitivity analysis and how to remove correlations using a Rosenblatt trasformation. These correlations also makes it harder for any optimization algorithm to

get to absolute minimum in the objective function space. For the sake of simplicity, we hereby consider a trivial example proposed by [13] and also used in more recent work [150] for the same purpose. Let's consider the following mass balance equation for a first order irreversible reaction consuming the species SP:

$$\frac{d[SP]}{dt} = -k[SP] \tag{2.32}$$

For isothermal experiments k is constant, this model has analytical solution:

$$y = [SP] = [SP]_0 exp(-kt) \tag{2.33}$$

where $[SP]_0$ is the concentration of SP for t=0. Considering the experimental data in table 2.1, the model in equ. 2.33 can be used for parameter estimation by minimizing the objective function in equation 2.23. For this problem, the global minimum is located at 0.010279. For the sake of simplicity, only A and E are optimized. The employed optimization algorithm is, a modified version of the Powell [136] algorithm, available in SciPy [196].
Once we get to the best estimate, the sensitivity matrix can be computed as follows:

$$B = \begin{bmatrix} \frac{\partial y_1}{\partial A} & \frac{\partial y_1}{\partial E} \\ \vdots & \vdots \\ \frac{\partial y_{NE}}{\partial A} & \frac{\partial y_{NE}}{\partial E} \end{bmatrix} \tag{2.34}$$

and the variance-coovariance matrix can be also computed as:

$$V = s^2 (B^T B)^{-1} \tag{2.35}$$

where s^2 is the constant variance of the experimental fluctuations.
If we formulate k as follows:

$$k = A exp(-\frac{\epsilon}{T}) \tag{2.36}$$

The optimization algorithm is not able to reach the global minimum 0.010279. In fact, it gets stuck in a local minimum 0.012029 corresponding to completely different values of the best parameters. This happens because of the non-linearity introduced in equation 2.33 by 2.36. This results in strongly correlated

Table 2.1: *Experimental data used in this example*

t [min]	T [K]	y	t [min]	T [K]	y
120.0	600	0.900	60.00	620	0.802
60.00	600	0.949	60.00	620	0.802
60.00	612	0.886	60.00	620	0.804
120.0	612	0.785	60.00	620	0.794
120.0	612	0.791	60.00	620	0.804
60.00	612	0.890	60.00	620	0.799
60.00	620	0.787	30.00	631	0.764
30.00	620	0.877	45.10	631	0.688
15.00	620	0.938	30.00	631	0.717
60.00	620	0.782	30.00	631	0.802
45.10	620	0.827	45.00	631	0.695
90.00	620	0.696	15.00	639	0.808
150.0	620	0.582	30.00	639	0.655
60.00	620	0.795	90.00	639	0.309
60.00	620	0.800	25.00	639	0.689
60.00	620	0.790	60.10	639	0.437
30.00	620	0.883	60.00	639	0.425
90.00	620	0.712	30.00	639	0.638
150.0	620	0.576	30.00	639	0.659
90.40	620	0.715	60.00	639	0.449
120.0	620	0.673	—	—	—

derivatives of the model responses with respect to parameters perturbations as shown in figure 2.9 a. Here, the pearson correlation is close to -1, and the estimation is therefore biased.

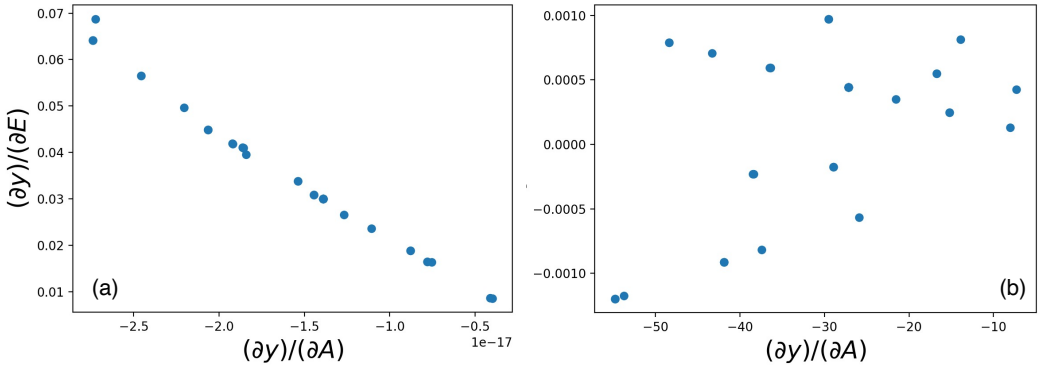

Figure 2.9: *Example of bootstrap procedure with 10 variations. Experimental data from [45]*

However, it is possible to achieve uncorrelated model responses (see 2.9 b),

if the Arrhenius equation is reparametrized. By applying this simple non-linear transformation of the pre-exponential factor:

$$A^* = Aexp(-\frac{\epsilon}{T_{ref}}) \tag{2.37}$$

the model becomes:

$$y = exp\left\{-tA^* exp\left[-\epsilon\left(\frac{1}{T} - \frac{1}{T_{ref}}\right)\right]\right\} \tag{2.38}$$

It should be noted that in 2.38, the correlation between model responses is also dependent on our choice of a new parameter, i.e. T_{ref}, which is usually chosen as equal to the average temperature of the experimental dataset. When $T_{ref} = 628.45K$ complete uncorrelation is achieved, as shown in (see 2.9 b). It is worth mentioning that in the form 2.38 the global minimum can be always reached regardless the choice of T_{ref}. However, figure 2.10 (a) shows that parameters correlation is really sensitive to T_{ref}. The same is true for the number of model evaluations that the optimizer need to get to the global minimum, which is minimized when the correlation is equal to 0. These results show that one should pay attention when selecting T_{ref} in 2.37 only when the performance of the optimization algorithm are concerned, and that chosing T_{ref} equal to the average of the operating temperature in experimental conditions is a good choice [150].
In case a modified Arrhenius equation is chosen, the following reparametrization can be adopted in optimization codes:

$$\begin{aligned} ln(k) &= ln(A) + nln\left(\frac{T}{T_{ref}}\right) - \frac{E_a}{R}\left(\frac{1}{T} - \frac{1}{T_{ref}}\right) \\ &= \alpha + nln\left(\frac{T}{T_{ref}}\right) - \epsilon\left(\frac{1}{T} - \frac{1}{T_{ref}}\right) \end{aligned} \tag{2.39}$$

2.5 Sensitivity analysis

Improving model accuracy is a task of critical importance. However, for large models with hundreds/thousands of parameters, to consider all of them simultaneously is particularly expensive from a computional point of view [95], even

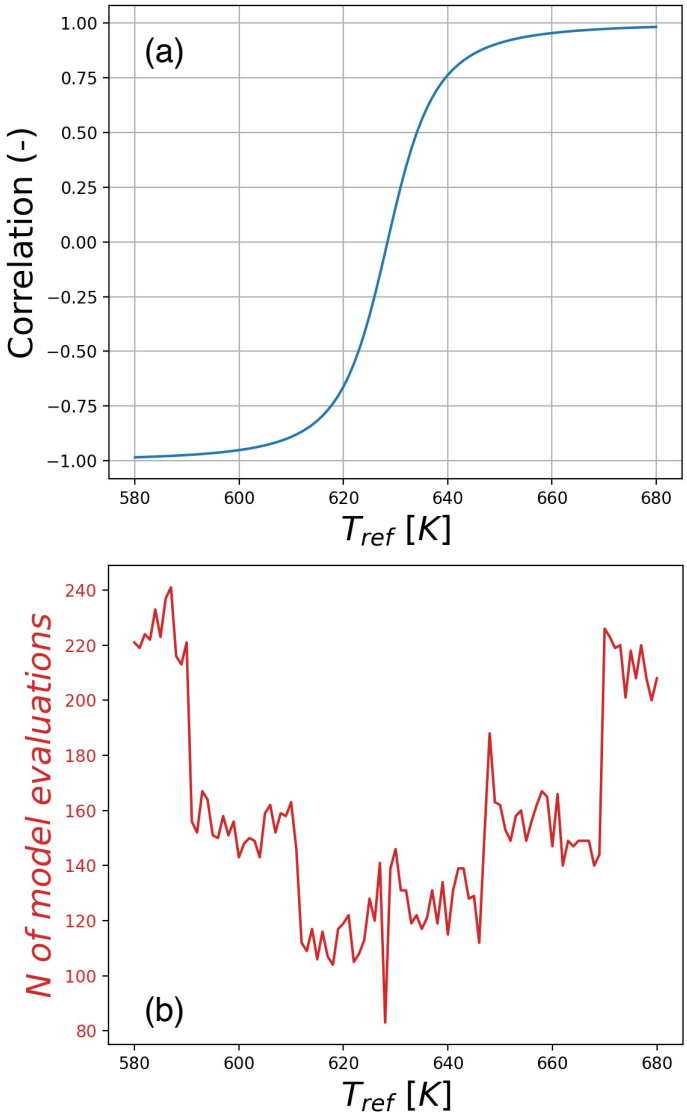

Figure 2.10: *(a) Correlation between modified Arrhenius parameters as a function of the adopted reference temperature. (b) Number of model evaluations requested by the optimizer to reach the error measure minimum as a function of the adopted reference temperature.*

with advanced and efficient tools. Sensitivity analysis allow to determine relative parameter importance, and to focus efforts on those parameters with the biggest influence on predictions. It would be incorrect to optimise parameters

for which there is no sensitivity to experimental data. An extensive review of all applied methods for sensitivity analysis in combustion was carried out by Alison Tomlin [180].

2.5.1 Local Sensitivity Analysis

The simulations of reacting gas mixtures are usually carried out in ideal reactors (e.g. perfectly stirred, batch and plug flow reactors, shock-tubes etc.) and laminar flames. A general reacting mixture is governed by the following system of coupled, first-order Odinary Differential equations (ODE):

$$\begin{cases} \frac{d\boldsymbol{y}}{d\zeta} = \boldsymbol{f}(\boldsymbol{y}, \zeta, \boldsymbol{p}) \\ \boldsymbol{y}(\psi_0) = \boldsymbol{y_0} \end{cases} \tag{2.40}$$

In 2.40, y is the vector of unknowns (temperature, pressure, and species concentration). ζ is the independent variable (time or spatial coordinate), and $f(y, \zeta, p)$ is a non-linear function of the unknowns and kinetic model parameters, p. The first order sensitivity coefficients for the i^{th} unknown and the j^{th} parameter are defined as follows:

$$s_{ij}^1 = \frac{\partial y_i}{\partial p_j} \tag{2.41}$$

The equations for the sensitivity coefficients can be easily obtained by differentiating the ODE system in equation 2.40:

$$\begin{cases} \frac{d\boldsymbol{s_j^1}}{d\zeta} = \boldsymbol{J}\boldsymbol{s_j^1} + \frac{\partial \boldsymbol{f}}{\partial p_j} \\ \boldsymbol{s^1}(\zeta_0) = 0 \end{cases} \tag{2.42}$$

where $\boldsymbol{J}$ is the jacobian matrix of 2.40, and $\boldsymbol{s_j^1}$ is the vector of the partial derivatives of unknowns with respect to the parameter p_j. In OpenSMOKE++ [35] sensitivity coefficient for each parameter p_j solving an independent ODE system (equation 2.42) in addition to 2.40. Finally, the raw sensitivity coefficients are normalized to make comparison between different reactions easier:

$$\tilde{s}_{ij}^1 = \frac{\partial ln(y_i)}{\partial ln(p_j)} = \frac{p_j}{y_i} s_{ij} \tag{2.43}$$

2.5.2 Cumulative Sensitivity/Impact Function

Warnatz [205] suggested the joined use of sensitivity and uncertainty to identify key reactions in a detailed kinetic mechanism. This concept was also used in optimization of kinetic models for the first time by Frenklach et al. [61], who selected the active variables using a ranking based on the "impact factor", i.e. considering the absolute values of sensitivity coefficients multiplied by their own uncertainty. Later on, this index was also referred to as "sensitivity-uncertainty index" [186] and "optimization potential" [25].

As in the context of this thesis we usually dealt with large datasets, composed by hundreds of experimental data points, parameters selection is performed separately for each Test Case (TC), in order to retain all the important elementary steps for the optimization. A test case is a dataset, containing N_d data points, coming from a single scientific article or expeirmental facility. The process of reaction selection is described in the following.

First, a local sensitivity analysis (decribed in 2.5.1), was performed for each data point in TC. This produces a $N_d \times N_r$ matrix, where each row $\boldsymbol{S}_d$ of size (i.e number of reactions), containing normalized sensitivity coefficients as defined in 2.43. This matrix can be used to compute average normalized sensitivity coefficient for the j^{th} reaction as follows:

$$\overline{s}_j = \frac{1}{N_d} \sum_{n=1}^{N_d} |\tilde{s}_{nj}| \tag{2.44}$$

The coefficients in equation 2.44 are obtained by perturbating the nominal values, and can be the stored in a vector $\overline{\boldsymbol{S}}$, sorted and elaborated in cumulative sum. The resulting vector is referred to as Cumulative Sensitivity Function (CSF). This procedure allows the exploitation of the cumulative sum properties, aiding the selection of reactions to be optimized with proper priority. In particular, a subset of sensitive reactions $\overline{\boldsymbol{s}}_s$ can be retrieved by establishing a threshold corresponding to a defined fraction of the sum of the 1st order sensitivity coefficients related to a specific TC. Subsequently, once the uncertainty factors are known for each identified reaction impact factor the j^{th} is evaluated as suggested in the literature:

$$\overline{I}_j = \overline{s}_j \cdot f_j \tag{2.45}$$

Figure 2.11 shows an example of Cumulative Impact Function (CIF) obtained by applying the cumulative sum on the vector $\overline{\boldsymbol{I}}$ for the test case from Song [168]. Here only 5 reactions, are responsible of 90% of the impact. The remaining set of 196 reactions retaining 10% of the total impact are excluded in further investigations.

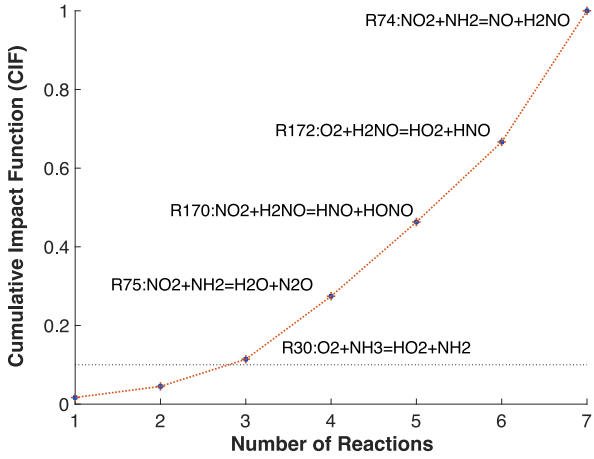

Figure 2.11: *Example of reaction selection through Cumulative Impact Function (CIF) for Song [168] test case. The horizontal line represents the chosen threshold of 90% of the total local impact*

2.5.3 Global sensitivity analysis

Global sensitivity analysis has been widely applied to combustion kinetics [88, 181, 213, 214], in this works, the High-Dimensional Model Representation was introduced and applied for uncertainty propagation and analysis of variance decompotion for global sensitivity.

Usually, local techniques do not allow for general considerations about the model as they strongly depend on the initial guess and do not account for interdependencies between parameters. In Figure 2.12 the difference between Local and Global methods is depicted. Both charts show an example response surface generated by varying the value of the model parameters, P_1 and P_2. Here, $\boldsymbol{P_0} = [P_{1,0}, P_{2,0}]$ is the initial model parametrization. As displayed in the top chart, the local sensitivity analysis would measure the derivatives of the model response with respect to $\boldsymbol{P_0}$. Indeed, it is reasonable to expect that de-

pending on P_0 these derivatives would change. This is the reason why LSA is strongly dependent on the initial model parametrization. Variance-based decomposition methods, or Global Sensitivity Analysis (GSA), consider the model response within the entire sample space of the parameters and does not depend on the initial model configuration [74].

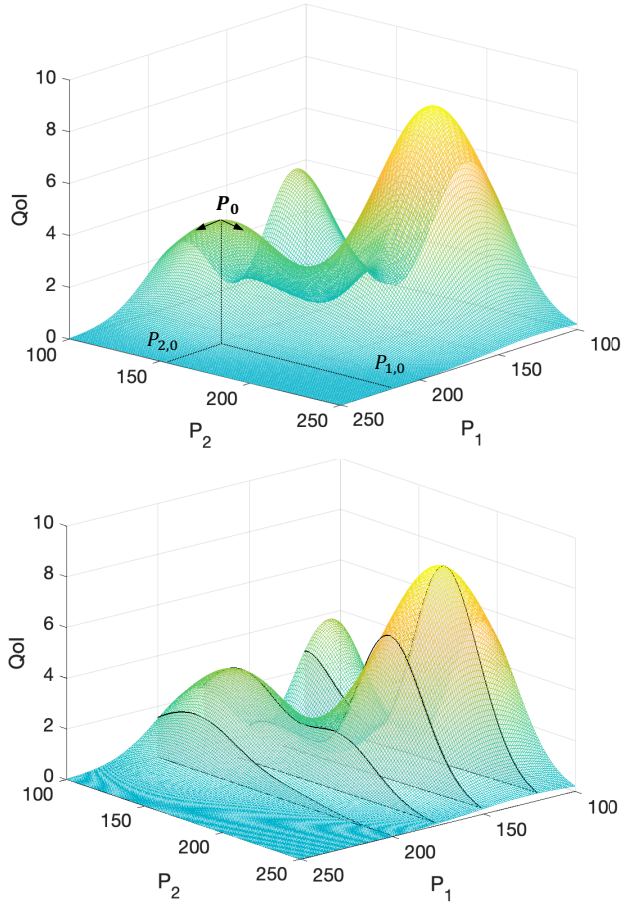

Figure 2.12: *Graphical description of the difference between Local Sensitivity and Global Sensitivity.*

Sobol [78] suggested the use of Monte Carlo (or quasi-Monte Carlo) methods for the calculation of sensitivity measures. The first order sensitivity coefficients:

$$S_i = \frac{V_{\omega_i}(E_{\omega_{\sim i}}(m(\boldsymbol{\omega}|\omega_i))}{V(m(\boldsymbol{\omega}))} \tag{2.46}$$

where $V(m(\boldsymbol{\omega}))$ is the total variance of the model response $m(\boldsymbol{\omega}))$, and the numerator represents the variance of the expected value of the model response, obtained by varying all the parameters while keeping the i^{th} one constant, i.e. by varying all the parameters but the i^{th} one ($\omega_{\sim i}$). This is displayed in the bottom graph of figure 2.12, where the estimated value of the model response to variations of P_2 can be computed for eah value of P_1 along the grey shaded area. Homma and Saltelli [79] introduced the 'total effect' parameter index. The latter provides a measure of the total effect of a given parameter, including all the possible synergetic terms between the parameter and all the others:

$$S_{Ti} = 1 - \frac{V_{\omega_{\sim i}}(E_{\omega_i}(m(\boldsymbol{\omega}|\omega_{\sim i}))}{V(m(\boldsymbol{\omega}))} \tag{2.47}$$

where the numerator of the second term is the first order effect of $\omega_{\sim i}$, so S_{Ti} must give the contribution of all terms in the variance decomposition which include ω_i. The description of efficient numerical methods for the estimation of S_i and S_{Ti} can be found elsewhere [80]. In general, K(2+N) model evaluations are required for the calculation of Sobol's indices [80], where N is the number of model parameters and K the considered number of input values combinations. For the example, if eight parameters were selected (N=8). To infer accurate statistics on the first and second moment of a given model response, Monte Carlo methods takes a considerable amount of parameters combinations (e.g. K=100). For this example, it would take 1000 model evaluations for GSA on a single model response.

In HDMR and PCE, the Analysis of Variance (ANOVA) allows to perform GSA by analyzing the *mode strengths* in the spectral expansion. In particular, the overall output variance can be computed as the sum of all *mode strengths* (α_i in equation 2.49):

$$\sigma^2(\boldsymbol{\xi}) = \sum_{i=1}^{P+1} \alpha_i^2 \tag{2.48}$$

Consequently, the fractional contribution of each α_i to $\sigma^2(\boldsymbol{\xi})$ represent the global

sensitivity coefficient related to the variables involved in the construction of the *mode functional* Ψ_i.

Adjoint sensitivity analysis

It is worth mentioning the work from Langer et al. [95], who used adjoint sensitivity analysis on kinetic, thermodynamical and transport properties showing the potential of using all mechanism parameters for optimization in the future. The adjoint sensitivity analysis for complex combustion kinetic model was initially proposed by Lemke et al. [98]

2.6 Uncertainty Quantification methods

Uncertainty Quantification or Propagation methods are a family of approaches, which can be used to construct the probability law of the solution of a model, given a set of independent random variables (RVs), usually called *germ*, representing the model inputs and their variability.

2.6.1 Monte Carlo (MC) methods

The MC method is the simplest approach to implement because the germ elements are considered statistically independent. For this reason, a sample set of independent realizations of the germ is withdrawn using a (pseudo) random number generator for each RV belonging to it. By computing the model responses for each individual realization, the probability law of the solution can be estimated with a sampling error, which converges to 0 as the sample set dimension increases. As for most applications the computational cost is dominated by the resolution of the model for a single parameter realization, more efficient sampling strategies were proposed, e.g. Latin Hypercube Sampling (LHS) [108] and Quasi Monte Carlo Sampling (QMCS) [115].

2.6.2 Spectral methods

The use of surrogate models comes to handy when extremely expensive tasks need to be performed for model improvement and/or analysis. The principle is common to all of them" approximate the model responses using a pre-defined meta-model structure, usually a polynomial, whose parameters are tuned to

match real model responses given variations of parameters values. In combustion, the most widely used are Solution Mapping (SM), from Frenklach [61], High-dimensional model representation (HDMR) [180] and Polynomial Chaos Expansion (PCE) [122]. In this thesis, PCE was employed and will therefore be discussed in the following.

Polynomial Chaos Expansion

Polynomial Chaos Expansion is a spectal method for uncertainty quantification, which aims at constructing the functional dependence between the vector of input parameters $\boldsymbol{\xi}$ and the response of a known model $m(\boldsymbol{\xi})$ to their perturbation. This functional dependence is usually expressed in terms of a infinite or finite-dimensional series:

$$m(\boldsymbol{\xi}) \approx f(\boldsymbol{\xi}) = \sum_{i=0}^{\infty} \alpha_i \Gamma_i(\boldsymbol{\xi}), \tag{2.49}$$

where Γ_i are adequate functionals (also known as *"mode functions"*) of $\boldsymbol{\xi}$, and α_i are the coefficients to be determined (or *"mode strengths"*). $\boldsymbol{\xi}$ is a random vector of standardized random variables. In real applications, the expansion is usually truncated at the order p and the number of terms $(P+1)$ in the expansion is given by:

$$P + 1 = \frac{(N+p)!}{N!p!} \tag{2.50}$$

where N is the dimensionality of the germ $\boldsymbol{\xi}$. Once available and validated, $f(\boldsymbol{\xi})$ may be immediately used to compute statistics of the real model responses. Let $\{\xi\}_{i=1}^{\infty}$ be a sequence of centered, normalized, mutually orthogonal, gaussian variables. Let $\hat{\Gamma}_p$ denote the space of polynomials in $\{\xi\}_{i=1}^{\infty}$ having degree less or equal to p. Γ_p denote the set of polynomials, which belong to $\hat{\Gamma}_p$, and are orthogonal to $\hat{\Gamma}_{p-1}$, and by $\widetilde{\Gamma}_p$ we denote the space spanned by Γ_p. Γ_p is termed a *Polynomial Chaos* of order p, and consists of all polynomials of order p, involving all possible combinations of the random variables $\{\xi\}_{i=1}^{\infty}$. For instance, the expansion of the random variable U, dependent of $N_p = 2$ input parameters and order p, becomes:

$$U = \alpha_0\Gamma_0 + \alpha_1\Gamma_1(\xi_1) + \alpha_2\Gamma_1(\xi_2) + \alpha_{11}\Gamma_2(\xi_1,\xi_1) + \alpha_{22}\Gamma_2(\xi_2,\xi_2) + \alpha_{12}\Gamma_2(\xi_1,\xi_2) \tag{2.51}$$

where $\Gamma_p = \{\Gamma_0, \Gamma_1(\xi_1), \Gamma_1(\xi_2), \Gamma_2(\xi_1,\xi_1), \Gamma_2(\xi_2,\xi_2), \Gamma_2(\xi_1,\xi_2)\}$ is the polynomial chaos, truncated at the order p, for this particular case. Let's take a N-dimensional case (i.e. with $\{\xi\}_{i=1}^{N}$) and define a multi-index $\gamma = \{\gamma_1, \gamma_2, ..., \gamma_N\}$ containing a polynomial order for each variable belonging to the germ. If we define $\lambda(p)$ as the set of all possible multi-indices:

$$\lambda(p) = \{\gamma : \sum_{i=1}^{N} \gamma_i = p\} \tag{2.52}$$

the PC of p^{th} order can be constructed according to:

$$\Gamma_p = \{\cup_{\gamma\in\lambda(p)} \prod_{\gamma_1}^{\gamma_N} \psi_{\gamma_i}(\xi_i)\} \tag{2.53}$$

where $\psi_{\gamma_i}(\xi_i)$ is a polynomial of order γ_i, belonging to a known or constructed family of orthogonal polynomials. Indeed, the underlying assumption is that the random vector (i.e. the *germ*) contains statistically independent variables. How shall we choose the optimal set of orthogonal polynomials to be used to build the functionals Γ_i? In general, one can assert that the optimal polynomial expansion is that constructed using the measure corresponding to the probability law of the random variable that we seek to represent. However, this probability law is often not known *a priori*. In this case, the probability laws chosen for the model parameters can be used to choose a corresponding family of orthogonal polynomials (see Table 2.2).

Table 2.2: *Optimal matches between input parameter probability laws and families of orthogonal polynomials.*

Distribution of ξ	Polynomials Family
Gaussian	Hermite
γ	Laguerre
β	Jacobi
Uniform	Legendre

The Figure 2.13 displays the first six polynomials for the families of polynomials which will be used in this thesis, namely Legendre and Hermite polynomials.

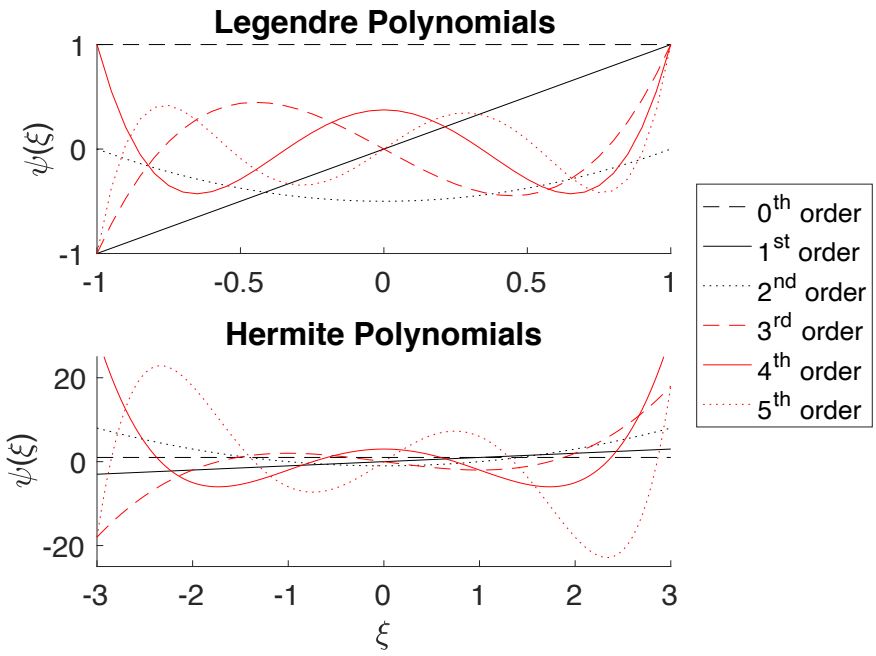

Figure 2.13: *First 6 polynomials for Legendre and Hermite families from Askey Scheme.*

The mode strengths α_i can be evaluated through a spectal projection against the space spanned by Γ_i:

$$\alpha_i = \frac{\langle m, \Gamma_i \rangle}{\langle \Gamma_i, \Gamma_i \rangle} = \frac{1}{\langle \Gamma_i, \Gamma_i \rangle} \int_\Omega m \Gamma_i \rho_x(\xi) d\xi = \frac{1}{\langle \Gamma_i, \Gamma_i \rangle} \left[\frac{1}{N_{cp}} \sum_{j=1}^{N_{cp}} m(\xi_j) \Gamma_i(\xi_j) \right] \quad (2.54)$$

where the inner product $\langle \Gamma_i, \Gamma_i \rangle$ is known from the construction of the PC basis, and the projection integral can be solved numerically. Indeed, N_{cp} is the number of collocation points, or chose combinations of parameters values, to evaluate the integral. The "choice" of the collocation points can be performed using random sampling techniques (Monte Carlo (MC), Latin Hypercube Sampling, Quasi-MC) or determistic methods, i.e. quadrature rules. Among the alternatives for deterministic methods, which ensure a lower number of model evaluations for low dimensional problems (i.e. N_{cp}), are *tensor product* and

sparse [165] quadrature rules. The latter has a weaker dependence on dimensionality with respect to the former and ensure a lower number of collocation point, with comparable accuracy. Figure 2.14 displays an example of grid built with the previously mentioned methods.

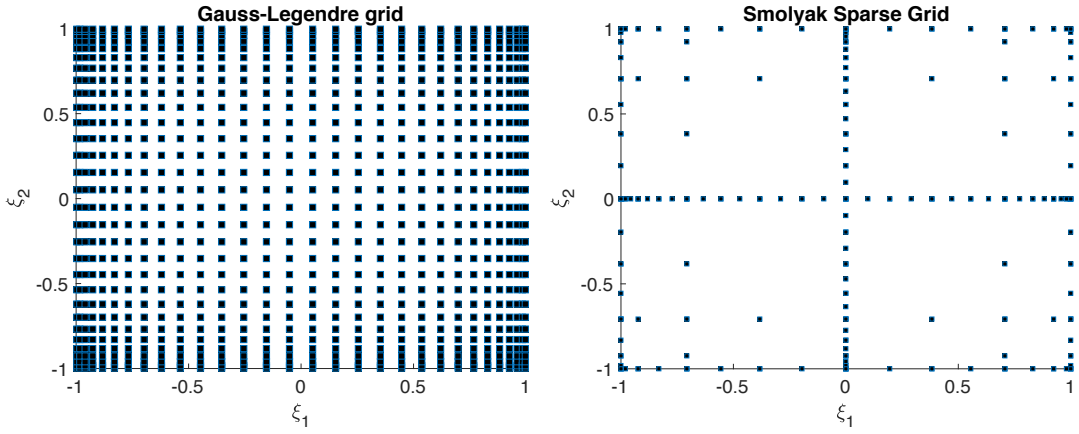

Figure 2.14: *Example of collocation points used to evaluate the coefficients in a spectral expansion of two variables. Left) tensor-product using Gauss-Legende rules. Right) Smolyak sparse grid.*

2.7 Elliptical and Likelihood confidence regions

In this work, we exploit the features of EA to obtain likelihood confidence or acceptance regions for parameters estimates [148, 150], which were used in combination with heuristic optimization algorithms elsewhere [149]. Assuming that is possible to linearize the objective function $S(\omega)$ around its minimum point estimate $\hat{\omega}$, its second-order Taylor expansion yields:

$$O(\boldsymbol{\omega}) = O(\hat{\boldsymbol{\omega}}) + (\boldsymbol{s\omega} - \hat{\boldsymbol{\omega}})\nabla O_{\hat{\boldsymbol{\omega}}} + \frac{1}{2}(\boldsymbol{\omega} - \hat{\boldsymbol{\omega}})^T H_{\hat{\boldsymbol{\omega}}}(\boldsymbol{\omega} - \hat{\boldsymbol{\omega}}) \tag{2.55}$$

where $\nabla O_{\hat{\boldsymbol{\omega}}}$ and $H_{\hat{\boldsymbol{\omega}}}$ are the gradient vector and the Hessian matrix of the objective function, respectively. Considering that $O(\boldsymbol{\omega})$ is a stationary point for $O(\boldsymbol{\omega})$, the first derivative of O with respect to any parameter is null (i.e. $\nabla S_{\hat{\boldsymbol{\omega}}} = 0$), and $H_{\hat{\boldsymbol{\omega}}}$ is equal to twice the covariance matrix of parameters estimates [13]. It follows:

$$O(\boldsymbol{\omega}) - O(\hat{\boldsymbol{\omega}}) = (\boldsymbol{\omega} - \hat{\boldsymbol{\omega}})^T V^{-1}(\boldsymbol{\omega} - \hat{\boldsymbol{\omega}}) \equiv \chi_p^2 \tag{2.56}$$

So, $O(\boldsymbol{\omega})$ - $O(\hat{\boldsymbol{\omega}})$ is a random value, which follows a chi-squared distribution. At the same time O itself follows a chi-squared distribution with $n - p$ degrees of freedom [13]. Therefore, by definition, the ratio between the two follows a F distribution with $(1 - \lambda)$ level of confidence and parameters p, and $(n - p)$:

$$\frac{O(\boldsymbol{\omega}) - O(\hat{\boldsymbol{\omega}})}{O(\boldsymbol{\omega})} \frac{n-p}{p} \equiv F_{p,n-p]}^{1-\lambda} \tag{2.57}$$

Finally, all the combinations corresponding to an objective function value such that:

$$O(\boldsymbol{\omega}) \leq O(\hat{\boldsymbol{\omega}}) \left[1 + \frac{p}{n-p} F_{p,n-p]}^{1-\lambda}\right] \tag{2.58}$$

compose the confidence region. Assuming a joint gaussian distribution for the probability of input parameters, all the combinations of parameter values belonging to the acceptance region, can be used to estimate its covariance matrix and display the confidence regions in its elliptical form.

CHAPTER 3

Optimization of a kinetic mechanism for ammonia combustion

This chapter is based on the following pubblication:

- *An evolutionary, data-driven approach for mechanism optimization: theory and application to ammonia combustion.* ***Bertolino, A.****, Fürst, M. B., Stagni, A., Frassoldati, A., Pelucchi, M., Cavallotti, C. A., Faravelli, T., Parente, A. Combustion and Flame.* https://doi.org/10.1016/j.combustflame.2021.02.012

3.1 Abstract

In this chapter, the approach for detailed kinetic mechanism optimization described in previous chapters is applied to ammonia combustion. The approach is based on a curve matching-based objective function and includes a novel methodology for the optimisation of pressure-dependent reactions via logarithmic interpolation (PLOG format). In order to highlight the advantages of the new formulation of the objective function, a comparison with L1 and L2 norm is performed. The selection of impactful reactions is carried out by means of a Cumulative Impact Function (CIF), while an Evolutionary Algorithm (EA) is adopted to perform the optimization. The capabilities of the proposed methodology were demonstrated using a database of 635 experimental datapoints on ammonia combustion, covering standard targets like ignition delay times, speciation and laminar flame speed. The optimization was carried out starting from a recently published mechanism [170] describing ammonia pyrolysis and oxidation, largely developed using first-principles calculation of rate constants.

After the selection of the 24 most impactful reactions, the related 101 normalized Arrhenius parameters were simultaneously varied, within their constraints. Their uncertainties were taken from the literature, when available, or estimated according to the level of theory adopted for the determination of the rate constant. Hence, guidelines to estimate uncertainty for reaction rate constants, derived from first principles calculations using well consolidated computational protocols as a reference, are provided. The optimized mechanism was found to improve the nominal one, showing a satisfactory agreement over the entire range of operating conditions. Moreover, the use of a 'curve matching' index was found to outperform the adoption of L_1 and L_2 norms. The comparison between the nominal mechanism and the one optimized via curve matching allowed a clear identification of different critical reaction pathways for different experimental targets.

3.2 Database

Figure 3.1 summarizes the features of each test case (TC) in the temperature, pressure and composition space. The experimental data considered in this work covers the entire space of operating conditions.

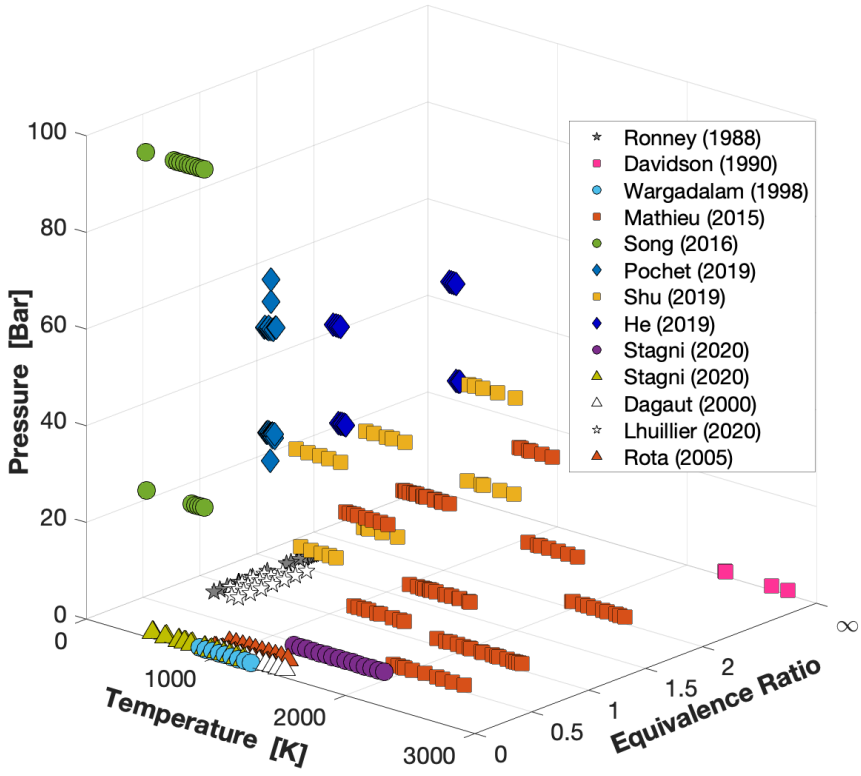

Figure 3.1: *Collected data on Ammonia combustion displayed in temperature, pressure, composition space.*

The database, consisting of 60 different datasets (with 635 experimental points) from different test cases, was divided in optimization and validation targets (i.e. 75% and 25%, respectively). For high-temperature conditions, the shock tube experiments from Mathieu and Petersen [107], and Shu et al. [159] cover ignition delay time in a wide range of composition (ϕ = 0.5 to 2.0) and pressures (10 to 40 bar). Stagni et al. [170] reported data for ammonia oxidation at nearly atmospheric pressure for lean mixtures in two different systems, namely

jet stirred and flow reactors. At low temperatures, He et al [75]and Pochet et al. [134] provided auto-ignition data at higher pressures, for lean, stoichiometric and rich mixtures in rapid compression machines. Wargadalam et al. [204] and Song et al. [168] published speciation data for very lean conditions, at pressure of 1, 30 and 100 bar, in flow reactors. Davidson et al. [41] investigated ammonia pyrolysis in a shock tube at extremely high temperatures (T>2500 K). The laminar burning speed experiments by Lhuillier et al. [99] were only considered for validation. However, flame speed targets were included by using the data from Ronney [45]. The TCs from Rota [142] and Dagaut [37] in jet stirred reactors were excluded from the optimisation set, yet used for validation, as they cover a part of the operating conditions space which is already populated with data from Stagni [170] and Wargadalam [204] (see fig. 3.1).

Details on models responses

For each data set the ignition delay times were calculated using the definition reported in the corresponding reference experimental paper, to ensure consistency. For the shock tubes, the assumption of constant volume was adopted for the case of Mathieu and Petersen [107] and Davidson [41]. To reproduce the data from Shu et al. [159], gas dynamic effects were accounted for following the methodology described in [96]. For the RCM data, the “adiabatic core hypothesis” was adopted [173], and detailed volume profiles from He [75] and Pochet [134] were used to properly account for the compression stroke and heat exchange effects in each experiment. In the flow reactor from Stagni [170] the experimental temperature profiles were imposed are reported in the reference paper.

3.3 Estimation of uncertainty factors for first principle calculations of rate constants

Among the reactions listed in table 3.1 13 out of 43 rates come from experiments, together with their uncertainty factors. In particular, for experimental data the uncertainty is assumed to be equal to that declared by the experimentalists. The remaining part involves phenomenological rate constants determined using first principle (ab-initio) calculations. Klippenstein et al. [89] declares that an uncertainty factor of 0.3 (see eq. 2.17) for the rate constants

can be obtained for reactions belonging to the reaction families considered in the present work. In a more recent publication Cavallotti et al. [29] showed that the level of accuracy attainable using the ab-initio master equation approach can be a factor of 0.3 (see eq. 2.17) or lower. The main factors contributing to uncertainty in a rate constant calculation derive from: 1) the level of theory used to determine the energy of stationary points on the potential energy surface (PES); 2) the theoretical methods adopted for the computation of the high pressure rate constant; 3) the level at which pressure effects and reaction dynamics on a multi-well PES are described; 4) the treatment of anharmonicities, most importantly the description of torsional motions, if active for a specific reaction; 5) the availability of experimental rate constant data. The values from the protocols of Cavallotti et al. [29] and Klippenstein et al. [89] are assumed as the lower uncertainty threshold in the present work, while the remaining ones are assigned with a policy of inverse proportionality to the adopted level of theory. This threshold corresponds to a fr factor equal to 0.3 (see eq. 2.17). The following penalty terms were used:

- Concerning the level at which electronic structure calculations were performed, computational protocols where energies are computed at the CCSD(T) / CBS or higher have no penalty term. For CBSQB3 calculations a 0.2 factor is added to fr, so that the uncertainty goes from 0.3 to 0.5. For DFT calculations, such as B3LYP, a factor of 0.3 is added, thus increasing the uncertainty factor to 0.6.
- High pressure rate constants can be determined using (in order of decreasing accuracy): i) Variable Reaction Coordinate Transition State Theory (VRC-TST), ii) variational transition state theory (VTST), or iii) conventional transition state theory (TST), where TST or VTST are assumed to be suitable to study abstraction or addition reactions, while VRC-TST or VTST are necessary to study barrierless processes such as recombination or bond dissociation reactions (i.e. unimolecular initiations reactions). A penalty of 0.3 and 0.1 was assigned to TST and VTST, respectively, in case of radical/radical recombination or decomposition reactions. Otherwise, penalties of 0.1 and 0.05 were assigned.
- Methods where the impact of pressure dependence and multi-well dynamics on the rate constant are studied using the Master equation approach

coupled with TST and ab initio calculations (AI-TST-ME), are generally more accurate than methods with lower theoretical detail, such as QRRK. The adopted penalty term is 0.4, so that for QRRK methods the estimated rates are associated with an uncertainty factor ranging between 0.7 and 1. This value was adapted to 0.5 for Dean and Bozzelli [43], who also compared their rates with experimental data and adjusted their recommendations accordingly.

- Anharmonicities can have a quite relevant impact on rate constants if torsional motions are present [124]. If no torsional motion treatment, such as the hindered rotor model, is used when torsional motions are active, a penalty term of 0.5 is added.

In order to further support the general validity of the optimization method, a sensitivity analysis to the assigned uncertainty parameters was carried out by performing three different optimizations with a limited number of targets [18]. The first was carried out with uncertainty factors used in this work, the others by multiplying all of them by a factor of 0.5, and 2. Results showed that the majority of the resulting kinetic rate constants overlap with those obtained with the nominal values of f (eq. 2.17), thus supporting the robustness of the methodology.

3.4 A novel method for the estimation of Arrhenius parameters bounds

As in [185, 192], all the parameters of the selected rate constants expressed according to the modified Arrhenius expression ($k = AT^{\beta}exp(-Ea/RT)$) undergo optimization, i.e. pre-exponential factors (A), temperature exponents (n), and activation energies (E_a). In equation 2.3, α, n and ϵ are continuous random variables representing the Arrhenius parameters, usually assumed to be uniformly [178] or normally [185] distributed. The problem of defining the constraints for the active parameters was dealt with in several studies. In the deterministic framework of B2B-DC [59], the feasible set is obtained by combining the initial bounds of both active variables and experimental data. In MUM-PCE [155], a statistical approach is adopted, which assumes “a priori” distributions for both the model parameters and the measurements, and produces “a posteriori” distributions for both model parameters and predictions. These two approaches were recently compared, and they were found to give

consistent results [57]. As we discuss earlier in this chapter, the nominal mechanism largely relies on ab-initio calculations. For this reason, the temperature dependence of f_r (eq. 2.17) is not accounted for, and uniform distributions for all the active variables are employed. As reported in equation 2.3, κ is a weighted sum of three random variables with joint uniform distribution, which results in a higher probability near κ_0 [121]. For the sake of simplicity, in the following we assume that for all temperatures the kinetic constant is a normally distributed random variable with mean value κ_0, corresponding to $\kappa(p_0)$, and standard deviationσ_κ, with $p_0 = [\alpha_0, \beta_0, \epsilon_0]$. As in [155, 178], we assume that f_r corresponds to the $2\sigma_\kappa$ of the distribution of κ, and we constrain it at 3σ. From equation (eq. 2.17), κ_{max} and κ_{min} can be obtained, i.e. the maximum and minimum linear constraints of κ in $T \in [Tmin, Tmax]$. As an element κ_i in κ can be retrieved by sampling from the distributions of the normalized Arrhenius parameters, f_r can also be propagated from κ to α, β, and ϵ to estimate their bounds. In the following, the hypothesis of mutual independence between parameters is used exclusively to achieve this goal. Given the equation:

$$10^{f_r} = \frac{\kappa_{max}(T)}{\kappa_0(T)} = \frac{\kappa_0(T)}{\kappa_{min}(T)} = exp[\Delta\alpha + \Delta n ln(T) - \Delta\epsilon T^{-1}] \tag{3.1}$$

and assuming that the maximum variation Δp_i of one parameter is determined by projecting the uncertainty of κ on the parameter itself (i.e. keeping constant the other two to their nominal values so that Δp_i=0), the following constraints can be retrieved:

$$\alpha_0 - ln\left(10^{f_r}\right) < \alpha < \alpha_0 + ln\left(10^{f_r}\right) \tag{3.2}$$

$$n_0 - \frac{f_r}{log_{10}(T)} < n < n_0 + \frac{f_r}{log_{10}(T)} \tag{3.3}$$

$$\epsilon_0 - f_r T ln(10) < \epsilon < \epsilon_0 + f_r T ln(10)) \tag{3.4}$$

This operation results in 2 non-linear constraints for n and ϵ in κ in $T \in [Tmin, Tmax]$. However, it can be shown that:

$$\lim_{T\to\infty} k(T) = exp(\alpha)T^n \tag{3.5}$$

$$\lim_{T\to 0} k(T) = exp(-\epsilon T^{-1}) \tag{3.6}$$

The limits (3.5) and (3.6) indicate that at high temperature, the term T^n controls the value of κ, while the contribution of ϵT^{-1} is progressively smaller. The opposite is true for low temperature. Thus, the sensitivity of κ to n is maximum at T_{max}. Conversely, the sensitivity of κ to ϵ is maximum at T_{min}. By bounding n and ϵ in equations 3.3 and 3.4 at T_{max} and T_{min}, respectively, we ensure that $\kappa(\alpha_0, \beta_{max}, \epsilon_0, T)$, $\kappa(\alpha_0, \beta_{min}, \epsilon_0, T)$, $\kappa(\alpha_0, \beta_0, \epsilon_{max}, T)$ and $\kappa(\alpha_0, \beta_0, \epsilon_{min}, T)$ never violate the linear constraints on $\kappa(T)$, when $T \in [Tmin, Tmax]$. In this work, the minimum and maximum temperatures are 300 and 3000 K, respectively. Indeed, from the definition of f_r in equation 2.17, also $\kappa(\alpha_{min}, \beta_0, \epsilon_0, T)$, $\kappa(\alpha_{max}, \beta_0, \epsilon_0, T)$ do not violate the mentioned constraints. The adoption of this methodology for the estimation of parameter boundaries has two main advantages. First, it reduces the probability of sampling a kinetic rate constant $\kappa(T)$, which violates the above mentioned linear constraints, with respect to previously proposed methods. Secondly, it also enables the optimization of PLOG-based reactions. As an example, the Figure 3.2 shows the projections of the parameters bounds on the kinetic constants of the reaction $NH_2 + NO_2 = H_2NO + NO$.

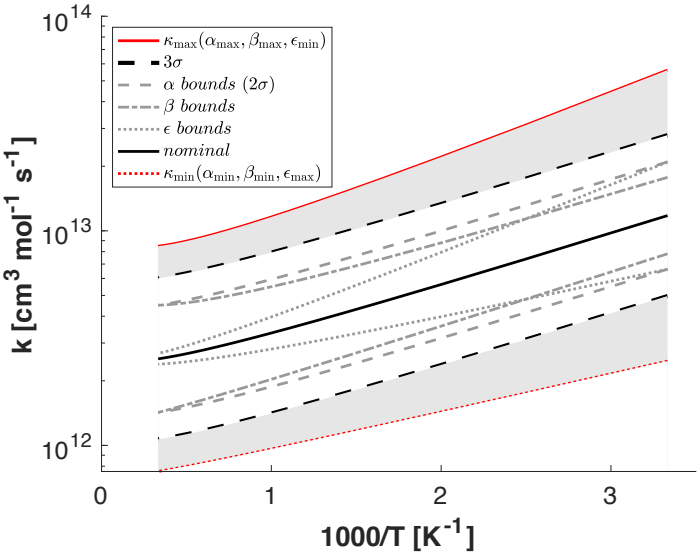

Figure 3.2: *Graphical example of reaction rate uncertainty:* $NO + O = NO_2$. *Adapted from [103]*

Those resulting from varying only α overlap with the 2σ of the distribution of κ. On the other hand, those resulting from the variation of n and ϵ only overlap with the 2σ of κ only at T_{max} and T_{min}, respectively, while not exceeding them along $T \in [T_{min}, T_{max}]$. The limit values of the corresponding κ distribution, i.e. $\kappa(\alpha_{max}, n_{max}, \epsilon_{min})$ and $\kappa(\alpha_{min}, n_{min}, \epsilon_{max})$, are also displayed. They include the entire space of κ and exceed it. In fact, since the parameters are statistically dependent [66], not all the combinations of the three are valid. All the combinations, which result in values of κ belonging to the area between the limit values and the 3σ bounds of the distribution of κ, are excluded from the set of eligible parameter combinations (see section 2.2).

3.5 Optimization of reaction PLOG formalism

For those reactions exhibiting a "fall-off" behaviour, the rate $k(T, P)$ is usually determined from the low and high-pressure limit constants, together with a blending function that smoothly connects the limiting rates across the fall-off regime, using different possible formulations. Among these, the Troe formulation [182] is the most widely used. An alternative formulation based on logarithmic interpolations, expressed with the so-called PLOG, has been recently proposed [140], and is rapidly growing in popularity because of the potentially superior accuracy, thus becoming the new standard formalism. PLOG reactions are typically introduced in a kinetic mechanism using multiple Arrhenius rate constants accounting for temperature dependence at constant pressures covering the entire range of conditions from the low to the high-pressure limits. Then, a proper (i.e. logarithmic) interpolation is adopted for the intermediate pressures. In this way, the combined effect of pressure (P) and temperature (T) on the rate constant k is properly accounted for. As a result, the three Arrhenius parameters for each pressure value cannot be optimized independently from each other, even within their own uncertainty ranges, in order to keep the physical consistency in the whole pressure domain. On the contrary, the same optimization performed using all the nominal pre-exponential factors, temperature exponents and activation energies, i.e. treating reactions at different pressures as independent from each other, would result in a non-monotonic behaviour with arguable physical meaning. Additionally, since the number of reactions within the same PLOG is the result of a fitting needed to describe complex

k(T, P) with a small acceptable error, the number of parameters to be handled scales accordingly. This may result in an abrupt increase in the number of parameters for a single reaction. For the first time in literature, we propose an approach to optimize the parameters at all pressures simultaneously, based on what proposed for the parameters bounds in the previous section, using only three, uniformly distributed random variables with an average value of 0, and constrained in the following ranges:

$$X_1 \in [-ln\left(10^{f_r}\right), ln\left(10^{f_r}\right)] \tag{3.7}$$

$$X_3 \in \left[-\frac{f_r}{log_{10}(T_{max})}, +\frac{f_r}{log_{10}(T_{max})}\right] \tag{3.8}$$

$$X_3 \in [-f_r T_{min} ln(10), +f_r T_{min} ln(10)] \tag{3.9}$$

These variables are associated with α, n and ϵ, at all pressures, respectively. The value of X_1 is sampled from its distribution and added to all the α, at different pressures, i.e. each reaction rate is changed by the same factor, and the same is applied for n_0 and ϵ_0, using X_2 and X_3. As an example, Figure 3.3 displays the comparison between nominal and optimized rate for the decomposition reaction HNO=H+NO, to which an uncertainty factor f_r. of 0.3 was attributed. The reported pressure values for this reaction are 0.1,1,10,100 and 1000 bar. Figure 3.3 highlights the preserved consistency in the pressure dependent behaviour of the reaction rates.

3.6 Selection of active variables for optimization

As outlined in section 2.5 sensitivity analysis was carried out for each test case contained in the database, and a corresponding Cumulative Sensitive Function (CSF) was obtained applying a 90% threshold on the total local sensitivity. The joint set of sensitive reaction is reported in table 3.1, which summarizes the sensitivity study and reports the uncertainty factor f each referenced reaction.

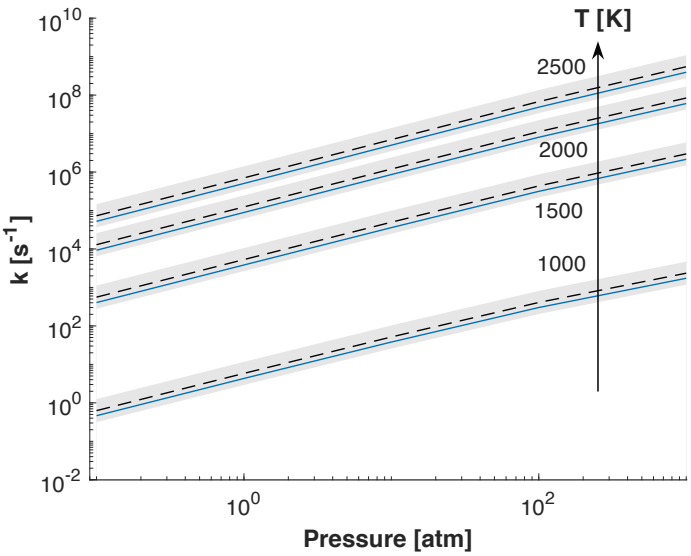

Figure 3.3: *3D behavior of PLOG reaction R143: HNO=H+NO, before (dashed line) and after optimization (continuous line)*

3.7 Analysis of the optimized mechanism

The model from Stagni et al. [170], hereafter reported as 'nominal', consists of 31 species and 210 reactions. The proposed methodology for mechanisms optimization aims at improving the nominal one considering all target datasets and uncertain parameters, simultaneously. This represents a significant difference from previously suggested approaches, where a hierarchical and systematic procedure was adopted instead [126]. As already explained in section 2.3, the 60 datasets within the database were split into two parts, i.e. optimization and validation targets (45 and 15, respectively). This was done in order to test a-posteriori the change in the predictability on the datasets which were not used in the optimization. The evaluation of the impact of different objective functions on the optimized model performance is the main purpose of this section. Using the same database, three detailed kinetic mechanisms were obtained using CM (eq. 2.31), L1-norm (eq. 2.25), and L2-norm (eq. 2.23). These are hereafter referred to as CM-mech, L1-mech, and L2-mech, respectively. Specifically, CM-mech is available in the Supplemental Material of Bertolino et al. [18]. The thermodynamic and transport properties (which were

Table 3.1: *Complete set of sensitive reactions for NH_3 combustion in the mechanism from Stagni [170]. Here, FIRST P.C. is short for first principle calculations.*

Index	Reaction	f	Reference	Type
24	$NH_3 = H + NH_2$	0.30	[170]	FIRST P.C.
25	$H + NH_2 = H_2 + NH$	0.18	[41]	EXPERIMENTS
26	$H + NH_3 = H_2 + NH_2$	0.30	[170]	FIRST P.C.
27	$OH + NH_3 = H_2O + NH_2$	0.30	[170]	FIRST P.C.
28	$O + NH_3 = OH + NH_2$	0.30	[170]	FIRST P.C.
29	$HO_2 + NH_3 = H_2O_2 + NH_2$	0.30	[170]	FIRST P.C.
30	$O_2 + NH_3 = HO_2 + NH_2$	0.30	[170]	FIRST P.C.
31	$O + NH_2 = H + HNO$	1.00	[172]	FIRST P.C.
32	$O + NH_2 = H + HNO$	1.00	[172]	FIRST P.C.
33	$O + NH_2 = OH + NH$	0.50	[43]	FIRST P.C.
35	$OH + NH_2 = H_2O + NH$	0.70	[117]	FIRST P.C.
37	$O_2 + NH_2 = O + H_2NO$	0.30	[89]	FIRST P.C.
38	$HO_2 + NH_2 = OH + H_2NO$	0.50	[43]	FIRST P.C.
39	$NH + NH_2 = H + N_2H_2$	0.18	[41]	EXPERIMENTS
43	$NH + NH = 2\,H + N_2$	0.30	[90]	FIRST P.C.
44	$2\,NH_2 = NH_3 + NH$	0.30	[90]	FIRST P.C.
45	$2\,NH_2 = N_2H_4$	0.50	[43]	FIRST P.C.
46	$2\,NH_2 = H + N_2H_3$	0.50	[43]	FIRST P.C.
69	$HO_2 + HNOH = O_2 + NH_2OH$	0.50	[43]	FIRST P.C.
74	$NO_2 + NH_2 = NO + H_2NO$	0.48	[67]	EXPERIMENTS
75	$NO_2 + NH_2 = H_2O + N_2O$	0.48	[67]	EXPERIMENTS
76	$NO + NH_2 = N_2 + H_2O$	0.08	[167]	EXPERIMENTS
77	$NO + NH_2 = OH + NNH$	0.08	[167]	EXPERIMENTS
78	$H + NH = H_2 + N$	0.30	[14]	DATABASE
79	$O + NH = H + NO$	0.70	[33]	DATABASE
80	$NH + OH = HNO + H$	0.70	[33]	DATABASE
82	$O_2 + NH = O + HNO$	0.70	[176]	FIRST P.C.
85	$NO + NH = H + N_2O$	0.65	[72]	FIRST P.C.
90	$O_2 + N = O + NO$	0.30	[15]	DATABASE
91	$NO + N = N_2 + O$	0.20	[15]	DATABASE
111	$N_2H_2 = H + NNH$	0.50	[43]	FIRST P.C.
112	$N_2H_2 = H + NNH$	0.50	[43]	FIRST P.C.
113	$H + N_2H_2 = H_2 + NNH$	0.35	[211]	FIRST P.C.
119	$N_2H_2 + NH_2 = NH_3 + NNH$	0.85	[102]	FIRST P.C.
140	$HO_2 + NO = OH + NO_2$	0.04	[78]	EXPERIMENTS
143	$HNO = H + NO$	0.30	[170]	FIRST P.C.
144	$H + HNO = H_2 + NO$	0.90	[123]	FIRST P.C.
148	$O_2 + HNO = HO_2 + NO$	0.50	[43]	FIRST P.C.
149	$HNO + NH_2 = NO + NH_3$	0.70	[109]	FIRST P.C.
161	$HONO + NH_2 = NO_2 + NH_3$	0.16	[179, 208]	EXPERIMENTS
170	$NO_2 + H_2NO = HNO + HONO$	0.70	[183]	ANALOGY AB-I
171	$NH_2 + H_2NO = HNO + NH_3$	0.50	[43]	FIRST P.C.
172	$O_2 + H_2NO = HO_2 + HNO$	0.60	[168]	FIRST P.C.

not involved in the optimization) were taken from [170]. The reactions to be optimized were selected using a cumulative sensitivity threshold (see section 2.5.2) equal to 90%, applied for each test case, leading to a sensitive subset

of 41 reactions. Once uncertainties were established (see section 2.3), a selected subset of 24 most impactful reactions was obtained using a threshold of 90% on the CIF (see section 2.5.2). More details about which reactions were included in this sub-set are given in SM. It is also important to mention that 4 out of 24 reactions (namely (R24, R111 and R112, and R143) are expressed with PLOG formalism. Indeed, R111 and R112 are duplicate of the same reaction, as evaluated by Dean and Bozzelli [43]. Overall, optimization was carried out considering 68 active variables. Nonetheless, only 56 out of 68 are directly linked to one single Arrhenius parameter, in pressure-independent reactions. Due to the nature of the four pressure-dependent reactions (i.e. PLOG), the remaining 12 uncertain parameters correspond to 45 Arrhenius parameters in the kinetic mechanism (see section 3.5). Subsequently, 101 kinetic parameters were optimized simultaneously.

Figure 3.4 shows a comparison between the optimized duplicate PLOG using the CM as objective function, and the nominal reaction. The former falls within the 2σ uncertainty band and it is increased by the same factor, for all pressures. In the case of a duplicate reactions the f (see 2.17) is to be applied to the sum of multiple kinetic rate constants and these constraints should be evaluated everytime the reactions' parameters are sampled/evaluated.

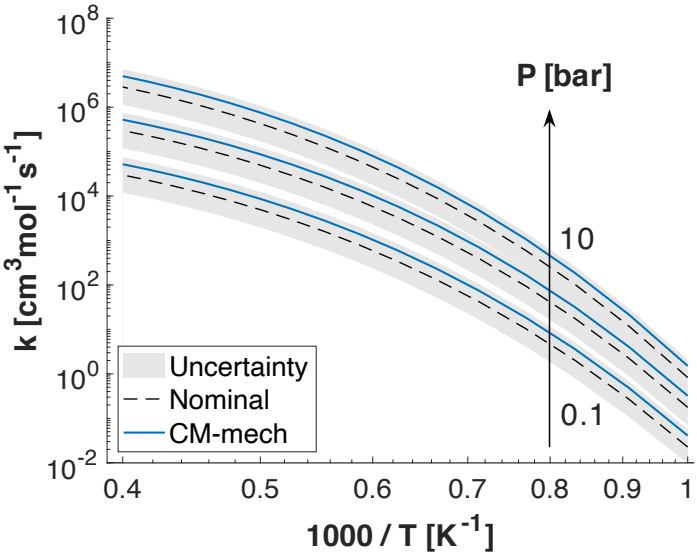

Figure 3.4: *Sum of reaction rates R111 and R112.*

On average, the optimized rate deviates from the nominal value by +76.4% at the low-pressure limit and by +78.2% at the high-pressure limit, due to the sum of R111 and R112 at different pressures. The pre-exponential factors of the three pressure logarithmic reaction rates were optimized by multiplying them by a factor of 1.567 and 1.221, for R111 and R112, respectively. Regarding other parameters, for R111 the temperature exponent is kept constant, while it increases for the R112 by a factor of 0.065. Inversely, a more significant change of -315.7 [cal/mol] in the energies of activation for R111, and no variation for the same parameter in R112, was observed. The agreement with the laminar flow reactor experiments from Stagni [170] is affected by reactions R24, R111, R112, R143 among the others. Remarkable results are obtained, with all objective functions, for predictions of O_2 consumption, NH_3 conversion, H_2O and NO formation, as highlighted in Figure 3.5. The major change occurs at 1523 K for NO, where also ammonia, oxygen, and water are significantly affected in shape. At this temperature, NH_3 consumption is delayed and NO volume fraction decreases by one order of magnitude (from 1.3 to 0.2 v/v %), resulting in a largely improved agreement with the experimental data for both CM-mech and L2-mech, while the L1-mech slightly underestimates the concentration of NO at this point. For temperatures between 1600 and 1800 K, a significant deviation from experimental data is anyway present considering all the models. For the temperature ranges [1523,1600] and [1800,2000] K, the L2-mech shows the best agreement with the experiments. For NO formation, the CM index (see eq. 2.31) increases from 0.849 to 0.9 for all the optimized mechanism. The L2-norm for this dataset decreases from 1560 to 172, 160 and 158 for CM-mech, L1-mech and L2-mech, respectively.

In order to discuss this case further, sensitivity and rate of production analysis of both nominal and CM-mech were performed at 1523 K to explain how modifying kinetic rate constants led to the improvement discussed above. Figure 3.6a shows the main sensitive reactions for the formation of NO. R26 is characterized by a negative sensitive coefficient, which relatively increases after optimization. This happens because the rate constant for this reaction increases of a factor of 2, as shown in Figure 3.6b, and strongly impacts ammonia conversion, as well as NO formation. Existing direct measurements for R26 reported a lower rate with respect to the nominal mechanism. Therefore, model optimization and measurements seem to recommend conflicting rate modification

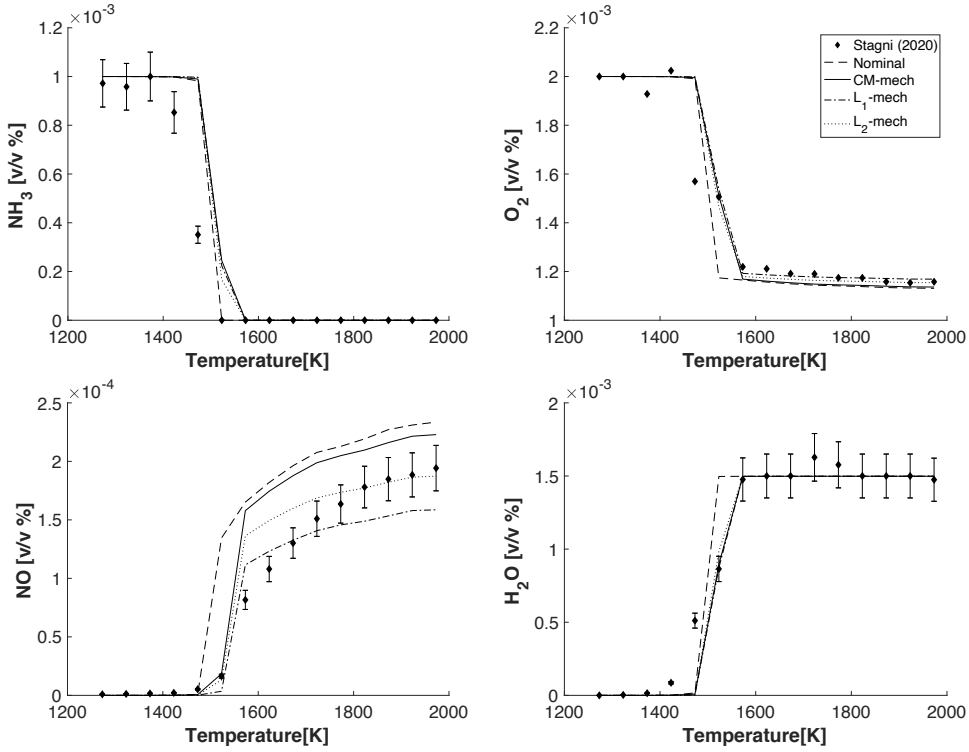

Figure 3.5: *Comparison between speciation predictions with nominal and optimized mechanism for lean NH_3/O_2 mixture in a flow reactor, at 1.25 bar. Experimental data from [170]*

for this reaction. However, recent advanced theoretical calculations reported an increased rate for R26 with respect to the nominal one, in agreement with results from the optimizer. In this context, a better characterization for this reaction is recommended for future mechanism development. For instance, new experiments may be carried out to confirm previous findings.

Globally, the rate of NH_3 consumption in the optimized mechanism decreases because of the competition between R26 and R27. The latter is the dominant kinetic step to form NH_2, which is then formed in a lower amount. This explains modified trend for ammonia in Figure 3.5. In spite of the 27% increase in the combined kinetic rate constant of R31 and R32 (see Figure 3.6c), HNO rate of production decreases due to the limited availability of NH_2. It is clear that in L2/L1-mech the reduced production of HNO is enhanced by a decrease in R31 and R32. As reported by Stagni et al. [170], HNO plays a key role in NOx formation. This species dissociates through R143, and undergoes H-abstraction

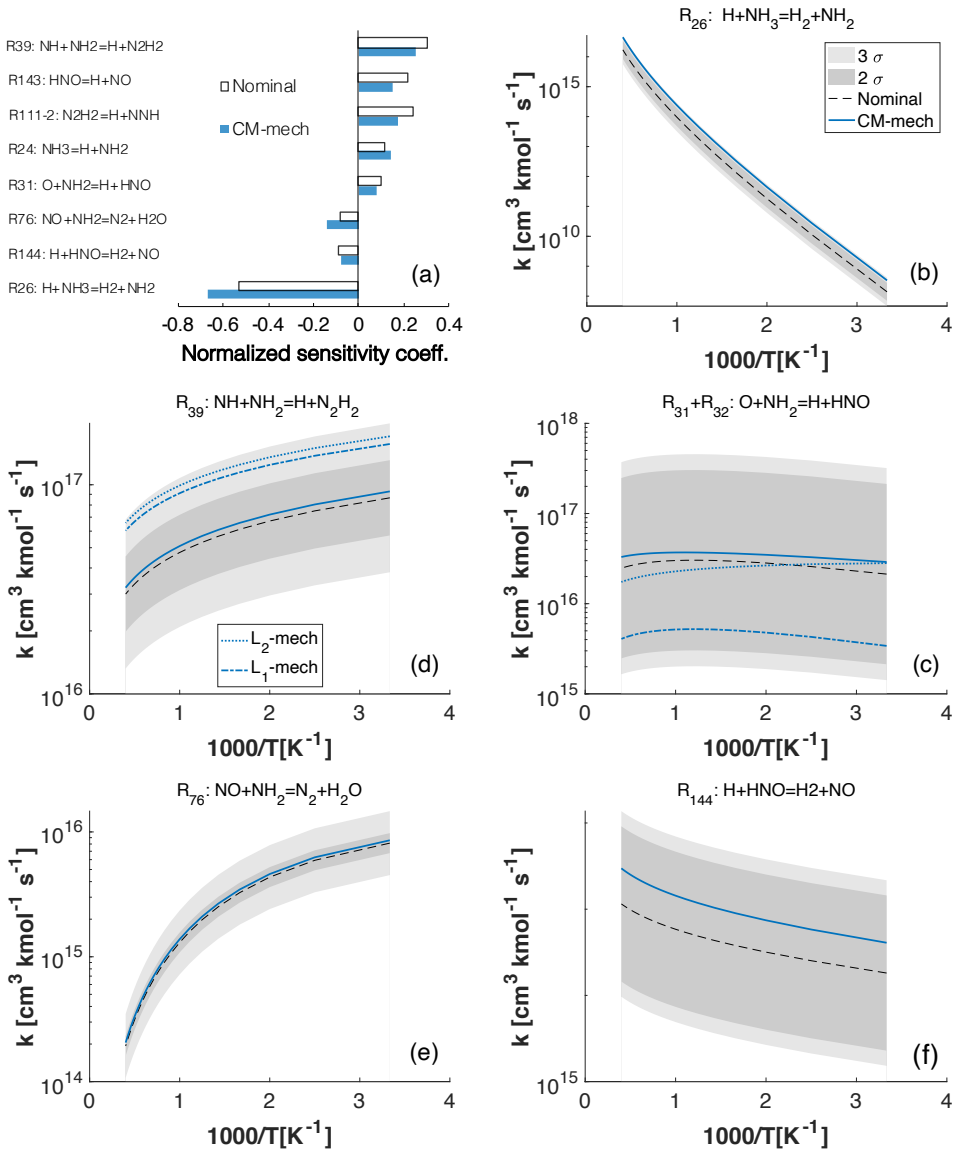

Figure 3.6: *Sensitivity analysis (a) and kinetic rate constants (b-f) of key reactions for NO formation in test case from Stagni [170], comparison between nominal and optimized mechanism.*

in R144, forming nitrogen-oxide (NO). As shown in 3.6a, R143 and R144 exhibit positive and negative sensitivity coefficients, respectively. Therefore, the reduction of R143 by a factor of 2 (see Figure 3.3) along with the increase of R144 by a factor of 2.5 (shown in 3.6f) cause the pronounced NO reduction at

1523 K. Figure 3.6e shows a 6% increase in k(T) for R76, which carries an enhanced negative sensitivity coefficient in the optimized mechanism. Therefore, NO reduction is also due to its conversion to final products through such reaction. Also, an average 7% increase in R39 (see Figure 3.6d), along with the abovementioned deviation of R111/R112 from the nominal values, displayed in Figure 3.4, strengthen the following path NH $\rightarrow$ N_2H_2 $\rightarrow$ NNH $\rightarrow$ N_2, which bypasses NO formation during ammonia oxidation, contributing to its reduction. Figure 3.6d also shows the rate constants obtained in L2/L1-mech, which are significantly higher than those of CM-mech. This reaction, together with R31 and R32, is responsible for the difference between the three optimized mechanisms in terms of NO formation. All of the reactions discussed above were also found to be impactful for laminar flame speed cases. The dataset from Ronney [45] was considered as a target in the optimization process, as measurements have been obtained in microgravity, where buoyancy effects do not affect the measurements. Indeed, this physical phenomenon was found to cause instabilities in the flame front for low-reactivity mixtures, i.e. high pressure [30], and was correlated to discrepancies between experimental data and predictions using 1D laminar flames [19], for rich conditions. Since ammonia exhibits a very low laminar burning speed, and the data from Lhuillier et al. [99] were not produced in microgravity conditions, they were used only for the validation. Figure 3.7a displays the comparison between the nominal, and the optimized mechanisms on data from Ronney [45]. The performance of CM-mech mostly falls within the experimental uncertainty and is comparable to the nominal one. On the contrary, using the point-wise definitions of the objective function, see equations 2.23 and 2.25, resulted in a loss in predictability. For the conditions in Figure 3.7a, the 4 most sensitive reactions (and their sensitivity coefficients) are $H+O_2 = O+OH$ (0.804), R39 (0.196), NO+NH2=OH+NNH (0.151), and R31-R32 (-0.095). As shown in Figure 3.6c and Figure 3.6d, R31-R32 decrease and R39 increases in both L2/L1-mechanisms. Since these reactions show a negative and a positive sensitivity coefficient, respectively, they determine an increase in reactivity for L2/L1-mech. In particular, R39 is pushed outside the 2σ of its distribution and approaches the upper bound at 3σ for both L_2/L_1-mech, resulting in a rate with lower probability than that of CM-mech. This reaction was found to be strongly impactful in the shock tube data from Davidson [41]. In Figure 9b, the L_2/L_1 mechanisms clearly outperform

the nominal model, as well as the CM-mech, for the formation of NH_2 during the pyrolysis of ammonia at 2300 K and atmospheric pressure. Conversely, in the same system and operating conditions, all of the models show satisfactory agreement for the experiment on NH formation (see Figure 3.7c). Thus, to improve the predictions in Figure 3.7b and the NO formation in Figure 3.5 using the objective functions in equations 2.23 and 2.25, the optimizer might force the kinetic parameters of R26 to less probable values (see Figure 3.6c/d). The same does not happen with CM-mech, where only 1 out of 24 reactions exceeds the 2σ. The details about kinetic rate constants of the considered reactions in optimization can be found in the appendix A.

As already discussed in [67], reactions R74 and R75 are crucial for modelling extremely lean mixtures, leading to formation of N_2O, and H_2NO. Accordingly, R172 was defined as strongly impactful for high O_2 excess and high pressures. In this work, the same three reactions were found to be strongly impactful for ignition delay time predictions at high pressure in both shock tube [159] and rapid compression machine [75] experiments. Figure 3.8 shows examples from the 6 ignition delay time datasets from Shu et al. [159], at high pressure. For this test case, CM-mech has the highest similarity with experiments, in fact the average CM value is 0.954, while the nominal one is 0.945. The highest similarity index, 0.983, is obtained at 40 bar for stoichiometric conditions. Even though L_2/L_1-mech yield very good agreement with this test case, their curve matching indices decreases to 0.927 and 0.931, respectively. At 20 bar and in rich conditions, all the mechanisms show satisfactory agreement with the experimental data. However, for low temperatures, none of them is consistent with the experimental uncertainty. This result suggests that, only for these three points, measurement uncertainty might be higher than 20%.

The reactions R74, R75 and R172 were also selected for the JSR data by Stagni [170], the RCM data by Pochet [134] and the PFR data from Wargadalam [204], and Song [168]. These test cases contain measurements obtained in similar operating conditions as those described by Glarborg et al. [67], as reported in Figure 3.1. In a similar temperature regime, experimental ignition delay times at high pressure (20 and 40 bar) recently reported in the literature by He et al. [75] give the most satisfying results in this work. Even for this test case, R74, R75 and R172 were found to be the governing reactions. In general, overall improvement can be appreciated in Figure 3.9.

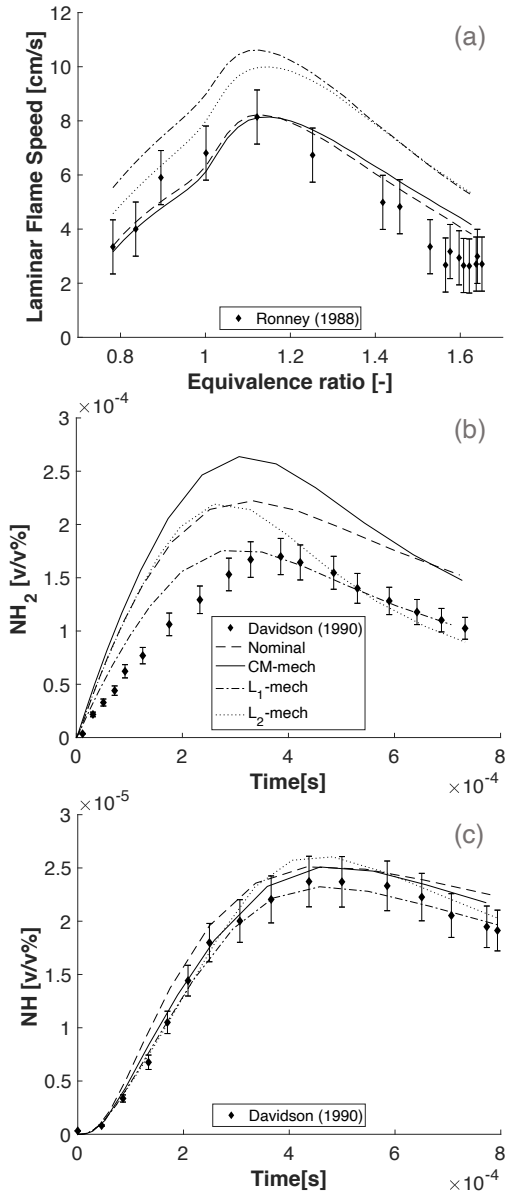

Figure 3.7: *Comparison of nominal and optimized mechanisms on different targets. (a) Laminar flame speed of NH_3/air mixtures in microgravity conditions at 300 K; (b) Molar fraction of NH_2 in a shock tube at 1.028 atm and 2301 K. (c) Molar fraction of NH in a shock tube at 0.986 atm and 2294 K. Experimental data from [41, 45]*

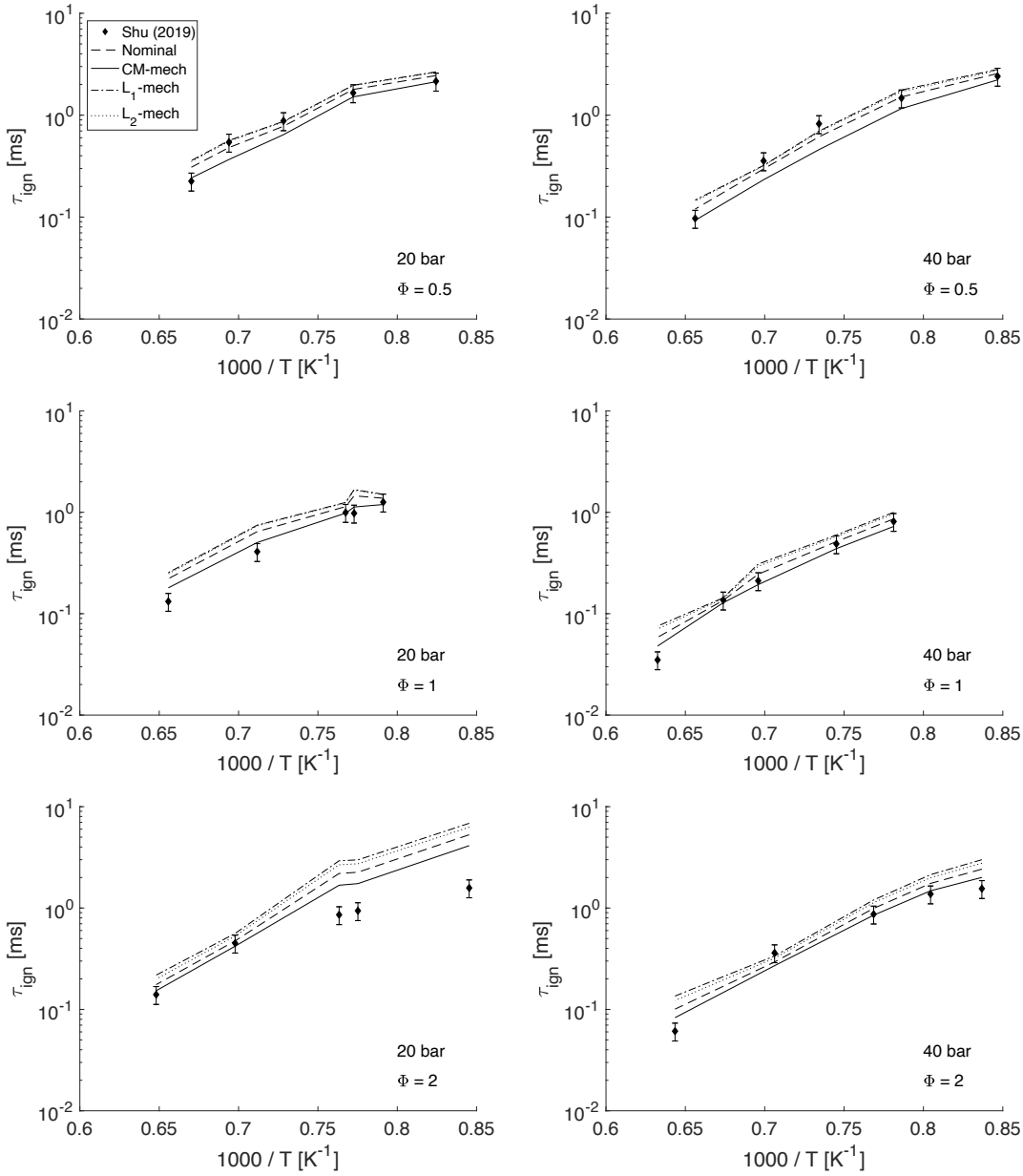

Figure 3.8: *High pressure ignition delay time of NH_3/air mixtures in a shock tube for different equivalence ratios, namely 0.5,1.0, and 2.0. Experimental data from [159].*

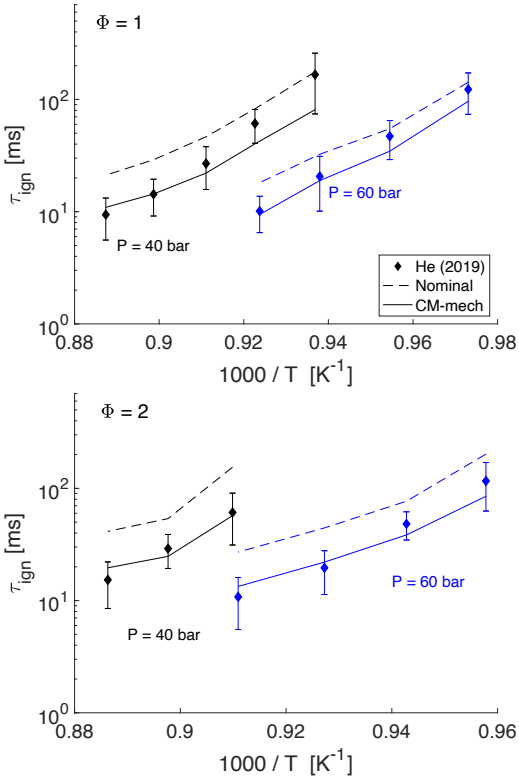

Figure 3.9: *Comparison between nominal and optimized mechanism for NH3 self-ignition at pressures between 40 and 60 bar in a Rapid compression machine. Experimental data from [75].*

Table 3.2 shows the overall objective function values for the optimized models and their deviations from those of the nominal mechanism. As expected, both L_1-mech and L_2-mech outperform the nominal mechanism in terms of L_1 and L_2-norms, but the first is characterized by lower a CM index (i.e. higher 1-CM), and the second shows little improvements. This indicates that using the objectives functions 2.23 / 2.25 on large databases, may lead to a lower CM index (i.e. lower agreement with experimental data) with respect to the nominal mechanism. On the other hand, the CM-mech performs better than the nominal mechanism for all the measurements, not only in terms of CM index, which is expected, but also in terms of L_2/L_1-norm (even though its gain is much lower than that of the other two optimized mechanisms).

Table 3.2: *Comparison between different error measures values of nominal and optimized mechanisms for the optimization subset.*

Mech. label	1-CM (% deviation)	L_1-norm (% deviation)	L_2-norm (% deviation)
Nominal	0.1919	3.77	176.35
CM-mech	0.1726 (-11.17%)	3.72 (-1.46%)	136.31 (-22.70%)
L_1-mech	0.1962 (+1.76%)	2.71 (-31.51%)	58.940 (-66.58%)
L_2-mech	0.1903 (-1.49%)	2.54 (-35.37%)	55.600 (-68.46%)

Overall, the deviations of the objective function values between optimized and nominal mechanisms are smaller using CM with respect to the L1/L2-norm. Indeed, in equation 2.31, performance gains and losses for each curve contribute equally to the average value, which is always between 0 and 1. Additionally, it is very difficult, if not impossible, for any mechanism to show no similarity, or dissimilarity with experimental data, if a large set is considered. For this reason, the possible range of values for CM is even more limited than [0,1]. In general, a well-constructed and validated kinetic model as the one used in this work is not expected to show outstanding global improvements in terms of curve matching metrics. Yet, significant differences between the nominal model and the CM-mech were observed in this work when looking at single curves. To further support this, the CM index was computed for the optimization target datasets inside the database (i.e. 44 out of 60), for all mechanisms (i.e. Stagni, CM/L1/L2-mech). Table 3.3 reports the number of negatively/positively impacted datasets in each optimized mechanism. The average, and maximum deviations from the nominal CM values are also reported. This deviation is the difference in percentage between the CM index of the nominal mechanism and

of the optimized ones, and it was computed for each of the 44 optimization target datasets.

Table 3.3: *Performance comparisons between mechanisms on target datasets in optimization.*

	Negative Impact			Positive Impact		
Adopted objective function	CM-mech	L_1-mech	L_2-mech	CM-mech	L_1-mech	L_2-mech
N^o of datasets	12.00	26.00	23.00	32.00	18.00	21.00
Ave.CM deviation (%)	-1.42	-3.29	-3.21	+3.99	+3.29	+4.54
Max. CM deviation (%)	-3.00	-8.75	-8.89	+14.39	+11.29	+18.35

The CM-based optimization approach leads to a significantly larger number of improved datasets, with respect to point-wise based approaches. In fact, L_1-mech shows reduced performances on a number of curves almost twice as big as the number of improved ones, and L_2-mech behaves similarly. Additionally, both average and maximum negative deviations are significantly lower for the CM-mech compared to the others. For this reason, the latter approach can be considered as more conservative than the other two. Moreover, average and peak improvements in CM-mech are comparable to those of the L_2-mech, which is the one leading to the biggest local improvement. All of this is graphically summarized in Figure 3.10, where the same information for the single dataset is delivered through a parity plot, for both optimization and validation sub-sets of the complete database. From Figure 3.10, it can be also concluded that the CM-mech yields the most homogeneous and consistent improvement over the entire subset of optimization target datasets even in terms of L_1 and L_2 norms.

Indeed, the absolute numerical values of relevant measures for combustion kinetic model validation (i.e. laminar burning speed, main and intermediate species concentration, and ignition delay time) range different order of magnitudes, namely from 10^{-6} to 10^{2}. As a consequence, the point-wise formulations of the objective function (i.e. eq. 2.23 / 2.25) are characterized by very different absolute values for each dataset, even when normalization is performed or the natural logarithm is adopted for the ignition delay time. Therefore, in mono-objective optimization study targeting a wide set of experimental data, the optimizer focuses on those contributing more to the full extent of the objective-function. CM prevents this issue, since it associates each curve with a score between 0 and 1.

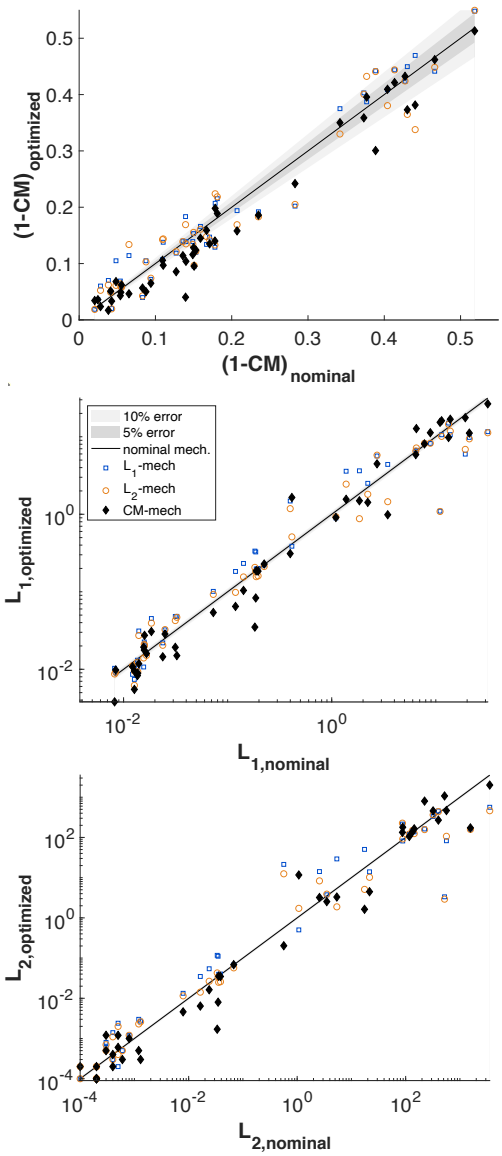

Figure 3.10: *Parity plot: curve matching indices comparison between nominal mechanism from Stagni et al. [170] and optimized mechanisms from this work.*

3.8 Concluding remarks

In this work, we proposed a novel data-driven approach for the optimisation of detailed kinetic mechanisms. The employed optimization algorithm is the Evo-

lutionary Algorithm (EA). For the first time the objective function was based on a recently published curve matching algorithm that is capable to quantitatively and qualitatively evaluate the agreement of kinetic models with experimental data, characterizing the agreement in terms of L_1 and L_2 norm as well as on the first derivatives and shapes of the curves. Also, a novel methodology to optimize the Arrhenius parameters of PLOG-based reactions was established. The interdependencies between Arrhenius expressions at different pressures were accounted for by handling three random variables for each PLOG, regardless of the number of discrete pressures specified in the mechanism. To the authors knowledge, PLOG reactions were consistently optimized for the first time within their entire temperature and pressure domain. An optimized mechanism for ammonia combustion was obtained, and it was found to outperform the nominal mechanism from Stagni et al. [170], as well as those obtained with point-wise formulations of the objective function (i.e. L_1 and L_2 norms), over a wide range of operating conditions involving more than 635 experimental data points. Addressed features of ammonia combustion were conversion, oxidation, pyrolysis, ignition and laminar flame speed in several systems. Improvements driven by optimization on all the impactful reactions were constrained to their uncertainty bounds when experiments on single elementary steps were available. For rates determined using first principles calculations, guidelines were established to estimate uncertainty ranges based on the level of theory adopted throughout the calculation protocols for electronic structures, potential energy surfaces and phenomenological reaction rate constants. In this process, 41 reactions were involved and 24 were finally selected as the most impactful by introducing a Cumulative Sensitivity Function (CSF) and a Cumulative Impact Function (CIF) for each test case in the database. As a result, the approach involved all 101 kinetic parameters, which were addressed contemporarily by the optimizer during optimum search. Finally, the comparison between nominal and optimized mechanisms was exploited to highlight crucial reaction pathways, needing further characterization, demonstrating the applicability of the methodology as a useful tool for a more accurate evaluation of crucial kinetic constants and for design of experiments. Finally, sensitivity and rate of production analysis of both nominal and CM-mech were performed to investigate how modifying kinetic rate constants led to the improvement discussed above. R26 sensitivity coefficient relatively increases after optimization.

This happens because the rate constant for this reaction increases of a factor of 2, as shown in Figure 3.6b, and strongly impacts ammonia conversion, as well as NO formation. Existing direct measurements for R26 reported a lower rate with respect to the nominal mechanism. Therefore, model optimization and measurements seem to recommend conflicting rate modification for this reaction. However, recent advanced theoretical calculations reported an increased rate for R26 with respect to the nominal one, in agreement with results from the optimizer. In this context, a better characterization for this reaction is recommended for future mechanism development. For instance, new experiments may be carried out to confirm previous findings.

CHAPTER 4

OptiSMOKE 2.0

THIS chapter showcases OptiSMOKE 2.0 capabilties through 9 practical examples. This toolbox embodies the methodology discussed in previous chapters. This chapter is partly based on the following pubblications:

- *OptiSMOKE++: A toolbox for optimization of chemical kinetic mechanisms. Fürst, M.,* ***Bertolino, A.****, Cuoci, A., Faravelli, T., Parente, A. Computer Physics Communications* `https://doi.org/10.1016/j.cpc.2021.107940`
- *Combined effect of experimental and kinetic uncertainties on NO predictions in low-pressurepremixed laminar $H_2/CH_4/CO$-air and $H_2/CH_4/CO/C_6H_6$-air flames, Iavarone, S.,* ***Bertolino, A.****, Cafiero, M., Parente, A., currently under preparation*

The OptiSMOKE 2.0 code is available at:

- https://github.com/burn-research/OptiSMOKE_toolbox.git

4.1 Workflow

An overall view of the OptiSMOKE++ workflow is depicted in Fig. 4.1. OpenSMOKE++ [35] is conceived for solving reacting systems with numerous species and reactions. OpenSMOKE++ utilizes advanced numerical techniques to reduce the computational cost of the simulation, without sacrificing accuracy or robustness. A more extensive description of the code and its utilities can be found in [35]. It consists of a series of solvers for 0D reactors (Batch Reactors, PFRs, PSRs, ST, RCM and laminar flames. DAKOTA (Design Analysis Kit for Optimization and Terascale Applications) is a framework developed at and distributed by Sandia National Laboratories [4]. It is a toolkit used for iterative parameter evaluations, which are key to perform optimization, sensitivity analysis, and uncertainty quantification.
The code runs through the following phases:

- Import the input files, i.e OptiSMOKE dictionary, kinetic mechanism maps, experimental data and opensmoke input files. It is important to notice that the data can be either present on a local storage or interactively downloaded from an online database, called SciExpeM, from Ramalli et al. [138].
- Initialize the set of OpenSMOKE++ simulations.
- Select the reaction through screening, based on Cumulative Sensitivity Function (CSF).
- Calculate Constraints for the selected reactions, based on user specified uncertainties.
- Run a user-defined optimization algorithm in DAKOTA [4], which strategically suggests new combination of chosen parameters. OptiSMOKE [64] then undates the kinetic maps accordingly, and check if the constraints. If even one of the constraint is not respected a penalty is applied to that evaluation and the simulations are not carried out. If all constraints are respected, OptiSMOKE [64] runs all OpenSMOKE [35] simulation, post-process the results and uses the to compute a user-defined objective function. Based on the objective function value and the optimization strategy,

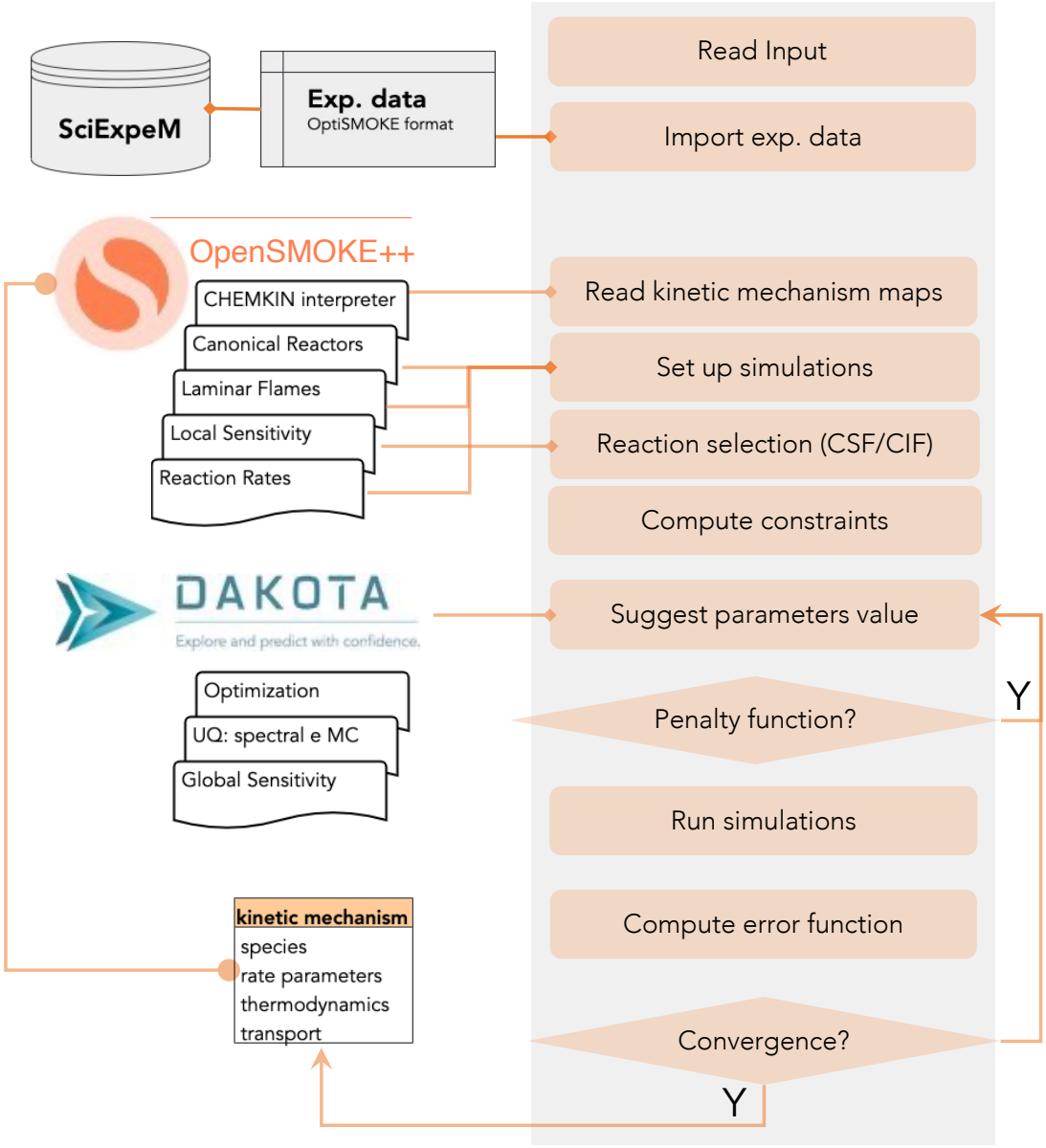

Figure 4.1: *Schematic workflow of OptiSMOKE++ and its Interactions with SciExpeM, OpenSMOKE++ [35] and DAKOTA [4]*

DAKOTA suggests a new set of parameter values and the process is repeated until at least one of the stopping criteria has been reached. These stopping criteria can depend on the optimization methodology used, but

typical universal ones are: maximum number of evaluations, maximum number of iterations, solution target, and convergence criteria.

- Write the optimal kinetic mechanism for off-line user activities.

4.2 OptiSMOKE features: application to different of Quantity of Interests (QoI)

The following section discusses 9 different examples, which demonstrate the functionality of OptiSMOKE++. Target data of direct and indirect nature can be used for mechanisms optimization, as proposed and intended by Turanyi et al. [185].

4.2.1 QoIs of direct (or least indirect) nature

This type of data represents experiments in fine and controlled conditions, where the set of sensitive mechanism reactions is reduced to a minimum size yet including the reaction of interest. The latter can be inferred from data using a model and assuming (i) correct mechanism and model representation, (ii) the uncertainty of the experiments and (iii) the uncertainty of all sensitive uncertain reactions in the reduced set are considered. These targets are directly compared with kinetic constant calculations in OpenSMOKE++, through OptiSMOKE++.

Test Case 1: Optimization of $O + OH = O_2 + H$

The following example involves one of the most famous reactions in combustion, $O + OH = O_2 + H$. For this reaction, 48 different sets of Arrhenius parameters from reviews, experiments and theory are available in NIST [103] database, from 1958 to 2011. Some of them are reported in figure 4.2.

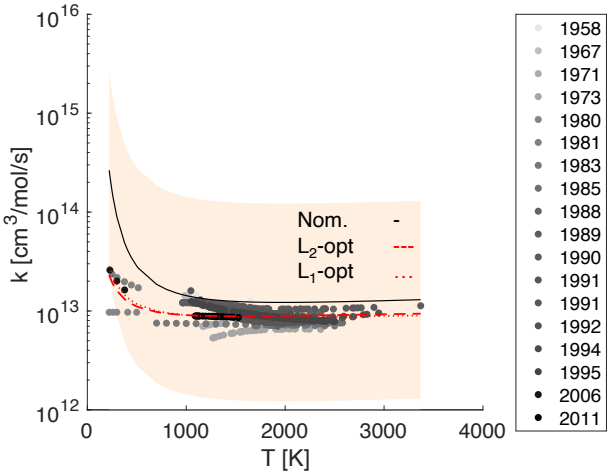

Figure 4.2: *Comparison between nominal (—) and optimized (- - -) rate constant for reactions $O + OH = O_2 + H$ in test case 1. Experiments from NIST [103]*

In this example, the starting point in optimization is referred to as *nominal* in table 4.1, and an uncertainty factor *f* of 1.0 (see equ. 2.17) was assumed to include almost all the available reference data. Because of the low computational cost of the model evaluations, EA (see section 2.3) was set with 20000 evaluations, comparable to a direct search. Using two different objective functions, i.e. L_2 and L_1 norms (see equ. 2.23 and 2.25), optimized parameters values can be obtained, and are reported in table 4.1. It is interesting to notice that optimization with both error functions find a local minimum for n = 0.239, while slightly different values for the other two parameters are obtained. Nonetheless, the optimized constants overlap in figure 4.2. It is important to clarify the weight of each experiments in the objective function is inversely proportional to the experimental uncertainty. For the sake of brevity and plot readibility, error bars are not reported here.

Table 4.1: *Objective function, and Arrhenius parameters values for nominal as well as optimized reaction rate for section 4.2.1*

Mechanism	L_2	L_1	A [cm-mol-s]	n [-]	E_a [cal/mol]
Nominal	7.973e-03	2.113e-01	1.2525e+11	0.533000	-2098.42
Opt. L_2	1.279e-03	—	1.2127e+12	0.238704	-725.85
Opt. L_1	—	1.162e-01	1.1425e+12	0.238704	-843.01

Test Case 2: Optimization of $H_2O_2(+M) = OH + OH(+M)$ in PLOG format

In this section, an exercise similar to that shown for TC1 is carried out for a pressure-dependent reaction expressed in PLOG format, following the methodology proposed in 3.5. The experimental data from Zellner [210] and Hong [77] are used as targets for different combinations of pressure and temperature. The $L_2 - norm$ (see equ. 2.23) was adopted as objective function in this example. $L_2 - norm$ values for each curve are given in figure 4.3 together with graphical results.

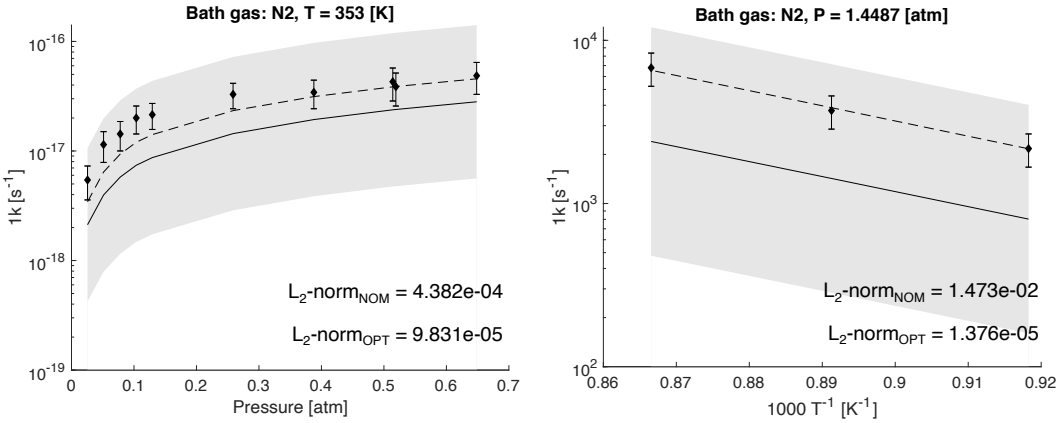

Figure 4.3: *Comparison between nominal (—) and optimized (- - -) rate constant for reactions $H_2O_2(+M) = 2OH(+M)$ in test case 2. Experimental data from Zellner [210] and Hong [77]*

In spite of the satisfying agreement between model responses and experimental data, a strong correlation between model responses exists. This becomes clear when looking at the 68% and 99% confidence regions of the optimization parameters for the PLOG reaction in figure 4.4. Here, $X_{1,2,3}$ represent the 3 random variables defined for PLOG optimization (see 3.5). The ellipticl regions dysplayed were obtained following the procedure described in section 2.7. As

well-documented in [150], rotated ellipse axes are a sign of parameters correlation (see section 2.4.2). Of course such correlations would make the job of any optimizer harder, as discussed in section 2.4.2. For this reason, heuristic algorithms with high number of evaluations are a good choice. Here, an Evolutionary Algorithm was run for 30'000 evaluations since the cost of a realization is close to $10^{-4}s$ as the entire process roughly takes 10 s.

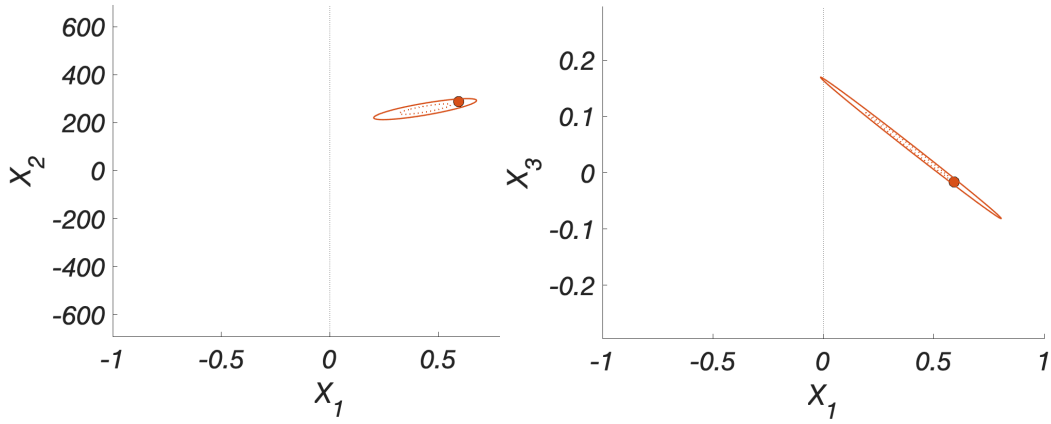

Figure 4.4: *The 68% (. . .) and 99% (—) confidence regions, and best estimate (marker) for PLOG optimization parameters in test case 2.*

4.3 QoIs of strong indirect nature

4.3.1 Test Case 3: Speciation and Temperature increase in a Non-Isothermal Perfectly Stirred Reactor (PSR)

In this example, the optimization targets consist of species concentrations and temperature increase during hydrogen oxidation at different initial temperatures in an Non-Isothermal Jet-stirred reactor (JSR) [145]. An experimental JSR can be modeled as a Perfectly Stirred Reactor (PSR), the injection occurs through jet nozzles with a high velocity, which ensures instantaneous mixing inside the reactor. The species concentrations were measured with fixed residence time (τ = 0.5 s), at 1.2 atm, ϕ= 0.5 and 94% dilution. The diluent is composed by 30% of H_2O and 70% of N_2 in volume. The target species for this study were limited to H_2 and O_2, but a larger number of species can be handled by OptiSMOKE++. The nominal kinetics used for this case was Aramco 2.0

[94], and the sensitivity study, for determining which reactions to consider in the optimization, was performed based on section 2.5.2. This resulted in 10 reactions and 30 kinetic parameters, which are not reported here for the sake of brevity, but are a subset of those reported in the next chapter (see chapter 5). A comparison between nominal and optimized mechanisms is reported in figure 4.5. It can clearly be seen that an overall improvement is achieved for each species profile, these improvements increase the average curve matching index (see 2.31) from 0.8835 to 0.9470.

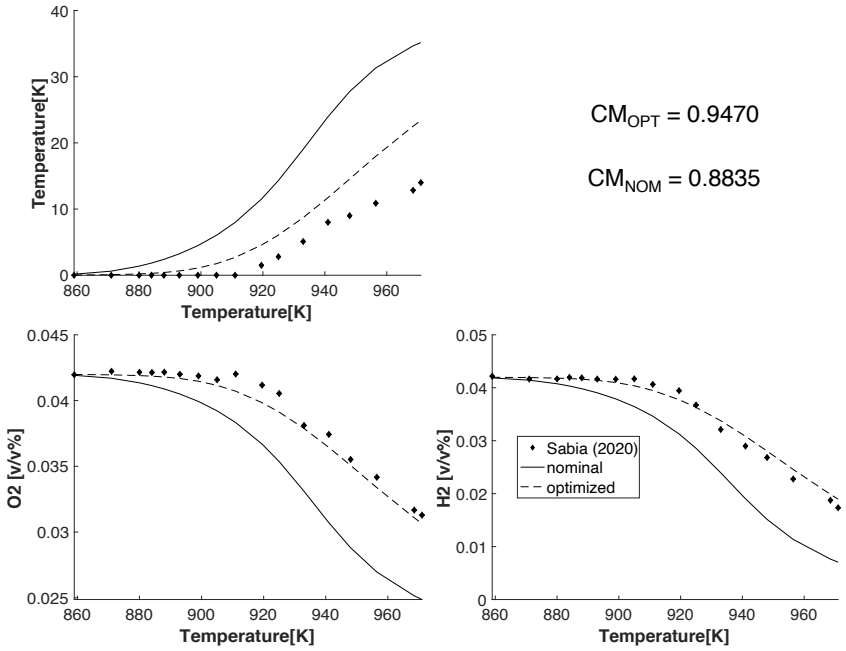

Figure 4.5: *Comparison between nominal (—) and optimized (- - -) model responses for test case 3. Experimental data from [145]*

4.3.2 Test Case 4: Temporal profiles of hydrogen, oxygen and water in a Plug Flow Reactor

In case of laminar flow reactors, it is possible to shift the species profiles using the 50% fuel depletion as recommended by Dryer [46]. This can be done before the calculation of any objective function in OptiSMOKE++, and needs to be done every time DAKOTA suggests a new combination of parameters. The data from Mueller [118], about H_2/O_2 oxidation at intermediate temperatures,

are a very good example for this QoI. The mechanism from ELTE [192] was used in optimization for seven reactions and a total of 21 kinetic parameters. Uncertainties for these kinetic steps were mainly taken from the collection of Baulch [14]. Figure 4.6a reports the fuel oxidation profile before time-shift for both nominal and optimized kinetic model. It is important to notice that while maximizing curve similarity, the time shift is also minimized. Figures 4.6b, c and d show the time-shift, computed on the fuel, applied to H_2, H_2O, and O_2. The agreement between optimized model and experiments is remarkable. In fact, the average Curve Matching for curves similarity increases from 0.85 to 0.93.

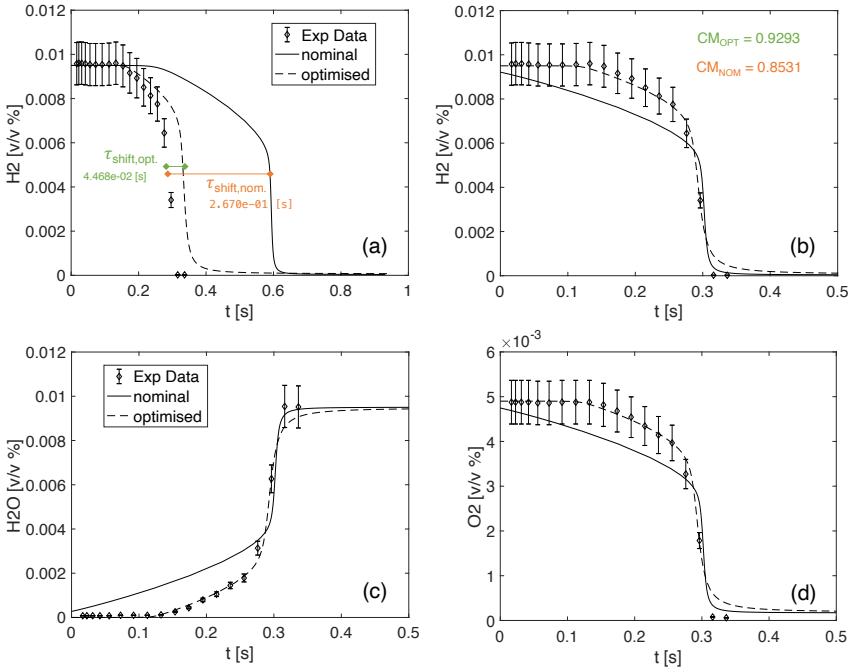

Figure 4.6: *Comparison between nominal (—) and optimized (- - -) model responses for test case 4. Calculated (a) and shifted (b) H_2 profiles from simulation. Shifted profiles for H_2O (c) and O_2 (d). Experimental data from Mueller [118]*

4.3.3 Test Case 5: Species concentration at the outlet of a Flow Reactor fed with nitromethane

This example aims at showing one possible application of OptiSMOKE++ to assess mechanism completeness. Isopropyl nitrate ($(CH_3)_2CHONO_2$, iPN) is an

organic molecule, used as a additive to prompt fuel reactivity in gas turbine engines, or in blends with diesel. iPN is a promising “green”, non-toxic, and non-corrosive monopropellant, which be used for a wide range of applications (e.g. space and aerial vehicles, underwater power sources). Additionally, iPN can be produced at low cost and has low susceptibility towards premature detonation. An example of pyrolysis data of isopropyl nitrate (iPN) in a tubular reactor at atmospheric pressure and temperatures ranging from 373 to 773K and residence times of 2 s. Preliminary results were published by Bourgalais [20], who described a mechanism for iPN decomposition, currently under development. The experimental setup has recently been described in detail elsewhere [158]. The major products of iPN decomposition are formaldehyde (CH_2O), nitromethane (CH_3NO_2), methanol (CH_3OH), formamide (CH_3NO), NO and others. The experimental data for some of these species are reported in figure 4.7. In Bourgalais [20], a modified POLIMI mechanism was able to predict the decomposition of iPN as well as some major product reasonably well. However, pronounced deviations for the major species indicate that further improvements are needed. Worst performances are observed especially for formaldehyde (CH_2O), nitromethane (CH_3NO_2), and methanol (CH_3OH) in figure 4.7 b,c, and d. The optimized reactions are neither reported nor discussed here because the mechanism has not been published yet, but it was rather obtained through personal communication with the authors [20], who contacted our lab to explore possibilities for mechanism improvement with OptiSMOKE++.
What is really interesting to notice here is that in spite of a general increase in performance, after the optimization was carried out (i.e. CM increases from 0.83 to 0.8754), the mechanism reproduction of formaldehyde (CH_2O) (see figure 4.7b) is far from satisfactory. After a thourough kinetic analysis and optimization involving 8 sensitive reactions, which were optimized with increasing uncertainty (i.e. f= 0.3, 0.5 and 0.7), the hypothesis that a critical kinetic step might be missing was formulated. Theoretical calculations to explore this possibility will be carried out by co-authors of Bourgalais [20].

4.3.4 Test Case 6: Ignition delay time in a shock tube

For shock tube simulations, constant volume batch reactors can be usually adopted. However, due to non-ideal facility behaviour, a constant pressure rise in time is observed at low temperatures before ignition, and should be

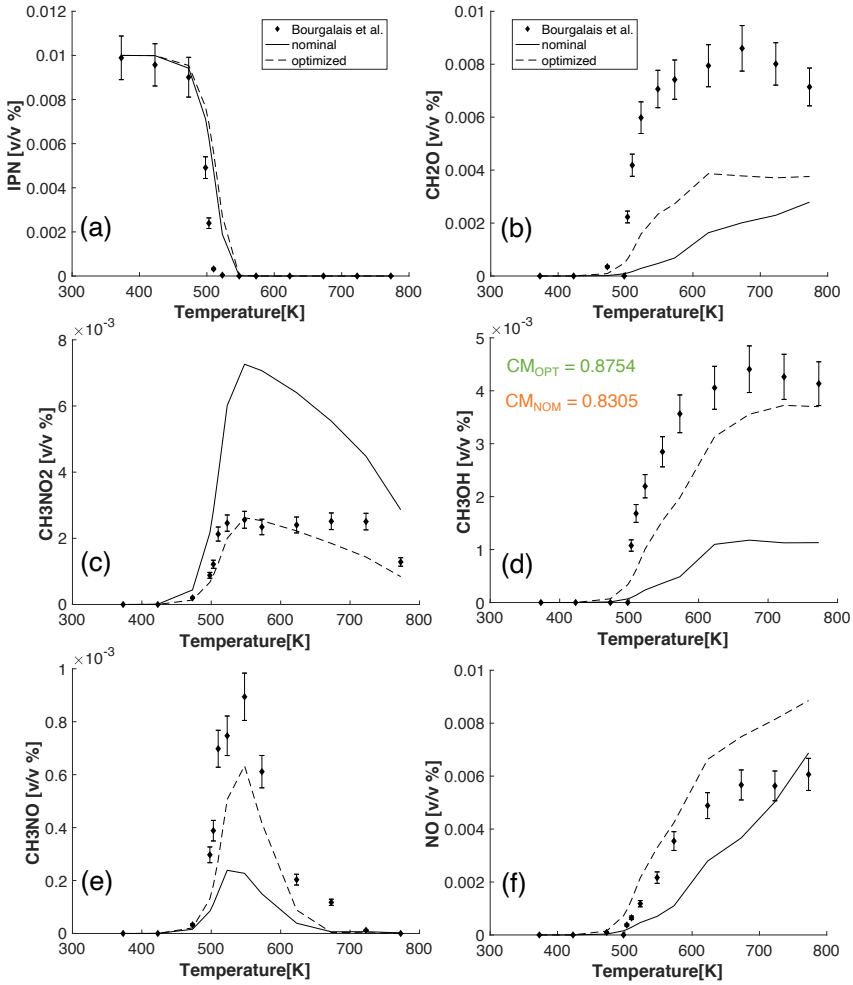

Figure 4.7: *Comparison between nominal (—) and optimized (- - -) model responses for in test case 5*

imposed in simulations as a percentage of the operating pressure [35]. This information can be included in simulations whether available from the reference papers. If not, it is suggested here to remove, from the target dataset, those data points where a pressure rise in time equal to the 3% of the initial pressure caused at least 10% variation in the calculated ignition delay time. This would ensure that parameters estimation is not biased by uncertainties due physical phenomena, which can not be reproduced with a simple batch reactor. Figure 4.8 reports the experimental data from Wang [202], which were "cleaned" from

possibly corrupted data. Here, the onset of ignition corresponds to the instant where the maximum rate of OH production is observed. The ignition delay times calculated using Aramco 2.0 [94] mechanisms as well as its optimized version, based on 7 elementary reactions and the third body efficiency of water in 2 reaction among the main set, are shown in figure 4.8. Finally, the increase in CM index is rather impressive for all curves but for that obtained with 25% water dilution and 9.5 [bar] pressure, which shows decreased performance.

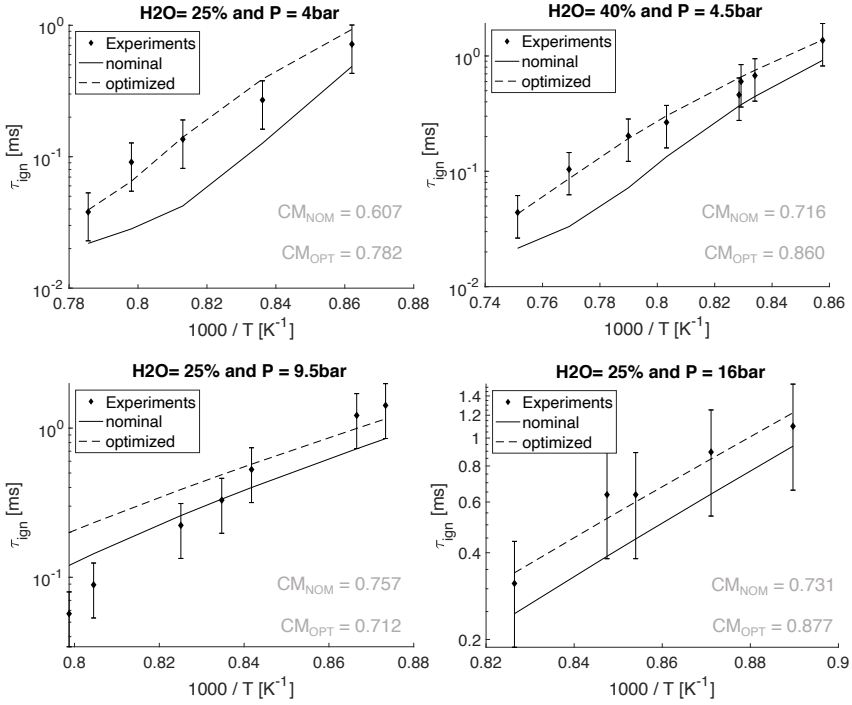

Figure 4.8: *Comparison between nominal (—) and optimized (- - -) model responses for in test case 6. Experimental data from Wang [202]*

4.3.5 Test Case 7: Ignition delay time in a rapid compression machine

As a key physico-chemical property of a specific mixture, the IDT is an important measure for determining if the kinetic mechanism is accurately predicting the onset of combustion correctly or not. The ignition strongly controls the successive combustion process, which is why it is commonly used as a target for kinetic mechanisms in both validation and optimization. For the Rapid Compression Machine (RCM) data for Ignition Delay time of strongly diluted stoichio-

metric hydrogen/oxygen mixtures from Das [40] the adiabatic core assumption needs to be adopted [173]. In particular, the experimental cold pressure traces were used to infer corresponding volume histories. The IDT was then computed as the time elapsed between the maximum pressure time-derivative and the minimum volume, corresponding to the end of compression. The ignition delay times calculated using Aramco 2.0 [94] mechanisms as well as its optimized version, based on 6 elementary reactions and the third body efficiency of water in 2 reaction among the main set, are shown in figure 4.9.

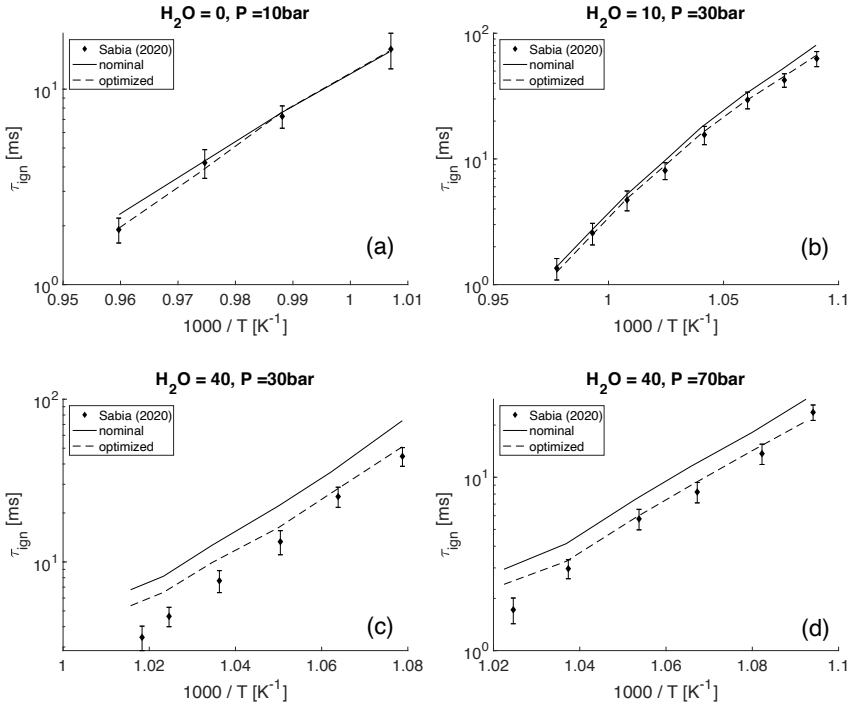

Figure 4.9: *Comparison between nominal (—) and optimized (- - -) model responses for in test case 7. Experimental data from [40].*

4.3.6 Test Case 8: laminar flame speed optimization for global mechanisms

As a key quantity for describing the combined effect of a mixtures' diffusivity, reactivity and exothermicity, the LFS is often used as a target for the development, validation and optimization of a kinetic mechanism at low temperatures. It describes at which speed the flame front is propagating back towards the un-

burned gases in a laminar flow. When the inlet velocity of the mixture is equal to the LFS, a stable flame front is established. The numerical evaluation of the LFS are usually carried out in 1D freely propagating flame simulations. The numerical solution of such a system depends on the inlet mixture composition, kinetic and thermodynamic parameters, as well as the transport properties. OptiSMOKE++ supports the application of LFS as targets for the optimization by using the premixed laminar flame solver of OpenSMOKE++. The experimental targets used for this test case consists of LFS data of methane/air, 1 bar and, temperature and equivalence ratio ranging from 300 to 500. The "experimental" measurements were produced by means of detailed mechanism for an equivalence ratio between 0.7 and 1.2 using a detailed C1-C3 mechanism from POLIMI (Creck modelling). The challenge in this example is to produce an optimized version of the Jones-Lindstedt [84] with the same laminar burning speed as the detailed mechanism. The results of the optimization can be seen in Fig. 4.10, and the optimized mechanism is able to capture the targets very well. Here, only the Arrhenius parameters were optimized, while the reaction orders with respect to reactant were kept equal to the original mechanism. Figure 4.10d shows the convergence of the EA optimization algorithm, which is basically achieved after 500 evaluations (i.e. 500*15 flame calculations) with number of penalties around 150. Only small improvements are observed afterward, while the number of penalties increases. This is a clear sign that the optimizer is still performing a global search in the parameters hyperspace, even though local minimum were found elsewhere. Tables 4.2 and 4.3 report the parameters values for the nominal and optimized global mechanisms, respectively.

Table 4.2: *Collection of kinetic parameters from the nominal Jones-Lindstedt [84] in this work. RO means reaction order.*

Reaction	A [cm-s-mol]	n	E_a [cal/mol]	RO CH_4	RO H_2	RO O_2
$CH_4 + 0.5O_2 => CO + 2H_2$	7.82E+13	0.00	30000.	0.5	—	1.25
$CH_4 + H_2O => CO + 3H_2$	3.00E+11	0.00	30000.	—	—	—
$H_2 + 0.5O_2 = H_2O$	1.209E+18	-1.0	40000.	—	0.25	1.5
$CO + H_2O = CO_2 + H_2$	2.75E+12	0.00	20000.	—	—	—

Table 4.3: *Collection of kinetic parameters from the optimized Jones-Lindstedt [84] in this work. RO means reaction order.*

Reaction	A [cm-s-mol]	n	E_a [cal/mol]	RO CH_4	RO H_2	RO O_2
$CH_4 + 0.5O_2 => CO + 2H_2$	5.571082e+13	0.00	29895.85	0.5	—	1.25
$CH_4 + H_2O => CO + 3H_2$	6.234473e+11	0.00	30460.47	—	—	—
$H_2 + 0.5O_2 = H_2O$	2.720403e+18	-1.0	39568.71	—	0.25	1.5
$CO + H_2O = CO_2 + H_2$	1.407710e+12	0.00	20516.79	—	—	—

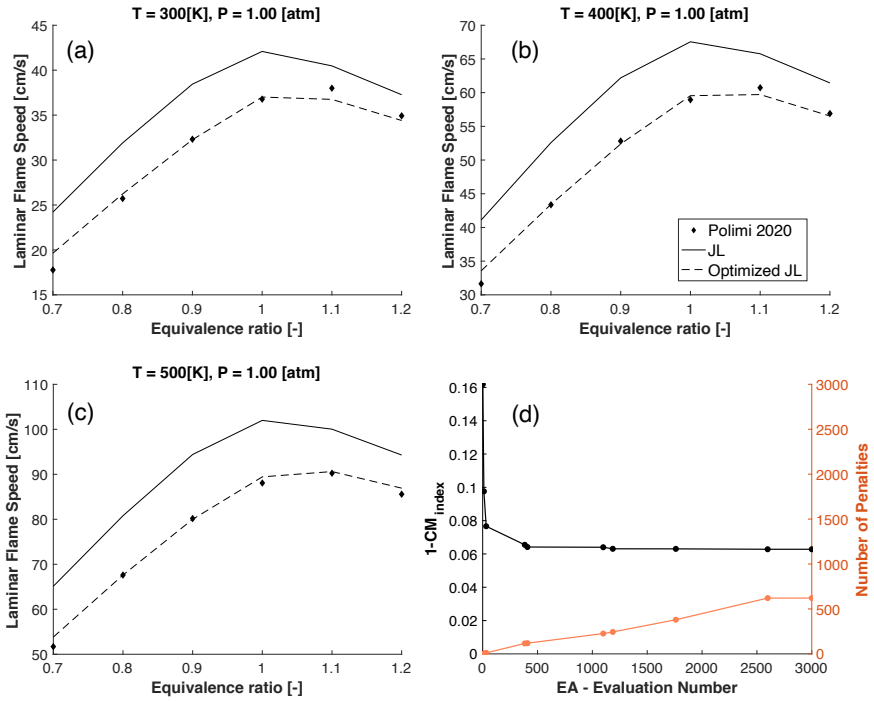

Figure 4.10: *Comparison between nominal (—) and optimized (- - -) model responses for in test case 8. Laminar burning speed of methane/air mixtures at 300 (a), 400 (b), and 500 (c) K. Convergence of the evolutionary algorithm is shown in (d) together with the number of penalized parameters combinations.*

4.3.7 Test Case 9: NO formation in a burner-stabilized flame

In this example, the capabilities of OptiSMOKE++ in handling species profiles measurements in low pressures (p]=7.5 kPa) burner stabilized flames is tested against rich CH_4/ CO/ H_2 mixture at measured by Cafiero [24], in a Spalding-Botha burner of diameter d=0.08 m. NO concentrations was measured via chemiluminescence, with an estimated experimental uncertainty of 15%. Also,

Table 4.4: *Selected uncertain reactions with nominal pre-exponential factor, adopted uncertain factors, mean and standard deviations.*

Number	Reaction	A [kmol/cm/s]	f	μ	σ
R5	$H + O_2 = O + OH$	1.14E+11	0.20	25.46	0.15
R6	$H + OH + M = H_2O + M$	3.50E+16	0.50	38.09	0.38
R32	$H + CH_4 = H_2 + CH_3$	6.14E+02	0.40	6.42	0.30
R53	$O_2 + CH_2 = OH + HCO$	1.06E+10	0.55	23.084	0.42
R56	$H + CH_2 = H_2 + CH$	3.00E+10	1.00	24.12	0.76
R63	$H + CH = H_2 + C$	1.10E+11	0.60	25.42	0.46
R72	$O + CH_3 = H + CH_2O$	5.54E+10	0.20	24.73	0.15
R73	$OH + CH_3 = H_2O + CH_2(S)$	PLOG	0.30	0.00	0.10
R6110	$LC_6H_5 = C_2H_2 + C_4H_3$	1.00E+14	0.74	32.24	0.56
R6111	$LC_6H_5 = 2C_2H_2 + C_2H$	2.00E+14	1.00	32.93	0.76
R7681	$NO + N = N_2 + O$	4.28E+10	0.15	24.48	0.11
R7726	$O + NNH = NO + NH$	5.20E+08	0.30	20.07	0.23
R7676	$NO + NH = H + N_2O$	5.33E+09	0.65	22.40	0.49
R7813	$O_2 + CN = CO + NO$	1.40E+09	0.30	21.06	0.23
R8024	$N_2 + CH = H + NCN$	PLOG	0.30	0.00	0.10
R8034	$H + NCN = N + HCN$	PLOG	0.38	0.00	0.13
R8036	$O + NCN = NO + CN$	2.50E+10	1.10	23.94	0.84

NO formation was discussed from a chemical perspective and many reactions were found to be impactful. In the following example, we extend the screening performed by Cafiero [24] with local sensitivity analysis using uncertainty propagation and global sensitivity analysis using polynomial chaos expansion, and model optimization. Table 4.4 reports the most impactful reactions along with the nominal pre-exponential factors, the uncertainty factors f, means μ and standard deviations σ.

Before analyzing the impact of temperature and kinetic uncertainties on the predictions of NO in the 1D premixed laminar flame, the accuracy of the PCE approach with sparse grid was assessed. The NO distributions obtained by PCE at two different heights above the burner (HAB) for the stoichiometric flame were compared to those extracted by near-randomly sampling the 17-dimensional uncertain parameter space via the Latin Hypercube Sampling (LHS) method [108]. The number of 1D simulations required to extract the reference distributions via LHS amounts to 4096, almost six times higher than those required to construct the polynomial expansion via a sparse grid, i.e. 757. In terms of computational costs, 4096 simulations required about 360 hours on a 16-core workstation. Figures 4.11 (left) and 4.11 (right) show the distribu-

tions obtained at HAB=0.80 cm and HAB=4.95 cm, respectively. The former represents the flame front distribution, while the latter the post-flame one.

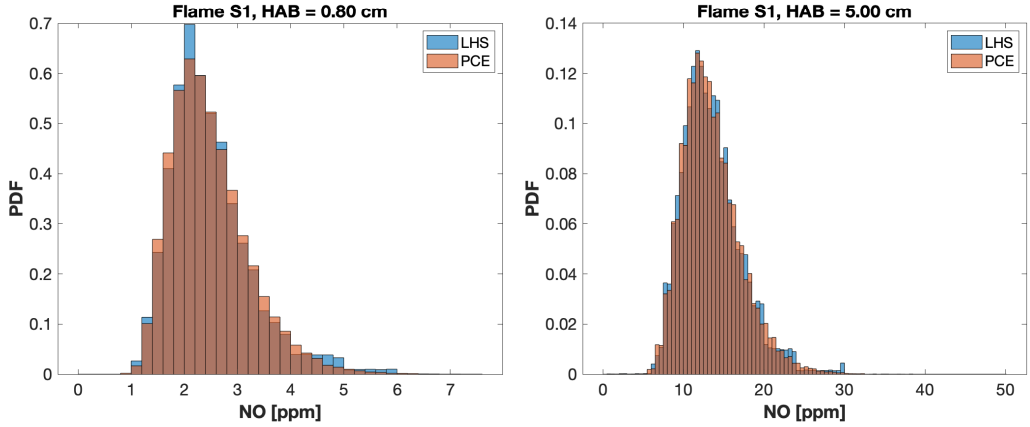

Figure 4.11: *NO distributions at heights above the burner HAB=0.80 cm (a) and HAB=5.00 cm (b) in the 1D premixed laminar flame S1 (stoichiometric conditions)*

To assess how each selected reaction contributes to the output variability, a global sensitivity analysis was performed using the expansion model built with PCE. Indeed, the impact of the i-th active variable can be measured in terms of the first order Sobol index or main effect (see section 2.5.3). Figure 4.12 shows such indices, normalized so that they sum up to 1, for many positions in the flame domain, revealing that different kinetic pathways are responsible for NO formation in different flame zones. It is interesting to report that second order terms sum up to a total which is less than 0.01% of the output variance, and are therefore omitted from the figure. The importance of the prompt pathway in the rich flame is proven by the magnitude of the Sobol indices for the reactions R56, R63, R8036 and R8024, that involve NCN and CH radicals. In particular, reaction R8024 is the rate limiting reaction for NO prompt route, since it forms NCN radical from the reaction between N_2 and CH radical, whereas reaction R56 is the main reaction of formation of CH radical in the investigated flames. The values of the Sobol indices for these reactions remain quite constant in the post-flame zone, indicating that NO are mainly formed in flame R1 via the prompt pathway, while the thermal NO pathway gives a negligible contribution to the overall NO formation [24].

Finally, the model uncertainty can be propagated, as shown in figure 4.13,

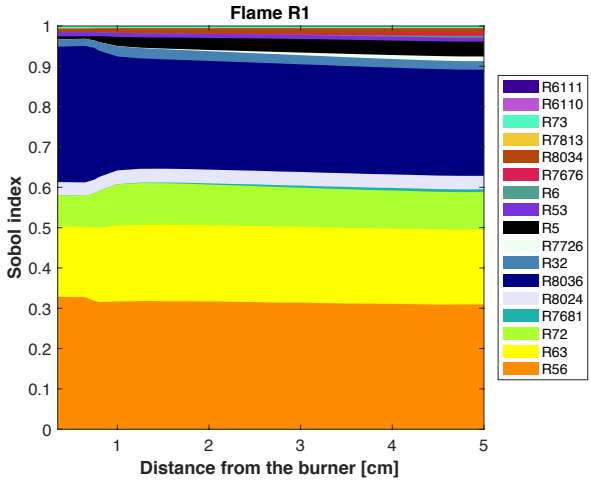

Figure 4.12: *First order, normalized, and variance-based sensitivity coefficients for important reactions in NO_x formation for CH_4/H_2 rich flame ($\phi = 1.2$).*

through PCE. In the plot, the light gray band contains the whole possible ranges of NO values, the dotted and dashed lines show the 95^{th} and 75^{th} percentiles, respectively, and the solid line depicts the median of the obtained NO distribution. The expected value of such distribution overlaps with the prediction of the nominal mechanism. The experimental uncertainty band is enclosed within the simulation one, indicating that there exists combinations of the kinetic parameters providing NO predictions that are included the experimental uncertainty. To conclude, 12 parameters from reactions R56, R63, R72 and 8036, which were found to be the most impactful in GS analysis, were optimized in OptiSMOKE++. The figure 4.13 shows model improvements in a red, straight line.

4.4 Conclusions

This chapter describes different features of OptiSMOKE++: a C++ interface between DAKOTA, OptiSMOKE++, and CurveMatching. Additionally, OptiSMOKE++ can rely on SciExpeM to retrieve OpenSMOKE++ inputs for simulations and experimental data from different sources. Here, nine different test cases were presented, which reflect the full spectrum of available models, data, and techniques in the OptiSMOKE++ framework. The latter can be used to optimize kinetic mechanisms, perform UQ of Arrhenius parameters (and others), and

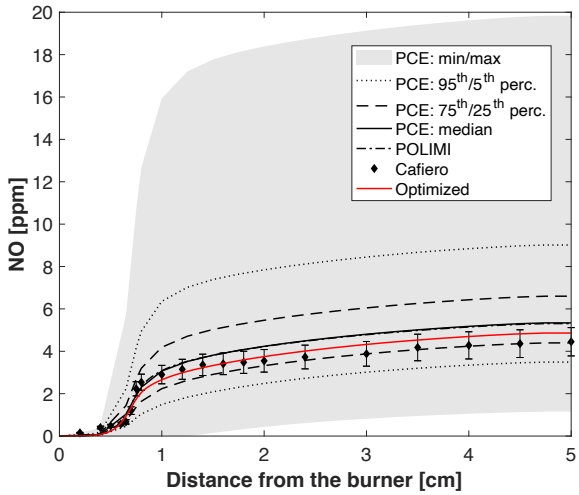

Figure 4.13: *Comparison between nominal (—) and optimized (- - -) model responses for test case 9, and uncertainty propagation by means of PCE. Experimental data from Cafiero.*

variance-based sensitivity analysis through polynomial chaos (PCE). These nine test cases are available for future users, together with the code at `https://github.com/burn-research/OptiSMOKE_toolbox.git`. I think OptiSMOKE should be used for mechanism optimization when a complete dataset, involving several different targets, is available or, for small sets, to detect possible ways of improving the model, and subsequently perform first principle investigation in that direction. As the latter is not in line with the aim of this work, the chapter is meant to showcase possible use of OptiSMOKE++ and as reference for future users, who would like to reproduce the work with their own data and reactions. The core value of OptiSMOKE++ is flexibility and user-friendlyness, which is reflected by the available reaction formats, and targets from different facilities, which can of course also be used simultaneously at will:

- Kinetic constant rate fitting from high-fidelity experimental data, for modified Arrhenius (see 4.2.1), Lindemann, TROE, PLOG and modified PLOG (see 4.2.1), and DUPLICATE;
- Perfectly Stirred Reactors, for species concentration (see 4.3.1);
- Plug Flow Reactor, also for speciation (see 4.3.2 and 4.3.3)and IDT;
- Batch ractors, mainly used for reproducing Ignition Delay Time (IDT) and

species concentration in Shock Tubes (4.3.4)and Rapid Compression Machines (4.3.5);

- Laminar one-dimensional flames, for both flame speed (4.3.6) and speciation (4.3.7).

The user can set up experimental data files and indicate reactions to be investigated with a limited amount of information, i.e. reaction indices (i.e. position within the CHEMKIN model), uncertainties and format. In general, different optimization algorithms can be employed using the DAKOTA toolkit. Then, OptiSMOKE++ ensures that the optimizer falls within the physically viable portion of the parameters sample space, by applying a penalty function to the unfeasible samples, i.e. it checks constraints for all reactions and forcefully increases the corresponding objective function value (i.e. without performing simulations and computing the real value) in case any non-eligible parameter is detected (sort of Sparta rule). Even though this procedure slows down the optimizer in terms of attempted model evalutions, the effective number of evaluated model responses is lower compared to other penalty function concepts implemented in Dakota, where non-eligible combinations are anyway evaluated, with the aim of preserving a continuous objective function space. On the other hand, discontinuities such as those introduced by the penalty function make the adoption of (more-efficient) gradient-based algorithms unfeasible. However, literature shows how a heuristic algorithm can overcome these issues and get closer to the global minimum, even though convergence is never garanteed. In addition, these algorithm allow for caractherization of acceptance regions for model input parameters, highlighting their strong correlation, when present (see figure 4.5). Still large room for improvements is available in H_2/O_2 core mechanism parametrization when the fuel/oxidiser mixtures are diluted in water (see figure 4.6 and 4.8). It is of crucial importance, to include a horizontal shifting parameter to meaninfully compare models and experiments, while optimizing the first using flow reactors data (see section 4.3.2). This is widely accepted in literature, and available in OptiSMOKE 2.0. Even though it might be obvious for the expert reader that, in case of missing elementary kinetic steps in the mechanism, the model tuning would result in non-physically meaningful kinetic parameters values, one of the possible day-to-day use of OptiSMOKE 2.0 is the verification of missing pathways. In particular, if an optimizer is not capable

to improve a model while considering all sensitive reactions with wide uncertainty, it is highly likely that the mechanism is incomplete (see discussion in section 4.3.3). Another possible use of the framework is tuning global/skeletal mechanisms, as demonstrated in section 4.3.6. Finally, the same framework might serve purposes of uncertainty quantification and variance-based sensitivity analysis as demonstrated in section 4.3.7.

CHAPTER 5

Estimation of third body efficiencies from experimental data: an application to hydrogen combustion

This chapter is based on the following pubblication:

- *Estimation of third body efficiencies from experimental data: an application to hydrogen combustion.* ***Bertolino, A.****, Frassoldati, A., Cuoci, A., Parente, A. International Journal of Hydrogen Energy.* `under_review`

5.1 Abstract

In this work, the role of H_2O and CO_2 as diluents is investigated , in operating conditions relevant to MILD combustion of hydrogen. Through virtual species analysis, the role of third body collisions emerges in phenomena such as ignition and speciation. Global sensitivity analysis shows that a single third body efficiency exhibits a larger impact than a group of sensitive reactions. For fall-off reactions, the adoption of a PLOG format, rather than a classical TROE can introduce errors as high as 2000% on macroscopic combustion targets due to the absence of key collision efficiencies. Heuristic optimization methods in OptiSMOKE++ provide best estimates and confidence regions for the third body efficiencies of H_2O and CO_2 in $H + O_2(+ M) = HO_2(+ M)$ and $H_2O_2(+ M) = 2\,OH(+ M)$ in TROE formulation. Eventually, a method to extract this information using the PLOG formulation is proposed. This approach is applicable to other reactions in case theoretical calculations are unavailable or difficult to perform.

5.2 Database

This work, involving the $H_2 - O_2$ core for diluted H_2/air mixtures, is based on 450 experimental data collected from literature from PSR, ST, RCM and spherical bombs. A summary of the operating conditions for each test case (TC) are summarized in Table 5.1.

Table 5.1: *List of experimental measurement studied in this section*

Label	System	T [K]	P [atm]	ϕ [-]	Diluents	Dilution	Ref.	N. of dp
TC1	RCM	907-1048	10,30, 70	1.0	N_2/H_2O	81.25%	[40]	51
TC2	RCM	889 – 1012	10,30,	0.5, 1.0, 2.0	N_2/H_2O/Ar	52-67%	[44]	30
TC3	ST	935 – 1331	4 ,10, 16	0.42	N_2/H_2O	67-80%	[202]	41
TC4	ST	955-1248	1.1	1.0	CO_2/Ar	94.00%	[21]	17
TC5	ST	1180-1340	11-32	1.0	N_2/H_2O/Ar/ CO_2	95.50%	[152]	29
TC6	PSR	825-1014	1.2	0.5	N_2/H_2O/Ar/ CO_2	92-94%	[145]	248
TC7	spherical vessel	298	0.5-1	1.0-1.8	N_2/He/Ar/ CO_2	26-73%	[137]	40

Details on models responses

For the RCM data from Das et al. [40] and Donohoe et al. [44], the adiabatic core assumption was adopted [173]. In particular, the experimental cold pressure traces, translated to volume histories, were used to infer corresponding volume histories. The IDT was then computed as the time elapsed between the maximum pressure time-derivative and the minimum volume, corresponding to the end of compression. For shock tube simulations, constant volume batch reactors can be usually adopted. However, due to non-ideal facility behaviour a constant pressure rise in time is observed at low temperatures before ignition, and should be imposed in simulations as a percentage of the operating pressure [129]. This information was included in simulations where available from the reference papers. If not, data points where a pressure rise in time equal to the 3% of the initial pressure caused at least 10% variation in the calculated ignition delay time were excluded. Brabbs and Robertson [21] suggested that in their facility the ignition occurs where a 2% rise in pressure was measured with respect to the initial value. For the test case of Wang et al. [202], the onset of ignition corresponds to the instant where the maximum rate of OH production was observed. In Shao et al. [152], the ignition delay time is determined by extrapolating the maximum slope of pressure signals back to the baseline. The same definitions were adopted in the present work. PSR measurements from

Sabia and De Joannon [145] where no oscillatory behaviour was experimentally observed were also considered. Every experiment reported in Table 5.2 is reproduced with a simulation in OpenSMOKE++ [35]. The adopted kinetic mechanism in this study is a subset of Aramco 2.0 [94], which is composed by 39 species and 193 reactions.

5.3 Reaction Selection

In performing optimization, the model responses corresponding to experimental observations are not equally influenced by all the parameters. On the contrary, a limited set of parameters need to be considered due to the phenomenon termed effect sparsity. Subsequently, a first screening on model parameters is usually performed by means of local sensitivity analysis [180]. By applying the methods described in section 2.5.2, and applied in chapter 3 the reactions in 5.2 were selected. In brief, a CSF calculation was performed for each test case in table 5.1, resulting in 7 separate sets of reactions. The final set of 13 reactions (5.2) was obtained by merging the latter sets.

Table 5.2: *List of reactions considered for optimization in this section.*

Label	Reaction	f	Ref.
R2	$H_2 + O = H + OH$	0.2	[14]
R3	$H_2 + OH = H + H_2O$	0.3	[14]
R5	$H + O_2 = O + OH$	0.2	[14]
R21	$H_2O_2 (+ M) = 2\,OH (+ M)$	0.2	[14]
R23	$H + H_2O_2 = HO_2 + H_2$	0.3	[103]
R27	$HO_2 + H = 2\,OH$	0.15	[14]
R28	$HO_2 + H = H_2 + O_2$	0.3	[14]
R29	$HO_2 + O = OH + O_2$	0.1	[103]
R32	$2\,HO_2 = O_2 + H_2O_2$	0.4	[103]
R33	$2\,HO_2 = O_2 + H_2O_2$	0.4	[103]
R34	$H + O_2 (+ M) = HO_2 (+ M)$	0.3	[14]
R36	$H + CO = H^+CO_2$	0.1	[14]
R37	$NH + CO = H^+CO_2$	0.1	[14]

5.4 Virtual Species Analysis

Methodology

According to Koroglu et al. [92], the influence of diluents such as CO_2, and H_2O on fuel combustion is three-folded, namely as reactants in reactions such as $CO_2 + H = CO + H$, colliders (e.g in termolecular reactions if their efficiency is greater than 1), and chemical species with pronounced heat specific, thus lowering the process temperature. In the following, we shall refer to these three separate contributions as "direct", "indirect" (participation to reactions) and "thermal" effects on combustion behavior. It is important to clarify that the "direct" effect do not indicate the reactivity of the activated complex in termolecular reactions, which was just recently discussed in the community, but just species involvement in reactions available within the actual CHEMKIN mechanism. Non-reactive diluent (e.g. N_2, Ar, Ne, Kr, He) only participate with a contribution of the third type (thermal) or as weak colliders. Virtual species can be introduced in a mechanism to isolate the three different effects of diluents [153]. A similar approach was recently adopted for hydrogen oxidation in diluted conditions [145]. In this work, six virtual species were included in Aramco 2.0, and their properties are listed in 5.3. The difference between macroscopic quantities calculated in presence of the original species X and X^{CH} is a measure of “chemical” effect of X. In fact, X^{CH} does not participate to any reaction, neither directly nor indirectly, and it has the same thermodynamic properties of X. Since X^{TB} has heat specific, enthalpy and entropy of N_2, and same chaperon efficiencies of the original species in all pressure-dependent reactions, discrepancies between quantities of interest calculated with X and X^{TB} measure the “third body” effect. Eventually, the effect of direct participation to reactions (DR) can be evaluated through the comparison between the X and a species X^{DR}, characterized by both its thermal and collision efficiency in each reaction.

Application to collected data

The experimental data in table 5.1 were simulated with H_2O, CO_2 and related virtual species (see table 5.3) to isolate single contributions of diluents to fuel reactivity in Figure 5.1 displays the results of the VSA for hydrogen IDT under steam dilution in rapid compression (Figure 5.1a) machines, and shock tubes (Figure 5.1b). For the sake of brevity, the VSA for hydrogen ignition in CO_2 di-

Table 5.3: *List of virtual species used in this section.*

Species	Thermodynamics	Indirect (collider)	Direct (Reactant)	Isolated effect
H_2O	H_2O	$(H_2O)_j$	Yes	-
H_2O^{CH}	H_2O	-	-	Chemical
H_2O^{TB}	N_2	$(H_2O)_j$	-	3^{rd} Body
H_2O^{DR}	H_2O	$(H_2O)_j$	-	Direct
CO_2	CO_2	$(CO_2)_j$	Yes	-
CO_2^{CH}	N_2	-	-	Chemical
CO_2^{TB}	CO_2	$(CO_2)_j$	-	3^{rd} Body
CO_2^{DR}	CO_2	$(CO_2)_j$	-	Direct

lution is reported in appendices. Ignition delay times in presence of the original and the three virtual diluent species are presented in abscissa and ordinate, respectively. The “chemical” effect does not reproduce the ignition delay time in diluted conditions (see 5.3). In fact, the ignition is overall faster with H_2O^{CH} as model responses values relative to this species gather within the area below the bisector. This is especially true for ST (i.e. TC3 and TC5) in Figure 5.1b, while in RCM (i.e TC1 and TC2) the trend is inverted when pressure rises above 30 atm (see Figure B8 c). Hence, the reactive process is globally slower/faster because of the kinetic effect of the diluent, and not because of its enhanced specific heat. As there is no difference between the results obtained with H_2O and H_2O^{DR}, which embodies both thermal and third body characteristics of water, the “direct” participation to reactions plays no role. In fact, the data points lie on the bisector. Also the curve that refers to H_2O^{TB} overlaps with the bisector. This suggests that by accounting only for the collisional contribution of the diluents it is possible to reproduce the effect of the original diluent on the ignition delay time. The last statement leads to the conclusion that the ignition of hydrogen in diluted conditions is third body driven. Therefore, an accurate estimation of third body efficiencies for strong colliders in fall-off reactions and their range of uncertainty is crucial for more accurate predictions.

To understand why this happens, a flux analysis using datasets TC1 and TC3 was performed, and it is displayed in 5.2. At 4 bars and 1150 K, the water addition effect on the system was studied through the test case by Wang et al. [202].

When there is no diluent, H radical is mainly formed through R2. The former also produces OH via R5. Finally, R3 terminates the process (i.e. produces

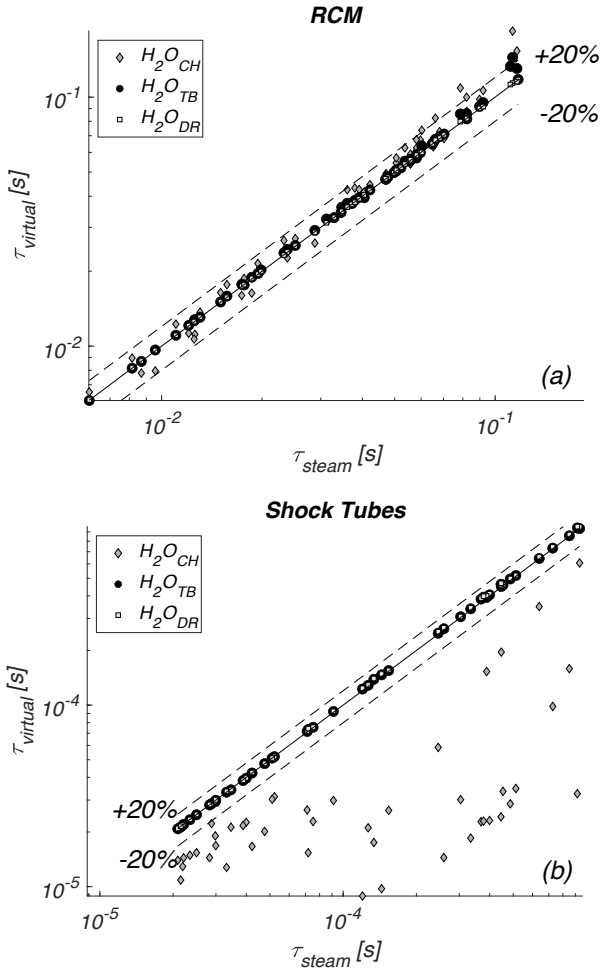

Figure 5.1: *Virtual species analysis for ignition delay time of hydrogen diluted with H_2O, in rapid compression machine (a) and shock tubes (b).*

H_2O). It is important to point out that in these conditions the branching ratio of H + O_2 reactions is in favour of R_5 instead of R_{34}, leading to fast ignition. The HO_2 resulting from the last reactions produces H_2 through R28, and eH_2O_2 is formed in backward R21. When steam constitutes 15, 25 and 40% of the initial mixture in volume, the reaction rate of R34 increase proportionally to the third body efficiency of the diluent. This leads to enhanced production of hydroperoxyl radical, and H_2O_2 is formed in R23, R32 and R33. This reactive pathway, together with R27, becomes competitive against R5 in hydroxyl radical production. Subsequently, OH is produced in R21. Indeed, at low pressure R21 is

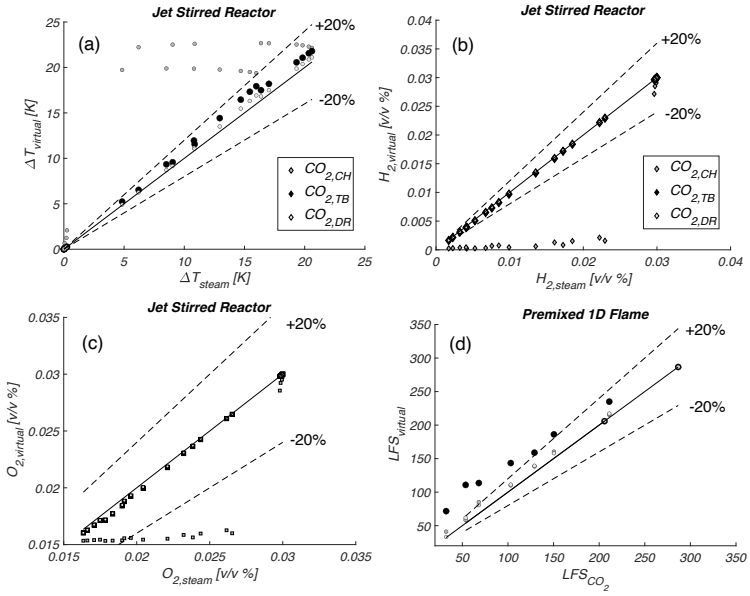

Figure 5.2: *Flux analysis for hydrogen ignition. Reaction pathways enhanced by the presence of a diluent are reported with straight line (-), while others in dashed (–).*

not as impactful as R27. The opportunity for the system to take this alternative longer pathway, explains why ignition in presence of water or carbon dioxide is slower. In fact, the latter molecules have very large third body efficiencies in R34, namely 10 for H_2O and 3.8 for CO_2. Lastly, when the third body of the diluent is set to 1 (i.e. X^{CH} is used in place of X) the system returns to fast ignition because of the OH production being led mainly by R5. At high pressure (30 and 70 bar), the ignition delay time in presence of H_2O^{CH} is higher than for H_2O and the other virtual species, meaning that the third body effect accelerates the chemistry in these conditions. Indeed, the pronounced third body efficiency of water causes the rate constant of R21 to rise enough to produce a significant amount of OH radical and prompt the ignition. Also Das et al. [40] reached similar conclusions for high pressures with H_2O dilution. Here we confirm and reinforce their statement as the same behaviour is observed in this work for experiments at 10 and 30 bar from Donohoe et al. [44]. Figure 5.3 displays VSA for temperature increase (a), hydrogen (b) and oxygen (c) conversion in a PSR close to atmospheric pressure. Similar conclusions to those for ignition can be drawn. In fact, simulations which were carried out with CO_2^{CH} as diluent show a more pronounced reactivity than those with other virtual species, as

their values are distant from the bisector. This happens because of R34, which is enhanced by CO_2 as collider. Again, when the third body efficiency of CO_2 is set to 1 (i.e.CO_2^{CH} is the diluent), R5 prevails and leads to higher energy release. Little chemical effect can be appreciated for temperature, while reactants conversion is fully third body driven. Conversely, thermal effects control flame propagation as expected (see Figure 5.3d). In fact, the laminar burning speed increases when CO_2 is replaced by CO_2^{TB} due to the lower heat capacity of the mixture, which translates to a higher maximum temperature as well as steeper temperature increase. Oppositely, the flame speeds calculated with CO_2^{DR} or CO_2^{CH} are equal and their difference with CO_2 is negligible. In conclusion, experimental measurements of macroscopic combustion quantities, such as species concentrations in perfectly stirred reactors and ignition delay times in diluted conditions are ideal targets for estimation of third body efficiencies as their parametrization embodies the driving physical phenomenon.

5.5 Estimation of third body efficiencies in TROE format

Unimolecular/recombination reactions are both temperature and pressure dependent. Generally, they follow a classical Arrhenius behaviour at the high-pressure limit. Diversely, at low pressures they require a third body collision to proceed, which usually involves inert as well as reacting colliders. Indeed, some colliders are more “efficient” than others, meaning that the reaction rate at the low-pressure limit can be higher or lower, depending on the molecule taking part to collision. In fact, chemical species can be classified as “weak” or “strong”, colliders. So, the value of the third body efficiency of a molecule in a certain reaction is a measure of its ability to prompt it through collision with reacting compounds. This was theorized by Lindemann [101], and it is usually parametrized in CHEMKIN using the TROE format [182]. This is the case for reactions R21 and R34 in the mechanism adopted for this study, i.e. Aramco 2.0 [94]. However, no consensus for the efficiencies of H_2O and CO_2 was reached. Table 5.4 shows maximum and minimum values from literature mechanisms for these two molecules. The efficiencies in reactions R21 and R34 were normalized by those of argon and N_2, respectively, to make comparison with values in the Aramco 2.0 [94] model easier.

To show the impact that such uncertainties can have on model responses a

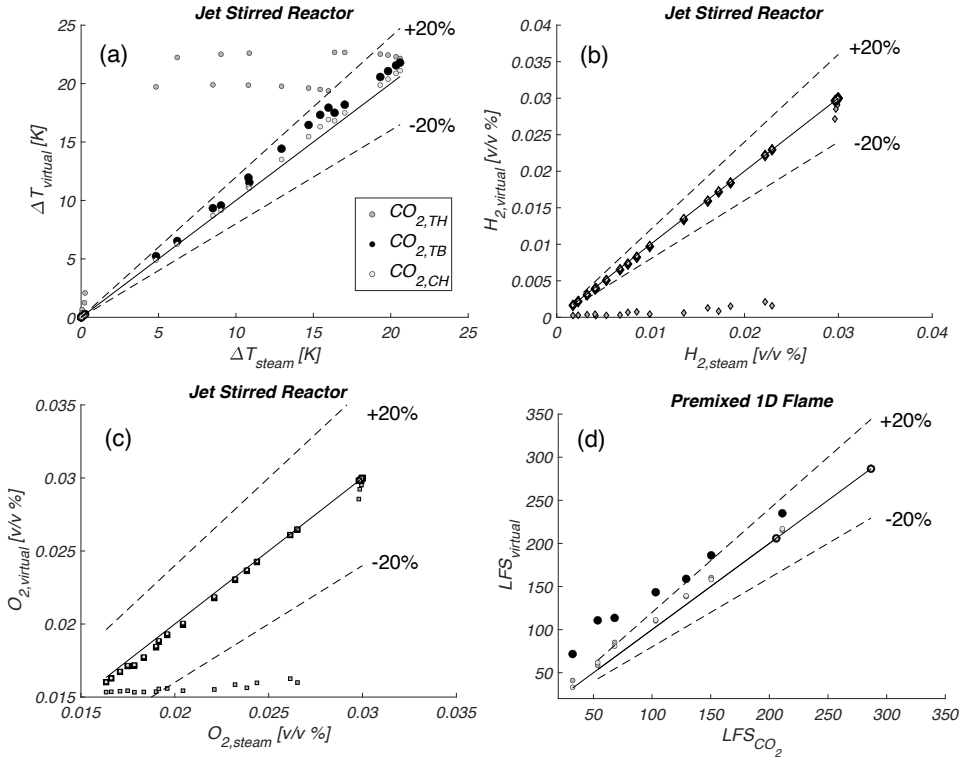

Figure 5.3: *Virtual species analysis for speciation and laminar flame speed of hydrogen diluted with CO_2. In (a) different normalized quantities of interests are reported: temperature increase (a), hydrogen (b) and oxygen (c) concentration, and laminar flame speed (d).*

Table 5.4: *Uncertainty range for third body efficiencies of CO_2 and H_2O in impactful fall-off reactions for test cases in this section. The reference bath gas (i.e. X) is argon for R21 and nitrogen for R34.*

Reaction Index	$\alpha_{H2O/X}$		$\alpha_{CO2/X}$	
-	min	max	min	max
R21	1.00	22.64	1.00	3.80
R34	10.00	16.00	1.00	5.95

global sensitivity analysis was carried out on ignition delay time measurement by Das et al. [40] at 30 bar with 0 and 40% of water inside the initial mixture. All the sensitive reactions, identified through a local sensitivity analysis (see Figure B2), were included in this analysis as well as the third body efficiencies of water for reactions R21 and R34, bounded with values reported in Table 5.4. Figure 5.4a shows the first order Sobol's indices (see section 2.5.3) for model

inputs, in absence of water. The reaction responsible for most of the variance in the model response is R23, forming hydrogen peroxide, which decomposes through R21, the second most impactful reaction. The Sobol's indices for reaction R33 are directly proportional to temperature, on the contrary R5 and R34 show inverse proportionality. Here, third body efficiencies play no role in the variability of the model responses. Conversely, 5.4b demonstrates that when ignition takes place in a strongly diluted environment, the impact of a single parameter might exceed that of an entire group of important reactions. In fact, the third body efficiency of water for R21 accounts for almost the 20% of the output variance. It is to be expected that for lower pressures the efficiency of H_2O in R34 would have a major impact instead

Another way to see this is to look at the uncertainty propagation to model responses using the metamodels produced by means of PCE, which is shown in Figure 5.5. Two separate surrogate models were built for each operating condition starting from two different germs (see section 2.5.3). The first surrogate model was built using a random vector containing the pre-exponential factors of all sensitive reactions identified by means of the CSF for the test case of Das et al. [40] (see Figure B2 in SM) and the third body efficiencies of water in R21 and R34. In the second meta-model instead, the third body efficiencies of water were excluded from the germ, but all the A factors of sensitive reactions were considered. While no difference between the uncertainty of the two models was observed in Figure 5.5a, the uncertainty of the model response in Figure 5.5b was significantly increased.

These results point out that an accurate estimation and uncertainty reduction for these parameters is crucial for diluted conditions, and that they represent an important degree of freedom to improve the performance of existing mechanisms. Finally, if these parameters were not included in optimization studies, the uncertainty in model responses might be improperly minimized by tuning other sensitive parameters. Indeed, it is important to characterize third body efficiencies both in terms of best values and confidence regions. In previous studies, inference of kinetic rate constants of pressure-dependent reaction R34 and its collision efficiencies was achieved using shock tubes experiments for IDT measurements, NO_2 concentration plateaus, and species time-histories. Shao [152] discussed the importance of finding conditions where the QoI is sensitive to the smallest possible set of elementary reactions. In their work,

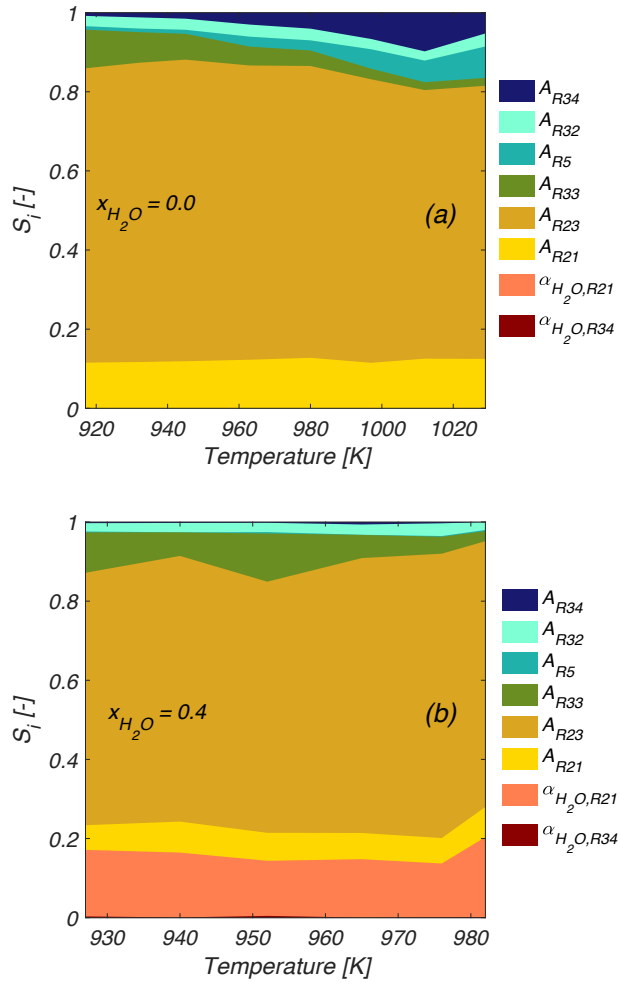

Figure 5.4: *Global Sensitivity Analysis for important reactions in a rapid compression machine, cases by Das et al. [40] at 30 bar, 0 (a) and 40 (b) % water dilution, as a function of temperature.*

they used IDT for H_2/O_2/diluent to evaluate the collision efficiency of N_2, CO_2 and H_2O relative to the one of Argon in R34. In the operating conditions which were accounted for, the IDT was strongly sensitive to R34, and R5. Indeed, the uncertainty of R5 in the adopted model would impact the parameters estimation for R34, but it was considered negligible. Also, this approach excludes the possibility to use experimental data for QoI in operating conditions where the number of sensitive reactions increases as for the RCM and PSR measure-

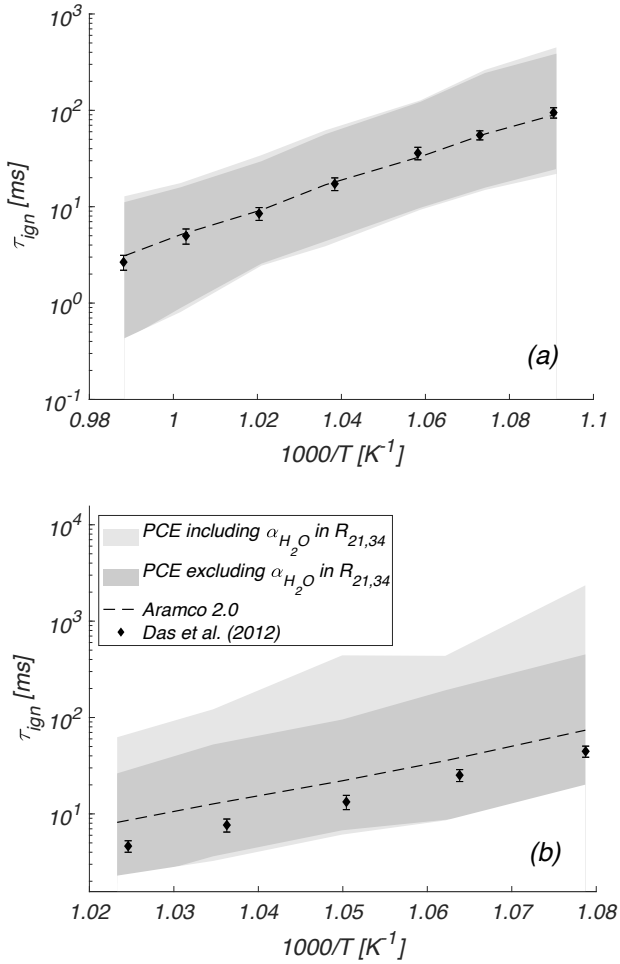

Figure 5.5: *Propagation of uncertainty from kinetic mechanism to model responses using a Polynomial Chaos Expansion based surrogate model built by considering and neglecting the contribution of third body efficiency of water to the model uncertainty, cases by Das et al. [40] at 30 bar, 0 (a) and 40 (b) % water dilution, as a function of temperature.*

ments from Das et al. [40] and Sabia and De Joannon [145], respectively (see Figure B). Global optimization approaches consider the uncertainties of all the sensitive reactions, and a large set of available experimental data in different operating conditions, simultaneously. In the following, these methods are applied and confidence regions (see section 2.7) are retrieved. For the sake of clarity, two aspects need further attention. First, the experimental data in 5.3 were divided in two separate sets, i.e. those involving H_2O and CO_2 as diluent,

respectively. The third body efficiencies of H_2O/CO_2 were estimated using only the first/second set as targets. Second, to highlight the importance of considering the entire set contemporarily and discuss the relevance of each test case to parameters estimation, optimization was also performed on each component of the dataset separately. Figure 5.6 shows that not only the best estimates are different for each test case, but also the confidence regions differ from each other significantly. For this reason, the estimation of third body efficiencies using experimental data from a single source is not recommended. In the case of water (see Figure 5.6a), suggested parameters values fall in the north-west quadrant of the sample space for Sabia and De Joannon [145], south-west quadrant for Donohoe et al. [44], and south-east one for Das et al. [40] and Wang et al. [202]. The size and the orientation of the elliptical confidence regions display the relevance of the test case for each parameter, and the correlation between them. The data from Shao et al. [152] are relevant for the estimation of α_{H2O} in R34, but not for R21, as the elliptical confidence region extend along the entire horizontal axis. This is due to the operating pressure, which is lower than 20 [bar] In fact, the most relevant data for the estimation of α_{H2O} are those from Das [40] as they were performed at operating pressure up to 70 bar. Regarding CO_2, the analysis of results shown Figure 5.6b leads to the conclusion that experimental data from Brabbs and Robertson [21] carry a lower amount of information about the parameter estimates with respect to other test cases. It is also interesting to notice that data from Shao [152] are significant for the estimation of α_{CO2} in R21.

In Figure 5.6a, and Figure 5.6b results from optimization procedures which were carried out using all data together are displayed, and a single well-defined uncertainty region can be observed for the four parameters, conditioned by the uncertainty of all the sensitive reactions in Table 5.3. It is interesting to notice that, while for CO_2 the uncertainty region overlaps with that identified by values in existing mechanisms, efficiencies of water fall outside the more populated region. Finally, this study strengthens our belief about how important it is to consider a wide variety of data when performing optimization. In particular, using each dataset separately, the modeller would end up in different parameters settings in disagreement with each other, mainly due to the heterogeneous set of adopted operating conditions, i.e. temperature, pressure, mixture composition, equivalence ratio, which reduces the general validity of parameters

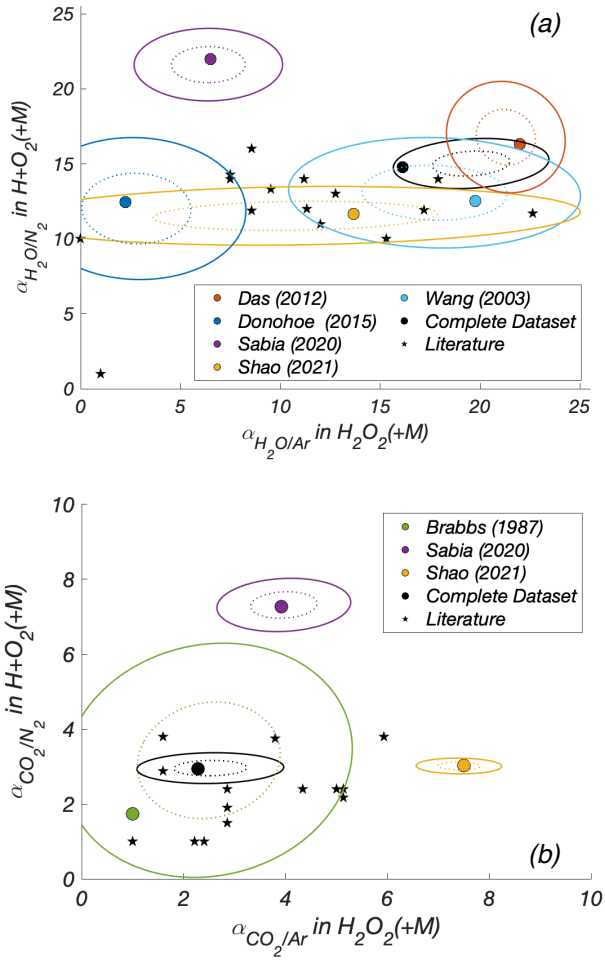

Figure 5.6: *Regions of 68% (. . .) and 99% (-) confidence for third body efficiencies of water (a) and carbon dioxide (b) in* $H2O2(+M) = 2OH(+M)$ *and* $H + O2(+M) = HO2(+M)$ *in TROE format estimated by using different datasets as target for optimization. The black stars mark parameters values from existing kinetic mechanisms, while best estimates are represented by circles.*

acceptance regions. The minimum and maximum values in the confidence region of the four considered parameters are displayed in Table 5.5.

In conclusion, new experimental data at high-pressure conditions with water dilution are needed to narrow the uncertainty range of α_{H2O} in R21. For CO_2, the range is well defined in R34 while is still broad in R21, this confirms that more data at high pressures are needed.

Table 5.5: *Uncertainty range for third body efficiencies of CO_2 and H_2O in impactful fall-off reactions for test cases in this section. The reference bath gas (i.e. X) is argon for R21 and nitrogen for R34.*

Reaction Index	$\alpha_{H2O/X}$			$\alpha_{CO2/X}$		
-	min	max	suggested	min	max	suggested
R21	15.60	23.40	16.15	1.10	3.96	2.30
R34	13.30	16.70	14.75	2.55	3.37	2.94

5.6 Importance and estimation of third body efficiencies in PLOG format

The PLOG formulation for fall-off reactions was recently introduced in the CHEMKIN format, in alternative to TROE's, to accommodate ab-initio calculations in kinetic mechanisms with a lower fitting error. A PLOG reaction consists of multiple Arrhenius rate constants at discrete pressures p_i (with i = 1, . . . , N_p), individually accounting for temperature dependence. Indeed, p_1 and p_{N_p} correspond to the low and high-pressure limit, respectively. A logarithmic interpolation is then adopted at intermediate pressures $\overline{p}$:

$$ln(k_{\overline{p}}) = ln(k_{p_i}) + \left[ln(k_{p_{i+1}}) - n(k_{p_i})\right] \left[\frac{ln(\overline{p}) - ln(p_i)}{ln(p_{i+1}) - ln(p_i)}\right] \tag{5.1}$$

In this form, the rate does not account for chaperon efficiencies. Thus, in case of diluted mixtures, error in prediction of macroscopic targets might be higher than those due to the fitting error of the TROE format [36, 86]. To quantify this error, two mechanisms were created from Aramco 2.0 [94], which are referred to in the following as "single bath" and "multi bath", respectively. In the first, the rates for R21 and R34 were converted from TROE to PLOG format considering all species with equal, unitary third body efficiency. This was done to emulate the replacement of a fall-off reaction in TROE format with a PLOG. In the second mechanism, the third body efficiencies for each species were considered during the conversion using an extended PLOG format proposed by Klippenstein (*personal communication*), where one PLOG is specified to separately model the contribution of the j^{th} bath gas, and the overall reaction rate constant can be retrieved using a linear mixture rule:

$$ln(k_{\bar{p}tot}) = \sum_{j=1}^{N_{bg}} ln(k_{\bar{p},j})x_j \tag{5.2}$$

N_{bg} is the number of considered bath gases, and x_j its molar fraction. To our knowledge, this format is not available in CHEMKIN yet, but it can be used in OpenSMOKE++ [35] and OptiSMOKE++ [64]. Figure 5.7a shows the predictions of temperature increase in the low-pressure PSR measurement by Sabia and De Joannon [145] with the three kinetic models (i.e. Aramco 2.0, single-bath, and multi-bath). A steep increase in temperature can be noted with the single-bath mechanism around the onset of ignition, while the difference between the other two models is negligible. The dotted curve represents the relative error between the predictions of Aramco 2.0 and the single-bath model. Its values, reaching a peak of 2000%, can be read on the secondary axis. The same procedure was carried out for the ignition delay time data by Das et al. [40] with 40% H2O dilution at elevated pressures. Here, the relative error on the ignition delay time induced by the PLOG is between 120 and 140%.

This new PLOG format allows to include accurate ab-initio calculations for each bath gas. However, due to higher complexities associated with calculations for strong colliders (e.g. CO_2 and H_2O), their efficiencies are not always available. On the other hand, if measurements are available for a certain bath gas, its efficiency can be estimated using optimization strategies, as shown in previous sections. In the following, we address the question: "**Is it possible to introduce new parameters to account for collision efficiency in PLOG reactions?**". Figure 5.8a reports a graphical example of the TROE fall-off behaviour in reaction R34 in mixtures with different third body efficiencies, namely 1, 5 and 10. Indeed, all three rates converge at the high-pressure limit. When this reaction is replaced with a PLOG format (see 5.8a) only one of the three curves will be available within the mechanism (i.e. the one with $\alpha = 1$). In principle, it should be possible to derive a correction, function of pressure and temperature, to express the rate dependence to the bath gas using the rate for reference one. If we consider a Lindemann formulation for pressure dependent reactions:

$$k = k_\infty \frac{P_r(M)}{1 + P_r(M)} \tag{5.3}$$

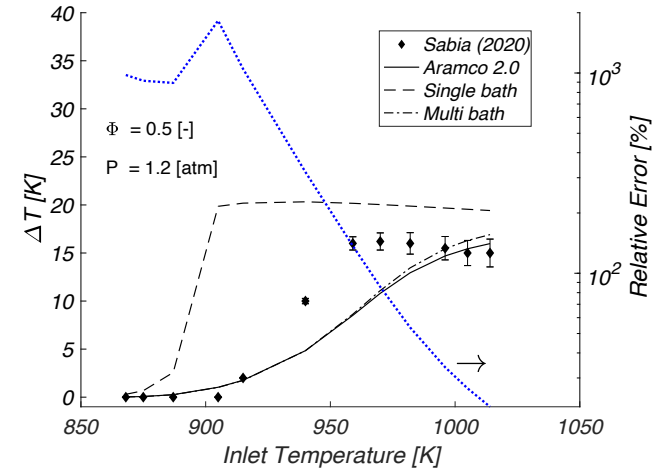

(a)

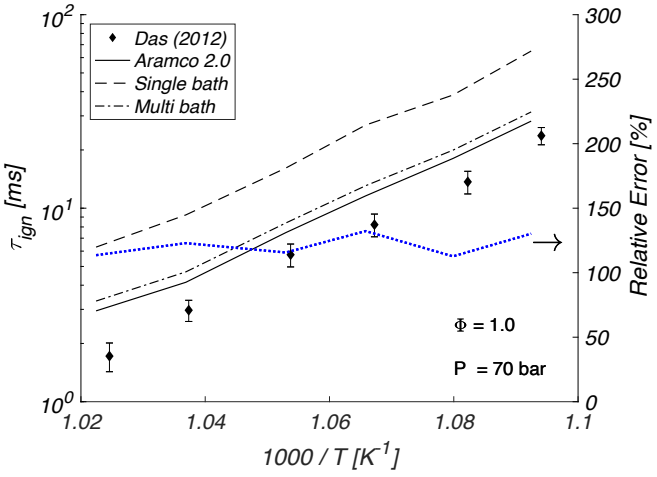

(b)

Figure 5.7: *Comparison between Aramco 2.0 (-), single-bath (–), and multi-bath (-··-) mechanisms performances. (a) Increase in temperature in a perfectly stirred reactor for lean $H_2/O_2/CO_2$ mixtures. (b) Ignition delay in a rapid compression machine for stoichiometric $H_2/O_2/N_2/H_2O$ mixtures. The relative error (···) between Aramco 2.0 (-) and single-bath (–) bath mechanisms is reported on the secondary axis. Experimental data from Sabia [145] and Das et al. [40]*

Where k_∞ is the high-pressure limit rate, or the Arrhenius with highest pressure in the reference PLOG, and P_r is the reduced pressure.

$$P_r(M) = \frac{k_{low}[M]}{k_\infty} \tag{5.4}$$

In equation 5.4, $k_{low}[M]$ represent low-pressure limit rate, or the Arrhenius with lowest pressure in the reference PLOG. Finally $[M]$ is the mixture concentration, enhanced by the average collision efficiency of the mixture:

$$[M] = \frac{P}{RT}\sum_{i}^{N_{sp}} x_i\alpha_i \tag{5.5}$$

Here, α_i is the third-body efficiency of the ith species (with $i \in [1, N_{sp}]$). The ratio between the rate with unitary efficiency k_0 and another rate k_1, characterized by higher efficiency, is equal to the desired correction $C(T, P, \beta)$:

$$\frac{k_1}{k_0} = C(T, P, \beta) = \frac{[M_1]}{[M_0]}\frac{k_{low}[M_0] + k_{\infty,p}}{k_{low}[M_1] + k_{\infty,p}} = \beta\frac{k_{low}[M_0] + k_{\infty,p}}{\beta k_{low}[M_0] + k_{\infty,p}} \tag{5.6}$$

It is trivial to prove that β is a relative third body efficiency, as it is the ratio between the average collision efficiencies of the two mixtures:

$$\frac{[M_1]}{[M_0]} = \frac{\left(\sum_i^{N_{sp}} x_i\alpha_i\right)_1}{\left(\sum_i^{N_{sp}} x_i\alpha_i\right)_0} = \beta \tag{5.7}$$

In equation 5.6, k_{low}, $k_{\inf}$, and $[M_0]$ can be easily computed from a reaction given in standard PLOG format (see eqn. 5.1). In fact, in a standard PLOG, the Arrhenius parameters for the lower discrete pressure give the rate constant at the low-pressure limit (i.e. k_{low} $[M_0]$) while those at the highest pressure represent the high-pressure limit (i.e. $k_{\inf}$). Finally, $[M_0]$ is easily retrieved from the ideal gas law. This rate is considered as reference in terms of bath gas, i.e. representative of all molecules with unitary third body efficiency. The estimation of β, for a bath gas with chaperon efficiency higher/lower than 1, becomes possible through optimization if the rate is expressed by:

$$ln(k_{\overline{p}tot}) = \sum_{j=1}^{N_{bg}} [ln(k_{\overline{p},j})x_j C(T, P, \beta_j)] \tag{5.8}$$

Equation 5.8 was implemented in OptiSMOKE++ to perform this task. Figure

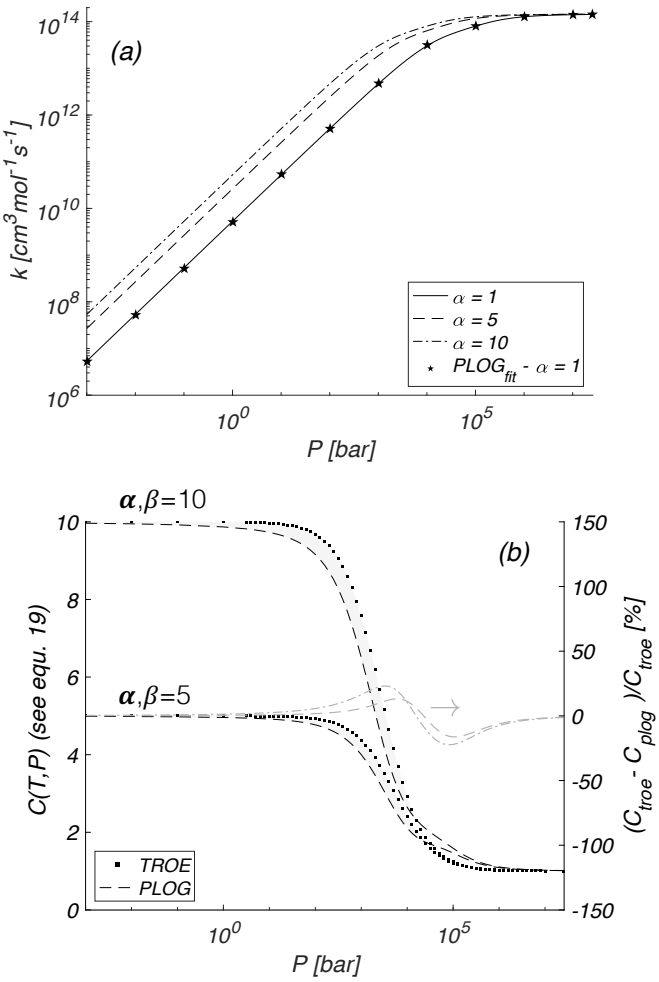

Figure 5.8: *(a) Fall-off behavior using TROE formulation for R34 for different values of efficiency, namely 1, 5, and 10. (b) Comparison between TROE and PLOG based corrections for fall-off behavior in R34 (primary y axis); Relative error between the two (secondary y axis). Efficiencies of 5, 10 were considered. Both graphs refer to T=990 K.*

5.8b quantifies the errors between TROE-based correction and Lindemann-based one, which was derived in this work for PLOG reactions. On the primary axis, the correction as a function of pressure is reported at two different ideal mixtures with efficiencies (i.e. 5 and 10) at constant temperature: 990 K. The relative error between the two formulations is also reported and can be read on the secondary axis. Equation 5.6 reproduces the desired trend and matches

the other quantitatively at the low and high-pressure limits. On the other hand, a relative error increase for pressures above $10^2/10^4$ bar can be observed. In this region, equation 5.6 may lead to overestimation/underestimation of the reaction rate. These errors increase with increasing collision efficiency, suggesting that the proposed method might lead to underestimation of the third body efficiency for very strong colliders like H_2O in R21 and R34. However, efficiencies higher than 6 are rare in fall-off reactions involving more complex species (e.g. in $C1 - C3$ or higher). To demonstrate the applicability of the proposed method another mechanism was created from Aramco 2.0. In this model, R21 and R34 are presented in the PLOG format suggested by Klippenstein (see equation 21). However, $\alpha_(H2O)$ and $\alpha_(CO2)$ were artificially set to 1 before fitting the Arrhenius parameters. On the contrary, the PLOG related to weaker colliders (e.g. He, Ar, and others) implicitly contains the information about their efficiency. Using the same datasets presented in the previous section, the same optimization procedure was applied to estimate β, and results are presented in Figure 5.9.

Figure 5.9a shows that the acceptance region of β_{H_2O} and α_{H_2O} are comparable (see Figure 5.6a). Conversely, for CO_2 a substantial difference exists between the estimated β and α. Ranges and suggested values from the analysis are available in Table 5.6.

Table 5.6: *Uncertainty range for third body efficiencies of CO_2 and H_2O in impactful fall-off reactions for test cases in this section. The reference bath gas (i.e. X) is argon for R21 and nitrogen for R34.*

Reaction Index	$\beta_{H2O/X}$			$\beta_{CO2/X}$		
-	min	max	suggested	min	max	suggested
R21	6.75	18.94	13.00	6.70	8.14	7.50
R34	9.80	16.65	13.08	2.81	3.88	3.25

In conclusion, the method presented in this section is general and it is intended to be used if the following conditions apply:

- Experimental measurement of macroscopic combustion targets, in diluted conditions, are available and were carried out in operating conditions where model responses are sensitive to a group of reactions including the fall-off reaction of interest.
- The uncertainties of all the reactions belonging to this set is known or easy

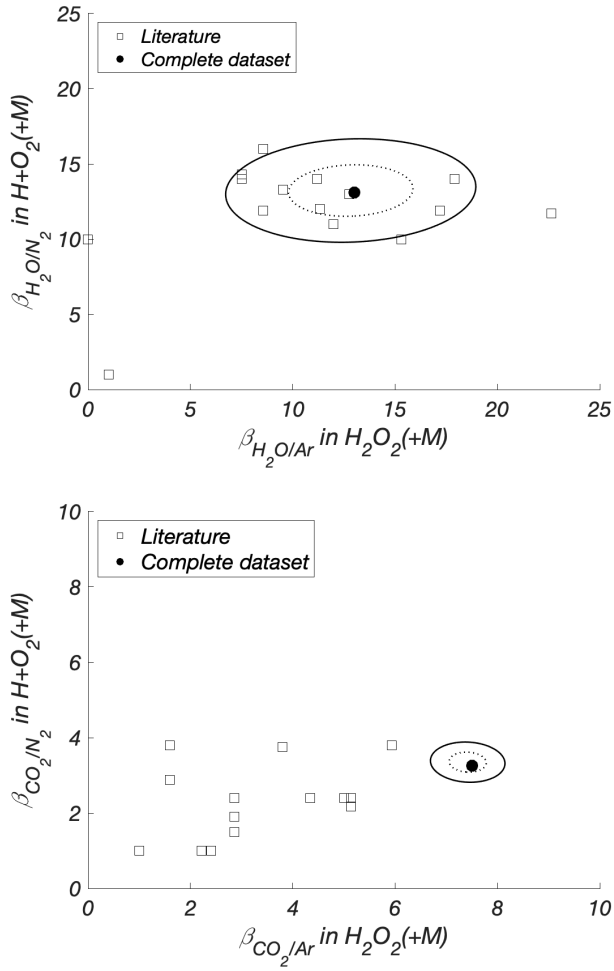

Figure 5.9: *Acceptance regions for third body efficiencies of water (a) and carbon dioxide (b) in* $H_2O_2(+M) = 2OH(+M)$ *and* $H + O_2(+M) = HO2(+M)$ *estimated from macroscopic combustion data using PLOG formulation.*

to estimate.

- The fall-off reaction of interest is expressed in the kinetic mechanism using the standard PLOG format, where all molecules are supposed to have unitary third body efficiency.

- High-level theoretical calculations are not readily available for the desired collider.

5.7 Concluding remarks

In this chapter, the role of diluents like H_2O and CO_2 in operating conditions relevant to applications for MILD combustion of hydrogen was discussed and analysed by means of a virtual species analysis (VSA). This approach allows to study the three main effects of H_2O and CO_2 (namely thermal, third body and chemical) on the fuel ignition, species consumption/formation and laminar flame speed. The VSA suggests that measurements of ignition delay time (IDT) and species concentrations in perfectly stirred reactors (PSR) in diluted conditions are ideal candidates for the estimation of collision efficiencies as their physics is significantly affected by third body effects. The analysis of literature mechanisms revealed a general disagreement for the values to be adopted for these parameters. After a first screening with local sensitivity analysis, all unimportant reactions were excluded from the study. The remaining subset, including two fall-off reactions (i.e. R21 and R34), was employed to perform a Global Sensitivity Analysis (GSA), with variance-based decomposition methods aided by surrogate models, created using non-intrusive methods for Polynomial Chaos Expansions. Results on ignition delay time (IDT) showed that, in diluted conditions, a single third body efficiency can manifest a Sobol's first order effect greater than a group of sensitive reactions. Thus, considering these parameters in optimization is important to avoid strong changes in other reactions to compensate for the missing contribution of collision efficiencies. Using an Evolutionary Algorithm (EA) enables parameters estimation and retrieval of confidence and/or acceptance regions regardless the dimensionality of the problem at hand. Separate optimization procedures for each test case highlight the need of considering experimental data from different sources simultaneously. Indeed, the confidence regions as well as the best parameter estimates for the collision efficiencies of H_2O and CO_2 were found to strongly depend on the adopted target dataset. The approach we propose in this work differs from existing ones for two reasons: (i) a combination of experimental measurements from different sources and reactors are employed. (ii) the uncertainties of all sensitive reactions are considered to weaken the dependence from starting model. Eventually, the errors introduced by the replacement of the TROE formulation for fall-off reactions with PLOG were quantified for hydrogen combustion, and a method to extract information from data about third

body efficiency of strong colliders in PLOG formulation was proposed in case high-level ab-initio calculations are not available.

CHAPTER 6

Uncertainty propagation through the numerical model of a flameless furnace, assisted with canonical reactors

This chapter is based on the following publication:

- *On the influence of kinetic uncertainties on the accuracy of numerical modelling of an industrial flameless furnace fired with NH_3/H_2 blends: a numerical and experimental study. Ferrarotti, M.,* ***Bertolino, A.****, Amaduzzi, R., Parente, A. Frontiers in Energy Research.* `https://doi.org/10.3389/fenrg.2020.597655`

6.1 Abstract

Ammonia/hydrogen-fueled combustion represents a very promising solution for the energy scenario to come. This study aims to shed light and understand the behaviour of ammonia/hydrogen blends under flameless conditions. A first-of-its-kind experimental campaign was conducted to test fuel-flexibility for different ammonia/hydrogen blends in a flameless burner, varying the air injector and the equivalence ratio. NO emissions increased drastically after injecting a small amount of NH_3 in pure hydrogen (10% in volume). An optimum trade-off between NOx emission and ammonia slip was found when working sufficiently close to stoichiometric conditions (ϕ = 0.95). In general a larger air injector (ID25) reduces the emissions, especially at ϕ = 0.8. A well stirred reactor (WSR) network with exhausts recirculation was developed exchanging information with Computational Fluid Dynamics (CFD) simulations, to model chemistry in diluted conditions. Such a simplified system was then used in two ways: (i) to explain the experimental trends of NOx emissions varying the ammonia molar fraction within the fuel blend, (ii) to perform an uncertainty quantification study. A sensitivity study coupled with Latin Hypercube Sampling (LHS) were used to evaluate the impact of kinetic uncertainties on NOx prediction in the WSR network model. The influence of the identified uncertainties was then tested in more complex numerical models, such as Reynolds Averaged Navier-Stokes (RANS) simulations of the furnace. The major over-predictions of existing kinetic scheme was then alleviated significantly, confirming the crucial role of a well-characterized detailed kinetic mechanism for the accuracy of predictive numerical model for NH_3/H_2 mixtures in flameless regime.

Author Contributions

- Marco Ferrarotti: Conceptualization, Experimental and Numerical Methodology, Validation, Investigation, Visualization, Writing - original draft;
- **Andrea Bertolino**: Conceptualization, Numerical Methodology, Investigation, Visualization, Writing - original draft;
- Ruggero Amaduzzi: Experimental methodology, Validation.
- Alessandro Parente: Conceptualization, Supervision, Writing - review & editing.

6.2 Experimental facility and measurement techniques

The furnace was introduced in [53] and it is shown in Figure 6.1. It is composed of a cubic combustion chamber (1100x1100x1100 mm), with inner dimensions of 700x700x700 mm. A recuperative Flame-FLOX burner (nominal power of 20 kW) is mounted at the bottom of the combustion chamber. The burner is equipped with an integrated heat exchanger for combustion air pre-heating from the enthalpy flue gases. The fuel is injected via a centrally located nozzle (inner diameter ID 8 mm) and surrounded by a coaxial air jet, whose dimensions can be varied to adjust the air jet entrainment (ID 16-20-25 mm). The unit is equipped with an air cooling system consisting of four cooling tubes (outer diameter OD of 80 mm), with a length of 630 mm inside the furnace. Varying the air flow allows the combustion chamber to operate at different stable conditions, thus simulating the effect of a variable load. Opening for measurements are available on the vertical walls. One side is used for OH* chemiluminescence measurements, while the others are insulated. One of three hosts 12 equally spaced (50 mm) ports for thermocouples, with inherent uncertainty of 0.5%. The exhaust gases temperature (before the heat exchanger) is obtained by means of another thermocouple positioned on the central plane and shifted 200 mm with respect to the axis, on the bottom wall. Other thermocouples are used to measure the temperature of the main operating parameters, such as fuel, cooling air, combustion air and exhaust gases after the heat exchanger. The outlet of the combustion chamber (after the heat exchanger) is equipped with a heated sampling probe to allow flue gas temperature and composition measurements, avoiding condensation. A Fourier Transform InfraRed (FTIR) analyser is used to measure pollutants (NH_3, NO_2 and NO), while a different analyser is used for oxygen, after condensing water from the exhaust gases.

The following experimental champaign considered a fixed thermal input power of 15 kW, while varying equivalence ratio between 0.8 and 1. Rich conditions were excluded from the study to ensure a full conversion of the fuel and to minimize the content of ammonia-slip released in atmosphere. The cooling power subtracted via the air cooling system was set to 5.1 kW to ensure an exhaust gases temperature of around 950°C before the heat exchanger. Two different air injector sizes (ID 16 and 25 mm) were used, varying therefore the injection velocity and residence time. Experiments were performed at steady-

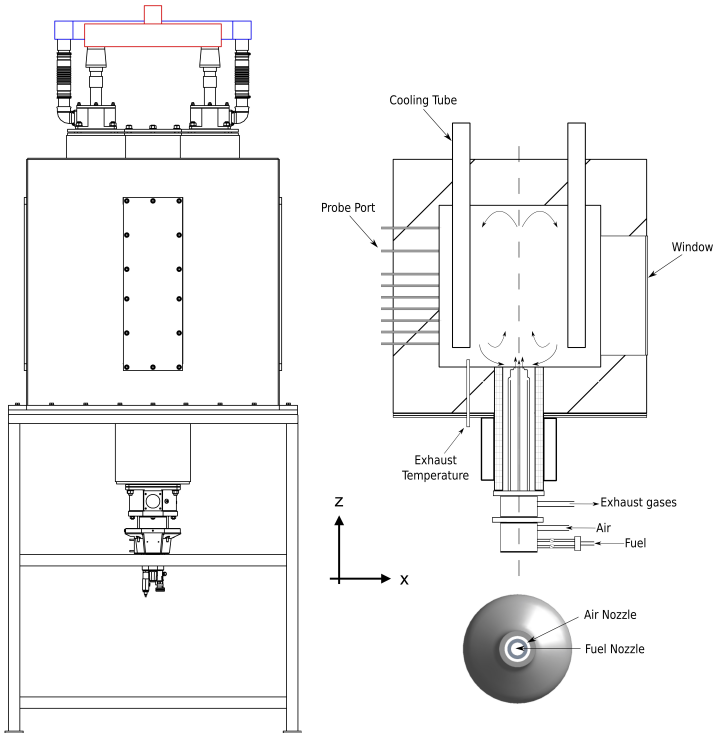

Figure 6.1: *Schematic of the furnace (left), vertical cross section (top right) and burner nozzle (bottom right). Courtesy of Marco Ferrarotti.*

state conditions, after a warming period of about 3 h, during which the same burner was used in normal flame conditions, acting on the fluid dynamic of the injection. In the following, "NxHy" term represents the fuel mixture of x $\%$vol. of NH_3 and y $\%$vol. of H_2. Figure 6.2 shows the intense yellow color typical of ammonia combustion for different NH_3-H_2 blends, for the case ID25 and ϕ = 1. Figures 6.3 and 6.4 compare averaged experimental temperature profiles extracted at different axial locations and OH* imaging for the N50H50 mixture, varying the air ID and the equivalence ratio (ER). Using ID16 and ϕ = 0.8, the reaction region is located in the region 110-160 mm from the nozzle, with a maximum temperature of around 1750 K, at z = 150 mm. The OH* contour also appears more spread and less intense compared to the other cases. Indeed, ID16 ensures a very high injection velocity ($\approx$ 185 m/s), leading to a high strain rate value close to the burner exit. When the latter is reduced, at a certain axial distance, ignition occurs, leading to a noticeable lift-off. Keeping the

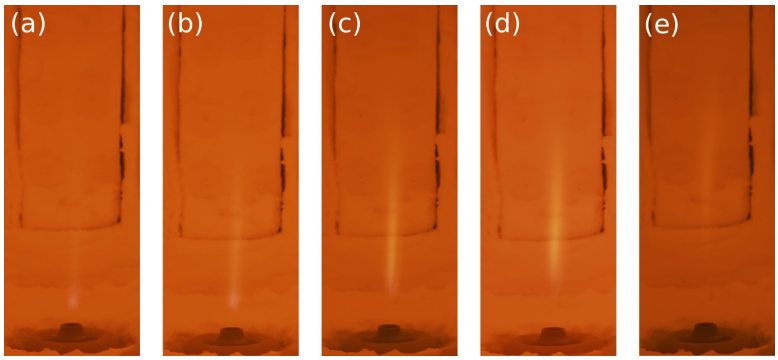

Figure 6.2: *Photographs of NH_3-H_2 combustion for (a) N10H90, (b) N20H80, (c) N40H60, (d) N50H50 and (e) N60H40. ID25, ϕ = 1. Canon EOS 80D 1/70 s exposure time. Courtesy of Marco Ferrarotti.*

same injector, but reducing the air excess (ϕ = 1), thinner reaction layer shifted towards the burner exit is observed. However, for this case, as well as for ID25, the actual maximum temperature is likely to be located below the first available measurement port (z = 100 mm). When the ID25 is employed, the OH* region is shifted even more upstream (between 50-80 mm) and the temperatures profiles are smoother for the investigated region.

Figure 6.5(left) shows the normalized NO and ammonia-slip emissions, varying the ammonia molar fraction and the ER for ID25. Differently from nitrogen-free fuels (i.e. methane and hydrogen), when a fuel blend containing ammonia is used, different pathways are involved. With a small amount of NH_3 (10$\%$ in volume), NO emissions grow considerably (from 159 to 827 ppm for ϕ = 0.8) reaching a peak at between 50$\%$ and 60$\%$ NH_3 of 3500 ppm.

Moreover, results suggest that the stoichiometry has a major impact on NO formation, confirming literature outcomes from [166] and [169]. As expected, the minimum NO emission levels were obtained close to stoichiometric conditions. Under these conditions, NO is less sensitive to the reaction $O+NH_2=H+HNO$ (R31 in Table 6.1) due to a lower availability of the radical O. HNO is then converted to NO via the reaction $HNO+H \rightarrow NO+H_2$ (more details in next Section). Furthermore, going towards ϕ = 1, the peak is shifted progressively towards lower ammonia molar fraction up to 10 $\%NH_3$ for ϕ = 1 (137 ppm). Very low NO emissions (single digit) can be achieved for this last condition (ϕ = 1), for a percentage of ammonia above 50$\%$. The stabilization of

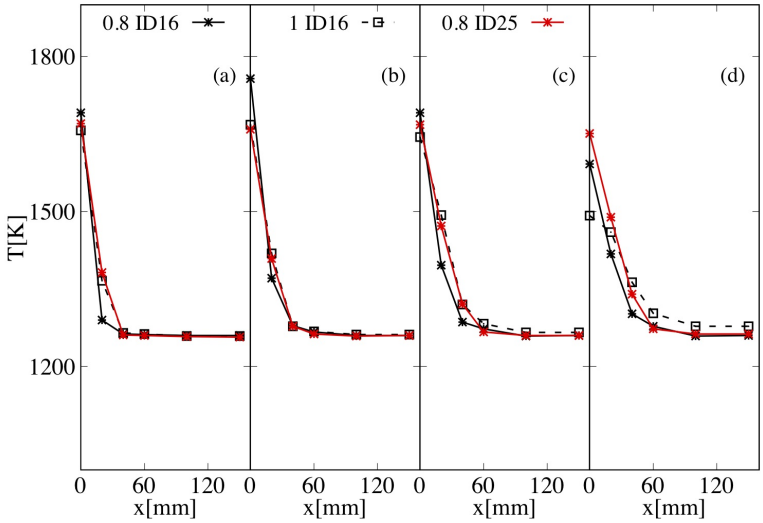

Figure 6.3: *Averaged temperature measured at (a) z=100 mm, (b) z=150 mm, (c) z=200 mm and (d) z=400 mm for N50H50, varying the air ID and ϕ. Averaged experimental uncertainty of 10 K. Courtesy of Marco Ferrarotti.*

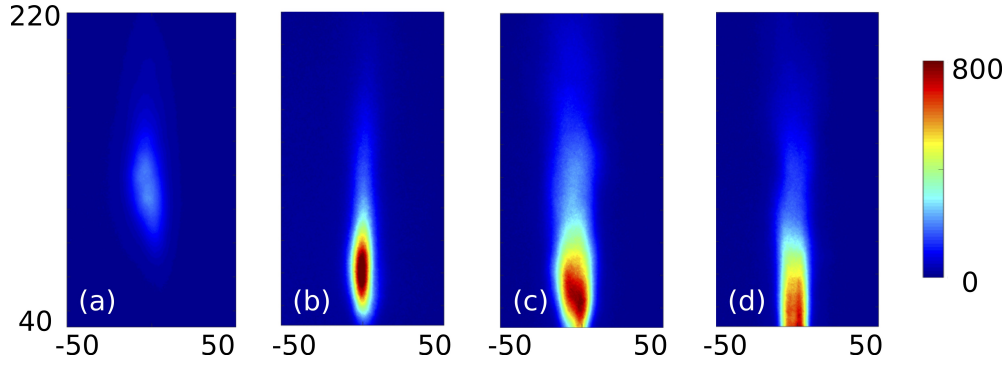

Figure 6.4: *Averaged OH* distribution for ID16 ϕ=0.8 (a) and ϕ=1 (b) and for ID25 ϕ=0.8 (c) and ϕ=1 (d). Units in mm and counts. N50H50. Courtesy of Marco Ferrarotti.*

pure ammonia combustion was not achieved, since extinction occurred above 80% NH_3, for all the investigated conditions. In literature, there are example of pure ammonia burning in MILD regime, for instance [169] managed to use pure ammonia in a cyclonic burner, under specific conditions. Finally, reaching conditions close to stoichiometry, unburned ammonia might be found in the exhaust gases (NH_3-slip). At ϕ = 1 (Figure 6.5(right)), NH_3-slip rapidly increases

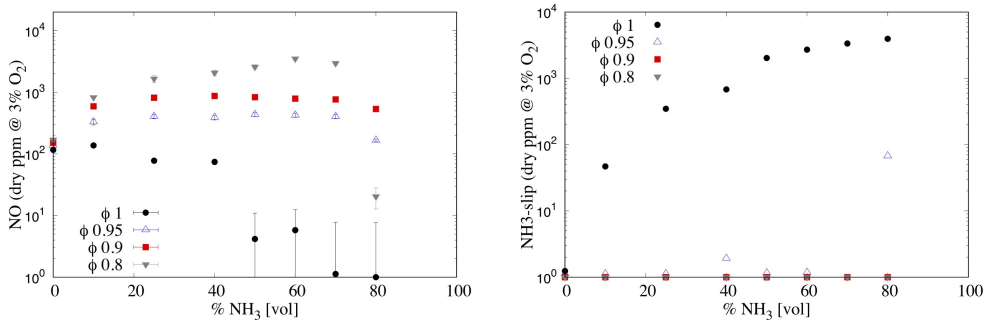

Figure 6.5: *(Left) NO and (Right) NH3-slip emissions varying the NH_3 percentage in the fuel (vol.) and the equivalence ratio ϕ for ID 25 mm. NH3-slip averaged relative uncertainty of 8%. Courtesy of Marco Ferrarotti.*

reaching values about $\approx$ 3000 ppm, while it is almost zero for lean conditions. An optimal window can be found between ϕ = 0.95 and ϕ = 1.00 with a strong reduction in NO emission (maximum value 400 ppm) as well as low NH_3-slip. However, It must be pointed out that it is easier to clean the exhaust gases removing ammonia (i.e. by condensation, adsorption) than adopting techniques to abate NO (i.e. DeNOx). The effect of the air injector ID is shown in Figures 6.6 for both NO (left) and NH3-slip (right) emissions. A higher air inlet velocity tends to increase NOx emissions as well. This might be explained considering the following: a higher recirculation ratio k_v decrease NO since it increases the level of dilution, however a reduced residence time (ID16) might not guarantee a sufficient time to convert NO into N_2.

6.3 CFD model

Reynolds-averaged Navier-Stokes (RANS) simulations were carried out with Fluent 19.3 by Ansys, Inc. Turbulence chemistry interactions were handled with the PaSR combustion model ([53, 54]). In the latter model, the chemical time scale is retrieved from the species formation rate, while a static formulation for the mixing time scale is computed as follows:

$$\tau_{mix} = C_{mix} \frac{k}{\epsilon} \tag{6.1}$$

The constant C_{mix} was set equal to 0.5 as suggested by [53, 54]. Standard k-ϵ

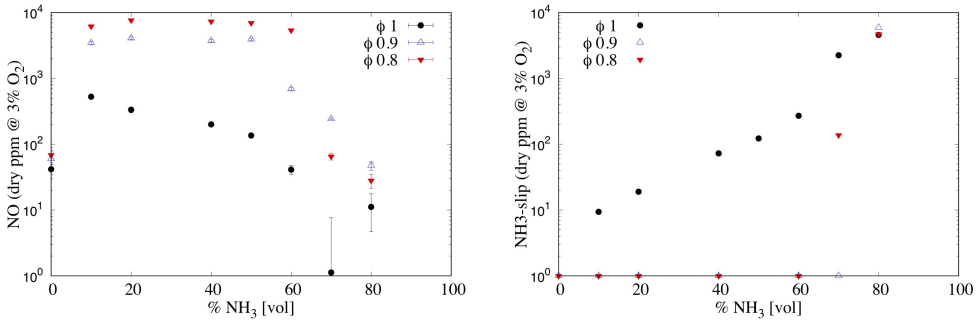

Figure 6.6: *(Left) NO and (Right) NH3-slip emissions varying the NH_3 percentage in the fuel (vol.) and the equivalence ratio ϕ for ID 16 mm. NH3-slip averaged relative uncertainty of 8%. Courtesy of Marco Ferrarotti.*

was used to model turbulence, while two kinetic schemes were used for the H_2/NH_3 chemistry, namely [170], composed by 31 species and 203 reactions, and [67], also containing an ammonia sub-mechanism consisting of 31 species and 211 reactions. Radiation was modeled using a discrete ordinate (DO) approach, combined with the weighted-sum-of-gray-gases (WSGG) model. The computational domain considers an angular sector of 45^o due to the symmetry of the problem. Indeed, the presence of the window was not considered in the present study, and the related heat loss was added to the cooling loss. A verification study to ensure grid independence was carried out, following directions from previous studies of the same system ([53]). The resulting 3D grid consists of 216k cells. Air and fuel flow rates were set according to the operating conditions of the experiments. The fuel blends were assumed to be fed into the furnace at 343 K, while the inlet air temperature was estimated by solving an energy balance across the heat exchanger. In order to model the cooling surfaces a constant negative heat flux condition was imposed, which also incorporates the energy loss by radiation through the window. The recirculation degree k_v was also estimated, considering the following equation:

$$k_v = \frac{\dot{m}_{rec}}{\dot{m}_a + \dot{m}_f} = \frac{\dot{m}_{mix} - (\dot{m}_a + \dot{m}_f)}{\dot{m}_a + \dot{m}_f}, \tag{6.2}$$

where $\dot{m}_{mix}$ represents the flow rate of the reactants mixed with exhaust gases (Figure 6.7).

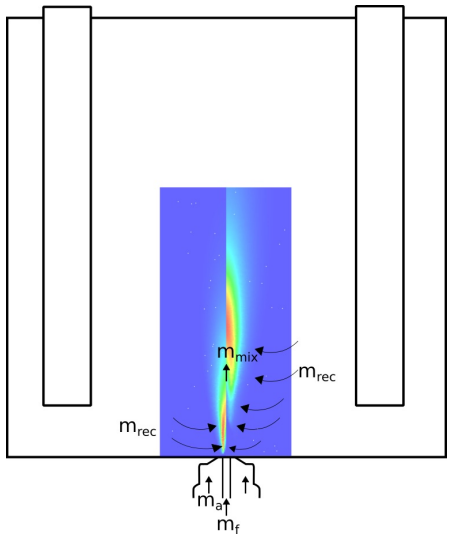

Figure 6.7: *Schematic representation of the internal recirculation pattern used to calculate $\dot{m}_{mix}$. N10H90 (left) and N50H50 (right).*

The latter can be calculated considering the above-mentioned reactive zone, identified using OH as marker. Within this region, three planes were defined at different axial locations. The flow rate passing through a clip of positive velocity (i.e. towards the top wall) was then calculated along these planes. $\dot{m}_{mix}$ was defined as the average between the resulting three values. A first validation for temperature profiles is presented for case N50H50 ID16 ϕ = 1. Here, a value of 0.5 was employed for C_{mix} in the PaSR model, together with standard k-ϵ for turbulence. Figure 6.8 shows the comparison between measured and predicted temperature profiles along the axis (a) and at different axial positions (b, c, d). The results from two different kinetic mechanisms, developed for ammonia combustion, i.e. [170] and [67] are also reported.

Looking at Figure 6.4, the reaction region (maximum of OH* counts) is located between 110 and 160 mm from the burner exit. However, the two models predict a late ignition compared to experimental data, as they under-predict the temperature peak at 100 mm away from the inlet. The above-mentioned under-prediction corresponds to a 2% and 1% relative error for [170] and [67] models, respectively.

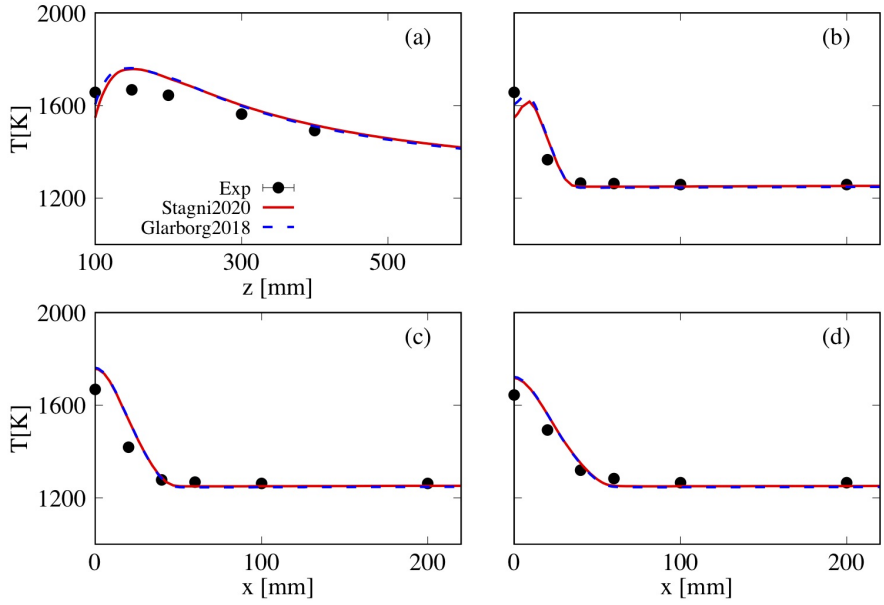

Figure 6.8: *Sensitivity of temperature predictions to different kinetic schemes, [170] and [67]. (a) Axial, (b) z=100 mm, (c) z=150 mm and (d) z=200 mm. C_{mix}=0.5, std k-ϵ. Averaged experimental uncertainty of 10 K. N50H50, ϕ=1, ID16.*

6.4 Well stirred reactor with EGR

As recommended by Medwell et al. [110], an adiabatic, non-isothermal well-stirred reactor, with recirculation, was adopted to model the chemistry of a highly diluted and preheated reactive mixture (i.e. MILD-like conditions). Indeed, as flameless combustion is characterized by a slower chemistry, ignition is likely to take place in flame kernels with premixed fuel and oxidizer, and relatively low strain rate, i.e. distant from the inlet. In this work, the use of WSR with recirculation is intended to map pollutants emissions (i.e. NOx) in different operating conditions, and to qualitatively reproduce experimental trends (not absolute values), and to be used for uncertainty quantification. Figure 6.9(top) shows a schematic representation of the adopted network and its links with experiments and CFD simulations.

The mixing unit receives three streams in input, namely fuel, air and exhaust gases. The temperature of each stream is equal to that of experiments. It has to be pointed out that the temperature of exhaust gases was assumed to

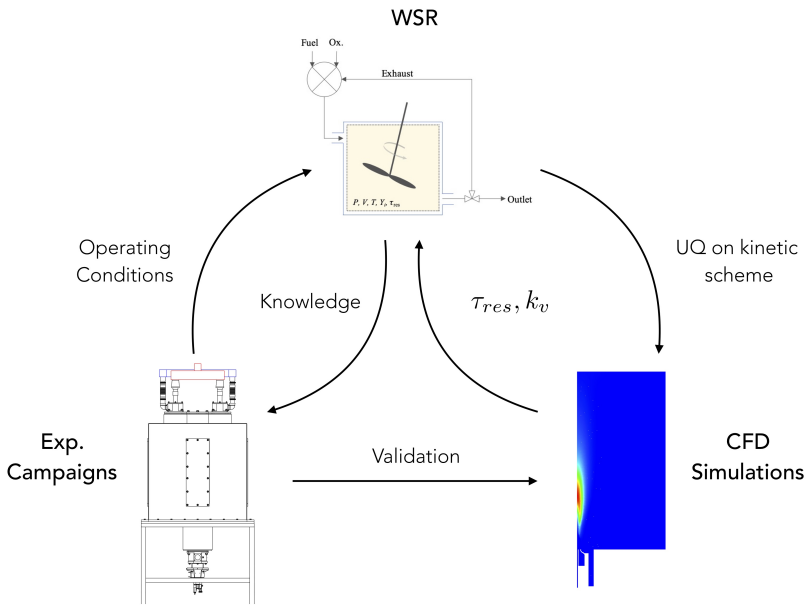

Figure 6.9: *Conceptual scheme about the interactions between experiments, CFD modeling and WSR model.*

be equal to that measured at the outlet (before the heat exchanger). This was done to avoid modelling of heat losses along the recirculation region, where the mixture may be assumed to be non-reactive ([212]). As proposed by [110], intermediate species were included in the exhaust gas recirculation (EGR), since they were found to take part in pre-ignition chemistry in MILD regime [160]. The complete list of recirculated species in the exhaust gas is: NH_3, H_2, O_2, N_2, H, O, H_2O, OH, HO_2, NO. The network consists of a MATLAB script involving the perfectly stirred reactor solver in OpenSMOKE++ [35]. The residence time τ_{res} and the recirculation degree, were estimated from CFD simulations (see Figure 6.9). For each operating conditions, the reactive region was identified using OH contour, and the residence time of the reactor was calculated as the average PaSR mixing time scale in this region (τ_{res}=τ_{mix}). The resulting mixture is then fed to the WSR solver. The first reactor in the network is solved by introducing air as oxidizer. Afterwards, the outlet composition is retrieved and

assumed to be equal to the EGR for the next simulation. This procedure is iteratively repeated untile convergence is achieved for both outlet temperature and NO concentration. The analysis was carried out using the recent mechanism from [170] in OpenSMOKE++ [35], which enables the user to perform sensitivity, and rate of production (ROP) analyses to identify influential reactions to be further investigated with uncertainty quantification (UQ). Figure 6.10 reports the most influential reactions for the mixtures N25H75 and N50H50, at different equivalence ratio, namely 0.8 and 1.0.

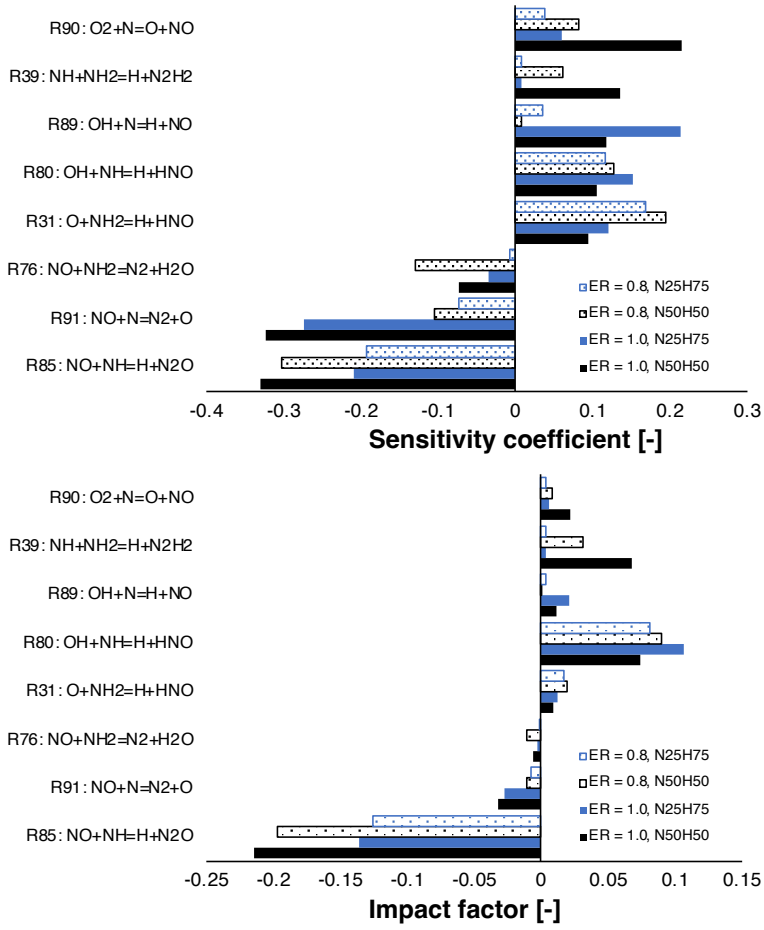

Figure 6.10: *NO normalized sensitivity coefficients and impact factors for NH_3/H_2 mixtures at different fuel compositions for ϕ=1. ID16.*

In particular, reactions involved in the hydrogen core mechanism were dis-

carded *a priori*. The sub-mechanism for thermal NOx, involving R89, R90 and R91, was found to be particularly sensitive, especially for stoichiometric mixtures. However, it was not considered for the uncertainty quantification, as the uncertainty in this mechanisms is very low (see [15] and Table 6.1). In fact, the impact factor for R80, R90 and R91 is significantly lower than other reactions' in Figure 6.10. Interestingly, R85 is the most impactful reaction with negative sensitivity coefficient. It is also important to point out that NO is very sensitive to R31, which forms HNO, for lean conditions, where more oxygen is available. Indeed, HNO is then converted to NO via HNO + H = NO +H_2. This may explain why lean conditions produce higher NO emissions. However, R31 as well as R76, were found to have high sensitivity coefficient for temperature and consequently ruled out from the UQ study. Regarding other reactions, R80 converts NH into HNO and impact positively the sensitivity, and R39 is only sensitive for higher ammonia content in the fuel than 25%. Indeed, this reaction affects more and more the formation of NO as NH_2, and NH production increase, due to higher availability of NH_3 as well as lower H and OH radicals concentrations. As a consequence, only R80, R85 and R39 were selected for the uncertainty quantification study. Table 6.1 reports the adopted uncertainty factors for reactions in Figure 6.10, based on literature information.

Table 6.1: *Details about identified sensitive reactions.*

Index	Reaction	f	Ref.
R31	$O+NH_2=HNO+H$	-	[172]
R39	$NH+NH_2=H+N_2H_2$	0.18	[41]
R76	$NO+NH_2=N_2+H_2O$	0.08	[167]
R80	$NH+OH=HNO+H$	0.7	[33]
R85	$NH+NO=H+N_2O$	0.65	[111]
R89	$OH+N=H+NO$	0.1	[15]
R90	$O_2+N=O+NO$	0.2	[15]
R91	$NO+N=N_2+O$	0.2	[15]

In addition, a flux analysis was performed for both N25H75 and N50H50 mixtures (see Figure 6.11), to explain the NO emissions trends.
Ammonia reactivity proceeds along $NH_2 \rightarrow NH \rightarrow N$, and NO is part of its oxidation. In fact, NH_2 mainly forms NH and HNO in R31, which gives NO. The NH

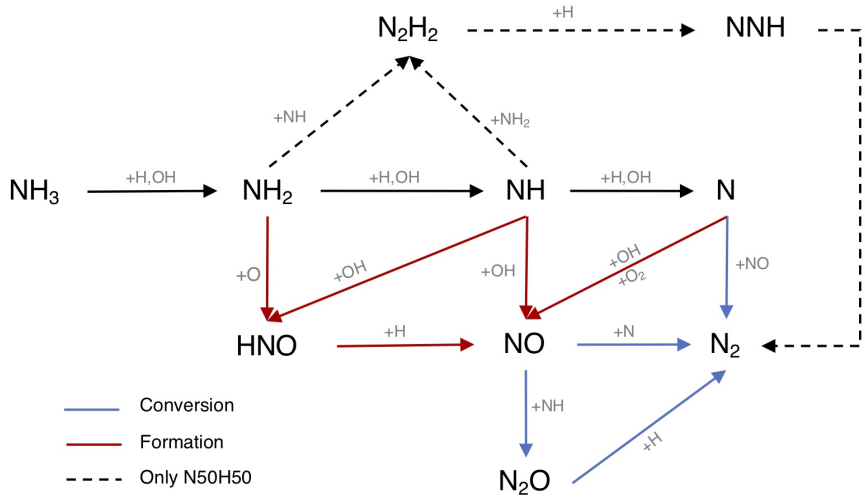

Figure 6.11: *ROP analysis for NH_3-H_2 mixtures. ID16.*

intermediate has a crucial role, as not only leads to NO through HNO in R80, but also reacts with it in R85 to form N_2O, which is almost completely converted to N_2 in the termination step H+N_2O=N_2+OH. In addition, NH is converted to N, which exhibits an analogous behaviour, i.e. it produces NO in R89 and R90, but also reacts with it in R91, again as a termination step. Up to N10H90, hydrogen concentration is so high that the radical pool is extremely rich in H and OH, prompting HNO production (R80) and its next conversion to NO, determining an emissions peak. The latter peak is even more pronounced at ϕ=0.8 because of the higher availability of local O radical, prompting the HNO production via R31. As the NH_3 percentage in the fuel increases (i.e. at N50H50), these pathways weaken, and R39 starts competing. The latter reaction, offers an alternative path to NH, namely $N_2H_2 \rightarrow NNH \rightarrow N_2$, which tends to reduce the NO formation by subtracting NH and NH_2 from the pool of reactants. So, R39 is part of the reason why richer fuel mixtures in NH_3 show decreased NO emissions. In fact, this reaction shows a positive impact of NO sensitivity in Figures 6.10 as it competes with $NH \rightarrow NO \rightarrow N_2O \rightarrow N_2$, which represents the preferential way for the system to reduce NO emissions. Finally, one possible explanation for the existence of a shifted peak at ϕ=0.8 (see Figure 6.5) is the higher oxygen content, which pushes the NO production through HNO in R31 for richer mixtures with respect to stoichiometric conditions, delaying the effect

of R39. As previously reported in Figure 6.12 the LHS study suggests that the maximum NO production in Figure 6.13 is located nearby the maximum of R85, minimum of R39 and R80. The opposite is true for the minimum NO formation in Figure 6.13, in agreement with the sensitivity and rop analysis. Finally, this analysis tell us that it would be better to operate the reactor with high internal recirculation ratio. Indeed, this would increase the NO concentration in the reacting mixture, which would react in R85, converting NH_3 intermediates to product directly. Thus reducing the overall emissions.

6.5 Uncertainty propagation

According to equation 2.3, the kinetic constant, for each reaction in a kinetic mechanism, can be addressed as a random variable with estimated uncertainty (i.e. with a factor of 10^f, see 2.17). Indeed, deviations from the nominal value of κ for the above-mentioned sensitive reactions (see section 6.4) might have a strong impact on the model output, NOx in this case. In order to evaluate the combined effect of those reactions, which were found to be influential for NOx formation, a Latin Hypercube Sampling (LHS) ([55,81]) was used. The uniform distributions of the pre-exponential factors of aforementioned reactions independently were sampled independently and new kinetic mechanisms are obtained, and corresponding model responses can be computed. Through this forward propagation, NOx emissions in each operating condition can be represented as a region, rather than a curve. Performing LHS study using RANS simulations would have been prohibitive from a computational point of view. For this reason, the WSR network was used instead. By analyzing the system responses to input variations, Arrhenius parameters combinations corresponding to both maximum and minimum of the NO formation distribution could be identified. Figure 6.12 shows the 500 samples, which were withdrawn from the three-dimensional space associated with the uncertainty ranges of pre-exponential factors in reactions R39, R85 and R80 in table 6.1. The deviation of the WSR model responses from the nominal mechanism is reported in terms of color: white points are characterized by null deviation, while black indicates maximum deviation. The two parameters combinations corresponding to the maximum negative (i.e. min NOx), and positive (i.e. max NOx) deviations are also reported.

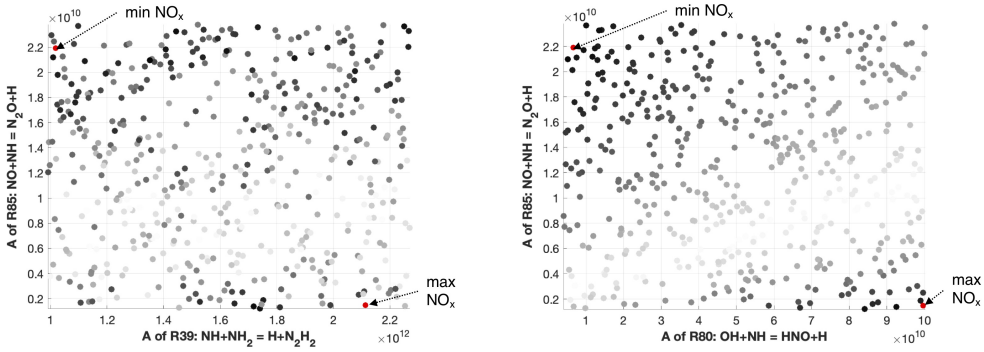

Figure 6.12: *Latin Hypercube Sampling samples for reactions R80, R85 and R39. Here, the grey scale represents in black the points with maximum NO deviation from the nominal mechanism, in white the points with minimum NO deviation.*

The WSR analysis is not intended to quantitatively predict the experimental data shown in Figures 6.5-6.6, but to provide qualitative information about NO formation in hydrogen-ammonia mixtures. Figure 6.13 shows the NO estimations computed with the WSR network, varying the ammonia molar fraction in the fuel, for the two different ER (i.e., ϕ = 0.8,1). These estimations are referred to as mean values. Their variability due to separate influence of the uncertainties in k_v, τ_{res} and kinetics, is also displayed. As the adopted k_v and τ_{res} values, for each fuel composition, are average quantities extracted from the reactive zone in RANS simulations (see section 6.4), a sensitivity analysis was performed by multiplying and dividing them by a factor of 2. The model responses are reported in Figure 6.13, where a higher sensitivity to the recirculation degree than to residence time is observed. Yet, uncertainties in the kinetic model yields a much greater impact on the NO variance, which is also reported in Figure 6.13. The displayed uncertainty bands come from the previously described LHS performed on the pre-exponential factors of reactions R39, R80, and R85.

Remarkably, the simplified reactor network is capable of qualitatively capturing the NOx dependence on the equivalence ratio, as observed experimentally (see figures 6.6 6.5). In fact, the following conclusions can be withdrawn by looking at the mean model predictions:

- at ϕ=1 (see Figure 6.13) (left), for the ID16 burner, a peak is observed

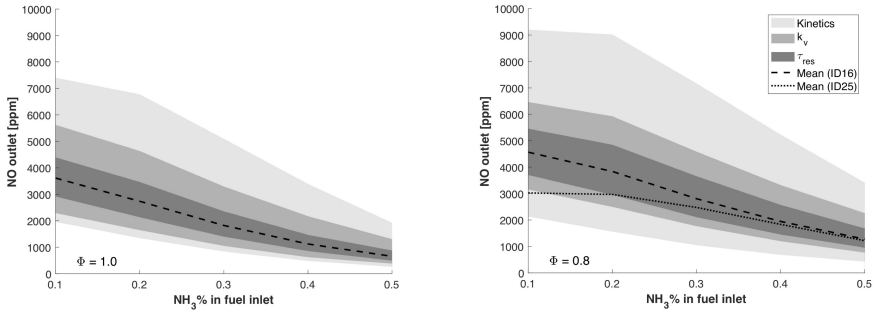

Figure 6.13: *Effect of the recirculation degree (k_v), the residence time, and kinetics uncertainties on the pollutant emission estimates from the WSR network, for equivalence ratio of 1.0 (left) and 0.8 (right) at different fuel composition.*

in correspondence of the N10H90 mixture, then emissions diminish as ammonia concentration in the fuel raises;

- at ϕ=0.8 (see Figure 6.13) (right), NO emissions increase with respect to stoichiometric conditions;

- at ϕ=0.8, a lower NO production can be achieved using a larger air injector (ID25). This is in line with what was found experimentally (see Figure 6.5). The lower inlet velocity, due to ID25 configuration, reduces the entrainment of exhaust gas (k_v), and increases residence time in the reactive zone (τ_{res}). Globally, this results in reduced emissions.

In the following, the characterized uncertainties in detailed kinetic mechanisms on NO predictions with more complex numerical models, i.e. RANS simulations with PaSR sub-model for turbulence/chemistry interaction. To do so, the two mechanisms were found to give maximum and minimum NO output values from the previously described LHS study were tested (Figure 6.12). Even though, both mechanisms [67, 170] performed well on temperature profiles, strong differences were detected for pollutant emissions estimates. Regarding NOx, a pronounced overestimation was observed using both models (see Figure 6.14). In particular, for ϕ = 1 (Figure 6.14 left), [67] predicts much higher values, i.e. 13580 and 5300 ppm at N25H75 and N50H50, respectively, versus 9473 and 2851 ppm for the mechanism from [170]. Anyway, even using the latter model, predictions are still far from the experimental data (460 ppm and

160 ppm for N25H75 and N50H50, respectively). Among the possible reasons for such discrepancies, it is worth mentioning that for such conditions a wider set of reaction might play non-negligible role in affecting model uncertainty and that considering turbulence model uncertainty might increase the local recirculation ratio, this should yield higher NO concentration before combustion and lead to enhanced re-burning and lower overall emissions.

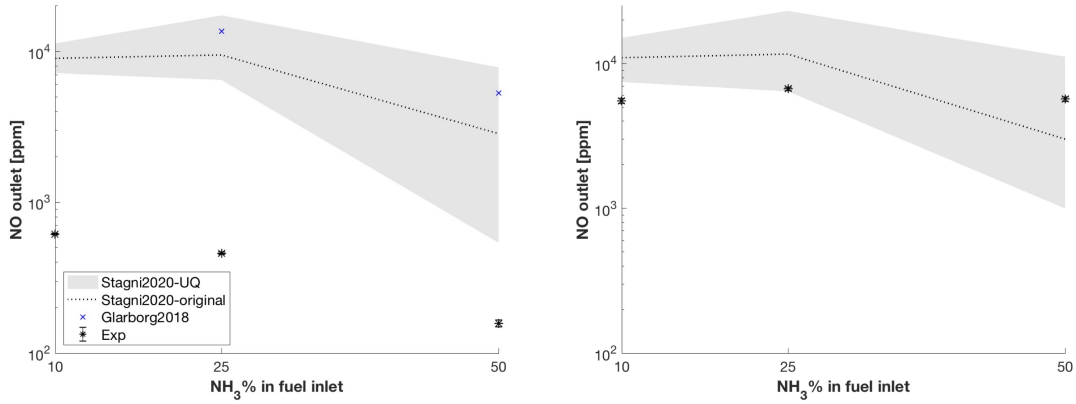

Figure 6.14: *Dry NO pollutant emissions predicted using different kinetic schemes. The gray area represents the uncertainty propagation of the LHS study for Stagni2020. ID16, ϕ = 1 (left) and ϕ = 0.8 (right). Relative experimental uncertainty 2%.*

For ϕ = 0.8 (Figure 6.14 right), a better agreement with experimental data is observed, even though the model under-predicts the NO emissions for N50H50. In order to verify the major role of an accurate kinetic sub-model in this chemistry-controlled regime (flameless), results from the previously performed LHS study on the WSR network were tested in CFD simulations. Again, this means performing additional simulations using the set of kinetic parameters corresponding to the maximum and minimum NO emissions on the LHS chart (Figure 6.12). Figure 6.14 also shows the uncertainty propagation associated with R39-80-85 on the NO emissions. At ϕ = 1, the lower band moves towards the experimental values, allowing a massive reduction compared to the original model from [170]. This is true especially for N50H50, where NO emissions decrease from 2851 ppm to 539 ppm. On the contrary, temperature profiles in the furnace (not shown here) remain almost constant, meaning that the effect of the kinetic of the three reactions is relevant only for NO. Much better results

were achieved at ϕ = 0.8, where the uncertainty bounds almost intersects the experimental data region for N10H90 and contains it for N25H75 and N50H50.

6.6 Concluding remarks

An experimental campaign was performed to investigate options for optimal operating conditions for the ULB flameless furnace fired with ammonia/hydrogen blends. In particular, the campaign aimed at identifying trade-off between NOx emissions and ammonia slip. Ammonia slip emissions are negligible in lean conditions, while they become relevant close to ϕ = 1. The optimal working point was identified for all fuel mixtures at ϕ = 0.95, which allows to reduce NO emissions with respect to leaner conditions, while keeping low NH_3-slip (below 10 ppm). In RANS simulations, the agreement between temperature measurements and estimations was found to be satisfactory (see Figure 6.8), and nearly insensitive to the adopted kinetics, i.e. [170] and [67]. However, in terms of NOx emissions, substantial differences between mechanisms predictions and experimental data were observed (see Figure 6.14(left)). This discrepancy can be partially attributed to the kinetic model uncertainties. A well-stirred reactor network (WSR) was designed, and fed with boundary conditions derived from experiments and CFD simulations (e.g. residence time (τ_{res}), and recirculation degree (k_v)). Sensitivity and rate of production analyses could be performed to identify influential reaction for NO, i.e. R39-80-85 in Table 6.1. A latin hypercube sampling (LHS) method was adopted to propagate the uncertainty of the above-mentioned reactions to NO production/emissions. Two kinetic mechanisms were then created from [170], representing the maximum and the minimum of the NO distribution, reported for both the WSR and for CFD simulations, in Figures 6.13 and 6.14, respectively. In conclusion, a significant part of the discrepancy between the pollutant emissions from simulations and experimental observations is associated to inherent uncertainties in recent kinetic mechanisms for ammonia/hydrogen combustion. In the future, a better characterization of specific reactions (i.e. R39-80-85 and others in Table 6.1), might reduce the uncertainty of CFD simulations for the prediction of pollutants emissions. This is particularly true for stoichiometric conditions, where the discrepancies between numerical models predictions and experiments was found to be most significant. Future experimental campaign will focus on reducing

the emissions of pollutants, namely NH_3 and NOx. Another option, which was not considered in this work, is to fire the furnace in fuel rich conditions in combination with ammonia slip capture at the furnace outlet. The latter approach would reduce the combustion efficiency though.

CHAPTER 7

Conclusions and future perspectives

In this final chapter, an overview of the accomplishments and contributions of this PhD project is presented.

7.1 Brief summary of the achievements of this thesis

In the present thesis, a novel **data-driven approach for the optimisation of detailed kinetic mechanisms** was proposed. This methodology is based on **heuristic optimization algorithms**, such as the Evolutionary Algorithm (EA). The **curve matching index** was proposed as alternative loss function to classical norms. In CM calculation the similarities between models responses and experimental data is measured quantitatively and qualitatively, considering also the first derivatives and shapes of corresponding splines. A novel **protocol for the optimization of PLOG** reactions was established. The interdependencies between Arrhenius expressions at different pressures were accounted for by handling three random variables for each PLOG, regardless of the number of discrete pressures specified in the mechanism. To the authors knowledge, PLOG reactions were consistently optimized for the first time within their entire temperature and pressure domain. The **Cumulative Sensitivity Function** (CSF) and a **Cumulative Impact Function** (CIF) were introduced to make reaction selection automatic, fast, and efficient pushing the use information local sensitivity analysis to its maximum extent. An **optimized mechanism for ammonia** combustion was obtained over a wide range of operating conditions. In this process, 41 reactions were involved and 24 were finally selected as the most impactful by introducing a for each test case in the database. As a result, the approach involved all 101 kinetic parameters simultaneously. For rates determined using first principles calculations, **guidelines** were established to estimate uncertainty ranges based on the level of theory adopted throughout the calculation protocols for electronic structures, potential energy surfaces and phenomenological reaction rate constants. Finally, the comparison between nominal and optimized mechanisms highlighted crucial reaction pathways, needing further characterization. The development above-mentioned methodology represents the underlying functioning of **OptiSMOKE++**, a new C++ toolbox for the optimization of detailed kinetic mechanisms. OptiSMOKE++ is an flexible interface for the communications between other open source softwares like OpenSMOKE++, DAKOTA, Curve Matching and SciExpeM. This framework enables the simultaneous use of experimental targets from different facilities, i.e. Batch Reactors, PFRs, PSRs, ST, RCMs and 1D flames. In order to produce a feasible optimized kinetic mechanism

(i.e. with physically viable kinetic parameters), OptiSMOKE++ utilizes a penalty function which forcefully increases the objective function value when a set of kinetic parameters gives a rate coefficient outside the uncertainty bounds. This ensures that the optimizer chooses an optimal point which still gives physically viable rate coefficient values, as well as it allows for computational savings as penalized parameter combinations are not evaluated using OpenSMOKE++. The **role of diluents like H_2O and CO_2 in operating conditions relevant to applications for MILD** combustion of **hydrogen and syngas** was discussed and analysed by means of a virtual species analysis (VSA), Global Sensitivity Analysis (GSA), and Optimization. The VSA suggests that measurements of ignition delay time (IDT) and species concentrations in perfectly stirred reactors (PSR) in diluted conditions are ideal candidates for the estimation of collision efficiencies as their physics is significantly **third body driven**. The **GSA, based on Polynomial Chaos Expansion** (PCE), performed on ignition delay time (IDT) showed that, in diluted conditions, a single third body efficiency can be more impactful than an entire subset of sensitive reactions. The use of heuristic optimization algorithms enables parameters estimation and estimation of the **confidence regions** regardless the dimensionality of the problem at hand. This approach proposed here surpasses existing ones for two reasons: (i) a combination of experimental measurements from different sources and reactors can be employed. (ii) the uncertainties of all sensitive reactions are considered to weaken the dependence from starting model. Eventually, the errors introduced by the replacement of the TROE formulation for fall-off reactions with PLOG were quantified for hydrogen combustion, and a **method to extract information from data about third body efficiency of strong colliders in PLOG** formulation was proposed in case high-level ab-initio calculations are not available. An **experimental campaign** was performed to investigate options for optimal operating conditions for the ULB **flameless furnace fired with ammonia/hydrogen blends**. In particular, the campaign aimed at identifying trade-off between NOx emissions and ammonia slip. In RANS simulations, the agreement between temperature measurements and estimations was found to be satisfactory (see Figure 6.8), and nearly insensitive to the adopted kinetics, i.e. [170] and [67]. However, in terms of NOx emissions, substantial differences between mechanisms predictions and experimental data were observed (see Figure 6.14(left)). A well-stirred reactor network (WSR) was designed, and

fed with boundary conditions derived from experiments and CFD simulations (e.g. residence time (τ_{res}), and recirculation degree (k_v)). Sensitivity and rate of production analyses could be performed to identify influential reaction for NO, i.e. R39-80-85 in Table 6.1. A latin hypercube sampling (LHS) method was adopted to propagate the uncertainty of the above-mentioned reactions to **NO production/emissions** in the WSR and subsequently also in CFD simulations. Future experimental campaign will focus on reducing the emissions of pollutants, namely NH_3 and NOx. Another option, which was not considered in this work, is to fire the furnace in fuel rich conditions in combination with ammonia slip capture at the furnace outlet.

7.2 Open questions for future work

During the writing phase of this manuscript I realized my work opened a series of research questions, which I leave open for future work and have partly been investigated in literature:

- As the dimensionality of optimization problems involving kinetics is considerable: will it be possible to perform an on-the-fly dimensionality reduction through PCA for performance acceleration?
- Since the interest toward integration of first principle calculations in detailed kinetic mechanisms is growing in the community: would optimizations tools, such as OptiSMOKE++, MESMER, OPTIMA++ and others, find application to master equation parameters rather than empirical ones, for mechanism development on a larger scale? Good examples are already available in the work of [151], who used MESMER to calibrate Potential Energy Surfaces (PES) parameters to high-fidelity experimental data for a single PES, and the Burke [22], who advocates for the future realisation of multi-scale informatics protocol. However, it is worth mentioning that implementation of Master Equation solvers and the definition of uncertainty for PES parameters are highly non-trivial tasks, which would require dedicated resources and involve more people and expertises than those available in a single research group.
- As the cost of CFD simulations of reacting flows strongly increases with the mechanism size. Can OptiSMOKE++ be coupled with reduction tech-

niques to produce tailored mechanisms for specific applications? Since there is a trade off between kinetics costs and improved turbulence modelling, which might be the cause of significant discrepancy, this would carve out some computational power to investigate more expensive turbulence models and their uncertainties.

- Is it worth to investigate more complex and structured reactor networks, through Uncertainty Quantification, to gain insights about the role of kinetic uncertainties in CFD simulations?

In conclusion, I believe that optimization and uncertainty quantification might be used to boost kinetic mechanisms development on many different levels.

List of publications

Peer reviewed journal publications

[1] **A. Bertolino**, A. Stagni, A. Cuoci, T. Faravelli, A. Parente, A. Frassoldati, "Prediction of flammable range for pure fuels and mixtures using detailed kinetics", Combustion and Flame, 207:120-133, 2019.

[2] M. Ferrarotti, **A. Bertolino**, R. Amaduzzi, A. Parente, "On the Influence of Kinetic uncertainties on the accuracy of numerical modeling of an industrial flameless furnace fired with NH_3/H_2 blends: a numerical and experimental study", Frontiers in Energy Research, 8:597655, 2020

[3] **A. Bertolino**, M. Fürst, A. Stagni, A. Frassoldati, M. Pelucchi, C.A. Cavallotti, T. Faravelli, A. Parente, "An evolutionary, data-driven approach for mechanism optimization: theory and application to ammonia combustion", Combustion and Flame, 229:111366, 2021.

[4] M. Fürst, **A. Bertolino**, A. Cuoci, T. Faravelli, A. Parente, "OptiSMOKE++: A toolbox for optimization of chemical kinetic mechanisms", Computer Physics Communications, 264:107940, 2021.

[5] L. Pratali Maffei, C. Cavallotti, M. Pelucchi, **A. Bertolino**, T. Faravelli, "Master equation lumping for multi-well potential energy surfaces: A bridge between ab initio based rate constant calculations and large kinetic mechanisms",

Chemical Engineering Journal, 422:129954, 2021.

[6] K. Bioche, L. Bricteux , C. Cavallotti, **A. Bertolino**, A. Parente, J. Blondeau, "Large Eddy Simulation of rich ammonia/hydrogen/air combustion in a gas turbine burner", International Journal of Hydrogen Energy, *in press*, 2021.

Work in the progress for publication

[7] **A. Bertolino**, A. Frassoldati, A. Cuoci, A. Parente, "Estimation of third body efficiencies from experimental data: an application to hydrogen combustion", International Journal of Hydrogen Energy, *under review*, 2021.

[8] S. Iavarone, **A. Bertolino**, M. Cafiero, A. Parente, "Combined effect of experimental and kinetic uncertainties on NO predictions in low-pressure premixed laminar H_2/CH_4/CO-air and H_2/CH_4/CO/C_6H_6-air flames", Fuel, *under review*, 2022.

Conference papers

[1] **A Bertolino**, A. Frassoldati, A. Parente, "An optimized core mechanism for H_2/CO combustion in mild-like conditions", 42nd Meeting of the Italian Section of the Combustion Institute, September 2019.

[2] **A Bertolino**, A. Frassoldati, A. Parente, "Optimisation of chemical mechanisms for MILD conditions", Seventeenth International Conference of Numerical Combustion, April 2019

[3] **A Bertolino**, A. Frassoldati, A. Parente, "Numerical study of the three-folded effect of steam dilution on hydrogen ignition in a RCM with detailed kinetics", 25th journées D'étude - Belgian Section of the Combustion Institute, April 2018

List of Figures

List of Tables

Appendices

APPENDIX $\mathcal{A}$

Supplementary information for Chapter 3

In this section, the cumulative sensitivity function for different test cases

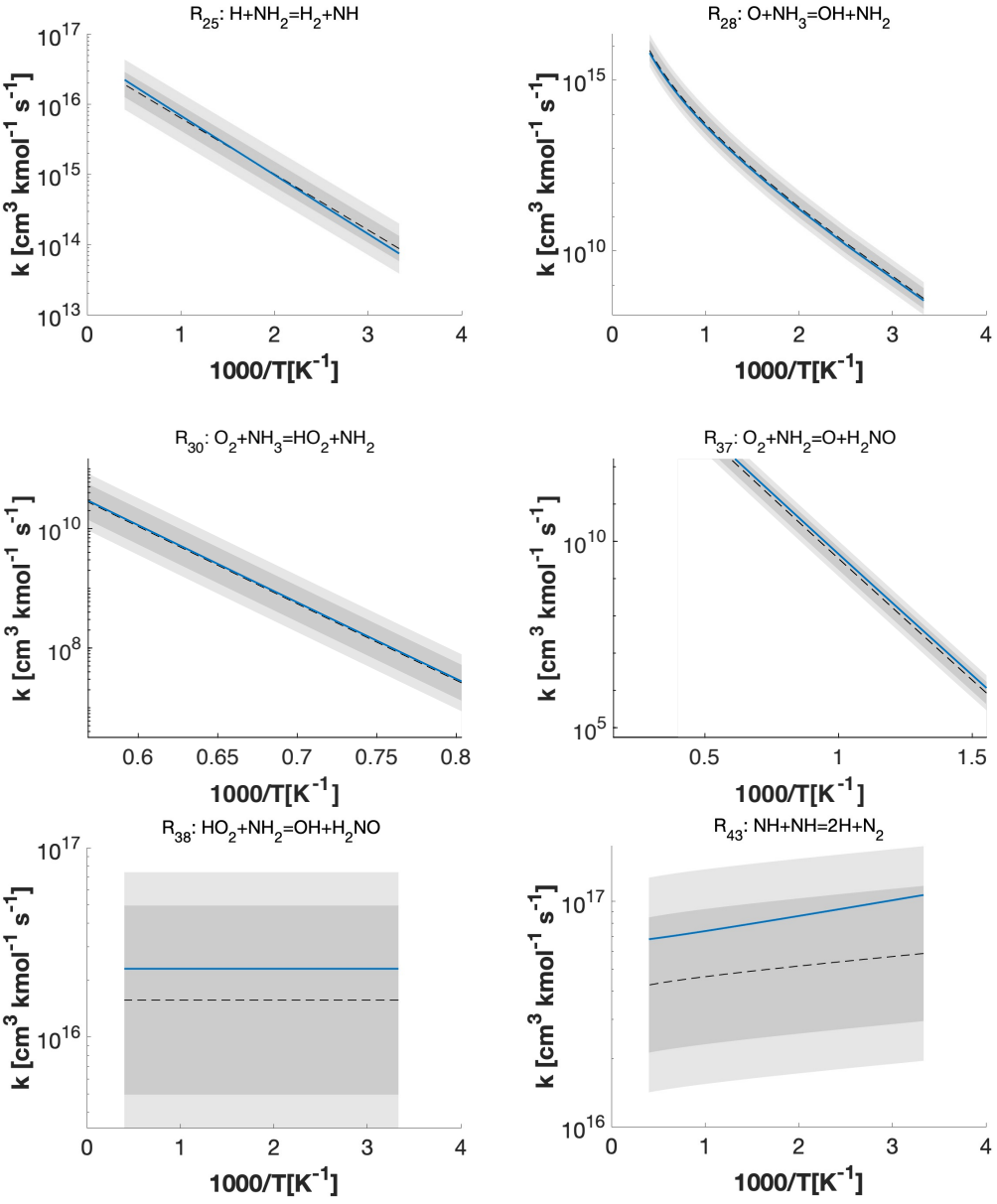

Figure A1: *Comparison between nominal and optimized mechanism (in blue, straight line) for considered reactions during optimization. Nominal values from Stagni [170]*

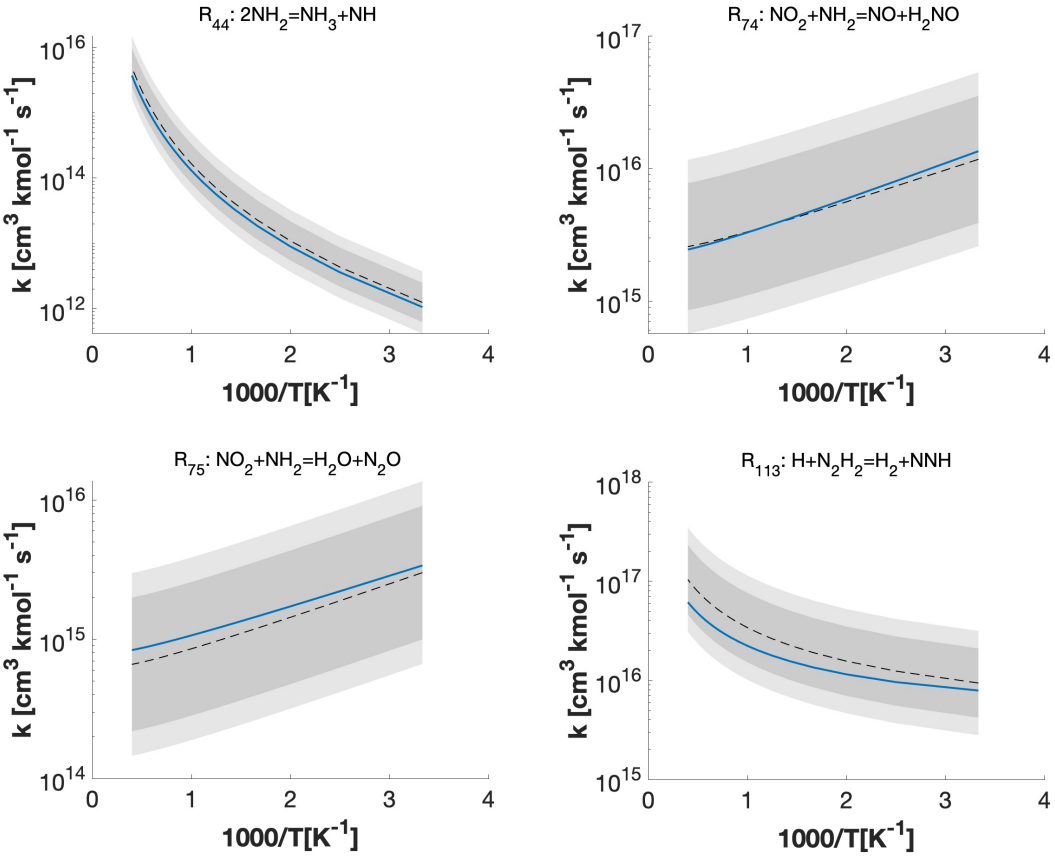

Figure A2: *Comparison between nominal and optimized mechanism (in blue, straight line) for considered reactions during optimization. Nominal values from Stagni [170]*

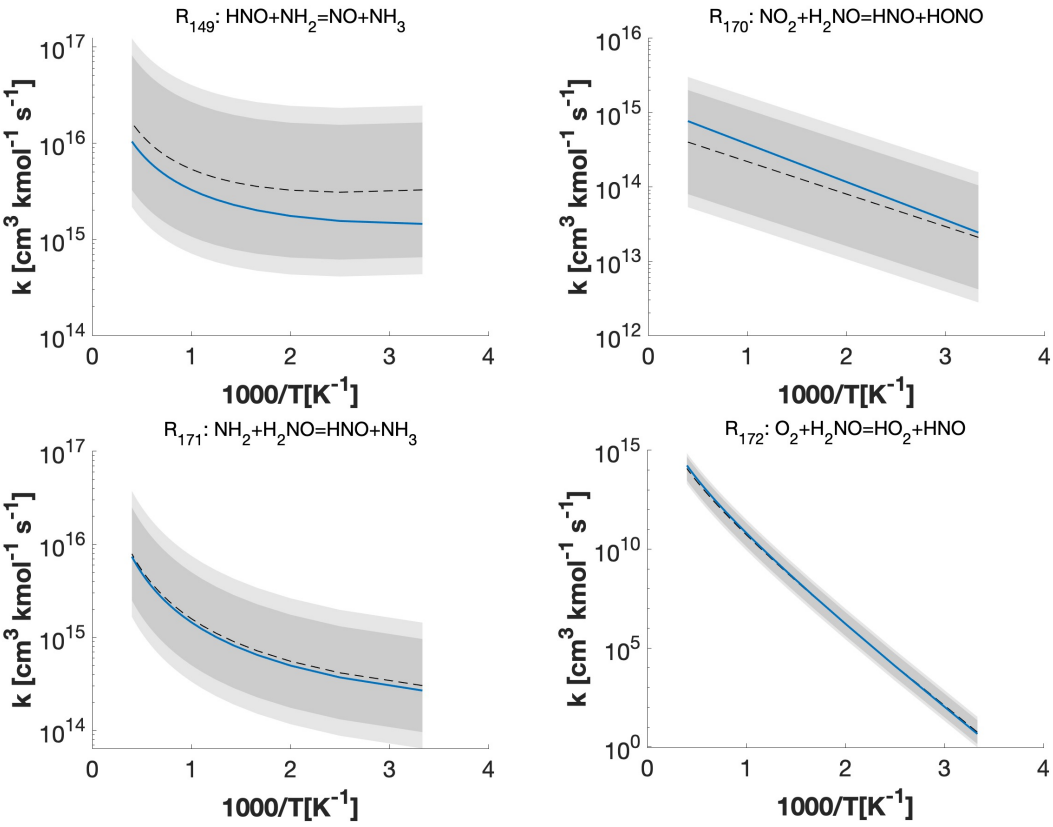

Figure A3: *Comparison between nominal and optimized mechanism (in blue, straight line) for considered reactions during optimization. Nominal values from [170]*

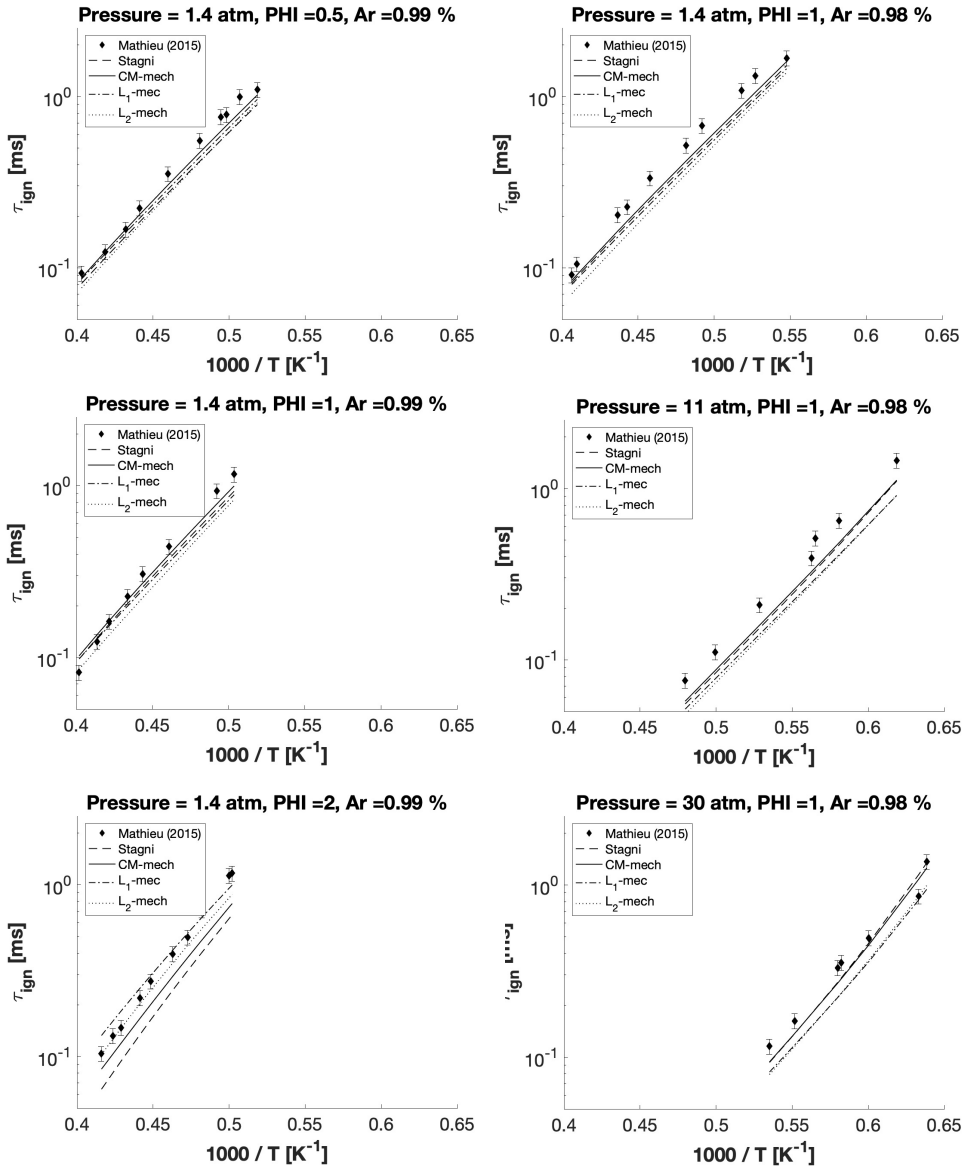

Figure A4: *Comparison between nominal and optimized mechanism. Experimental data from Mathieu and Petersen [107]*

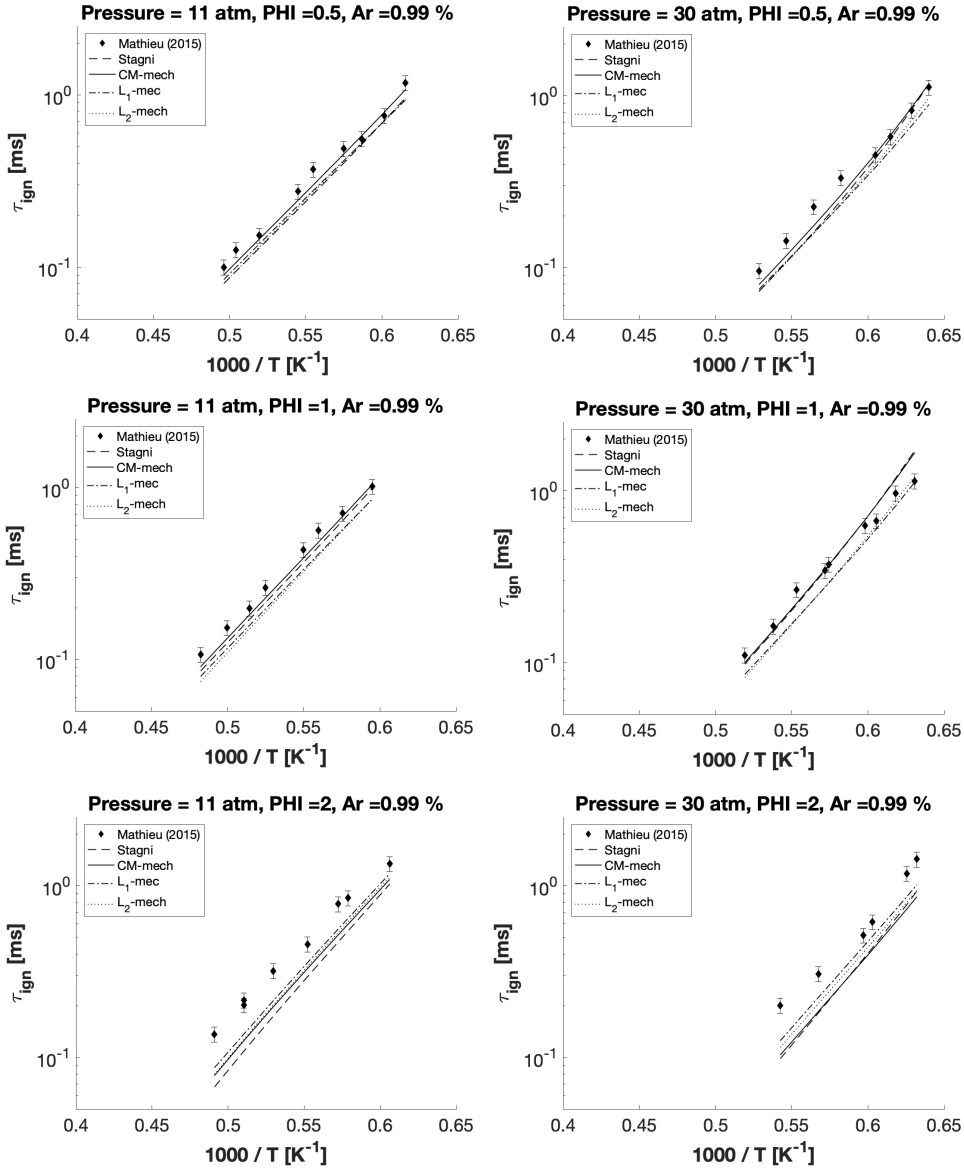

Figure A5: *Comparison between nominal and optimized mechanism. Experimental data from Mathieu and Petersen [107]*

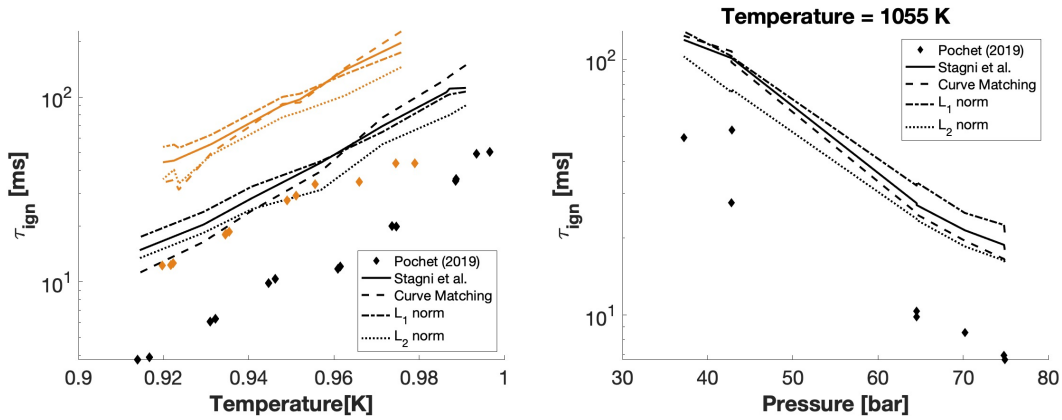

Figure A6: *Comparison between nominal and optimized mechanism. Experimental data from Pochet et al. [134]*

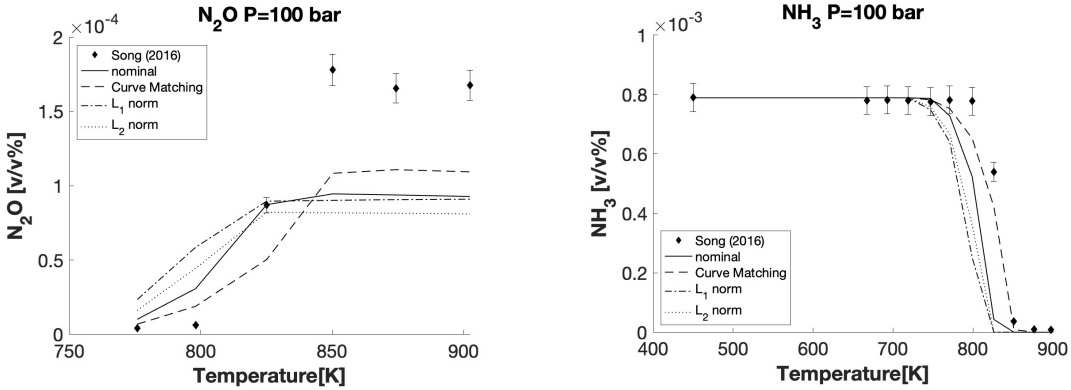

Figure A7: *Comparison between nominal and optimized mechanism. Experimental data from Song et al. [168]*

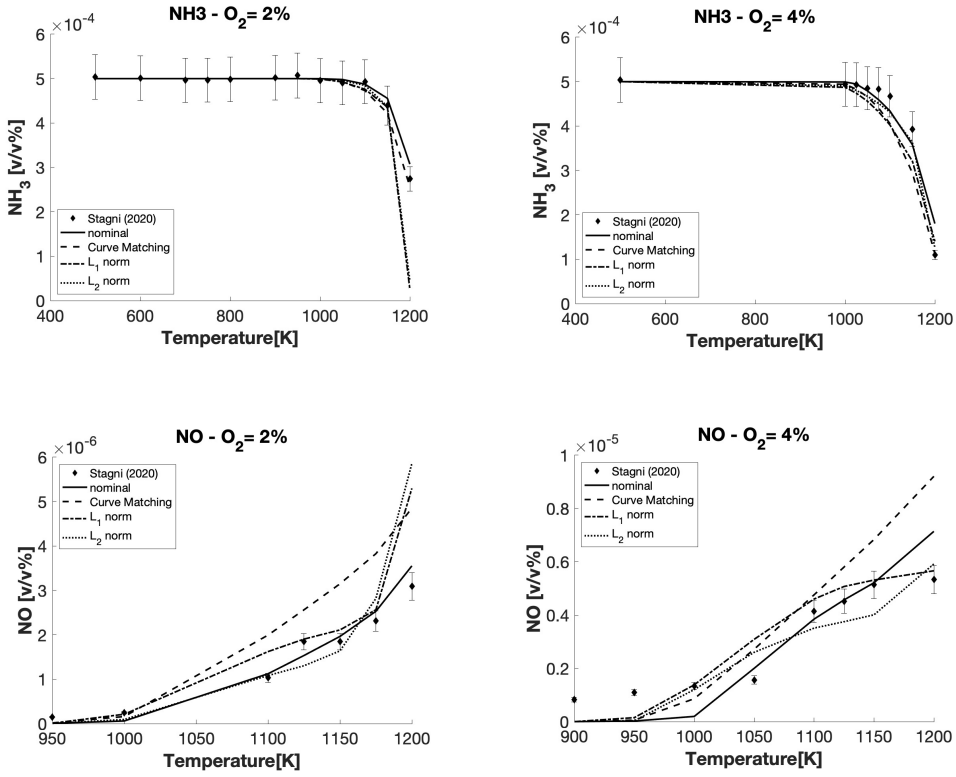

Figure A8: *Comparison between nominal and optimized mechanism. Experimental data from Stagni et al. [170]*

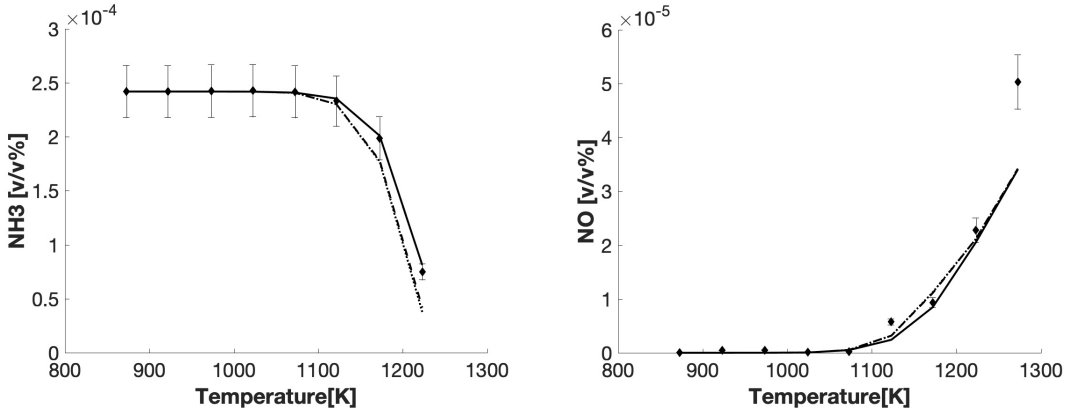

Figure A9: *Comparison between nominal and optimized mechanism. Experimental data from Wargadalam et al. [204]*

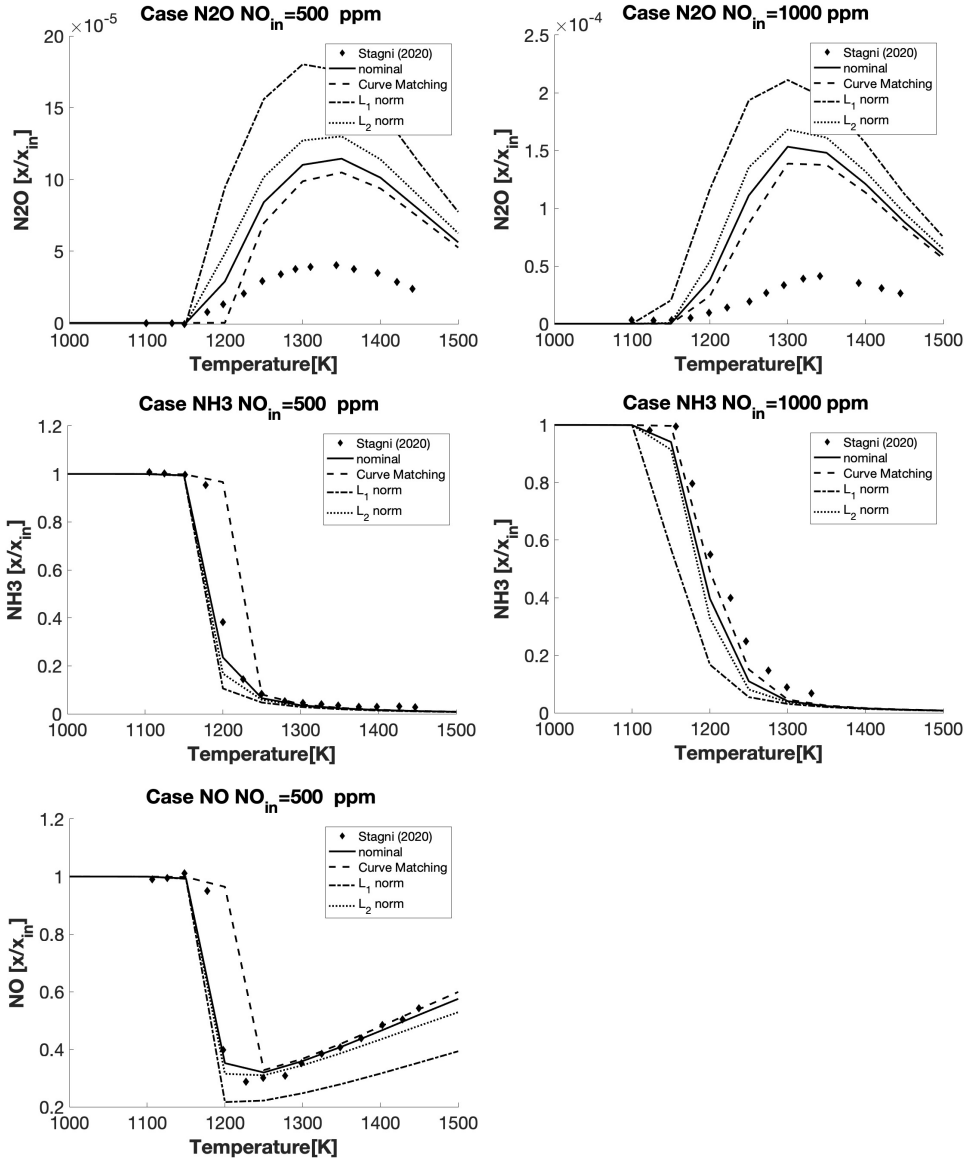

Figure A10: *Comparison between nominal and optimized mechanism. Experimental data from Dagaut [37]*

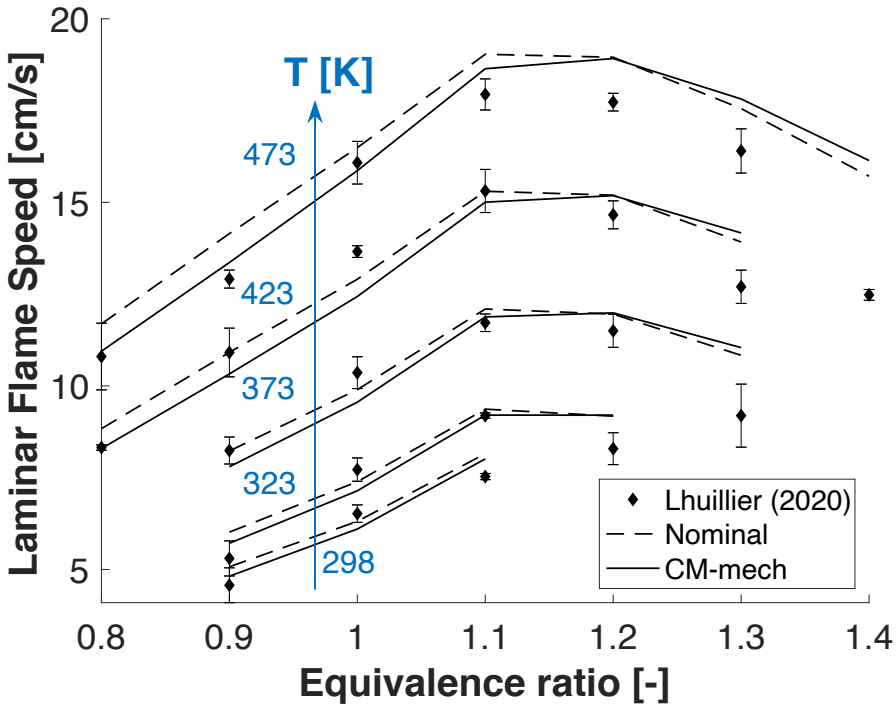

Figure A11: *Comparison between nominal and optimized mechanism. Experimental data from Lhuillier et al. [99]*

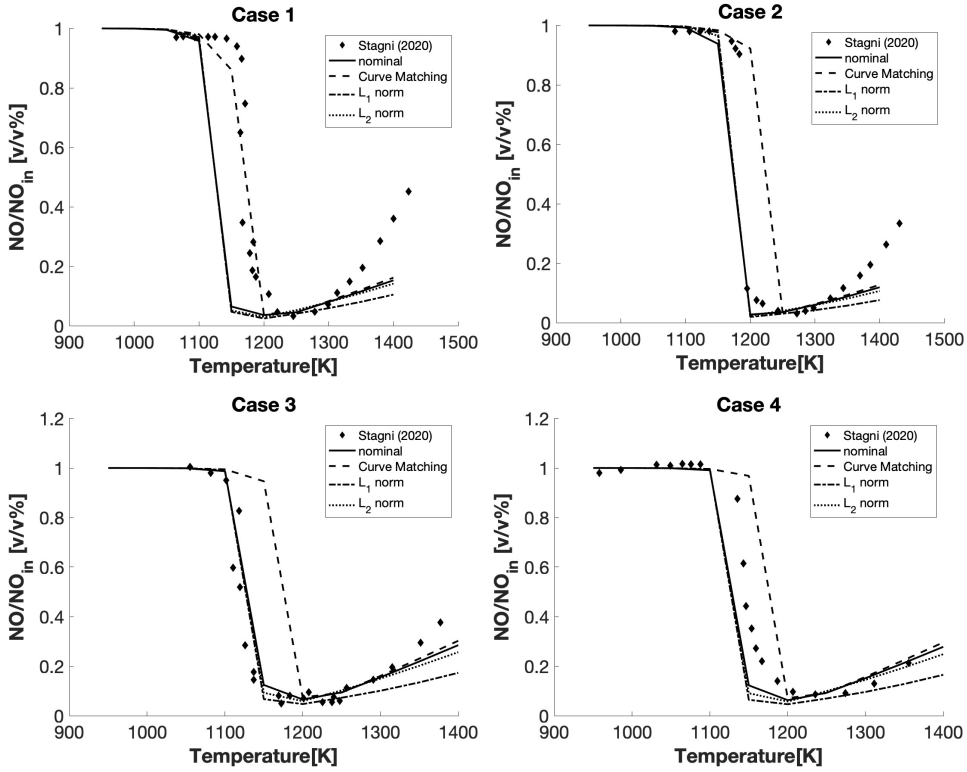

Figure A12: *Comparison between nominal and optimized mechanism. Experimental data from Rota [142]*

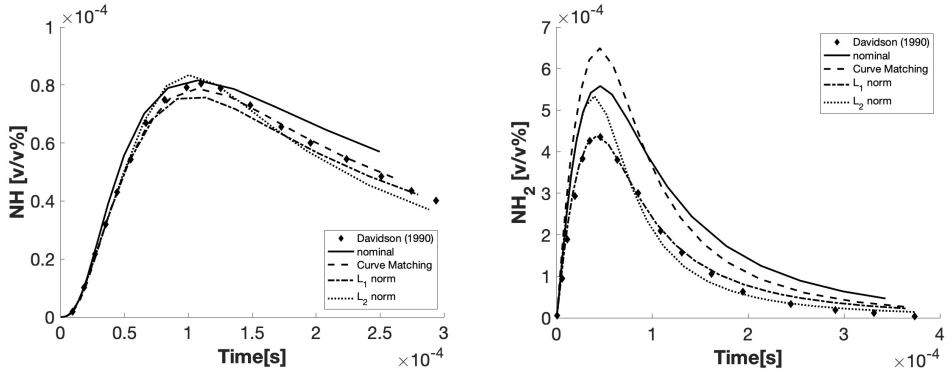

Figure A13: *Comparison between nominal and optimized mechanism. Experimental data from Davidson [41]*

APPENDIX B

Supplementary information for Chapter 5

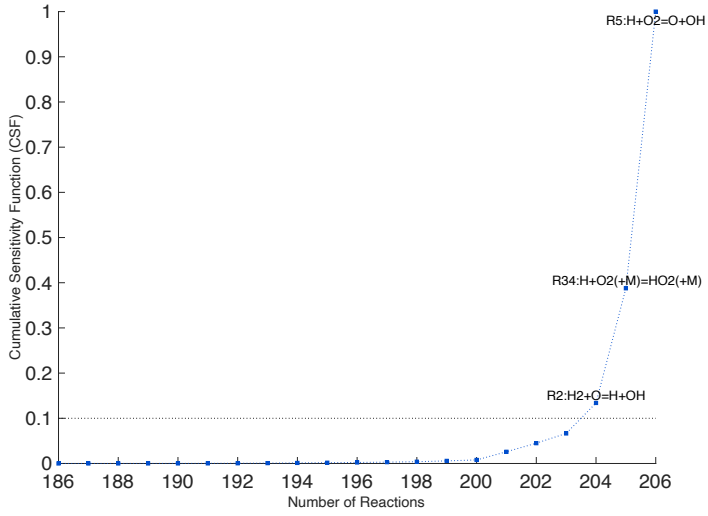

Figure B1: *Cumulative Sensitivity Function for the test case from Brabbs and Robertson [21]*

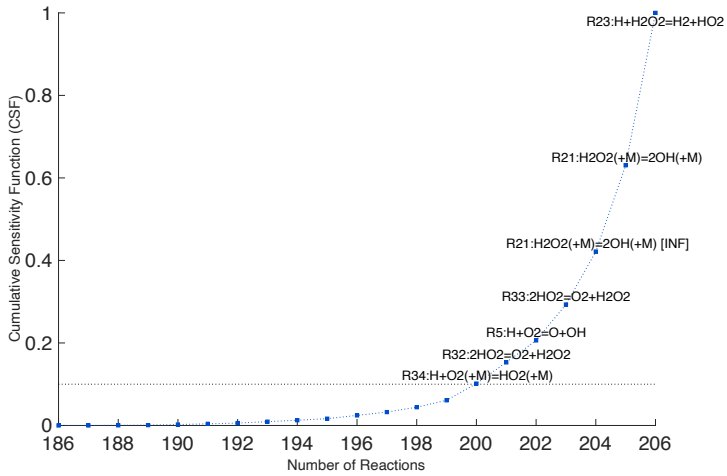

Figure B2: *Cumulative Sensitivity Function for the test case from Das et al. [40]*

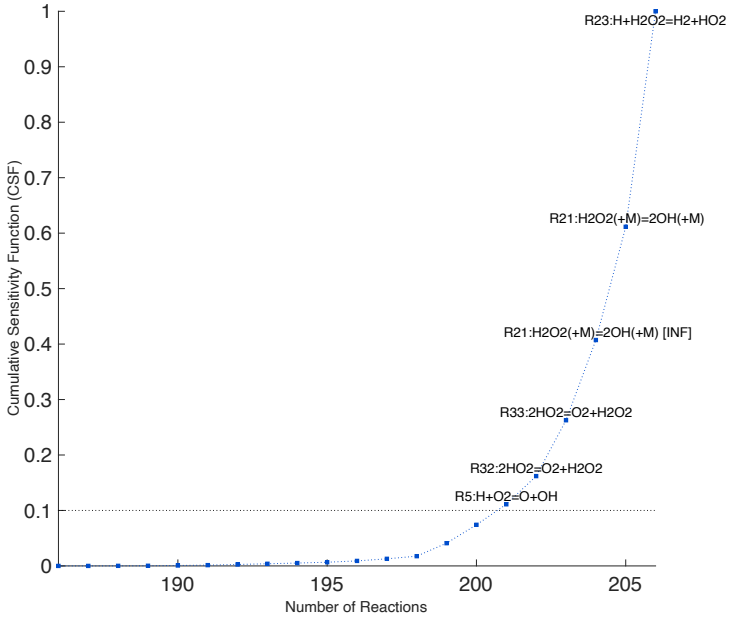

Figure B3: *Cumulative Sensitivity Function for the test case from Donohoe et al. [44]*

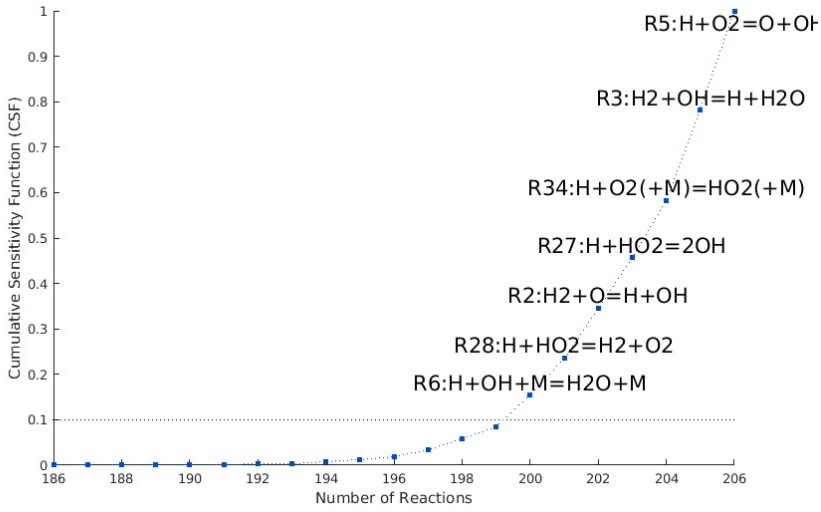

Figure B4: *Cumulative Sensitivity Function for the test case from Quiao et al. [137]*

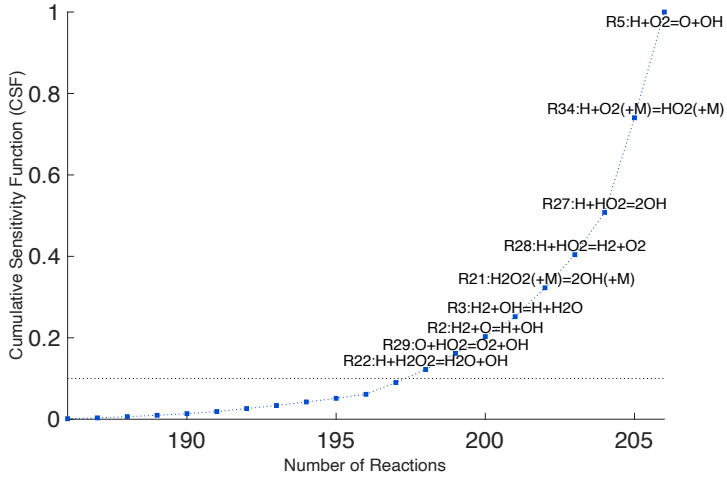

Figure B5: *Cumulative Sensitivity Function for the test case from Sabia et al. [145]*

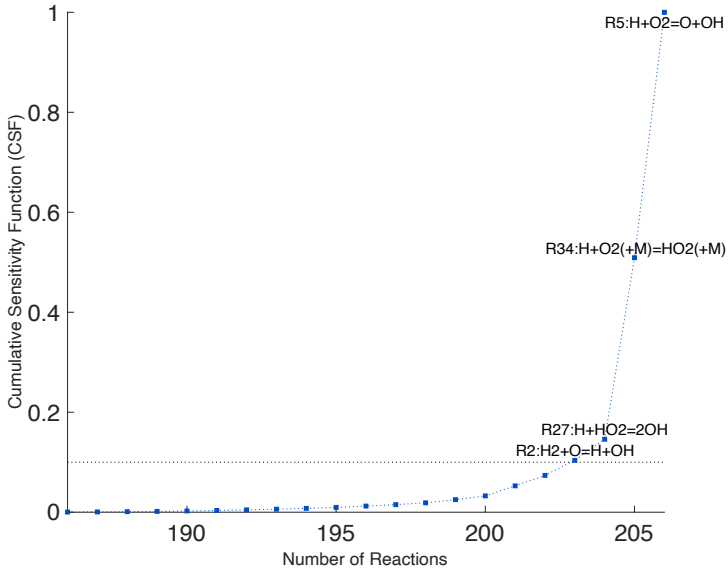

Figure B6: *Cumulative Sensitivity Function for the test case from Shao et al. [152]*

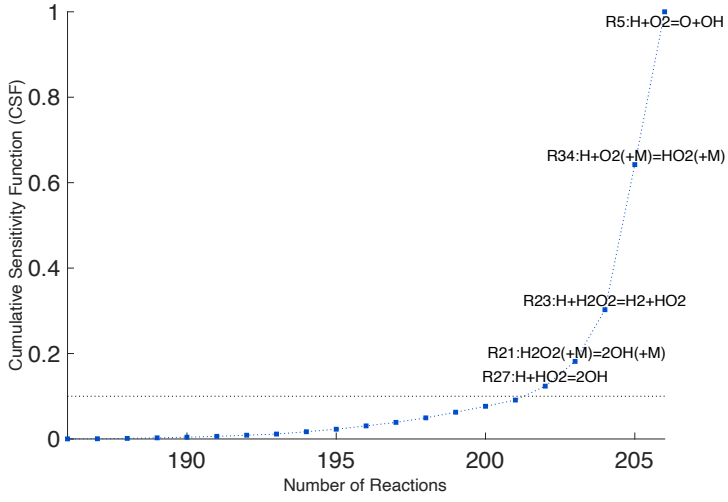

Figure B7: *Cumulative Sensitivity Function for the test case from Wang [202]*

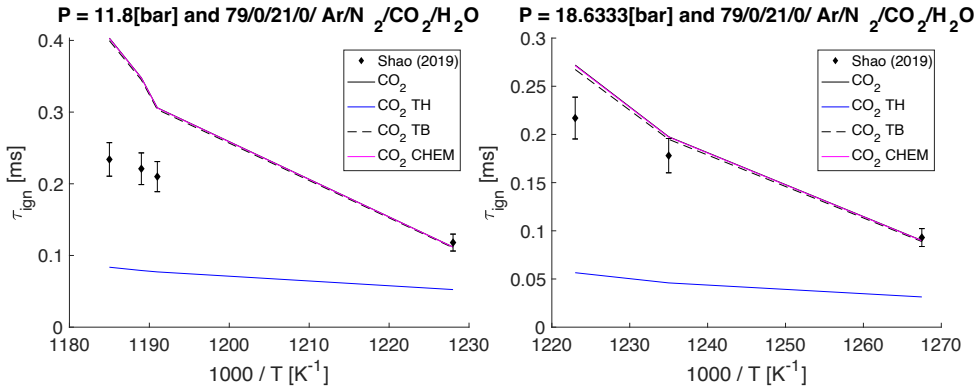

Figure B8: *Virtual Species Analysis for the test case from Shao et al. [152]*

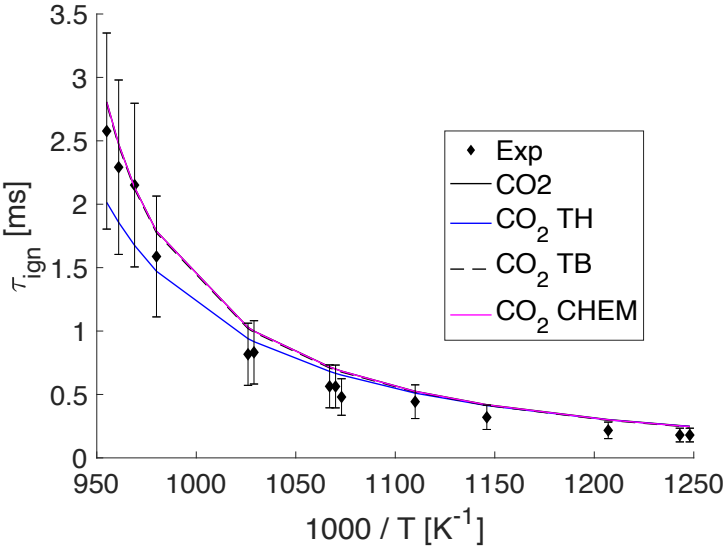

Figure B9: *Virtual Species Analysis for the test case from Brabbs and Robertson [21]*

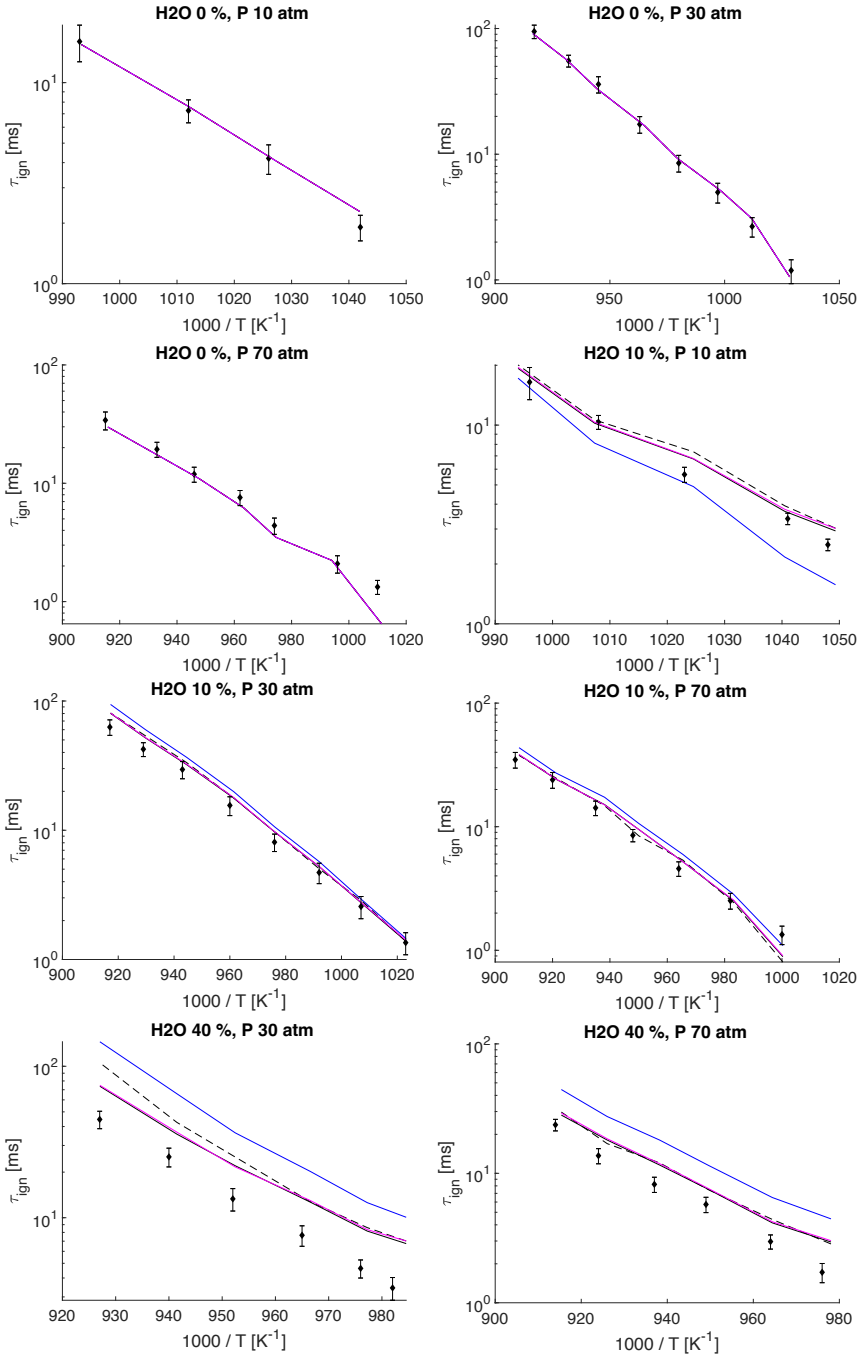

Figure B10: *Virtual Species Analysis for the test case from Das et al. [40]*

List of publications

Peer reviewed journal publications

[1] **A. Bertolino**, A. Stagni, A. Cuoci, T. Faravelli, A. Parente, A. Frassoldati, "Prediction of flammable range for pure fuels and mixtures using detailed kinetics", Combustion and Flame, 207:120-133, 2019.

[2] M. Ferrarotti, **A. Bertolino**, R. Amaduzzi, A. Parente, "On the Influence of Kinetic uncertainties on the accuracy of numerical modeling of an industrial flameless furnace fired with NH_3/H_2 blends: a numerical and experimental study", Frontiers in Energy Research, 8:597655, 2020

[3] **A. Bertolino**, M. Fürst, A. Stagni, A. Frassoldati, M. Pelucchi, C.A. Cavallotti, T. Faravelli, A. Parente, "An evolutionary, data-driven approach for mechanism optimization: theory and application to ammonia combustion", Combustion and Flame, 229:111366, 2021.

[4] M. Fürst, **A. Bertolino**, A. Cuoci, T. Faravelli, A. Parente, "OptiSMOKE++: A toolbox for optimization of chemical kinetic mechanisms", Computer Physics Communications, 264:107940, 2021.

[5] L. Pratali Maffei, C. Cavallotti, M. Pelucchi, **A. Bertolino**, T. Faravelli, "Master equation lumping for multi-well potential energy surfaces: A bridge between ab initio based rate constant calculations and large kinetic mechanisms",

Chemical Engineering Journal, 422:129954, 2021.

[6] K. Bioche, L. Bricteux , C. Cavallotti, **A. Bertolino**, A. Parente, J. Blondeau, "Large Eddy Simulation of rich ammonia/hydrogen/air combustion in a gas turbine burner", International Journal of Hydrogen Energy, *in press*, 2021.

Work in the progress for publication

[7] **A. Bertolino**, A. Frassoldati, A. Cuoci, A. Parente, "Estimation of third body efficiencies from experimental data: an application to hydrogen combustion", International Journal of Hydrogen Energy, *under review*, 2021.

[8] S. Iavarone, **A. Bertolino**, M. Cafiero, A. Parente, "Combined effect of experimental and kinetic uncertainties on NO predictions in low-pressure premixed laminar H_2/CH_4/CO-air and H_2/CH_4/CO/C_6H_6-air flames", Fuel, *under review*, 2022.

Conference papers

[1] **A Bertolino**, A. Frassoldati, A. Parente, "An optimized core mechanism for H_2/CO combustion in mild-like conditions", 42nd Meeting of the Italian Section of the Combustion Institute, September 2019.

[2] **A Bertolino**, A. Frassoldati, A. Parente, "Optimisation of chemical mechanisms for MILD conditions", Seventeenth International Conference of Numerical Combustion, April 2019

[3] **A Bertolino**, A. Frassoldati, A. Parente, "Numerical study of the three-folded effect of steam dilution on hydrogen ignition in a RCM with detailed kinetics", 25th journées D'étude - Belgian Section of the Combustion Institute, April 2018

Bibliography

[1] 2030 climate & energy framework.

[2] Prime. primekinetics.org.

[3] Respecth. respecth.chem.elte.hu/respecth/index.php.

[4] B. M. Adams, W. J. TBohnhoff, K. R. Dalbey, J. P. Eddy, M. S. Eldred, D. M. Gay, K. Haskell, P. D. Hough, and L. P. Swiler. *DAKOTA, a multilevel parallel object-oriented framework for design optimization, parameter estimation, uncertainty quantification, and sensitivity analysis: version 5.0 user's manual*. Sandia National Laboratories, Tech. Rep. SAND2010-2183, 2009.

[5] L. Appels, J. Baeyens, J. Degrève, and R. Dewil. Principles and potential of the anaerobic digestion of waste-activated sludge. *Progress in Energy and Combustion Science*, 34(6):755–781, 2008.

[6] V. K. Arghode and A. K. Gupta. Effect of flow field for colorless distributed combustion (CDC) for gas turbine combustion. *Applied Energy*, 87(5):1631–1640, 2010.

[7] V. K. Arghode, A. K. Gupta, and K. M. Bryden. High intensity colorless distributed combustion for ultra low emissions and enhanced performance. *Applied Energy*, 92:822–830, 2012.

[8] S. Arunthanayothin, A. Stagni, Y. Song, O. Herbinet, T. Faravelli, and F. Battin-Leclerc. Ammonia–methane interaction in jet-stirred and flow reactors: An experimental and kinetic modeling study. *Proceedings of the Combustion Institute*, 38(1):345–353, 2021.

[9] P. J. Ashman and B. S. Haynes. RATE COEFFICIENT OF H+O 2+M→ HO2+M (M = H2O, N2, Ar, CO2). *Proceedings of the Combustion Institute*, pages 185–191, 1998.

[10] M. Ayoub, C. Rottier, S. Carpentier, C. Villermaux, A. M. Boukhalfa, and D. Honore. An experimental study of mild flameless combustion of methane/hydrogen mixtures. *International Journal of Hydrogen Energy*, 37(8):6912–6921, 2012.

[11] G. Bagheri, E. Ranzi, M. Pelucchi, A. Parente, A. Frassoldati, and T. Faravelli. Comprehensive kinetic study of combustion technologies for low environmental impact : Mild and oxy-fuel combustion of methane. *Combustion and Flame*, 212(x):142–155, 2020.

[12] T. Bak, J. Nowotny, M. Rekas, and C. C. Sorrell. Photo-electrochemical hydrogen generation from water using solar energy. materials-related aspects. *International Journal of Hydrogen Energy*, 27(10):991–1022, 2002.

[13] J. F. Bard. *Nonlinear parameter estimation*. New York ; London : Academic Press., 1974.

[14] D. Baulch, C. T. Bowman, C. J. Cobos, R. Cox, T. Just, J. Kerr, M. Pilling, D. Stocker, J. Troe, W. Tsang, et al. Evaluated kinetic data for combustion modeling: supplement ii. *Journal of physical and chemical reference data*, 34(3):757–1397, 2005.

[15] D. Baulch, C. Cobos, R. Cox, P. Frank, G. Hayman, T. Just, J. Kerr, T. Murrells, M. Pilling, J. Troe, et al. Evaluated kinetic data for combustion modeling. supplement i. *Journal of Physical and Chemical Reference Data*, 23(6):847–848, 1994.

[16] S. W. Benson. *Thermochemical kinetics*. Wiley, 1976.

[17] M. S. Bernardi, M. Pelucchi, A. Stagni, L. M. Sangalli, A. Cuoci, A. Frassoldati, P. Secchi, and T. Faravelli. Curve matching, a generalized framework for models/experiments comparison: An application to n-heptane combustion kinetic mechanisms. *Combustion and Flame*, 168:186–203, 2016.

[18] A. Bertolino, M. Fürst, A. Stagni, A. Frassoldati, M. Pelucchi, C. Cavallotti, T. Faravelli, and A. Parente. An evolutionary, data-driven approach for mechanism optimization: theory and application to ammonia combustion. *Combustion and Flame*, 229:111366, 2021.

[19] A. Bertolino, A. Stagni, A. Cuoci, T. Faravelli, A. Parente, and A. Frassoldati. Prediction of flammable range for pure fuels and mixtures using detailed kinetics. *Combustion and Flame*, 207:120–133, 2019.

[20] J. Bourgalais, N. Vin, O. Herbinet, H.-H. Carstensen, M. U. Azuelta, and F. Battin-Leclerc1. A combined theoretical/experimental laboratory study on isopropyl nitrate pyrolysis. *Proceedings of the European Combustion Meeting 2021*, 261:116349, 2021.

[21] T. A. Brabbs and T. F. Robertson. The Carbon Dioxide Chaperon Efficiency for the reaction H+O2+M=HO2+M from ignition delay times behind reflected shock waves. Technical report, NASA, 1987.

[22] M. P. Burke, C. F. Goldsmith, S. J. Klippenstein, O. Welz, H. Huang, I. O. Antonov, J. D. Savee, D. L. Osborn, J. Za, C. A. Taatjes, and L. Sheps. Multiscale Informatics for Low-Temperature Propane Oxidation: further Complexities in Studies of Complex Reactions. *The journal of physical chemistry*, 119:7095–7115, 2015.

[23] M. P. Burke and R. Song. Evaluating mixture rules for multi-component pressure dependence : H+o2 (+m)= ho2 (+m). *Proceedings of the Combustion Institute*, 36(1):245–253, 2017.

[24] M. Cafiero, V. Dias, A. Stagni, P. D. Nguyen, M. Nowakowska, A. Coussement, H. Jeanmart, and A. Parente. The effect of benzene on the structure of low-pressure premixed h2/ch4/co-air flames and related no formation at different equivalence ratios. *Combustion and Flame*, 232:111510, 2021.

[25] L. Cai and H. Pitsch. Mechanism optimization based on reaction rate rules. *Combustion and Flame*, 161(2):405–415, 2014.

[26] L. Cai and H. Pitsch. Optimized chemical mechanism for combustion of gasoline surrogate fuels. *Combustion and Flame*, 162(5):1623–1637, 2015.

[27] L. Cai, H. Pitsch, S. Y. Mohamed, V. Raman, J. Bugler, H. Curran, and S. M. Sarathy. Optimized reaction mechanism rate rules for ignition of normal alkanes. *Combustion and Flame*, pages 468–482, 2016.

[28] A. Cavaliere and M. de Joannon. Mild Combustion. *Progress in Energy and Combustion Science*, 30(4):329–366, 2004.

[29] C. Cavallotti, M. Pelucchi, Y. Georgievskii, and S. J. Klippenstein. EStokTP: Electronic Structure to Temperature- and Pressure-Dependent Rate Constants-A Code for Automatically Predicting the Thermal Kinetics of Reactions. *Journal of Chemical Theory and Computation*, 15(2):1122–1145, 2019.

[30] J.-R. Chen, H.-Y. Tsai, J.-H. Chien, and H.-J. Pan. Flow and flame visualization near the upper flammability limits of methane/air and propane/air mixtures at elevated pressures. *Journal of Loss Prevention in the Process Industries*, 24(5):662–670, 2011.

[31] Z. Chen, V. M. Reddy, S. Ruan, N. A. Doan, W. L. Roberts, and N. Swaminathan. Simulation of MILD combustion using Perfectly Stirred Reactor model. *Proceedings of the Combustion Institute*, 36(3):4279–4286, 2017.

[32] N. Cohen and K. Westberg. Chemical kinetic data sheets for high-temperature chemical reactions. *Journal of physical and chemical reference data*, 12:531–590, 1983.

[33] N. Cohen and K. Westberg. Chemical kinetic data sheets for high-temperature reactions. part ii. *Journal of physical and chemical reference data*, 20:1211–1311, 1991.

[34] M. A. Cremer, C. J. Montgomery, D. H. Wang, M. P. Heap, and J. Y. Chen. Development and implementation of reduced chemistry for computional fluid dynamics modeling of selective non-catalytic reduction. *Proceedings of the Combustion Institute*, 28(2):2427–2434, 2000.

[35] A. Cuoci, A. Frassoldati, T. Faravelli, and E. Ranzi. Opensmoke++: An object-oriented framework for the numerical modeling of reactive systems with detailed kinetic mechanisms. *Computer Physics Communications*, 192:237–264, 2015.

[36] H. J. Curran. Developing detailed chemical kinetic mechanisms for fuel combustion. *Proceedings of the Combustion Institute*, 37(1):57–81, 2019.

[37] P. Dagaut and A. Nicolle. Experimental and kinetic modeling study of the effect of so2 on the reduction of no by ammonia. *Proceedings of the Combustion Institute*, 30(1):1211–1218, 2005.

[38] L. Dai, H. Hashemi, P. Glarborg, S. Gersen, P. Marshall, A. Mokhov, and H. Levinsky. Ignition delay times of nh3 /dme blends at high pressure and low dme fraction: Rcm experiments and simulations. *Combustion and Flame*, 227:120–134, 2021.

[39] B. B. Dally, E. Riesmeier, and N. Peters. Effect of fuel mixture on moderate and intense low oxygen dilution combustion. *Combustion and Flame*, 137(4):418–431, 2004.

[40] A. K. Das, C.-J. Sung, Y. Zhang, and G. Mittal. Ignition delay study of moist hydrogen/oxidizer mixtures using a rapid compression machine. *International Journal of Hydrogen Energy*, 37(8):6901–6911, 2012.

[41] D. F. Davidson, K. Kohse-Höinghaus, A. Y. Chang, and R. K. Hanson. A pyrolysis mechanism for ammonia. *International Journal of Chemical Kinetics*, 22(5):513–535, 1990.

[42] R. de Vijver and J. Zádor. KinBot: Automated stationary point search on potential energy surfaces. *Computer Physics Communications*, 248:106947, 2020.

[43] A. M. Dean and J. W. Bozzelli. *Combustion Chemistry of Nitrogen*, pages 125–341. Springer New York, New York, NY, 2000.

[44] N. Donohoe, K. A. Heufer, C. J. Aul, E. L. Petersen, G. Bourque, R. Gordon, and H. J. Curran. Influence of steam dilution on the ignition of hydrogen, syngas and natural gas blends at elevated pressures. *Combustion and Flame*, 162(4):1126–1135, 2015.

[45] P. D.Ronney. Effect of chemistry and transport properties on near-limit flames at microgravity. *Combustion Science and Technology*, 59(1-3):123–141, 1988.

[46] F. L. Dryer, F. M. Haas, J. Santner, T. I. Farouk, and M. Chaos. Interpreting chemical kinetics from complex reaction–advection–diffusion systems: Modeling of flow reactors and related experiments. *Progress in energy and combustion science*, 44:19–39, 2014.

[47] L. Elliott, D. Ingham, A. Kyne, N. Mera, M. Pourkashanian, and C. Wilson. Genetic algorithms for optimisation of chemical kinetics reaction mechanisms. *Progress in Energy and Combustion Science*, 30(3):297–328, 2004.

[48] L. Elliott, D. Ingham, A. Kyne, N. Mera, M. Pourkashanian, and C. W. Wilson. Incorporation of physical bounds on rate parameters for reaction mechanism optimization using genetic algorithms. *Combustion Science and Technology*, 175(4):619–648, 2003.

[49] L. Elliott, D. B. Ingham, A. G. Kyne, N. S. Mera, M. Pourkashanian, and C. W. Wilson. Multiobjective genetic algorithm optimization for calculating the reaction rate coefficients for hydrogen combustion. *Industrial and Engineering Chemistry Research*, 42(6):1215–1224, 2003.

[50] A. Evans, V. Strezov, and T. J. Evans. Assessment of utility energy storage options for increased renewable energy penetration. *Renewable and Sustainable Energy Reviews*, 16(6):4141–4147, 2012.

[51] R. Feeley, P. Seiler, A. Packard, and M. Frenklach. Consistency of a Reaction Dataset. *J. Phys. Chem.*, 108:9573–9583, 2004.

[52] R. X. Fernandes, K. Luther, J. Troe, and V. G. Ushakov. Experimental and modelling study of the recombination reaction H+O2(+M)=HO2 (+M) between 300 and 900 K , 1 . 5 and 950 bar , and in the bath gases M = He , Ar , and N 2. *Physical Chemistry Chemical Physics*, 2:4313–4321, 2008.

[53] M. Ferrarotti, M. Fürst, E. Cresci, W. de Paepe, and A. Parente. Key Modeling Aspects in the Simulation of a Quasi-industrial 20 kW Moderate or Intense Low-oxygen Dilution Combustion Chamber. *Energy & Fuels*, 32(10):10228–10241, oct 2018.

[54] M. Ferrarotti, Z. Li, and A. Parente. On the role of mixing models in the simulation of MILD combustion using finite-rate chemistry combustion models. *Proceedings of the Combustion Institute*, 37(4):4531–4538, 2019.

[55] A. Florian. An efficient sampling scheme: Updated Latin Hypercube Sampling. *Probabilistic Engineering Mechanics*, 7(2):123–130, 1992.

[56] M. Frenklach. Transforming data into knowledge — Process Informatics for combustion chemistry. *Proceedings of the Combustion Institute*, 31:125–140, 2007.

[57] M. Frenklach, A. Packard, G. Garcia-donato, R. Paulo, and J. Sacks. Comparison of Statistical and Deterministic Frameworks of Uncertainty Quantification. *SIAM/ASA Journal on Uncertainty Quantification*, 4:875–901, 2016.

[58] M. Frenklach, A. Packard, P. Seiler, and R. Feeley. Processing in Developing Predictive Models of Complex Reaction Systems. *International Journal of Chemical Kinetics*, 36:57–66, 2003.

[59] M. Frenklach, A. Packard, P. Seiler, and R. Feeley. Collaborative data processing in developing predictive models of complex reaction systems. *International Journal of Chemical Kinetics*, 36(1):57–66, 2004.

[60] M. Frenklach, H. Wang, M. Goldenberg, G. P. Smith, and D. M. Golden. GRI-MECH: An optimized detailed chemical reaction mechanism for methane combustion. Topical report, September 1992-August 1995. Technical report, U.S. Department of Energy Office of Scientific and Technical Information, United States, 1995.

[61] M. Frenklach, H. Wang, and M. J. Rabinowitz. Optimization and analysis of large chemical kinetic mechanisms using the solution mapping method—combustion of methane. *Progress in Energy and Combustion Science*, 18(1):47–73, 1992.

[62] S. Frigo and R. Gentili. Analysis of the behaviour of a 4-stroke Si engine fuelled with ammonia and hydrogen. *International Journal of Hydrogen Energy*, 38(3):1607–1615, 2013.

[63] M. B. Fürst, P. Sabia, M. Lubrano Lavadera, G. Aversano, M. D. Joannon, A. Frassoldati, and A. Parente. Optimization of chemical kinetics for methane and biomass pyrolysis products in mild combustion. *Energy and Fuels*, 32:10194–10201, 2018.

[64] M. Fürst, A. Bertolino, A. Cuoci, T. Faravelli, A. Frassoldati, and A. Parente. Optismoke++: A toolbox for optimization of chemical kinetic mechanisms. *Computer Physics Communications*, 264:107940, 2021.

[65] C. Galletti, M. Ferrarotti, A. Parente, and L. Tognotti. Reduced no formation models for cfd simulations of mild combustion. *International Journal of Hydrogen Energy*, 40(14):4884–4897, 2015.

[66] P. Glarborg and L. L. B. Bentzen. Chemical effects of a high co2 concentration in oxy-fuel combustion of methane. *Energy and Fuels*, 22(20):291–296, 2008.

[67] P. Glarborg, J. A. Miller, B. Ruscic, and S. J. Klippenstein. Modeling nitrogen chemistry in combustion. *Progress in Energy and Combustion Science*, 67:31–68, 2018.

[68] D. R. Glowacki, C. H. Liang, C. Morley, M. J. Pilling, and S. H. Robertson. MESMER: An open-source master equation solver for Multi-Energy well reactions. *Journal of Physical Chemistry A*, 116(38):9545–9560, 2012.

[69] C. F. Goldsmith, A. S. Tomlin, and S. J. Klippenstein. Uncertainty propagation in the derivation of phenomenological rate coefficients from theory: A case study of n-propyl radical oxidation. *Proceedings of the Combustion Institute*, 34(1):177–185, 2013.

[70] S. Gordon and B. J. McBride. Computer program for calculation of complex chemical equilibrium. *NASA reference publication*, 1311, 1994.

[71] R. M. Green and J. A. Miller. The measurement of relative concentration profiles of NH2 using laser absorption spectroscopy. *Journal of Quantitative Spectroscopy and Radiative Transfer*, 26(4):313–327, 1981.

[72] N. L. Haworth, J. C. Mackie, and G. B. Bacskay. An ab initio quantum chemical and kinetic study of the NNH + O reaction potential energy surface: How important is this route to NO in combustion? *Journal of Physical Chemistry A*, 107(35):6792–6803, 2003.

[73] A. Hayakawa, T. Goto, R. Mimoto, Y. Arakawa, T. Kudo, and H. Kobayashi. Laminar burning velocity and Markstein length of ammonia/air premixed flames at various pressures. *Fuel*, 159:98–106, 2015.

[74] M. He, A. W. Jasper, and J. A. Miller. Theoretical Unimolecular Kinetics for CH4+M=CH3+H+M in Eight Baths, M = He, Ne, Ar, Kr, H2, N2, CO and CH4. *The journal of physical chemistry*, 115:6438–6455, 2011.

[75] X. He, B. Shu, D. Nascimento, K. Moshammer, M. Costa, and R. Fernandes. Auto-ignition kinetics of ammonia and ammonia/hydrogen mixtures at intermediate temperatures and high pressures. *Combustion and Flame*, 206:189–200, 2019.

[76] J. O. Hirschfelder, C. F. Curtiss, and R. B. Bird. Molecular theory of gases and liquids. *Wiley*, 1964.

[77] Z. Hong, A. Farooq, E. A. Barbour, D. F. Davidson, and R. K. Hanson. Hydrogen peroxide decomposition rate: A shock tube study using tunable laser absorption of H2O near 2.5 μm. *Fall Technical Meeting of the Western States Section of the Combustion Institute 2009, WSS/CI 2009 Fall Meeting*, 2:796–804, 2009.

[78] C. J. Howard. Kinetic study of the equilibrium ho2+ no=oh+ no2 and the thermochemistry of ho2. *Journal of the American Chemical Society*, 102(23):6937–6941, 1980.

[79] X. Huang. *Measurements and model development for flameless combustion in a Lab-scale furnace*. PhD thesis, TUDelft, 2018.

[80] S. Iavarone, J. Oreluk, S. T. Smith, A. Hegde, W. Li, A. Packard, M. Frenklach, P. J. Smith, F. Contino, and A. Parente. Application of Bound-to-Bound Data Collaboration approach for development and uncertainty quantification of a reduced char combustion model. *Fuel*, 232(May):769–779, 2018.

[81] R. L. Iman and W. J. Conover. Small sample sensitivity analysis techniques for computer models, with an application to risk assessment. *Communications in Statistics - Theory and Methods*, 9(17):1749–1842, 1980.

[82] A. W. Jasper. " Third-body " collision parameters for hydrocarbons , alcohols , and hydroperoxides and an effective internal rotor approach for estimating them. *International Journal of Chemical Kinetics*, pages 387–402, 2020.

[83] A. W. Jasper, J. A. Miller, and S. J. Klippenstein. Collision Efficiency of Water in the Unimolecular Reaction CH4(+H2O)=CH3+H(+H2O): One-Dimensional and Two-Dimensional Solutions of the Low-Pressure-Limit Master Equation. *Journal of Physical Chemistry*, 4:12243–12255, 2013.

[84] W. Jones and R. Lindstedt. Global reaction schemes for hydrocarbon combustion. *Combustion and flame*, 73(3):233–249, 1988.

[85] M. Katsuki and T. Hasegawa. The science and technology of combustion in highly preheated air. *Symposium (International) on Combustion*, 27(2):3135–3146, 1998.

[86] S. J. Klippenstein. From theoretical reaction dynamics to chemical modeling of combustion. *Proceedings of the Combustion Institute*, 36:77–111, 2017.

[87] S. J. Klippenstein. Personal Communication, 2020.

[88] S. J. Klippenstein, L. B. Harding, M. J. Davis, A. S. Tomlin, and R. T. Skodje. Uncertainty driven theoretical kinetics studies for ch3oh ignition: Ho2+ch3oh and o2+ch3oh. *Proceedings of the Combustion Institute*, 33(1):351–357, 2011.

[89] S. J. Klippenstein, L. B. Harding, P. Glarborg, and J. A. Miller. The role of nnh in no formation and control. *Combustion and Flame*, 158(4):774–789, 2011. Special Issue on Kinetics.

[90] S. J. Klippenstein, L. B. Harding, B. Ruscic, R. Sivaramakrishnan, N. K. Srinivasan, M. Su, and J. V. Michael. Thermal Decomposition of NH2OH and Subsequent Reactions : Ab Initio Transition State Theory and Reflected Shock Tube Experiments. *The journal of physical chemistry*, 113(38):10241–10259, 2009.

[91] H. Kobayashi, A. Hayakawa, K. Somarathne, and E. Okafor. Science and technology of ammonia combustion. *Proceedings of the Combustion Institute*, 000:1–25, 2018.

[92] B. Koroglu, O. M. Pryor, J. Lopez, L. Nash, and S. S. Vasu. Shock tube ignition delay times and methane time-histories measurements during excess co2 diluted oxy-methane combustion. *Combustion and Flame*, 164:152–163, 2016.

[93] M. Kovács, M. Papp, I. G. Zsély, and T. Turányi. Determination of rate parameters of key N/H/O elementary reactions based on H2/O2/NOx combustion experiments. *Fuel*, 264(December 2019):116720, 2020.

[94] A. Kéromnès, W. K. Metcalfe, K. A. Heufer, N. Donohoe, A. K. Das, C.-J. Sung, J. Herzler, C. Naumann, P. Griebel, O. Mathieu, M. C. Krejci, E. L. Petersen, W. J. Pitz, and H. J. Curran. An experimental and detailed chemical kinetic modeling study of hydrogen and syngas mixture oxidation at elevated pressures. *Combustion and Flame*, 160(6):995–1011, 2013.

[95] R. Langer, J. Lotz, L. Cai, F. vom Lehn, K. Leppkes, U. Naumann, and H. Pitsch. Adjoint sensitivity analysis of kinetic, thermochemical, and transport data of nitrogen and ammonia chemistry. *Proceedings of the Combustion Institute*, 38(1):777–785, 2021.

[96] C. Lee, S. Vranckx, K. A. Heufer, S. V. Khomik, Y. Uygun, H. Olivier, and R. X. Fernandez. On the chemical kinetics of ethanol oxidation: Shock tube, rapid compression machine and detailed modeling study:. *Zeitschrift für Physikalische Chemie*, 226(1):1–28, 2012.

[97] L. Lei and M. P. Burke. Mixture rules and falloff are now major uncertainties in experimentally derived rate parameters for H+O2(+M)=HO2(+M). *Combustion and Flame*, 213:467–474, 2020.

[98] M. Lemke, L. Cai, J. Reiss, H. Pitsch, and J. Sesterhenn. Adjoint-based sensitivity analysis of quantities of interest of complex combustion models. *Combustion Theory and Modelling*, 23(1):180–196, 2019.

[99] C. Lhuillier, P. Brequigny, N. Lamoureux, F. Contino, and C. Mounaïm-Rousselle. Experimental investigation on laminar burning velocities of ammonia/hydrogen/air mixtures at elevated temperatures. *Fuel*, 263:116653, 2020.

[100] R. Li, A. A. Konnov, G. He, F. Qin, and D. Zhang. Chemical mechanism development and reduction for combustion of nh3/h2/ch4 mixtures. *Fuel*, 257:116059, 2019.

[101] F. A. Lindemann, S. Arrhenius, I. Langmuir, N. Dhar, J. Perrin, and W. M. Lewis. Discussion on "the radiation theory of chemical action". *Transactions of the Faraday Society*, 17:598–606, 1922.

[102] D. P. Linder, X. Duan, and M. Page. Thermal rate constants for r+n2h2→rh+n2h (r=h, oh, nh2) determined from multireference configuration interaction and variational transition state theory calculations. *The Journal of Chemical Physics*, 104(16):6298–6307, 1996.

[103] P. Linstrom and W. Mallard. Nist chemistry webbook, nist standard reference database number 69. `https://kinetics.nist.gov/kinetics/index.jsp`.

[104] T. Lu and C. K. Law. Toward accommodating realistic fuel chemistry in large-scale computations. *Progress in Energy and Combustion Science*, 35(2):192–215, 2009.

[105] M. Lubrano Lavadera, P. Sabia, G. Sorrentino, R. Ragucci, and M. de Joannon. Experimental study of the effect of co2 on propane oxidation in a jet stirred flow reactor. *Fuel*, 184:876–888, 2016.

[106] D. I. Maclean and H. G. Wagner. The structure of the reaction zones of ammonia-oxygen and hydrazine-decomposition flames. *Symposium (International) on Combustion*, 11(1):871–878, 1967.

[107] O. Mathieu and E. L. Petersen. Experimental and modeling study on the high-temperature oxidation of ammonia and related nox chemistry. *Combustion and Flame*, 162(3):554–570, 2015.

[108] M. D. McKay, R. J. Beckman, and W. J. Conover. A comparison of three methods for selecting values of input variables in the analysis of output from a computer code. *Technometrics*, 21(2):239–245, 1979.

[109] A. M. Mebel, E. W. G. Diau, M. C. Lin, and K. Morokuma. Theoretical Rate Constants for the NH3+NO =NH2+HNOx (x=1,2) Reactions by ab Initio MO/VTST Calculations. *The journal of physical chemistry*, 3654(x):7517–7525, 1996.

[110] P. R. Medwell, M. J. Evans, Q. N. Chan, and V. R. Katta. Laminar flame calculations for analyzing trends in autoignitive jet flames in a hot and vitiated coflow. *Energy and Fuels*, 30(10):8680–8690, 2016.

[111] J. D. Mertens, A. Y. Chang, R. K. Hanson, and C. T. Bowman. A shock tube study of the reactions of NH with NO, O2, and O. *International Journal of Chemical Kinetics*, 23(2):173–196, 1991.

[112] J. V. Michael, M. Su, J. W. Sutherland, J. J. Carroll, and A. F. Wagner. Rate Constants For H+O2+M=HO2+M in Seven Bath Gases. *Journal of Physical Chemistry*, 106:5297–5313, 2002.

[113] J. A. Miller and C. T. Bowman. Mechanism and modeling of nitrogen chemistry in combustion. *Progress in Energy and Combustion Science*, 15:287–338, 1989.

[114] Y. Minamoto and N. Swaminathan. Subgrid scale modelling for mild combustion. *Proceedings of the Combustion Institute*, 35(3):3529–3536, 2015.

[115] W. J. Morokoff and R. E. Caflisch. Quasi-monte carlo integration. *Journal of computational physics*, 122(2):218–230, 1995.

[116] G. Mosca. *Experimental and Numerical Study of MILD Combustion*. PhD thesis, University of Mons, 2017.

[117] S. H. Mousavipour, F. Pirhadi, and A. Habibagahi. A theoretical investigation on the kinetics and mechanism of the reaction of amidogen with hydroxyl radical. *The journal of physical chemistry*, 113(46):12961–12971, 2009.

[118] M. Mueller, T. Kim, R. Yetter, and F. Dryer. Flow reactor studies and kinetic modeling of the h2/o2 reaction. *International journal of chemical kinetics*, 31(2):113–125, 1999.

[119] T. Nagy and T. Turányi. Uncertainty of Arrhenius Parameters. *International Journal of Chemical Kinetics*, 43(7):359–378, 2011.

[120] T. Nagy, É. Valkó, I. Sedyó, I. G. Zsély, M. J. Pilling, and T. Turányi. Uncertainty of the rate parameters of several important elementary reactions of the h2 and syngas combustion systems. *Combustion and Flame*, 162(5):2059–2076, 2015.

[121] T. Nagy, E. Valkó, I. Sedyó, I. G. Zsély, M. J. Pilling, and T. Turányi. Uncertainty of the rate parameters of several important elementary reactions of the h2 and syngas combustion systems. *Combustion and Flame*, 162(5):2059–2076, 2015.

[122] H. N. Najm, B. J. Debusschere, Y. M. Marzouk, and S. Widmer. Uncertainty quantification in chemical systems. *International Journal of Numerical Methods in Engineering*, 80:789–814, 2009.

[123] H. M. T. Nguyen, S. Zhang, J. Peeters, T. N. Truong, and M. T. Nguyen. Direct ab initio dynamics studies of the reactions of hno with h and oh radicals. *Chemical Physics Letters*, 388(1):94–99, 2004.

[124] T. L. Nguyen and J. R. Barker. Sums and Densities of Fully Coupled Anharmonic Vibrational States : A Comparison of Three Practical Methods. *Journal of Physical Chemistry*, 40(2):3718–3730, 2010.

[125] C. Olm, T. Varga, É. Valkó, H. J. Curran, and T. Turányi. Uncertainty quantification of a newly optimized methanol and formaldehyde combustion mechanism. *Combustion and Flame*, 186:45–64, 2017.

[126] C. Olm, T. Varga, E. Valkó, S. Hartl, C. Hasse, and T. Turányi. Development of an ethanol combustion mechanism based on a hierarchical optimization approach. *International Journal of Chemical Kinetics*, 48(8):423–441, 2016.

[127] J. Otomo, M. Koshi, T. Mitsumori, H. Iwasaki, and K. Yamada. Chemical kinetic modeling of ammonia oxidation with improved reaction mechanism for ammonia/air and ammonia/hydrogen/air combustion. *International Journal of Hydrogen Energy*, 43(5):3004 – 3014, 2018.

[128] I. B. Özdemir and N. Peters. Characteristics of the reaction zone in a combustor operating at mild combustion. *Experiments in Fluids*, 30(6):683–695, 2001.

[129] G. Pang, D. Davidson, and R. Hanson. Experimental study and modeling of shock tube ignition delay times for hydrogen–oxygen–argon mixtures at low temperatures. *Proceedings of the Combustion Institute*, 32(1):181–188, 2009.

[130] O. Park, P. S. Veloo, D. A. Sheen, Y. Tao, F. N. Egolfopoulos, and H. Wang. Chemical kinetic model uncertainty minimization through laminar flame speed measurements. *Combustion and Flame*, 172:136–152, 2016.

[131] M. Pelucchi, A. Stagni, and T. Faravelli. Chapter 15 - Addressing the complexity of combustion kinetics: Data management and automatic model validation. In T. Faravelli, F. Manenti, and E. B. T. C. A. C. E. Ranzi, editors, *Mathematical Modelling of Gas-Phase Complex Reaction Systems: Pyrolysis and Combustion*, volume 45, pages 763–798. Elsevier, 2019.

[132] C. Philibert. Producing ammonia and fertilizers : new opportunities from renewables one half being used for producing ammonia. *IEA Report*, pages 1–6, 2017.

[133] T. Plessing, N. Peters, and J. G. Wünning. Laseroptical investigation of highly preheated combustion with strong exhaust gas recirculation. *Symposium (International) on Combustion*, 27(2):3197–3204, 1998.

[134] M. Pochet, V. Dias, B. Moreau, F. Foucher, H. Jeanmart, and F. Contino. Experimental and numerical study, under ltc conditions, of ammonia ignition delay with and without hydrogen addition. *Proceedings of the Combustion Institute*, 37(1):621–629, 2019.

[135] W. Polifke, W. Geng, and K. Döbbeling. Optimization of rate coefficients for simplified reaction mechanisms with genetic algorithms. *Combustion and Flame*, 113(1):119–134, 1998.

[136] M. J. Powell. An efficient method for finding the minimum of a function of several variables without calculating derivatives. *The computer journal*, 7(2):155–162, 1964.

[137] L. Qiao, C. H. Kim, and G. M. Faeth. Suppression effects of diluents on laminar premixed hydrogen/oxygen/ nitrogen flames. *Combustion and Flame*, 143(1-2):79–96, 2005.

[138] E. Ramalli, G. Scalia, B. Pernici, A. Stagni, A. Cuoci, and T. Faravelli. Data ecosystems for scientific experiments: managing combustion experiments and simulation analyses in chemical engineering. *Frontiers in big Data*, page 67, 2021.

[139] E. Ranzi, A. Frassoldati, R. Grana, A. Cuoci, T. Faravelli, A. Kelley, and C. K. Law. Hierarchical and comparative kinetic modeling of laminar flame speeds of hydrocarbon and oxygenated fuels. *Progress in Energy and Combustion Science*, 38(4):468–501, 2012.

[140] Reaction Design: San Diego. *ANSYS Chemkin Theory Manual 17.0 (15151)*. ANSYS, 2015.

[141] R. C. Rocha, M. Costa, and X. S. Bai. Combustion and Emission Characteristics of Ammonia under Conditions Relevant to Modern Gas Turbines. *Combustion Science and Technology*, 00(00):1–20, 2020.

[142] R. Rota, D. Antos, E. Zanoelo, and S. Carra. Experimental study and kinetic modelling of nitric oxide reduction with ammonia. *Combustion Science and Technology*, 163(1):25–47, 2001.

[143] T. Russi, A. Packard, R. Feeley, and M. Frenklach. Sensitivity Analysis of Uncertainty in Model Prediction. *Journal of Physical Chemistry*, 112:2579–2588, 2008.

[144] T. Russi, A. Packard, and M. Frenklach. Uncertainty quantification : Making predictions of complex reaction systems reliable. *Chemical Physics Letters*, 499(1-3):1–8, 2010.

[145] P. Sabia and M. De Joannon. On H2-O2 oxidation in several bath gases. *International Journal of Hydrogen Energy*, 45(15):8151–8167, 2020.

[146] P. Sabia, M. Lubrano Lavadera, G. Sorrentino, P. Giudicianni, R. Ragucci, and M. de Joannon. H2o and co2 dilution in mild combustion of simple hydrocarbons. *Flow, Turbulence and Combustion*, 96(2):433–448, 2016.

[147] P. Sabia, G. Sorrentino, P. Bozza, G. Ceriello, R. Ragucci, and M. De Joannon. Fuel and thermal load flexibility of a MILD burner. *Proceedings of the Combustion Institute*, 37(4), 2019.

[148] M. Schwaab, E. C. Biscaia, J. L. Monteiro, and J. C. Pinto. Nonlinear parameter estimation through particle swarm optimization. *Chemical Engineering Science*, 63:1542–1552, 2008.

[149] M. Schwaab, L. P. Lemos, and J. C. Pinto. Optimum reference temperature for reparameterization of the Arrhenius equation . Part 2 : Problems involving multiple reparameterizations. *Chemical Engineering Science*, 63:2895 – 2906, 2008.

[150] M. Schwaab and J. C. Pinto. Optimum reference temperature for reparameterization of the Arrhenius equation . Part 1 : Problems involving one kinetic constant. *Chemical Engineering Science*, 62:2750–2764, 2007.

[151] R. Shannon, A. Tomlin, S. Robertson, M. Blitz, M. Pilling, and P. Seakins. Global uncertainty propagation and sensitivity analysis in the ch3och2+o2 system: combining experiment and theory to constrain key rate coefficients in dme combustion. *The Journal of Physical Chemistry A*, 119(28):7430–7438, 2015.

[152] J. Shao, R. Choudhary, A. Susa, D. F. Davidson, and R. K. Hanson. Shock tube study of the rate constants for H+O2+M→HO2+M (M=Ar, H2O, CO2, N2) at elevated pressures. *Proceedings of the Combustion Institute*, 37(1):145–152, 2019.

[153] F. B. Shareh, G. Silcox, and E. G. Eddings. Calculated Impacts of Diluents on Flame Temperature, Ignition Delay, and Flame Speed of Methane–Oxygen Mixtures at High Pressure and Low to Moderate Temperatures. *Energy & Fuels*, 32(3):3891–3899, mar 2018.

[154] D. A. Sheen, C. M. Rosado-Reyes, and W. Tsang. Kinetics of h atom attack on unsaturated hydrocarbons using spectral uncertainty propagation and minimization techniques. *Proceedings of the Combustion Institute*, 34(1):527–536, 2013.

[155] D. A. Sheen and H. Wang. The method of uncertainty quantification and minimization using polynomial chaos expansions. *Combustion and Flame*, 158(12):2358–2374, 2011.

[156] D. A. Sheen and H. Wang. The method of uncertainty quantification and minimization using polynomial chaos expansions. *Combustion and Flame*, 158(12):2358–2374, 2011.

[157] K. P. Shrestha, L. Seidel, T. Zeuch, and F. Mauss. Detailed Kinetic Mechanism for the Oxidation of Ammonia Including the Formation and Reduction of Nitrogen Oxides. *Energy and Fuels*, 32(10):10202–10217, 2018.

[158] K. P. Shrestha, N. Vin, O. Herbinet, L. Seidel, F. Battin-Leclerc, T. Zeuch, and F. Mauss. Insights into nitromethane combustion from detailed kinetic modeling – pyrolysis experiments in jet-stirred and flow reactors. *Fuel*, 261:116349, 2020.

[159] B. Shu, S. Vallabhuni, X. He, G. Issayev, K. Moshammer, A. Farooq, and R. Fernandes. A shock tube and modeling study on the autoignition properties of ammonia at intermediate temperatures. *Proceedings of the Combustion Institute*, 37(1):205–211, 2019.

[160] J. Sidey, E. Mastorakos, and R. L. Gordon. Simulations of autoignition and laminar premixed flames in methane/air mixtures diluted with hot products. *Combustion Science and Technology*, 186(4-5):453–465, 2014.

[161] N. Sikalo, O. Hasemann, C. Schulz, A. Kempf, and I. Wlokas. A genetic algorithm–based method for the optimization of reduced kinetics mechanisms. *International Journal of Chemical Kinetics*, 47(11):695–723, 2015.

[162] M. W. Slack. Rate coefficient for h+o2+m=ho2+m evaluated from shock tube measurements of induction times. *Combustion and Flame*, 28(C):241–249, 1977.

[163] N. A. Slavinskaya, M. Abbasi, J. H. Starcke, R. Whitside, A. Mirzayeva, U. Riedel, W. Li, J. Oreluk, A. Hegde, A. Packard, M. Frenklach, G. Gerasimov, and O. Shatalov. Development of an Uncertainty Quantification Predictive Chemical Reaction Model for Syngas Combustion. *Energy and Fuels*, 31:2274–2297, 2017.

[164] G. Smith, Y. Tao, and H. Wang. Foundational fuel chemistry model version 1.0 (FFCM-1), 2016.

[165] S. Smolyak. Quadrature and interpolation formulas for tensor products of certain classes of functions. *Doklady Akademii Nauk SSSR*, 148:1042–1045, 1963.

[166] K. D. K. A. Somarathne, S. Hatakeyama, A. Hayakawa, and H. Kobayashi. Numerical study of a low emission gas turbine like combustor for turbulent ammonia/air premixed swirl flames with a secondary air injection at high pressure. *International Journal of Hydrogen Energy*, 42(44):27388–27399, 2017.

[167] S. Song, R. K. Hanson, C. T. Bowman, and D. M. Golden. Shock Tube Determination of the Overall Rate of NH 2 + NO → Products in the Thermal De-NOx Temperature Window. *Internation Journal of Chemical Kinetics*, 2001.

[168] Y. Song, H. Hashemi, J. M. Christensen, C. Zou, P. Marshall, and P. Glarborg. Ammonia oxidation at high pressure and intermediate temperatures. *Fuel*, 181:358–365, 2016.

[169] G. Sorrentino, P. Sabia, P. Bozza, R. Ragucci, and M. de Joannon. Low-NOx conversion of pure ammonia in a cyclonic burner under locally diluted and preheated conditions. *Applied Energy*, 254(x):1–7, 2019.

[170] A. Stagni, C. Cavallotti, S. Arunthanayothin, Y. Song, O. Herbinet, F. Battin-Leclerc, and T. Faravelli. An experimental, theoretical and kinetic-modeling study of the gas-phase oxidation of ammonia. *Reaction Chemistry & Engineering*, 5(4):696–711, 2020.

[171] D. P. Strik, A. M. Domnanovich, and P. Holubar. A ph-based control of ammonia in biogas during anaerobic digestion of artificial pig manure and maize silage. *Process Biochemistry*, 41(6):1235–1238, 2006.

[172] R. Sumathi, D. Sengupta, and M. T. Nguyen. Theoretical study of the h 2 + no and related reactions of [h 2 no] isomers. *The journal of physical chemistry*, 5639(98):3175–3183, 2000.

[173] C.-J. Sung and H. J. Curran. Using rapid compression machines for chemical kinetics studies. *Progress in Energy and Combustion Science*, 44:1–18, 2014.

[174] G. Szegö, B. B. Dally, and G. Nathan. Scaling of NOx emissions from a laboratory-scale mild combustion furnace. *Combustion and Flame*, 154:281–295, 2008.

[175] K. Takizawa, A. Takahashi, K. Tokuhashi, S. Kondo, and A. Sekiya. Burning velocity measurements of nitrogen-containing compounds. *Journal of Hazardous Materials*, 155:144–153, 2008.

[176] M. R. Talipov, S. L. Khursan, and R. L. Safiullin. RRKM and Ab Initio Investigation of the NH(X) Oxidation by Dioxygen. *The journal of physical chemistry*, 19(X):6468–6476, 2009.

[177] Y. Tao, G. P. Smith, and H. Wang. Critical kinetic uncertainties in modeling hydrogen/carbon monoxide, methane, methanol, formaldehyde, and ethylene combustion. *Combustion and Flame*, 195:18–29, 2018. Special Commemorative Issue: Professor Chung King (Ed) Law 70th Birthday.

[178] Y. Tao and H. Wang. Joint probability distribution of arrhenius parameters in reaction model optimization and uncertainty minimization. *Proceedings of the Combustion Institute*, 37(1):817–824, 2019.

[179] A. G. Thaxton, C.-C. Hsu, and M. C. Lin. Rate constant for the nh3 + no2 → nh2 + hono reaction: Comparison of kinetically modeled and predicted results. *International Journal of Chemical Kinetics*, 29(4):245–251, 1997.

[180] A. S. Tomlin. The role of sensitivity and uncertainty analysis in combustion modelling. *Proceedings of the Combustion Institute*, 34(1):159–176, 2013.

[181] A. S. Tomlin and T. Ziehn. The use of global sensitivity methods for the analysis, evaluation and improvement of complex modelling systems. In *Coping with Complexity: Model Reduction and Data Analysis*, pages 9–36. Springer Berlin Heidelberg, 2011.

[182] J. Troe. Predictive possibilities of unimolecular rate theory. *Journal of Physical Chemistry*, 83(1):114–126, 1979.

[183] W. Tsang and J. T. Herron. Chemical kinetic data base for propellant combustion i. reactions involving no, no2, hno, hno2, hcn and n2o. *Journal of Physical and Chemical Reference Data*, 20(4):609–663, 1991.

[184] T. Turányi and A. S. Tomlin. *Analysis of kinetic reaction mechanisms*. Springer, 2014.

[185] T. Turányi, T. Nagy, I. G. Zsély, M. Cserháti, T. Varga, B. T. Szabó, I. Sedyó, P. T. Kiss, A. Zempléni, and H. J. Curran. Determination of rate parameters based on both direct and indirect measurements. *International Journal of Chemical Kinetics*, 44(5):284–302, 2012.

[186] T. Turányi, L. Zalotai, S. Dóbé, and T. Bérces. Effect of the uncertainty of kinetic and thermodynamic data on methane flame simulation results. *Physical Chemistry Chemical Physics*, 4:2568–2578, 2002.

[187] United-Nations. Framework Convention on Climate Change, Adoption of the Paris Agreement. Technical report, United-Nations, 2015.

[188] A. Valera-Medina, M. Gutesa, H. Xiao, D. Pugh, A. Giles, B. Goktepe, R. Marsh, and P. Bowen. Premixed ammonia/hydrogen swirl combustion under rich fuel conditions for gas turbines operation. *International Journal of Hydrogen Energy*, 44(16):8615 – 8626, 2019.

[189] A. Valera-Medina, R. Marsh, J. Runyon, D. Pugh, P. Beasley, T. Hughes, and P. Bowen. Ammonia–methane combustion in tangential swirl burners for gas turbine power generation. *Applied Energy*, 185:1362–1371, 2017.

[190] E. Valkó, T. Varga, A. Tomlin, and T. Turányi. Investigation of the effect of correlated uncertain rate parameters on a model of hydrogen combustion using a generalized hdmr method. *Proceedings of the Combustion Institute*, 36(1):681–689, 2017.

[191] N. Vandewiele, K. Van Geem, M.-F. Reyniers, and G. Marin. Genesys: kinetic model construction using chemo-informatics. *Chemical Engineering Journal*, 207-208:526–538, 2012.

[192] T. Varga, T. Nagy, C. Olm, I. Zsély, R. Pálvölgyi, E. Valkó, G. Vincze, M. Cserháti, H. Curran, and T. Turányi. Optimization of a hydrogen combustion mechanism using both direct and indirect measurements. *Proceedings of the Combustion Institute*, 35(1):589–596, 2015.

[193] T. Varga, C. Olm, T. Nagy, I. G. Zsély, É. Valkó, R. Pálvölgyi, H. J. Curran, and T. Turányi. Development of a Joint Hydrogen and Syngas Combustion Mechanism Based on an Optimization Approach. *International Journal of Chemical Kinetics*, 48(8):407–422, 2016.

[194] A. S. Veríssimo, A. M. Rocha, and M. Costa. Operational, combustion, and emission characteristics of a small-scale combustor. *Energy and Fuels*, 25(6):2469–2480, 2011.

[195] A. S. Veríssimo, A. M. Rocha, and M. Costa. Importance of the inlet air velocity on the establishment of flameless combustion in a laboratory combustor. *Experimental Thermal and Fluid Science*, 44:75–81, 2013.

[196] P. Virtanen, R. Gommers, T. E. Oliphant, M. Haberland, T. Reddy, D. Cournapeau, E. Burovski, P. Peterson, W. Weckesser, J. Bright, S. J. van der Walt, M. Brett, J. Wilson, K. J. Millman, N. Mayorov, A. R. J. Nelson, E. Jones, R. Kern, E. Larson, C. J. Carey, İ. Polat, Y. Feng, E. W. Moore, J. VanderPlas, D. Laxalde, J. Perktold, R. Cimrman, I. Henriksen, E. A. Quintero, C. R. Harris, A. M. Archibald, A. H. Ribeiro, F. Pedregosa, P. van Mulbregt, and SciPy 1.0 Contributors. SciPy 1.0: Fundamental Algorithms for Scientific Computing in Python. *Nature Methods*, 17:261–272, 2020.

[197] F. vom Lehn, L. Cai, and H. Pitsch. Impact of thermochemistry on optimized kinetic model predictions: Auto-ignition of diethyl ether. *Combustion and Flame*, 210:454–466, 2019.

[198] F. vom Lehn, L. Cai, and H. Pitsch. Sensitivity analysis, uncertainty quantification, and optimization for thermochemical properties in chemical kinetic combustion models. *Proceedings of the Combustion Institute*, 37(1):771–779, 2019.

[199] F. vom Lehn, L. Cai, and H. Pitsch. Investigating the impacts of thermochemical group additivity values on kinetic model predictions through sensitivity and uncertainty analyses. *Combustion and Flame*, 213:394–408, 2020.

[200] F. vom Lehn, L. Cai, and H. Pitsch. Iterative model-based experimental design for efficient uncertainty minimization of chemical mechanisms. *Proceedings of the Combustion Institute*, 38(1):1033–1042, 2021.

[201] T. Wall, Y. Liu, C. Spero, L. Elliott, S. Khare, R. Rathnam, F. Zeenathal, B. Moghtaderi, B. Buhre, C. Sheng, R. Gupta, T. Yamada, K. Makino, and J. Yu. An overview on oxyfuel coal combustion—state of the art research and technology development. *Chemical Engineering Research and Design*, 87(8):1003–1016, 2009.

[202] B. L. Wang, H. Olivier, and H. Grönig. Ignition of shock-heated H2-air-steam mixtures. *Combustion and Flame*, 133(1):93–106, 2003.

[203] H. Wang and D. A. Sheen. Combustion kinetic model uncertainty quantification, propagation and minimization. *Progress in Energy and Combustion Science*, 47:1–31, 2015.

[204] V. Wargadalam, G. Löffler, F. Winter, and H. Hofbauer. Homogeneous formation of no and n2o from the oxidation of hcn and nh3 at 600–1000°c. *Combustion and Flame*, 120(4):465–478, 2000.

[205] J. Warnatz. Resolution of gas phase and surface combustion chemistry into elementary reactions. *Symposium (International) on Combustion*, 24(1):553–579, 1992. Twenty-Fourth Symposium on Combustion.

[206] J. A. Wünning and J. G. Wünning. Flameless oxidation to reduce thermal no-formation. *Progress in Energy and Combustion Science*, 23(1):81–94, 1997.

[207] Y. Xin, D. A. Sheen, H. Wang, and C. K. Law. Skeletal reaction model generation, uncertainty quantification and minimization: Combustion of butane. *Combustion and Flame*, 161(12):3031–3039, 2014.

[208] S. Xu and M. C. Lin. Ab initio chemical kinetics for the nh2 + hnox reactions, part i: Kinetics and mechanism for nh2 + hno. *International Journal of Chemical Kinetics*, 41(11):667–677, 2009.

[209] X. You, T. Russi, A. Packard, and M. Frenklach. Optimization of combustion kinetic models on a feasible set. *Proceedings of the Combustion Institute*, 33(1):509–516, 2011.

[210] R. Zellner, F. Ewig, R. Paschke, and G. Wagner. Pressure and temperature dependence of the gas-phase recombination of hydroxyl radicals. *Journal of Physical Chemistry*, 92(14):4184–4190, 1988.

[211] J. Zheng, R. J. Rocha, M. Pelegrini, L. F. A. Ferrão, E. F. V. Carvalho, O. Roberto-Neto, F. B. C. Machado, and D. G. Truhlar. A product branching ratio controlled by vibrational adiabaticity and variational effects: Kinetics of the h + trans-n2h2 reactions. *The Journal of Chemical Physics*, 136(18):184310, 2012.

[212] M. Zieba, A. Brink, A. Schuster, M. Hupa, and G. Scheffknecht. Ammonia chemistry in a flameless jet. *Combustion and Flame*, 156(10):1950–1956, 2019.

[213] T. Ziehn and A. Tomlin. Gui–hdmr – a software tool for global sensitivity analysis of complex models. *Environmental Modelling Software*, 24(7):775–785, 2009.

[214] T. Ziehn and A. Tomlin. Chapter 15 - efficient tools for global sensitivity analysis based on high-dimensional model representation. In G. P. Petropoulos and P. K. Srivastava, editors, *Sensitivity Analysis in Earth Observation Modelling*, pages 297–318. Elsevier, 2017.